

ABSTRACT

ZELENAK, DOMINIC CHARLES. An Investigation of the Krypton Laser-Induced Fluorescence Spectral Lineshape for Composition-Independent Thermometry Applied to Combustion Environments. (Under the direction of Dr. Venkat Narayanaswamy).

Temperature is an important thermochemical property in combustion that holds the key to uncovering several combustion phenomena. Laser diagnostics have become popular tools for non-disruptive thermochemical measurements in reacting flows, owing to their relative simplicity in implementation and their ability to provide multi-dimensional, temporal, and multi-variable measurements. In a practical combustion environment, the local composition is typically unknown, which hinders the effectiveness of many traditional non-intrusive thermometry techniques. This study aims to offset this limitation by developing laser-based thermometry techniques that do not require prior knowledge of the local composition. Recent developments of Kr LIF have encouraged its extension to composition-independent thermometry and pressure measurements in gaseous combustion, as seeded krypton gas offers several significant advantages over other seeded or in situ species extensively featured in previous works.

The principal of thermometry techniques developed in this work leverage the thermochemical dependence of the overlap integral, and therefore required an extensive analysis the Kr LIF absorption spectrum. First, the compositional dependencies of w_C and δ_C were determined by performing two-photon excitation scans of the Kr $4p^6 S_0^1 \rightarrow 5p \left[\frac{3}{2} \right]_2$ transition with various perturber gases at 1 atm and 300K to obtain w_C and δ_C via Voigt profile deconvolution. In the Kr LIF system, $w_C \propto (n_p - 1)^{0.4} \times \mu^{-0.3}$ and $\delta_C \propto \mu^{-0.3}$.

To determine the temperature scaling of the two-photon w_D , experiments were performed to isolate the Doppler broadening in heated low-pressure environments and premixed CH₄ flat

flame exhaust, which yielded that w_D corresponding to a two-photon process scales as $\sqrt{2}$ times the single-photon w_D .

Temperature dependencies of w_C and δ_C were resolved by performing excitation scans with air, N_2 , CO_2 , and CH_4 in environments ranging from 300K to 900K. The collisional width and shift vary with temperature as $T^{-0.8}$ and $T^{-0.6}$, respectively, and these exponents were found to hold for all gases tested, implying they are independent on gas composition. Temperature exponents of -0.8 and -0.6 agree well with values reported using NO and CO as absorbing species in other studies and predicted by dispersive interaction theory.

The above discoveries lead to the development of two composition-independent mean Kr PLIF thermometry techniques. In the first method, the local Doppler broadening is extracted from an excitation scan to yield the corresponding temperature, while the second method utilizes compositional scaling information of w_C and δ_C to determine the temperature from an excitation scan. Both methods are demonstrated by measuring the radial temperature profile of a steady laminar CH_4/N_2 diffusion flame with an air co-flow.

To extend Kr PLIF thermometry to uses on an instantaneous 2D basis, a dual-wavelength temperature imaging technique was developed and demonstrated on CH_4/N_2 and C_2H_4/N_2 diffusion flames. The choice of the excitation wavelengths are made using the knowledge of the fuel mixture and pressure. The two excitation wavelengths lie within the same transition, and their selection is informed such that the resulting Kr PLIF signal ratio depends primarily on the temperature and negligibly on the local composition. Mean temperature fields show excellent agreement when compared to FLUENT simulations, while single-shot temperature measurements exhibit slightly degraded accuracy.

Kr LIF excitation scans were recorded with 0 – 10 atm of N₂ pressure to introduce the effects of high pressure on the Kr LIF spectral line. An asymmetric lineshape model was developed to determine possible mechanisms responsible for departure from symmetric Voigt behavior or those explained by the quasistatic approximation. The w_C , δ_C , and a increase with increasing perturber gas pressure, suggesting that the Kr LIF spectral line is influenced by collision-time asymmetry. Further work is needed to develop an accurate lineshape model that describes physical interactions and to resolve the enhanced broadening at high pressures.

© Copyright 2018 by Dominic Zelenak

All Rights Reserved

An Investigation of the Krypton Laser-Induced Fluorescence Spectral Lineshape for
Composition-Independent Thermometry Applied to Combustion Environments

by
Dominic Charles Zelenak

A dissertation submitted to the Graduate Faculty of
North Carolina State University
in partial fulfillment of the
requirements for the degree of
Doctor of Philosophy

Aerospace Engineering

Raleigh, North Carolina
2018

APPROVED BY:

Dr. Venkat Narayanaswamy
Committee Chair

Dr. Kevin Lyons

Dr. Chih-Hao Chang

Dr. Alexi Saveliev

BIOGRAPHY

Dominic Zelenak, son of Ray (Sr.) and Denise and brother to Ray (Jr.) and Amanda, was raised in Fostoria, Ohio. He attended Trine University in Angola, Indiana, and obtained his Bachelor of Science in Mechanical Engineering in May 2014. Following graduation, Dominic accepted an offer to join the Turbulent Shear Flow Laboratory at North Carolina State University's Department of Mechanical and Aerospace Engineering under the advisement of Dr. Venkat Narayanaswamy in August 2014 to pursue his MS and PhD in Aerospace Engineering. At the focus of his research project was the development and demonstration of composition-independent laser diagnostic techniques using krypton planar laser-induced fluorescence to measure temperature in combustion flows. Dominic received his Master of Science in Aerospace Engineering in December 2017 and continued graduate school to complete his PhD. Upon graduation, Dominic will be beginning his career with NASA Marshall Space Flight Center in Huntsville, Alabama.

ACKNOWLEDGEMENTS

To my advisor, Professor Venkat Narayanaswamy, whom I am grateful for the opportunity granted to me. I will be forever indebted to you for placing your trust in me to progress this research. I wish to thank Forrest Gray Kidd for his experimental mentorship during my first semester. My PhD committee members Drs. Kevin Lyons, Alexi Saveliev, and Chih-Hao Chang, offering more than just merely their time to serve on this committee, have provided immense support during my tenure in graduate school, be it in the laboratory, during their office hours, or in the classroom. To Dr. James Kribs, for always looking out for my well-being and enthusiastically coming to my support. Thank you to Gary Lofton and Steve Cameron for their machining expertise and practical advice in support of my research endeavors. And a very special thank you is extended to Annie Erwin, one of the most caring, considerate, and hardworking people I had the pleasure of meeting at NC State. Lastly, to my Trine University professors, for shaping me into the engineer that I have become and aspire to be.

To my fellow colleagues and friends, for their support inside and outside of the laboratory and their enriching friendships. In particular, thank you to Aravind Ramachandran, for his selfless assistance, deep conversations involving all things life, and cross-culture Indian/American cuisine. To Morgan Funderburk, when the support of a like-minded individual is necessary and a frisbee partner is needed to kill some time. To my fellow bar trivia team, for welcoming my personality and obscure knowledge of film, sports, science, U.S. facts, and music from the '80s every Tuesday night. Lastly, to all past Trine University friends for their continued friendship, and all other NC State friends whose love for the Wolfpack brought us closer together.

This research was funded by the National Science Foundation CBET grant 1511216 and the Air Force Office of Scientific Research grant FA9550-16-1-0190.

DEDICATION

This dissertation is dedicated to my family. My mother Denise Zelenak, for her love, support, sacrifice, and friendship. My sister and her husband, Amanda and Sean Ciechowski; I wish you the best of luck in raising Henry. My brother Ray, whom I have considered my best friend and role model. And my father, Ray Zelenak Sr.; without your discipline, this could not have been possible.

TABLE OF CONTENTS

| | |
|--|------|
| LIST OF TABLES | vii |
| LIST OF FIGURES | viii |
| TABLE OF TERMS | xi |
| Chapter 1: Introduction..... | 1 |
| 1.1 Motivation and Goals | 1 |
| 1.2 Summary of Laser Diagnostic Techniques for Combustion Thermometry | 3 |
| 1.3 Summary of Laser Diagnostic Techniques for Pressure Measurements | 9 |
| 1.4 Approach..... | 11 |
| 1.5 The Spectral Line | 13 |
| 1.6 Overview of Dissertation..... | 17 |
| Chapter 2: Collisional Broadening | 19 |
| 2.1 Introduction to Collisional Parameters..... | 19 |
| 2.2 Physical Description of Collisional Broadening | 20 |
| 2.3 The Impact Approximation..... | 23 |
| 2.4 The Quasistatic Approximation | 26 |
| 2.5 Theoretical Composition Scaling of the Collisional Broadening Parameters..... | 28 |
| Chapter 3: Experiment..... | 33 |
| 3.1 PLIF Optical Setup..... | 33 |
| 3.2 Rayleigh Scattering | 35 |
| 3.3 Nd:YAG..... | 36 |
| 3.4 Dye Laser..... | 37 |
| 3.5 RFLSE Injection Seeder | 39 |
| 3.6 214nm Generation | 41 |
| 3.7 Triggering and Camera Systems | 43 |
| 3.8 Experimental Apparatuses | 46 |
| Chapter 4: Data Processing | 53 |
| 4.1 Kr PLIF Excitation Scans | 53 |
| 4.2 Rayleigh Scattering | 54 |
| Chapter 5: Compositional Scaling of Kr LIF Collisional Parameters..... | 55 |
| 5.1 Experimental Procedure | 55 |
| 5.2 Data Analysis | 56 |
| 5.3 Results and Discussion | 57 |

| | |
|---|-----|
| 5.4 Generality of Scaling | 63 |
| Chapter 6: Two-Photon Excitation Doppler Broadening Temperature Scaling | 66 |
| 6.1 Experimental Procedure | 67 |
| 6.2 Data Analysis and Results | 68 |
| Chapter 7: Collisional Parameter Temperature Scaling | 72 |
| 7.1 Procedure | 72 |
| 7.2 Results | 73 |
| Chapter 8: Development and Demonstration of Composition-Independent Kr PLIF Thermometry Techniques Using the Spectral Line | 76 |
| 8.1 Relations for Thermometry Methods 1 and 2 | 76 |
| 8.2 Experimental Procedure | 77 |
| 8.3 Data Analysis | 79 |
| 8.4 Results and Discussion | 82 |
| Chapter 9: Two-Line Kr PLIF 2D Temperature Imaging Technique | 95 |
| 9.1 Principle of Technique | 95 |
| 9.2 Procedure | 99 |
| 9.3 Results and Discussion | 100 |
| Chapter 10: An introduction to the Kr PLIF Spectral Line at High Pressures | 115 |
| 10.1 Review of the Spectral Line at Increased Perturber Pressures | 116 |
| 10.2 Experimental Procedure | 123 |
| 10.3 Data Analysis | 124 |
| 10.4 Results | 126 |
| 10.5 Hypothesis on the Pressure-Broadening Mechanisms of the Kr LIF Spectral Line | 134 |
| Chapter 11: Summary and Recommendations for Future Study | 143 |
| 11.1 Summary | 143 |
| 11.2 Recommendations for Future Work | 151 |
| APPENDICES | 164 |
| Appendix A: Zircar Ceramic Insulation | 165 |
| Appendix B: Burner | 167 |
| Appendix C: Osram SureHeat Jet | 172 |
| Appendix D: Theoretical Calculations of w_c and δ_c | 182 |
| Appendix E: High-Pressure Lineshape Supplemental References | 183 |

LIST OF TABLES

| | | |
|------------|--|-----|
| Table 3.1 | Dye concentrations..... | 38 |
| Table 5.1 | Absorber and perturber properties | 57 |
| Table 5.2 | Experimental and theoretical values of collisional width and shift | 58 |
| Table 7.1 | Temperature exponents for the collisional width and shift of air, N ₂ , CO ₂ , and CH ₄ | 74 |
| Table 9.1 | Temperature uncertainty due to wavenumber deviation caused by spectral jitter in Flame 1..... | 111 |
| Table 9.2 | Temperature uncertainty due to wavenumber deviation caused by spectral jitter in Flame 2..... | 112 |
| Table 10.1 | Self-broadening and shift of Kr at various pressures..... | 123 |
| Table 10.2 | Testing conditions for the Kr PLIF high-pressure lineshape examination | 124 |
| Table 10.3 | Results of lineshape parameters obtain from the synthetic asymmetric fits at each pressure. Widths and shifts are in units cm ⁻¹ and a is unitless. RMS errors are normalized | 131 |
| Table 10.4 | Results of lineshape parameters obtained from the synthetic symmetric Voigt fits at each pressure in the 0 – 1 atm pressure range. Widths and shifts are in units cm ⁻¹ and a is unitless. RMS errors are normalized..... | 131 |

LIST OF FIGURES

| | | |
|------------|---|----|
| Figure 1.1 | Schematic of energy levels of Kr used in this study | 12 |
| Figure 1.2 | Illustration of contributions of different spectral line broadening mechanisms and sources towards the measured spectrum..... | 16 |
| Figure 2.1 | Perturbations of the energy levels E_1 and E_2 as a function of perturber distance R . The lower diagram shows the resulting frequency shift where $\Delta\nu = (V_2 - V_1)/h$ with V_2 and V_1 being the perturbations of E_2 and E_1 [68]..... | 22 |
| Figure 2.2 | Illustration of collisional broadening and shift | 25 |
| Figure 2.3 | Perturbations for the upper (2) and lower (1) states of transition. The intermolecular difference potential $\Delta v/h$ has a minimum at R_0 , and if $R_0 < \rho$, this minimum may give rise to satellites [68] | 28 |
| Figure 3.1 | Schematic of the experimental setup illustrating the laser setup and camera arrangement | 34 |
| Figure 3.2 | Nd:YAG internal components | 37 |
| Figure 3.3 | Injection seeder circuit | 40 |
| Figure 3.4 | Diagram illustrating the internal triggering system | 44 |
| Figure 3.5 | Diagram illustrating the external triggering system..... | 45 |
| Figure 3.6 | Schematic of the static test cell used for low pressure and compositional scaling scans | 47 |
| Figure 3.7 | In-house designed reconfigurable jet in co-flow or premixed flat flame burner | 49 |
| Figure 3.8 | High-pressure cell | 51 |
| Figure 3.9 | Gas circuit..... | 52 |
| Figure 5.1 | Sample excitation scan with air as the perturber and the corresponding Voigt fit | 57 |
| Figure 5.2 | Comparison of compositional scaling of w_c based on (a) $\mu^{-0.3}$ and (b) $(n_p - 1)^{0.4}\mu^{-0.3}$. The scaling parameters are normalized by those of air. | 60 |
| Figure 5.3 | Comparison of compositional scaling of δ_c based on (a) $\mu^{-0.3}$ and (b) $(n_p - 1)^{0.4}\mu^{-0.3}$. The scaling parameters are normalized by those of air. | 61 |
| Figure 5.4 | Dispersive and inductive atomic energies for freon and CH_4 as a function of distance R . The impact parameter is marked by a '+' symbol | 63 |
| Figure 5.5 | Compositional scaling of w_c and δ_c of NO (γ band) on reduced mass and refractive index with data from [92, 91, 73, 93, 94]: (a) w_c scaled using Equation (29); and (b) δ_c scaled using Equation (30). Dashed line represents the expected value based on the scaling from the present work..... | 64 |
| Figure 6.1 | Photograph of a premixed flat flame used for Doppler broadening temperature calibration..... | 68 |
| Figure 6.2 | Rayleigh scattering temperature measurements for the premixed CH_4 flat flames used in this study | 69 |
| Figure 6.3 | Variation of the Gaussian FWHM with temperature obtained from excitation scans at different temperatures. Data shown compiles the | |

| | | |
|------------|--|-----|
| | experiments performed in vacuum furnace as well as premixed flat flame exhaust at 1 atm..... | 71 |
| Figure 7.1 | Temperature scaling of the a) collisional FWHM and b) collisional shift for N ₂ , CO ₂ , and CH ₄ | 74 |
| Figure 7.2 | Temperature scaling of the collisional parameters of air and premixed methane exhaust corrected for compositional differences | 75 |
| Figure 8.1 | Photographs of the CH ₄ /N ₂ diffusion flame used for this work and an illustration of the measurement domain | 78 |
| Figure 8.2 | Sample experimental excitation scan for the fuel mixture at the jet centerline fitted with (a) Voigt profile and (b) asymmetric Voigt profile. Data points are illustrated with blue squares with the corresponding Voigt fit as a solid red line | 81 |
| Figure 8.3 | Radial profile of the normalized Rayleigh scattering signals across the laminar diffusion flame at an axial location 15mm above the jet exit. The signals were normalized by those of air at 300K and 1 atm..... | 83 |
| Figure 8.4 | Background-subtracted Kr PLIF images of the CH ₄ /N ₂ diffusion flame excitation scan corresponding to peak excitation wavelength of fuel mixture: a) raw Kr PLIF image; and b) sheet corrected Kr PLIF field..... | 85 |
| Figure 8.5 | Excitation scans corresponding to a) the potential core ($T_{M1} = 340\text{K}$, $T_{M2} = 307\text{K}$), b) the intermediate heating region ($T_{M1} = 1270\text{K}$, $T_{M2} = 1157\text{K}$), and c) the reaction zone ($T_{M1} = 1848\text{K}$, $T_{M2} = 1821\text{K}$) | 86 |
| Figure 8.6 | Radial profiles of different lineshape parameters obtained from Kr PLIF excitation scans and their comparison with normalized Rayleigh scattering signal radial profile. The radial profiles correspond to an axial location 15mm downstream of the jet exit. | 87 |
| Figure 8.7 | Comparison of experimental temperature profiles obtained for the laminar CH ₄ /N ₂ diffusion flame with the computed profile: a) comparison between Method 1 and computed profile; and b) comparison between Method 2 and computed profile. Profiles correspond to an axial location 15mm downstream of the jet exit. | 88 |
| Figure 8.8 | Radial temperature profiles using Method 2 at different downstream distances for the CH ₄ /N ₂ flame..... | 90 |
| Figure 9.1 | Kr PLIF signal ratio (R_{Kr}) as a function of temperature for Flame 1 for the wavenumber combination $\omega_{L1} = \omega_L - 0.255\text{cm}^{-1}$, $\omega_{L2} = \omega_L + 0.1\text{cm}^{-1}$ | 98 |
| Figure 9.2 | CH* chemiluminescence images of a) Flame 1 and b) Flame 2 | 100 |
| Figure 9.3 | 1D profiles of the Kr PLIF signal and square of CCD intensity at a single radial location for Flame 1 | 101 |
| Figure 9.4 | (a) Raw and (b) corrected Kr PLIF sheet images at ω_1 with (c) the associated CCD intensity image for Flame 1 | 103 |
| Figure 9.5 | (a) Raw and (b) corrected Kr PLIF sheet images at ω_2 for Flame 1..... | 103 |
| Figure 9.6 | (a) R_{Kr} and (b) Rayleigh scattering (RS) fields of Flame 1 | 105 |
| Figure 9.7 | (a) R_{Kr} and (b) Rayleigh scattering (RS) fields of Flame 2 | 105 |
| Figure 9.8 | Temperature fields of the Kr PLIF two-line thermometry technique for (a) average and (b) single-shot images, with (c) a FLUENT simulation for comparison for Flame 1 | 107 |

| | | |
|-------------|--|-----|
| Figure 9.9 | Temperature fields of the Kr PLIF two-line thermometry technique for (a) average and (b) single-shot images for Flame 2..... | 108 |
| Figure 9.10 | a) Radial temperature profiles of the Kr PLIF fields and FLUENT simulation at $X = 6\text{mm}$ for Flames 1 and 2 | 109 |
| Figure 9.11 | Average temperature flames for a) Flame 1 using $\omega_{L1} = \omega_L - 0.255\text{cm}^{-1}$, $\omega_{L2} = \omega_L + 0.11\text{cm}^{-1}$ and b) Flame 2 using $\omega_{L1} = \omega_L - 0.25\text{cm}^{-1}$, $\omega_{L2} = \omega_L + 0.062\text{cm}^{-1}$ | 110 |
| Figure 10.1 | Speed probability density function at a temperature of 300K for Kr | 121 |
| Figure 10.2 | Excitation scans of Kr fluorescence 0 - 1 atm. Profiles have been offset vertically for legibility..... | 128 |
| Figure 10.3 | Excitation scans of Kr fluorescence 1 - 10 atm | 131 |
| Figure 10.4 | Collisional FWHM of N_2 as a function of pressure | 133 |
| Figure 10.5 | Collisional shift of N_2 as a function of pressure | 133 |
| Figure 10.6 | Asymmetry parameter of N_2 as a function of pressure | 134 |

TABLE OF TERMS

| Symbol | Description |
|--|---|
| A | Einstein Coefficient |
| a | asymmetry parameter |
| a_0 | atomic radius of absorber |
| α | polarizability |
| α_a, α_p | polarizability of absorber, perturber |
| c | speed of light in vacuum |
| C_d | detector parameter |
| C_k, C_6 | constant of proportionality |
| χ_f | mole fraction of species f |
| $\Delta\nu$ | observed frequency shift caused by the perturbation |
| $\delta\nu_{1/2}$ | theoretical collisional FWHM from Lorentz |
| δ_C | collisional shift |
| δ_D | Doppler shift |
| E | unperturbed energy level |
| e | electron charge |
| E_k | unperturbed energy level of state k |
| $\langle e^2 r^2 \rangle$ | square of transition dipole moment |
| $\langle e^2 r^2 \rangle_a, \langle e^2 r^2 \rangle_p$ | square of transition dipole moment of the absorber, perturber |
| ϵ_0 | dielectric permeability |
| $\eta(\rho)$ | phase-shift that results from frequency shift |
| $f(v)$ | molecular speed PDF |
| $f_{aa'}, f_{pp'}$ | Absorber, perturber oscillator strength |
| G | overlap integral |
| g_A | absorption spectrum lineshape function |
| g_C | collisional broadening lineshape function |
| g_D | Doppler broadening lineshape function |
| g_L | laser lineshape function |
| h | Plank's constant |
| I_0 | incident laser intensity |
| i | Laser propagation unit vector |
| k | Rayleigh scattering constant |
| k_c, k_c' | collisional parameter constants |
| k_B | Boltzmann's constant |
| M | molar mass |
| M_a, M_p | molar mass of absorber, perturber |
| M_{Kr} | molar mass of Kr |
| m_a, m_p | mass of the absorber, perturber |
| m_e | electron mass |
| μ | reduced mass |
| N | local number density |

| | |
|----------------------------|---|
| n | refractive index |
| n_a, n_p | refractive index of absorber, perturber |
| n_0 | refractive index in vacuum |
| N_A | Avagadros number |
| N_p | number density of perturber |
| μ_0 | unperturbed frequency |
| ω | wave number |
| ω_0, ω_L | laser center wave number |
| ω_A | absorption spectrum center wave number |
| $\omega_{a\beta}$ | transition wavenumber |
| ω_{L1}, ω_{L2} | Kr PLIF static excitation frequency |
| p | pressure |
| \bar{p} | permanent dipole moment |
| \bar{p}_a^2 | mean square dipole moment of the absorber |
| p_p | dipole moment of the perturber |
| Q | quenching deactivation rate |
| R | radius |
| r | distance from nucleus to outer electron shell |
| \bar{R} | universal gas constant 8.314 J/mol-K |
| R_{Kr} | Kr PLIF signal ratio |
| ρ | distance of closest approach |
| ρ_W | impact parameter |
| S_f | fluorescence of species f |
| S_{Kr1}, S_{Kr2} | Kr signal at ω_{L1}, ω_{L2} |
| σ_{RS} | Rayleigh scattering cross-section |
| t | time |
| T | temperature |
| t_0 | time between collisions |
| τ_C | time of collision |
| U_{disp} | dispersive interaction energy |
| U_{ind} | dipole inducted dipole interaction energy |
| v | velocity |
| v_p, v_{avg}, v_{rms} | Most probable, average, and root mean square velocities |
| \bar{v} | mean relative velocity |
| V | Flow velocity vector |
| $V(R)$ | perturbed energy of level E |
| V_6 | dispersive energy perturbation |
| w | total spectral scan FWHM |
| w_C | collisional broadening FWHM |
| w_D | Doppler broadening FWHM |
| w_L | laser lineshape FWHM |
| w_{Lor} | total Lorentzian FWHM |
| $w_{Lor,0}$ | "average" Lorentzian width |
| X | downstream distance |

Chapter 1 : Introduction

1.1 Motivation and Goals

Laser diagnostic techniques have become popular tools for non-disruptive thermochemical measurements in reacting flows, owing to their relative simplicity in implementation and their ability to provide multi-dimensional, temporal, and multi-variable measurements. Among various target measurement properties, temperature has garnered significant attention owing to its ability to uncover critical parameters such as pollutant formation, flame extinction, and heat release, all of which are crucial in future clean energy systems like homogeneous charge-compression ignition (HCCI) and flameless oxidation (FLOX), among others. Of course, such environments introduce many challenges towards obtaining two-dimensional temperature measurements, such as large spatial temperature gradients, rapid temporal evolution of thermodynamic properties, and varying gas compositions. Perhaps the most important challenge of typical reacting flows is the non-availability of local composition information, which precludes most traditional scattering and spectroscopic techniques. Numerous studies have addressed these complications in recent history and developed laser-based spectroscopic measurements of species concentration and temperature in practical combustion systems, which include pointwise, 1D, and 2D measurements of thermochemical properties [1, 2, 3, 4, 5].

There are several applications that would benefit from acquiring temperature information in a combustion environment of an unknown composition to diagnose commonly experienced adverse effects. For example, combustion instability and lean blowout is experienced frequently in gas turbine and afterburners in off-design conditions. These instabilities occur during large pressure fluctuations (1 to 5 atm) that couple with aero-structural resonant frequencies. Temperature and pressure field information is critical in diagnosing and preventing such scenarios.

The tight coupling of temperature and pressure in a rapidly varying combustion environment require measurements to be made without prior knowledge of the composition. Pulsed detonation engines (PDEs) offer higher thermodynamic efficiencies compared to traditional gas turbines. In PDEs, combustion occurs in highly variable temperature and pressure fields. It is necessary to learn how the chemical kinetics evolve in unsteady thermodynamic environments to advance these technologies and promote practical implementation. Due to the unsteadiness, compositional information is still mostly unknown. The key issues faced to further develop these technologies include fast and efficient fuel to oxidizer mixing, prevention of auto-ignition, and proper inlet-nozzle integration. Scramjet propulsion technology has suffered to an inability to achieve reliable auto-ignition and sustained combustion. Again, these chemical reactions occur in varying temperature, pressure, and composition environments. And lastly, chemical kinetics models require exact temperature and pressure information as reactions progress. The information obtained from this research can vastly improve the fidelity of current chemical kinetics models. An evolving composition during chemical reactions requires a diagnostic tool which is insensitive to local composition to successfully obtain temperature and pressure.

From the above discussions, there exists a need to develop diagnostic tools to provide 2D temperature fields in reacting flows, while still circumventing the obstacle of unknown local gas compositions. Additionally, there is an increasing need to measure other quantities such as mixture fraction and soot concentration to enhance high-fidelity combustion and flow models. Due to these demands, the purpose of this dissertation is to develop spectroscopic laser diagnostic thermometry techniques that may be applied to arbitrary combustion mixtures, without requiring knowledge on the local composition. The proposed diagnostic tools shall also have the potential to acquire

pressure measurements in reacting flows, as such a measurement technique is currently lacking within the laser diagnostics community.

1.2 Summary of Laser Diagnostic Techniques for Combustion Thermometry

Over the last several decades, many laser-based thermometry techniques have been developed and applied to high speed non-reacting/reacting flows and novel combustion environments. These techniques include, but are not limited to, Rayleigh scattering, Raman scattering, Coherent anti-Stokes Raman spectroscopy (CARS), absorption, and planar laser-induced fluorescence (PLIF). A brief explanation and literature review of each of these techniques pertaining to combustion thermometry is provided below.

Planar laser-induced fluorescence (PLIF) has garnered significant attention towards obtaining multi-dimensional temperature and species concentration measurements in reacting environments, owing to its high signal yield and sensitivity [6, 7]. PLIF relies upon the resonant excitation of a specific species, either externally seeded or present in the flow, to acquire flow properties such as species concentration, velocity, temperature, and density. PLIF strategies have been developed that employ excitation of electronic transitions of atomic species or vibrational/rotational transitions of molecular species. Planar laser-induced fluorescence imaging of radicals such as OH and NO have been two of the most common thermometry techniques that have been researched extensively in the past due to their natural occurrence in high temperature environments and several accessible molecular transitions. OH and NO PLIF thermometry imaging involves determining the Boltzmann distribution of the molecule's population at one or two vibrational-rotational energy levels, which depends on local gas temperature. Heinze et al. performed OH PLIF in combination with absorption in a lean premixed laminar flame (where OH is plentiful throughout) by measuring the absolute concentration of the OH radical and temperature

[8]. Common variations of this technique include two-line OH PLIF thermometry, which has shown to provide accurate instantaneous 2D fields of temperature in reacting and high-speed flows. Two-line approaches utilize the ratio of two broadband PLIF images excited from separate ground states. The resulting signal ratio becomes sufficiently independent of number density, variations in the overlap integral, and fluorescence yield (including fluorescence quenching) and is primarily a function of laser energy, system parameters, and Boltzmann statistics of the absorbing states. Some of the earliest works in two-line OH PLIF thermometry were undertaken by Professor Hanson's group, demonstrated mainly in high-speed H_2/O_2 reacting flows [9, 10, 11]. Two-Line OH PLIF thermometry has since been expanded to lean methane/air flames [12] in areas of adequate OH concentration ($T \geq 1500\text{K}$). NO PLIF has been used to obtain temperature contours of a rod-stabilized lean premixed methane flame using Boltzmann statistics and several underlying assumptions to allow for single-line excitation [13]. An important advantage of NO is that it may be externally seeded into the flow to achieve desired signal levels. Similarly, NO PLIF soon evolved for uses on a two-line basis, producing temperature measurements in under-expanded jets [14], transverse jets in cross-flow [15], and NO seeded flames [16]. Additional work in NO PLIF has demonstrated its use for the detection of NO in high pressure flames [17, 18].

However, molecular fluorescence techniques are not without demerits. A limitation of OH PLIF is the availability of temperature data only in the fuel lean regions where OH is typically found. Because of this, temperature measurements using OH PLIF are restricted to temperatures above 1400K, making it most commonly used for concentration measurements and reaction zone demarcation for combustion applications [19, 20, 21]. Though NO may be externally seeded, proper care must be taken due to its toxicity which may restrict overall signal levels. Additionally, seeded NO has a proclivity to react with the combustion mixture, which will alter the

thermochemical properties of the flow. Furthermore, molecular two-line PLIF strategies are susceptible to background emission and trapping due to UV excitation, require high laser intensities and complex setups, and encounter problems in fuel rich environments.

In a different approach to thermometry, ketones may be employed to obtain temperature field measurements by using PLIF [7]. Naphthalene has been used in this role, as the temperature-dependent wavelength shift of naphthalene may be used to obtain temperature [22]. Since naphthalene is present over large parts of fuel rich regions, temperature measurements can span a larger domain compared to OH. Further, naphthalene is one of the naturally occurring species in the combustion of long-chain hydrocarbons like gasoline and diesel; hence, naphthalene PLIF can be used for thermometry within fuel-rich regions without external seeding. Laser-induced fluorescence of toluene has also been demonstrated in recent history, being used to measure temperature in shock tube flows [23] and heated gas jets [24].

One of the greatest disadvantages with using diatomic and polyatomic molecules or radicals for PLIF imaging at high pressures is the collisional narrowing effect, which severely inhibits data reduction. Hence, PLIF imaging of atomic species has gained popularity for thermometry in the recent years, namely two-line atomic fluorescence (TLAF) of seeded indium atoms in reacting flows. Dec & Keller noted the potential use of indium atoms, which have closely spaced energy levels that lead to a Boltzmann-type population distribution, by performing point-wise In PLIF temperature measurements for a number of laminar flames contained within a high-pressure combustion chamber [25]. Later, Professor Kaminski's group demonstrated that In TLAF scanning techniques may be used to obtain mean temperature measurements in fuel-rich sooting flames [26] and by the use of diode lasers, noting its potential use in high temperature reacting environments [27]. A number of works by Professor Nathan's group have demonstrated

instantaneous In PLIF temperature fields in laminar and turbulent sooting [28, 29, 30] and non-sooting flames [31], with the capability of reporting temperature measurements in the range of 800 – 2600K so long as indium atoms are present in the combustion mixture [32]. Additionally, In TLAF has seen use in turbulent spray flames [33] using similar approaches.

Other than fluorescence techniques, Rayleigh scattering imaging of local combustion mixtures is another common thermometry technique [34, 35]. This technique involves imaging the elastic scattering of a laser beam/sheet from the gases in a combustion mixture. The scattering intensity is proportional to the local number density and scattering cross-section of the local mixture (which depends on local mixture composition), and the temperature is determined from the local number density. Thus, in general combustion mixtures, additional information about the local chemical composition is necessary for temperature measurements using Rayleigh scattering imaging. Despite this shortcoming, Rayleigh scattering has proven to be a very effective tool in determining temperatures in the well-characterized DLR $\text{CH}_4/\text{H}_2/\text{N}_2$ turbulent flames due to its relatively constant scattering cross-section [36], as well as providing vapor-fuel concentrations in diesel jets [37]. Further, scattering cross-sections may be achieved through estimates of the combustion composition supplied via simulation calculations of sophisticated chemical kinetics codes [21]. An important derivative of Rayleigh scattering is Filtered Rayleigh Scattering (FRS) imaging [38, 39], which enhances flow qualities by removing abnormal signals from laden particles and unwanted background reflections. More importantly, FRS images the spectral wings of the Rayleigh scattering spectra by filtering the emission with a molecular iodine filter, which may provide temperature, velocity, and pressure field information of known compositions. An iodine filter blocks the center portion of the Rayleigh-Brillouin (R-B) spectrum, so the intensity of the wings passes through the filter. This intensity is relatively independent of pressure yet depends

upon temperature and density due to spectral broadening, and velocity due to Doppler shift. Elliot et al. employed this technique with a H₂/air flame and reported temperatures within 2% of expected values [40], and was also used to produce 2D temperature fields in turbulent non-premixed jet flames [41].

As an inelastic counterpart to Rayleigh scattering, Raman scattering measurements have been performed in many previous studies to determine the temperature in turbulent and laminar flames. The principle of thermometry in Raman scattering is determining the ratio of Stokes and anti-Stokes scattering signals, which is a monotonic function of temperature [42, 43]. Like Rayleigh scattering, Raman scattering can provide temperature information across the entire combustion field. Furthermore, in contrast to Rayleigh scattering, Raman scattering does not require information about local composition to obtain temperature. However, the limitations of Raman scattering thermometry include very poor signals for a given laser energy (about 1/1000th of Rayleigh scattering signals), constraints to combustion fields without laden particles like soot, and being utilized only for combustion of simple fuels. To counteract these shortcomings, multiple techniques may be used in combination with Raman scattering, such as OH/CO/NO PLIF and Rayleigh scattering [19, 20]. However, such experimental setups are highly complex and require numerous excitation sources, calibration devices, and detection systems. Some of the efforts to improve the signal levels in Raman scattering and to extend the applicability to complex fuels has resulted in development of Coherent Anti-Stokes Raman Scattering [44] (CARS). Similar to Raman scattering, CARS probes vibrational signatures of molecules but uses multiple photons from multiple laser sources to create a coherent signal which may provide temperature and density information via its spectral distribution. Thermometry using CARS and its more recent derivatives like fs-CARS has found wide applications such as simple flames [45, 46], under-expanded sonic

jets [47], supersonic combustion [48], and ground testing of propulsion devices [49]. Unfortunately, implementation of CARS requires at least three high intensity lasers with pico-/femto-second systems for adequate signal quality and measurements are confined to points. Further, CARS is restricted to moderate pressure environments due to spectrum complications posed by collisional narrowing effects.

Apart from scattering techniques, absorption spectroscopy techniques, most often those that employ tunable diode lasers, may provide precise measurements of species concentration, velocity, pressure, and temperature [2, 50]. Absorption spectroscopy operates on the relatively simple premise of the Beer-Lambert law by measuring the laser irradiance before and after the probe beam enters the imaging domain. The relative laser transmission is a function on the distance traversed and the absorption coefficient, which depends upon the absorbing species partial pressure, the line strength, and the lineshape function. Some of the early applications of tunable diode laser absorption spectroscopy (TDLAS) to measure temperature in a combustion environment was performed by Hanson's group, in which the temperature of the post-flame region of a premixed flat flame was acquired [51]. This technique involves rapidly modulating the wavelength across a narrow spectral interval, imaging the laser transmittance of two similar transitions originating from different vibrational levels. This two-line approach relates the ratio of the relative transmittance of these CO transitions to the temperature using the Beer-Lambert absorption law. This technique has since seen several improvements and has been used in many scenarios, including infrared absorption of water vapor in a scramjet engine to obtain path-integrated temperature [52]. Such techniques employ distributed feedback tunable diode lasers with kilohertz repetition rates for rapid wavelength tuning and are capable of high SNRs, which have seen use in high temperature (1050K) and pressure (25 atm) environments to produce

temperature and H₂O concentration measurements [53] and in shock heated oxygen flows to obtain multiple thermodynamic properties [54]. The important shortcoming of TDLAS is that it provides only line of sight integrated measurements, which can be an issue when highly turbulent and heterogeneous environments are probed.

1.3 Summary of Laser Diagnostic Techniques for Pressure Measurements

Though significant work has been done in laser-based temperature measurements, there exists only limited contributions of spectroscopic pressure (or density) measurements in variable property flows, the majority of which is exclusive to non-reacting homogenous gas environments. One of the most common techniques for spectroscopic density measurements in known compositions is Rayleigh scattering. For simplistic flows such as high-speed air jets, if the composition of the flow is known, and reference images are acquired to calibrate the optical system, Rayleigh scattering may provide density and temperature measurements to acquire pressure measurements using the ideal gas law. FRS has since commanded a significant majority of this market, which has shown to provide pressure field information of known compositions [55], and specifically in supersonic free jets [56]. As explained by George et al. 2014 [56], the iodine filter blocks the center portion of the Rayleigh-Brillouin (R-B) spectrum, so the intensity of the wings passes through the filter. This intensity is relatively independent of pressure yet depends upon temperature and density due to spectral broadening, and velocity due to Doppler shift. It is important to note that because of the spectral broadening, the scattering intensity will increase with increasing temperature for a given density, but due to the ideal gas law, the density would actually decrease with increasing temperature. A possible solution to remove temperature sensitive density measurements is to tune the laser wavelength near the edge of the blocking region of the iodine absorption line, thereby enabling the filter to still block unwanted scattering and produce FRS

signals that are less sensitive to temperature. In an idealized scenario due to a symmetric R-B spectrum, half of the lineshape would be filtered with a perfectly vertical iodine cutoff wavelength, making the signal a sole function of density. Unfortunately, iodine filters have a finite cutoff slope, which still makes the FRS signal have a finite temperature sensitivity using this method [56]. George et al. [56] have noted that in their experimentation of supersonic free jets, the FRS images offer greater contrast between pre- and post-shock regions because of the ideal gas law tradeoff between density and temperature, and may offer quantitative density measurements if temperature effects are compensated for and if the laser is tuned to the iodine filter's 50% absorption line [56]. Elliot et al. [57] performed filtered angularly resolved Rayleigh scattering (FARRS) and conventional Rayleigh scattering on an under-expanded supersonic axisymmetric jet for simultaneous velocity, density, and temperature measurements, in conjunction with iterative computational Rayleigh scattering intensity models. In a later study, Boguszko and Elliott [58] used an FRS scanning technique to evaluate velocity, temperature, density, and in turn, the pressure in a free jet. An injection-seeded Nd:YAG laser was scanned over a range of laser frequencies to obtain FRS intensity distributions, which were functions of velocity and thermodynamic properties, and the properties were then determined using a curve fitting algorithm and the ideal gas law. Results for subsonic and supersonic cases demonstrate the ability of the technique to resolve gradual property gradients as well as under-expanded Mach diamonds.

PLIF has also been adapted to obtaining pressure measurements in gaseous flows. PLIF of NO and OH has been used by Palmer and Hanson [59] to image temperature and density variations for high-speed, transient flow fields produced by a reflection shock tunnel, using both N₂ and Ar as test gases. NO molecules were excited in an under-expanded jet issuing from a converging-diverging nozzle and within the shock reservoir to yield images qualitatively demonstrating

density field variations over different time steps. Similarly, OH PLIF images were acquired to illustrate the formation of combustion gases issuing from a supersonic free jet. For both techniques, however, quantitative measurements of density or pressure were not reconstructed from PLIF signal levels, due to PLIF signal dependence of temperature and pressure (lower state Boltzmann fraction, spectral convolution, fluorescence quenching, etc.) making PLIF images difficult to analyze [59]. This concept becomes most apparent in the combustion mixture OH PLIF images, where areas of greatest density do not provide the greatest signal levels due to temperature sensitivity and changing flow conditions. More recently, Narayanaswamy et al. [60] used externally seeded Kr in supersonic flows to perform two-photon PLIF with air as the test gas for pressure extraction. By neglecting lineshape effects due to low temperatures and pressures and assuming a constant fluorescence quenching, the local number density acquired from PLIF signals was related to the local temperature using isentropic flow relations, and density jumps were determined using shock relations. Lastly, CARS has also been used to determine pressure of known composition sonic flows [47].

1.4 Approach

From the above discussions, there exists a need to develop diagnostic tools to provide 2D temperature fields in reacting flows over the entire combustion temperature domain, while still circumventing the obstacle of unknown local gas compositions. Additionally, there is an increasing need to measure other quantities such as mixture fraction and soot concentration to enhance high-fidelity combustion and flow models. Furthermore, the scientific community would benefit greatly if such a technique may be adapted to provide pressure measurements in reacting flows. Due to these demands, krypton planar laser-induced fluorescence (Kr PLIF) [61] has attained significant attention in recent years by imaging 2D mixture fraction in turbulent non-sooting and sooting

flames [62, 63], scalar fields in supersonic/hypersonic flow [60, 64], 1D measurements of velocity in hypersonic flow fields [65], and steady state temperature fields in reacting flows [66]. Furthermore, Kr PLIF has been expanded to demonstrate the feasibility of simultaneous measurements of mixture fraction and soot volume fraction in turbulent non-premixed flames [63]. Krypton is non-reactive, non-toxic, and does not suffer from the limitations presented by diatomic or polyatomic tracers.

The transition of interest for this study is the $4p^6 S_0^1 \rightarrow 5p \left[\frac{3}{2} \right]_2$, which is illustrated in Figure 1.1. The krypton atoms are excited using a two-photon excitation scheme centered at $\lambda = 214\text{nm}$. The atoms undergo a radiative decay to intermediate states $5s \left[\frac{3}{2} \right]_1$ and $5s \left[\frac{3}{2} \right]_2$ with a branching ratio of 29% and 71% respectively [67].

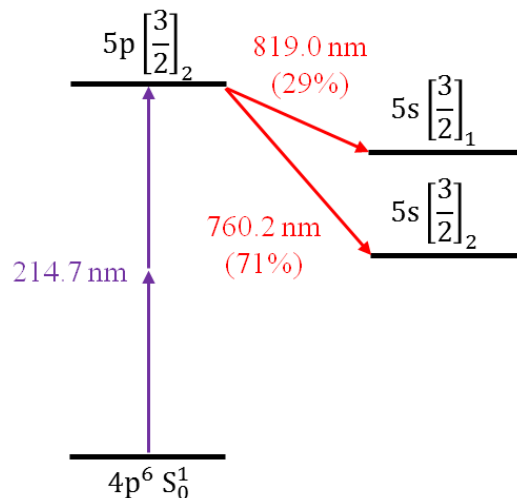


Figure 1.1: Schematic of energy levels of Kr used in this study.

As previously mentioned, the central goal of this dissertation is to develop composition-independent Kr PLIF thermometry techniques with the potential to expand to pressure measurements. But first, an inquiry to the Kr PLIF $4p^6 S_0^1 \rightarrow 5p \left[\frac{3}{2} \right]_2$ spectral line is necessary to resolve the thermochemical dependencies and scaling of the line broadening parameters, namely the collisional broadening.

The thermometry methods developed in this work use the spectral lineshape of a target absorbing species (Kr), to determine the temperature. The rationale behind using spectral lineshape information stems from the relatively simple dependence of spectral broadening parameters on local (mixture-averaged) environment properties without being species specific. This contrasts with other variables contributing to the excitation scan like fluorescence quenching, which has a species-specific relation on the quenching partner depending on the complex (many times unresolved) chemical pathways between the fluorescing and quenching species. The two-photon excitation fluorescence equation for the species f is given by the following [2].

$$S_f = C\chi_f N I_0^2 \frac{A}{A + Q} G \quad (1)$$

The overlap integral, which the variable of specific interest for this study, is the convolution of the incident laser spectrum and the broadening spectrum of the absorbing species as given by the following equation.

$$G = \int_{-\infty}^{\infty} g_L(\omega, \omega_L) g_A(\omega, \omega_A) d\omega \quad (2)$$

It should be noted that like Q and χ_f , the overlap integral is also function of the local composition and temperature at a given pressure. In the thermometry methods demonstrated in this dissertation, the overlap integral's dependence on local composition will be accounted for to determine the local temperature. Details on the absorption spectrum's, and in turn the overlap integral's, thermochemical dependence is provided in subsequent sections.

1.5 The Spectral Line

The width and shape of spectral lines centered at the transition's resonant frequency is influenced by a multitude of processes via the convolution of each respective broadening

characteristic. These processes include natural broadening, power broadening, instrument broadening, Doppler broadening, and broadening caused by interactions with neighboring particles, otherwise known as collisional or pressure broadening. These lineshapes may be examined by absorption or emission processes, and the importance is measured by the spectrum's full-width at half-maximum (FWHM). The FWHM depends upon the broadening processes but does not give any information about the wings of the lineshape [68].

Natural broadening, a consequence of the finite lifetime of an excited state due to spontaneous emission, results in a Lorentzian profile and has a FWHM on the order of 0.1 – 100 MHz or $10^{-5} - 10^{-2} \text{ cm}^{-1}$, which is significantly smaller than the range of Doppler widths normally encountered [68]. Power broadening, or saturation broadening, is the broadening of the spectral line that results from intense excitation sources but occurs only in situations with extremely intense laser fields. Instrument broadening occurs due to a known finite width contribution of the laser line (w_L) used for excitation, which is strictly a result of probing the measurement domain and is not influenced by a physical interaction in the flow.

Characteristics of the thermodynamic environment may be deduced from the Doppler broadening and collisional broadening, which comprise the most prominent broadening phenomena in neutral gaseous environments of atoms/molecules. These contributions yield strong dependencies on the local composition and thermodynamic conditions for the absorption lineshape. Figure 1.2 illustrates each of these contributions along with the spectral broadening parameters that will be used in this manuscript. Doppler broadening is the result of the Doppler Effect, which is the apparent shift in wavelength of the signal from a source moving towards (blue shift) or away (red shift) from the observer. This shift arises from the thermal motions of emitting atoms or molecules and occurs when the observer sees a spread in shifts corresponding to a spread

of velocities. The emitter velocity distribution can be described by the Maxwellian distribution, giving rise to a Gaussian profile of the line with a FWHM of w_D . This causes the Doppler width to be dependent on the temperature and absorber molecular weight and independent of perturber density, if assuming velocity changing collisions are absent (free motion) and is not shifted from the laser centerline (ω_0). Doppler broadening is considered inhomogeneous broadening, in that it is caused by effects in which different atoms or molecules provide dissimilar contributions. On the other hand, collisional broadening, or pressure broadening, is caused by collisions and interactions of the absorbing species with other surrounding gas particles, making it dependent upon the local properties of the surrounding medium, temperature, and pressure. It is a well-known fact that lines are broadened, sometimes asymmetrically, and often shifted by increasing gas pressure [68]. Collisional broadening is considered homogeneous broadening, in that it is a form of broadening which affects all absorbing atoms in the same way. Collisional broadening is the result of the effective lifetime of transition (which results in natural broadening) being reduced due to collisions with perturbing molecules/atoms. It is characterized by the randomized phase of the emitted radiation caused by frequent impacts of perturbers. This profile is Lorentzian in shape if the collisional broadening (w_C) and shift (δ_C) is proportional to pressure at a fixed temperature [69].

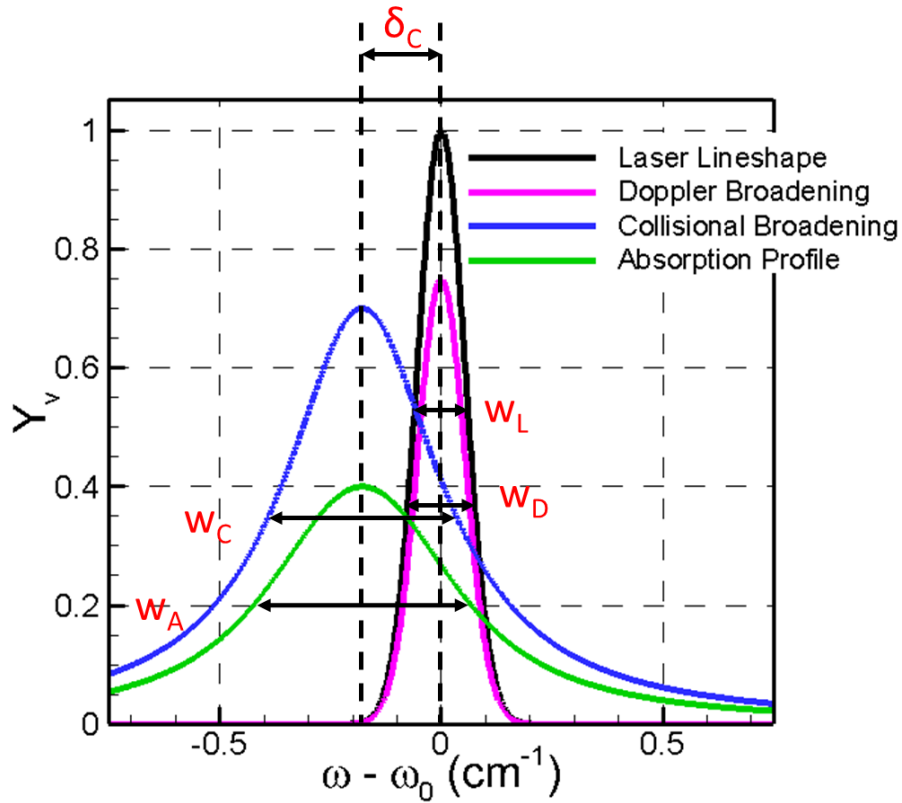


Figure 1.2: Illustration of contributions of different spectral line broadening mechanisms and sources towards the measured spectrum.

When collisions giving rise to Doppler broadening and pressure broadening are uncorrelated or independent, the resulting spectral lineshape or absorption profile takes the form of a symmetric Voigt profile, which is the convolution of each of the above line broadening contributions:

$$g_A(\omega, w_A) = g_D(\omega_0, w_D) \otimes g_C(\omega_0 + \delta_C, w_C) \quad (3)$$

This assertion is valid for intermediate pressures. However, in certain circumstances when these broadening characteristics can no longer be considered independent, departures from the idealistic Voigt profile may be observed, most notably resulting in narrowing or asymmetry of the spectral line. These departures occur due to enhanced collisional broadening influenced by increasing gas pressure. This concept will be revisited in later chapters.

1.6 Overview of Dissertation

At the focus of this dissertation is the goal of developing and demonstrating composition-independent Kr PLIF thermometry techniques applied to combustion environments. However, to do so an in-dept understand on the Kr PLIF spectral line and broadening phenomena is necessary to deduce the thermochemical dependencies that lie therein. Chapter 2 provides a physical explanation of the collisional width and shift and two theoretical cases that must be considered to understand the theoretical basis of collisional broadening. A discussion follows concerning two limiting cases on the compositional scaling of the collisional parameters according to large or small energy level separations of the absorber and perturber when dispersive forces dominate the collision interaction. Chapter 3 provides detail descriptions of the experimental setup and all apparatuses used for this study. Chapter 4 briefly explains the data processing routines used on a majority of the specific studies in this dissertation. Chapter 5 covers the first experimental investigation of this research, where the compositional scaling of the collisional broadening parameters is determined by performing excitation scans on various perturber gases at 300K. In Chapter 6, the Doppler broadening according to a two-photon excitation process is scaled with temperature to assess the validity of the classical interpretation of the Doppler width on the current Kr LIF lineshape. Chapter 7 performs a similar analysis, wherein the temperature scaling of the collisional width and shift are determined for several different gas compositions. Upon completion of the work in Chapters 5, 6, and 7, the Kr LIF line broadening parameters' thermochemical dependencies were fully determined, and thus Chapter 8 provides the first development and demonstration of two composition-independent Kr LIF thermometry techniques applied to a non-sooting laminar diffusion flame. Both techniques extract temperature by exploiting the thermochemical dependencies of the line broadening parameters covered in the preceding

chapters. Chapter 9 introduces a newly developed two-line Kr PLIF thermometry technique that may be applied to arbitrary combustion mixtures with knowledge of the fuel species and pressure. This technique is demonstrated on two different steady laminar diffusion flames and has the ability to produce 2-D temperature measurements on a shot-by-shot basis, suggesting that its use may be extended to turbulent flames. And lastly, Chapter 10 offers an introduction to the Kr LIF spectral line when exposed to high-pressure environments. Krypton is subjected to N_2 pressures up to 10 atm to determine the physical mechanisms, if present, are at play in the Kr PLIF system so that high-pressure flames may be studied in the future. Chapter 11 closes with a summary and suggestions for future work.

Chapter 2 : Collisional Broadening

2.1 Introduction to Collisional Parameters

Most spectroscopic techniques (tunable diode-laser absorption spectroscopy, for example) involve making spectrally resolved measurements and fitting the measured spectrum with a synthetic curve that accounts for various line broadening phenomena. Hence, line broadening of absorption spectra has been a subject of investigation over several decades owing to its application in combustion science. There have been many reputable reviews [70] and textbooks [68] that are concerned with the theoretical analysis of line broadening phenomenon and surveying different experiments that were performed over several decades. In an environment involving neutral species, Doppler and collisional broadening are the two mechanisms responsible for line broadening. Among the two, collisional broadening and shift have elicited significant research efforts owing to the complexity of causative interactions and the resultant compositional dependence. Traditionally, the collisional width and shift in a mixture containing different species at pressure p is given by,

$$w_c = p \sum_{i=0}^n \chi_i \times w_{c,i} \quad (4)$$

$$\delta_c = p \sum_{i=0}^n \chi_i \times \delta_{c,i} \quad (5)$$

The collisional width and shift of the individual species are known from theoretical considerations or through experimental determinations. Some of the earliest semi-classical theories were developed several decades back to predict the theoretical expressions for the collisional broadening parameters (discussed in greater detail in proceeding sections). The most common treatment of interactions is made by assuming London dispersive forces are the dominant interacting forces, by which the compositional scaling of the collisional width and shift were

derived. Lindholm and Forley further showed a simplification of the compositional scaling of collisional broadening width and shift when the perturber electronic energy gap is much larger than absorber electronic energy gap. This simplification was validated in the line broadening of alkali and alkaline earth metals by inert gases [71], and more recently for iodine spectral broadening in air and nitrogen [72]. In contrast, the predicted simplification was not found to be valid for NO spectral shift by common combustion species, as reported by Hanson's group [73, 74]. The importance of this Kr-combustion perturber study is that the assumption of perturber energy gap being much larger than absorber energy gap is not valid in their absorber/perturber combinations, suggesting that the simplification of Lindholm-Forley is not extendable to these situations.

Prior to developing and demonstrating composition-independent thermometry techniques, compositional and thermodynamic scaling of collisional broadening parameters of Kr $4p^6 S_0^1 \rightarrow 5p \left[\begin{smallmatrix} 3 \\ 2 \end{smallmatrix} \right]_2$ transition in an environment containing different combustion species will be investigated. This combination of absorber and perturber, again, does not fall into the regime that leads to simplifications of Lindholm-Forley. But first, a physical description of collisional broadening is provided in the next sections.

2.2 Physical Description of Collisional Broadening

The simplest model describing the process of collisional broadening was proposed by Lorentz, which states that the wave-trains (time dependence of emitted radiation) from the absorbing atoms are cut off abruptly during collisions after an average time t_0 . The number of undisturbed atoms after time t is related to the mean lifetime

$$N(t) = N(0)e^{-\frac{t}{t_0}} \quad (6)$$

which is the same expression describing spontaneous decay. The resulting line profile is Lorentzian with a FWHM given by

$$\delta\nu_{\frac{1}{2}} = \frac{1}{2}\pi t_0 \quad (7)$$

The collisions of other particles “interrupt” the emission process, increasing the emission energy uncertainty, thereby broadening the spectral line. This model, unfortunately, does not provide an explanation for collisional shift, nor does it account for asymmetry which is sometimes observed in pressure broadened lines. To understand these aspects of a collisionally broadened spectral line, the physical origins of collisional broadening from a classical perspective are explored.

Consider an absorber separated from a perturber by a distance R . There exist three typical intermolecular forces (all attractive) between these two species: electrostatic, dipole-induced-dipole, and dispersion. The effect of these three forces depends upon the nature of the perturber and absorber. In the situation where both the absorber and the perturber have a permanent dipole (polar species), the intermolecular forces are dominated by electrostatic forces. In the situation when one of the species is polar (possesses a strong dipole moment) while the other is non-polar, the dipole-induced-dipole interactions may provide a dominant contribution. Finally, when the absorber and perturber are both non-polar, London dispersive forces dominate the interactions. In this situation, the instantaneous dipole caused by an asymmetric electron cloud distribution in one species alters the electron cloud distribution in the other, resulting in an attractive force. In general, an interaction which is a function of R and tends to zero for large R may be expressed as a power series in $1/R$ [68].

$$V(R) = \sum_k C_k R^{-k} = h\Delta\nu \quad (8)$$

The type of interaction determines the 1st non-vanishing term in the series and can be expressed as the following for any interaction type.

$$V(R) = \frac{C_n}{R^n} + \text{terms of shorter range} \quad (9)$$

Physically from a broad point of view, a collision event influenced by any of the molecular interactions described above causes a shift in the absorbing atom's energy levels, resulting in the observed collisional broadening and shift (see Figure 2.1). The upper energy level is more perturbed than the lower energy level, which results in a net decrease in their separation, corresponding to a decrease in the frequency transition ("red shift"). An explanation of the above claim will be provided in section 2.5.

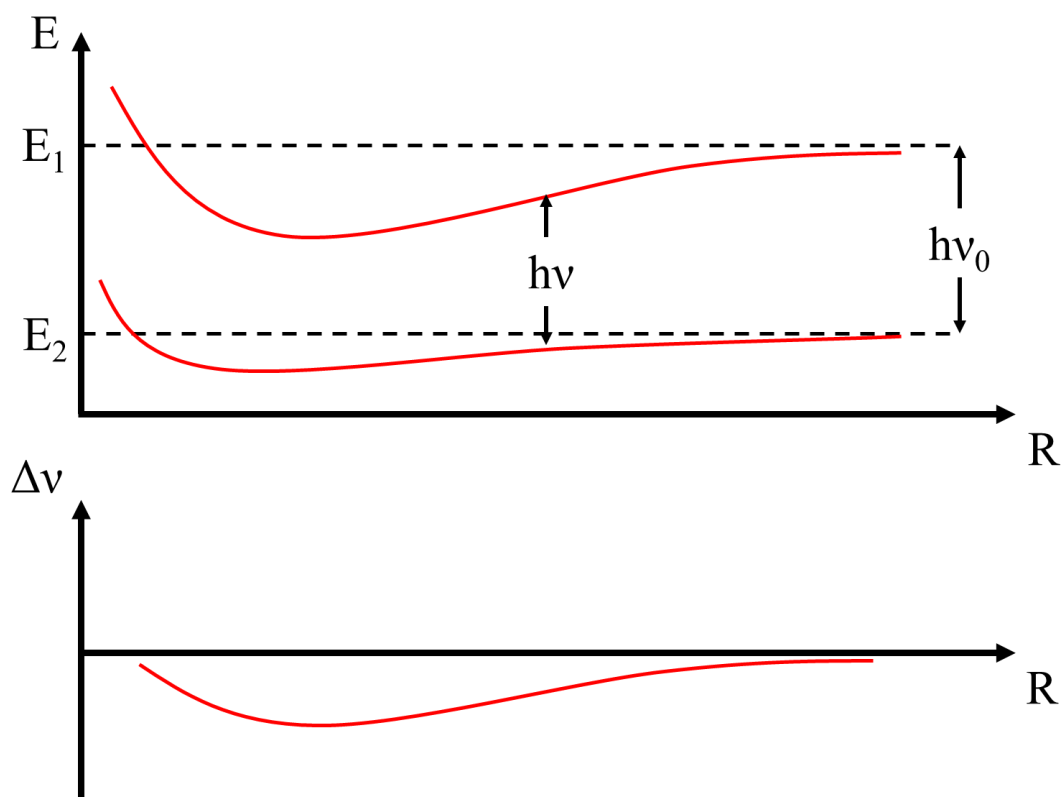


Figure 2.1: Perturbations of the energy levels E_1 and E_2 as a function of perturber distance R . The lower diagram shows the resulting frequency shift where $\Delta\nu = \frac{V_2 - V_1}{h}$ with V_2 and V_1 being the perturbations of E_2 and E_1 [68]

2.3 The Impact Approximation

Next, it is necessary to take two limiting cases of collision events to properly describe distinctive features of the spectral line in different collision regimes: the impact approximation and the quasistatic approximation. The impact approximation assumes an instantaneous collision while the quasistatic approximation assumes nearly constant perturbation. Furthermore, the impact approximation also makes two other assumptions: the binary approximation and the classical path approximation, which state that each collision involves one perturber and that the path of the perturber relative to the radiating atom is unchanged by the interaction, respectively [68]. The impact approximation may be taken as the simplified case when the spectrum is not dominated by significant collisional interactions. It may be used most of the time so long as perturber pressures are not overwhelmingly high. On the other hand, the quasistatic approximation is useful when describing collisional interactions where perturber gas densities are great, leading to spectral line characteristics that cannot be described by Voigt characteristics. However, these theories are not mutually exclusive. The line center may be described by the impact approximation, while the wings may be described using the quasistatic approach.

The impact approximation is valid when the time during collision is much less than the mean time between collisions ($\tau_c \ll t_0$), implying that the total radiation emitted mostly originates from intervals between collisions [70]. This allows treatment of the individual collisions as uncorrelated from the radiative process since they occur on different time scales [75]. This assertion makes impact theory useful within a few half widths of the line center, but not the wings. Under this approximation, the collisional broadening may be represented as a symmetric Lorentzian profile. To establish the conditions in which short isolated collisions are justified, the following terms are defined. Take ρ to be the distance of closest approach, defining the distance R

that a collision event occurs, and v to be the mean relative velocity of the two particles. In the impact approximation, R decreases from ∞ to the minimum value of ρ and increases to ∞ again.

The collision duration may be estimated as

$$\tau_c \cong \frac{\rho}{\bar{v}} \quad (10)$$

Using Equation (7), the criterion for the impact approximation for the average intercollisional interval is defined as

$$\delta v_{\frac{1}{2}} < \frac{\bar{v}}{2\pi\rho} \quad (11)$$

Given that the line wings are contributed by atoms with an unperturbed lifetime shorter than the average, the frequency difference out to $|v - v_0|$ must satisfy the following.

$$|v - v_0| < \frac{\bar{v}}{2\pi\rho} \quad (12)$$

Now, under the impact approximation, the lowering of energy with separation (ΔV) causes a continuous shift in absorption frequency during the collision event given by,

$$\Delta v = \frac{\Delta V}{h} = \frac{\Delta C_6}{h \times \rho^6} \quad (13)$$

In the impact model, the variation in frequency during a collision produces a net phase-shift between the wave-trains before and after the perturbation, and if this perturbation is “large”, the wave-trains may no longer be regarded as coherent, as argued by Weisskopf [68]. The net phase-shift that results from frequency shift may be calculated as follows.

$$\eta(\rho) = \int_0^{\tau_c} 2 \times \pi \times \Delta v dt \quad (14)$$

Evidently, the phase-shift resulting from collisions with a shorter closest approach distance is larger than that from a larger closest approach distance. An impact parameter ρ_w is defined as the closest approach when the phase-shift is one radian (“large” perturbation), which Weisskopf arbitrarily set to mark the collision. Thus, paraphrasing from [70] and [68]:

- Collisional broadening is caused by approach events that result in a phase shift of one radian or more between the wave-trains before and after collision ($\rho < \rho_w$)
- Collisional shift is caused by approach events with a phase shift less than one radian ($\rho > \rho_w$). These hypotheses are illustrated below.

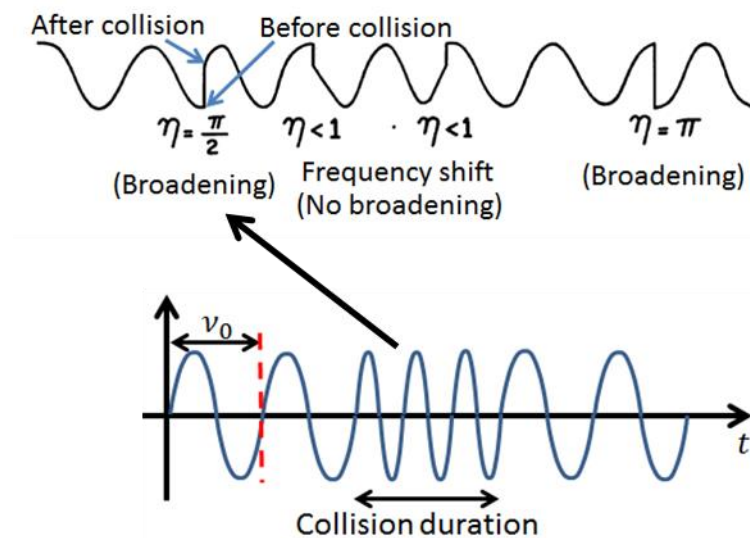


Figure 2.2: Illustration of collisional broadening and shift.

Under the impact approximation, collisionally broadened spectral lines have a Lorentzian profile near line center, which can be related to the Fourier transform of the radiation wave in which short duration collisions produce sudden phase changes [76]. The width, shift, and asymmetry (if present) are linearly dependent on the perturber pressure [77], as shown in lines affected by collisional narrowing, correlated collisions, and speed-dependent effects (covered in Chapter 10).

2.4 The Quasistatic Approximation

In contrast, the quasistatic approach, which was first treated by Holtzmark, treats the collision as an almost constant perturbation. Under this condition, densities must be great for several perturbers to be simultaneously present within radiating atoms [70]. The radiation observed in the line wing arises from the moment of the actual collision, which contrasts with the impact approximation. According to the Frank-Condon principal, transitions take place at a constant value of R [68]. The frequency shift for any given absorber-perturber pair reaches its maximum stationary value at $R = \rho$, and the validity of this approximation depends on each atom being allowed to radiate at its shifted frequency $\nu(\rho)$ for long enough that the broadening associated with τ_C is small compared to $\Delta\nu(\rho)$. In other words,

$$|\nu_0 - \nu| > \frac{\bar{\nu}}{2\pi\rho}; 2\pi\tau_C\Delta\nu > 1 \quad (15)$$

The above implies a phase change greater than unity, i.e. $\rho < \rho_w$, making the validity condition for the quasistatic approximation as the following, and opposite of the impact approximation.

$$|\nu_0 - \nu| \geq \Delta\nu(\rho_w) > \frac{\bar{\nu}}{2\pi\rho_w} \quad (16)$$

For the quasistatic approximation, the transition frequency is shifted from an unperturbed value of ν_0 , with the shift occurring predominantly in the upper levels.

$$\Delta\nu(R) = \nu_0 - \nu(R) = \frac{[V_2(R) - V_1(R)]}{h} \approx \frac{V_2(R)}{h} = \frac{C'_n}{R^n} \quad (17)$$

The line broadening is found by first evaluating the shift (see above) for a single atom-perturber pair and then averaging over the statistical distribution of all separations of R . Since $\Delta\nu$ always has the same sign (usually negative), the averaging results in an asymmetric spectral line with a wing extending to one side (“red side” or long wavelength side) [68]. This is in contrast to the impact approximation which may produce asymmetric lines, but in most cases the asymmetry is small enough that it cannot be observed within a few half-widths, and must be small for the impact approximation to be valid [70].

Pressure broadening of neutral species explained under the quasistatic approximation may be directly related to the close connection of the interatomic potentials and the lineshape characteristics. The most striking features of an asymmetric lineshape are caused by extrema in the interatomic difference potentials [70], and a representative figure displaying the potential pattern and corresponding frequency difference is shown below in Figure 2.3. Physically, there exists a singularity in the intensity distribution at the value of $\Delta\nu$ for which $dv/dR = 0$ at R_0 , and if $R_0 < \rho_w$, this minimum may give rise to satellites, or resolvable shoulders, on the spectral line, most commonly occurring in the red wing. At higher densities, these satellites can grow to intensities comparable to low pressure line core FWHMs [70]. The new line profile may shift to the satellite peak, resulting in dramatic changes to the width and shift. The position of the satellite, $\Delta\nu(R_0)$, relative to peak, is given by the “depth” of the minimum at R_0 , and the condition of its appearance is that $\Delta\nu(R_0)$ should exceed the impact broadened line core. The overall intensity of the satellite depends on the depth of minimum and the temperature [68], while the shape is dependent on the curvature of the potential curve [70].

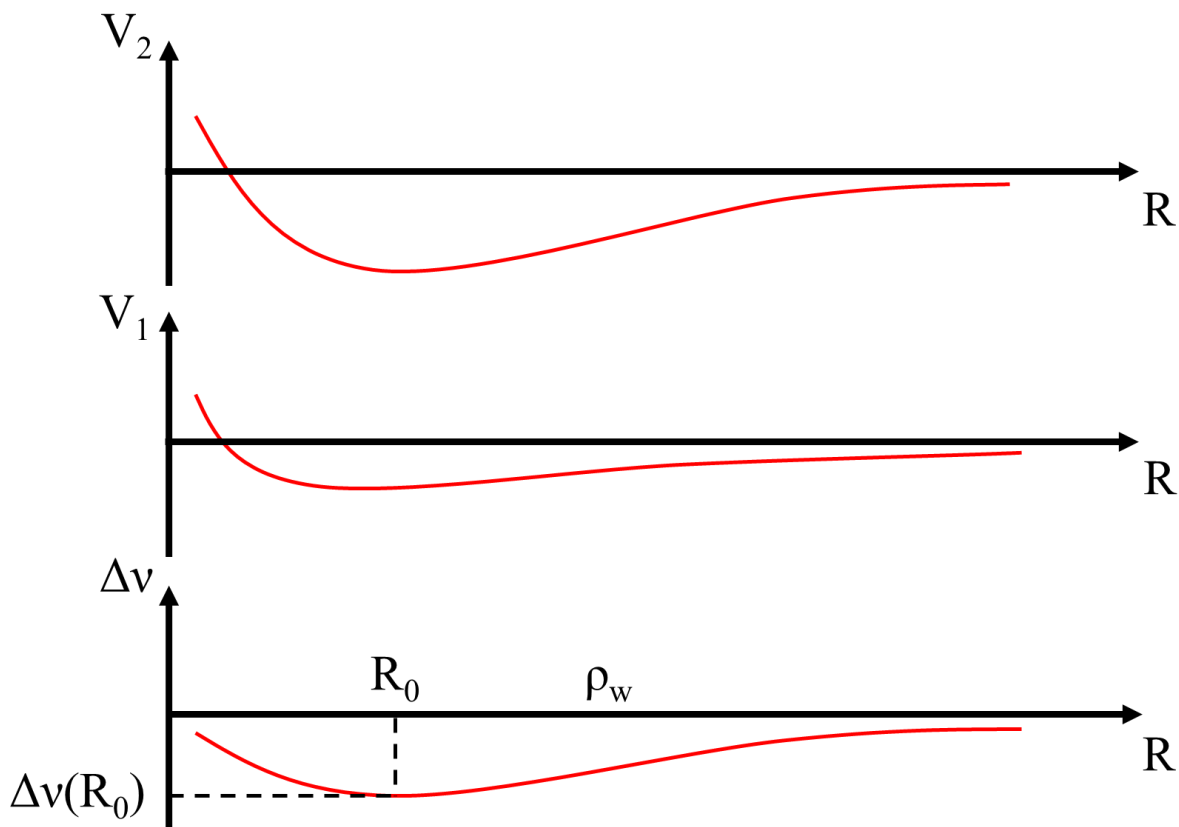


Figure 2.3: Perturbations for the upper (2) and lower (1) states of transition. The intermolecular difference potential $\Delta v/h$ has a minimum at R_0 , and if $R_0 < \rho$, this minimum may give rise to satellites [68].

In summary, it is important to note that the Voigt function does not consider asymmetry such as the lines broadened by the interactions described by the quasistatic approximation. Though the impact approximation provides a simplified description of short isolated collisions that may sufficiently predict the line core, the quasistatic approximation is necessary to consider when significantly high pressures introduce line mixing and collision-time asymmetry effects to the spectral line (covered in Chapter 10).

2.5 Theoretical Composition Scaling of the Collisional Broadening Parameters

First, consider the simplest situation where collisional broadening is caused only by dispersive interactions, which is the primary interaction between Kr and combustion products. The dispersion interactions (London dispersive forces) between the absorbing and perturbing species

results in a reduction of the absorbing species' energy. The induced energy given by Equation (9) may be simplified to

$$V_6 = -\frac{C_6}{R^6} \quad (18)$$

The negative sign indicates that the energy is being reduced (attractive force). The constant of proportionality C_6 depends on the properties of the absorber and perturber, but in the context of the physical origin of collisional broadening and shift is that $C_6 \sim r^2$, where r is related to the distance between the outer shell of electrons and the nucleus of the absorbing species. This causes the upper electronic states to have a larger C_6 and a greater reduction of energy compared to the ground state (see Figure 2.1), which results in observed collisional shift and broadening [70].

In situations dominated by dispersive forces, the decrease in energy due to a collision is given by

$$\Delta V_6 = R^{-6} \frac{3e^4 h^4}{2m_e^2} \sum_{\substack{a \neq a' \\ p \neq p'}} \frac{f_{aa'} f_{pp'}}{(E_{a'} - E_a)(E_{p'} - E_p)(E_{a'} - E_a + E_{p'} - E_p)} \quad (19)$$

Where $f_{aa'}$ and $f_{pp'}$ represent the oscillator strengths of the absorber and perturber for transition corresponding to the electronic states $a \rightarrow a'$ and $p \rightarrow p'$, respectively. The parameter E_k represents the unperturbed energy of the electronic state k , and m_e represents electron mass. Comparing Equation (18) with (19),

$$\Delta C_6 = \frac{3e^4 h^4}{2m_e^2} \sum_{\substack{a \neq a' \\ p \neq p'}} \frac{f_{aa'} f_{pp'}}{(E_{a'} - E_a)(E_{p'} - E_p)(E_{a'} - E_a + E_{p'} - E_p)} \quad (20)$$

Equation (20) can be simplified to two extreme situations: 1) when the perturber has much larger energy separation than the absorber (i.e. $E_{p'} - E_p \gg E_{a'} - E_a$); and 2) when the perturber

has a much smaller energy separation than the absorber (i.e. $E_{p'} - E_p \ll E_{p'} - E_p$). The former situation is typical of metals (especially alkali metals) perturbed by inert gases, which has been studied extensively in past works [71]. In this situation, Equation (20) can be further simplified to $\Delta C_6 = \frac{\alpha_p \times \langle e^2 \times r^2 \rangle_a}{(4 \times \pi \times \epsilon_0)^2}$. The polarizability can be further related to the refractive index of the perturber using the relation, $\alpha_p = \frac{2 \times \epsilon_0 \times (n_p - 1)}{N_A}$. Considering that collisional broadening occurs only when the distance between the absorber and perturber is less than ρ_w the collisional frequency is determined by finding the flux of species that are within the area described by the radius ρ_w ($v_c = N \pi \rho_w^2 v$). The collisional broadening FWHM and shift are given by [68],

$$w_c (cm^{-1}) = k_c p T^{-0.7} (n_p - 1)^{0.4} \mu^{-0.3} \quad (21)$$

$$\delta_c (cm^{-1}) = k'_c p (n_p - 1)^{0.4} T^{-0.7} \mu^{-0.3} \quad (22)$$

In the above, μ represents the reduced molar mass of the perturber-absorber system, given by $\frac{1}{\mu} = \frac{1}{M_a} + \frac{1}{M_p}$. These relationships have been verified by numerous works with various metals such as sodium, potassium, and calcium, among others, with inert gases as perturbers. DiRosa & Hanson [74] also reported the validity of Equation (21) to describe the collisional broadening FWHM of NO broadening in the presence of representative combustion species. It can be observed from Equations (21) and (22) that the perturber properties that determine w_c and δ_c are refractive index and molar mass.

The other extreme situation is when the absorber has a much larger energy separation than the perturber. This situation is typical of inert gases like helium and neon as absorbers and metal atoms as perturbers. In this situation, Equation (20) can be further simplified to $\Delta C_6 = \frac{\alpha_a \times \langle e^2 \times r^2 \rangle_p}{(4 \times \pi \times \epsilon_0)^2}$.

Once again, the polarizability of the absorber can be further related to its refractive index using the relation $\alpha_a = \frac{2 \times \epsilon_0 \times (n_a - 1)}{N_a}$. The corresponding collisional broadening FWHM and shift are,

$$w_c (cm^{-1}) = k_c p T^{-0.7} (n_a - 1)^{0.4} \mu^{-0.3} \langle e^2 r^2 \rangle_p^{0.4} \quad (23)$$

$$\delta_c (cm^{-1}) = k'_c p (n_a - 1)^{0.4} T^{-0.7} \mu^{-0.3} \langle e^2 r^2 \rangle_p^{0.4} \quad (24)$$

In the above, the term $\langle e^2 r^2 \rangle_p$ is the square of the transition dipole moment of the perturber, which is summed over different possible electronic transitions from its ground state. The above equations may be simplified further with careful examination. Several previous works have documented the oscillator strengths (directly related to transition dipole moment [68]) for different gaseous species, which includes diatomic molecules as well as alkali metals. Few interesting trends could be observed. The oscillator strength is typically very high for transitions involving ground to first (and sometimes second) excited energy levels, followed by a steep decrease for transitions into higher electronic levels (e.g., [78]). Thus, the value of $\langle e^2 r^2 \rangle_p^{0.4}$ in Equations (23) and (24) is dominated by the transition of these excited levels. Interestingly, the oscillator strengths for common homonuclear and heteronuclear combustion-relevant diatomics corresponding to different rovibronic transitions range between 0.005 – 0.02 (e.g., from [79], O₂ (Schumann-Runge system): 0.007 – 0.02, CO (first negative system): 0.01 – 0.02, CN (violet system): 0.019, CN (red system): 0.005 – 0.01; C₂ (Swan): 0.004 – 0.01). Readers may refer to [79, 80, 81, 82] for a more exhaustive database of oscillator strengths. Thus, it can be observed that $\langle e^2 r^2 \rangle_p$ values for different perturber species in combustion environments are within the same order of magnitude. Further, because of the weak power dependence of the collisional broadening parameters on transition dipole, it is hypothesized that the collisional broadening parameters are given by,

$$w_c (cm^{-1}) = k_c p T^{-0.7} (n_a - 1)^{0.4} \mu^{-0.3} \quad (25)$$

$$\delta_c (cm^{-1}) = k'_c p (n_a - 1)^{0.4} T^{-0.7} \mu^{-0.3} \quad (26)$$

In this situation of absorber energy level spacing being much smaller than perturber energy level spacing with common combustion species as perturbers, the only property of the perturber that influences the collisional broadening and shift is the molar mass of the perturber.

Krypton differs from the above extreme situations in that the energy separation of krypton is comparable to those of the representative combustion species such as CO_2 , N_2 , CO , etc., which are the common perturbers in a reacting environment (i.e. $E_{p'} - E_p \sim E_{a'} - E_a$). When the energy separation of the absorber is comparable to that of the perturber, further simplification of Equation (20) is not possible. Additionally, no past works have addressed this scenario. Several questions arise in this situation, which will be addressed in this work:

- 1) Do the collisional broadening FWHM and shift depend on additional properties of the perturber?
- 2) Do the collisional broadening FWHM and shift have closed-form dependence like Equations (21) – (26)?
- 3) How should the absorber and perturber energy level difference compare with one another to fit in this regime?

Chapter 3 : Experiment

3.1 PLIF Optical Setup

A schematic of the experimental setup is illustrated in Figure 3.1. The fundamental harmonic (1064nm) of an Nd: YAG laser (Continuum Inc., Model: Surelite III) fitted with an injection-seeder (Continuum Inc./NP Photonics, RFLSE) was frequency-doubled and tripled to produce 532nm and 355nm with maximum pulse energies of 185mJ and 55mJ, respectively. This combination provided the maximum value of 214nm conversion. These energies were measured using a Coherent Fieldmax II energy meter. The laser was pulsed at 10Hz with 5ns wide pulses. The doubler used for this study was a Type-II variety, ensuring that the 532nm beam was vertically polarized. To ensure that the 355nm beam was vertically polarized, an adjusted $\lambda/2$ wave plate was placed immediately downstream of the 355nm output. These beams were separated via dichroic beam separators, and the 1064nm beam was discarded. The 532nm beam pumped a dye laser (Continuum Inc., Jaguar Series using Radiant Dyes supporting equipment) circulating fluorescein 548 dye to produce 544nm beam (manufacturer specified 0.06 cm^{-1} FWHM) with 25mJ pulse energy. The dye laser allowed for precise tuning of the output wavelength to facilitate excitation scans. The 544nm and 355nm beams were temporally aligned by using an optical delay loop, passed through each of their own respective Galilean telescopes for efficient beam mixing, and spatially overlapped using a dichroic mirror. The beams were then sum-frequency mixed using a barium borate (BBO) crystal (Inrad Optics Inc., Model: Autotracker III) to generate the 214nm beam (0.06 cm^{-1} FWHM) for Kr excitation. Immediately downstream of the BBO crystal was a Pellin Broca prism, which directed the output 214nm beam to the measurement area and separated the residual 544nm and 355nm beams. For the experiments conducted in this study, energies up to 10mJ of 214nm could be used.

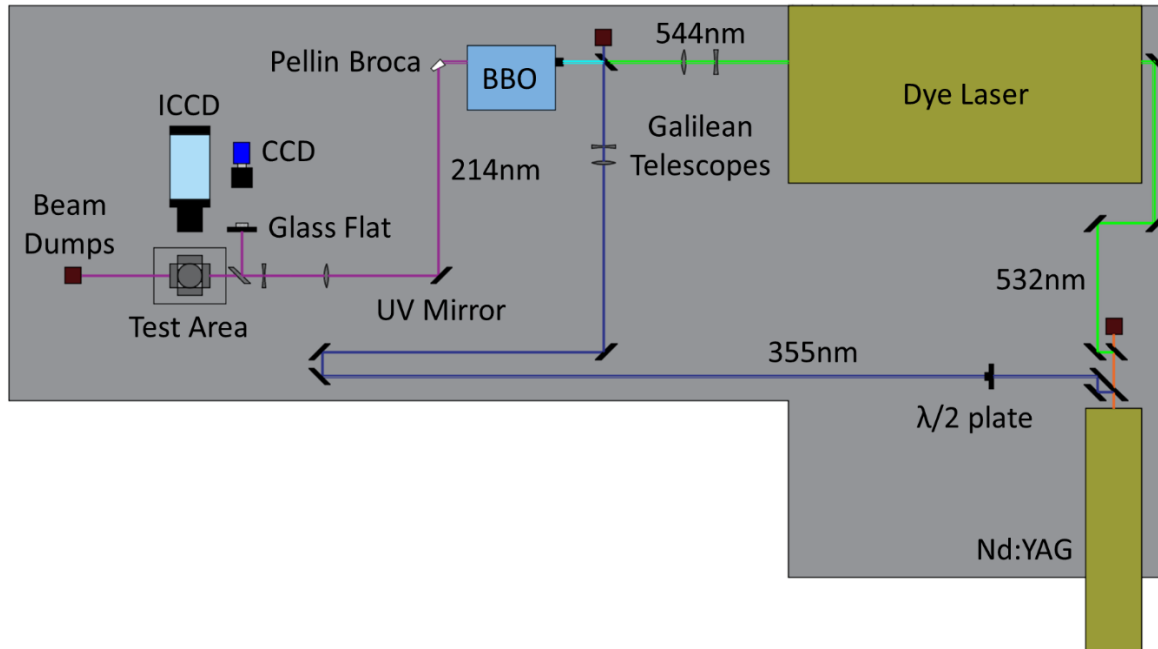


Figure 3.1: Schematic of the experimental setup illustrating the laser setup and camera arrangement.

The 214nm beam was made into a sheet using 400mm spherical convex and 200mm cylindrical concave UV fused silica lenses. A small fraction ($\approx 5\%$) of the 214nm sheet was diverted to excite the fluorescence of a commercial grade BK7 glass flat, which was imaged by an interline CCD camera (PCO Pixelfly) to obtain simultaneous laser intensity measurements for sheet correction and energy normalization. It was experimentally verified that the glass fluorescence signals scaled linearly with 214nm energy for small intensities that were used in the present experiments. Variations in the laser beam profile obtained from the CCD camera were not substantial when scanning the dye laser, as the laser sheet profiles are determined by the dye laser input and Nd:YAG beam profiles. During wavelength tuning, there were negligible changes in either of these sources; hence, there were very minor, if any, changes in the 214nm beam profiles. Using the CCD camera images, the 214nm sheet was measured to be 8mm tall and 0.3mm thick (FWHM) at the focus where the measurements were made. The measurement domain extended over a region of $10\text{mm} \times 50\text{mm}$ with a spatial resolution of $50 \mu\text{m}/\text{pixel}$. Sheet dimension

variations across the measurement domain were assumed negligible in determining the lineshape parameters due to the long focal length convex spherical lens and relatively small measurement domain. To verify this, beam profile images were acquired at multiple locations through the radius of the measurement domain. It was observed that both the laser sheet thickness and signal levels varied by less than 5% due optical distortion. So long as the signals are unsaturated, acquisition of the Voigt FWHM and collisional shift were undeterred.

The Kr fluorescence was collected by a Gen IV ICCD camera (Princeton Instruments Inc., Model: PI-MAX 4) fitted with an f/1.2 50mm lens. A 760nm interference filter (10nm FWHM) was placed in front of the ICCD camera to remove any scattering produced from the laser and the 819nm krypton fluorescence band [67] while transmitting all the fluorescence signals from the 760 nm branch. This filter possesses 90% transmissivity at 760nm. The Nd:YAG laser may be triggered internally or externally using a Stanford Research Systems (SRS) pulse generator, but a majority of the experiments performed for this dissertation were done internally. The SRS pulse generator was used to trigger the ICCD and CCD cameras to temporally align each camera's gate exposure with the associated laser pulse. This is accomplished by using a Tektronix oscilloscope and a ThorLabs photodiode.

3.2 Rayleigh Scattering

Rayleigh scattering (RS) experiments were obtained with the same detector setup with minor deviations and omissions of equipment. An unseeded frequency-doubled 532nm beam was made into a sheet 20mm tall and 0.5mm thick at the focus. This was accomplished by using a Galilean telescope to expand the 532nm beam to two times its original diameter and focusing it into a sheet using a 300mm convex cylindrical lens. Typical laser energy was 190mJ for the experiments, and the laser energy remained consistent (1% RMS) throughout test runs. The

measurement domain encompassed the Kr PLIF measurement region with identical spatial resolution. The same ICCD camera and lens setup used for Kr PLIF was used for RS imaging, apart from a 532nm interference filter being used instead of the 760nm filter used for Kr PLIF. Rayleigh scattering measurements were performed on premixed methane flame exhaust to calculate temperatures for two-photon Doppler broadening temperature calibration and to verify the temperature dependence of the collisional parameters. Also, Rayleigh scattering combustion images were normalized with Rayleigh scattering images of air as an additional input into a composition-independent thermometry technique and to create 2D flame structure images. Experimental procedures and data analysis routines for Rayleigh scattering tasks are covered in the following chapter.

3.3 Nd:YAG

The Nd:YAG laser [83] used for this study was a Q-switched [84] flash lamp pumped 10Hz pulsed laser. Q-switching was achieved using an electro-optical circuit (Figure 3.2) featuring a Pockel Cell, two $\lambda/4$ plates located in front and behind the rod head assembly, and a polarizer downstream of the rod assembly. The waveplates prevented spatial hole burning (circular polarization) and the Pockel Cell acted as a waveplate when an electric field was applied. A compensator was placed downstream of the head assembly to adjust the beam path and a shaping optic influences the beam shape. This laser produced a maximum 1064nm energy of approximately 660mJ unseeded and 630mJ seeded. The energy values were optimized by using a Coherent Fieldmax II energy meter and adjusting the two back mirror mounting screws until the energy is maximized. Similarly, the harmonics (532nm and 355nm) were maximized with the energy meter while making slight rotations to the doubler's and tripler's manual adjustment knobs. The 532nm crystal was held in place with three long mounting screws and the 355nm crystal threads onto the

532nm crystal. Removal and installation of these components required re-optimization of their energies but should not affect downstream alignment. Routine maintenance, such as maintaining the cooling circuit and changing flash lamp tubes, and additional specifications may be found in the manual.

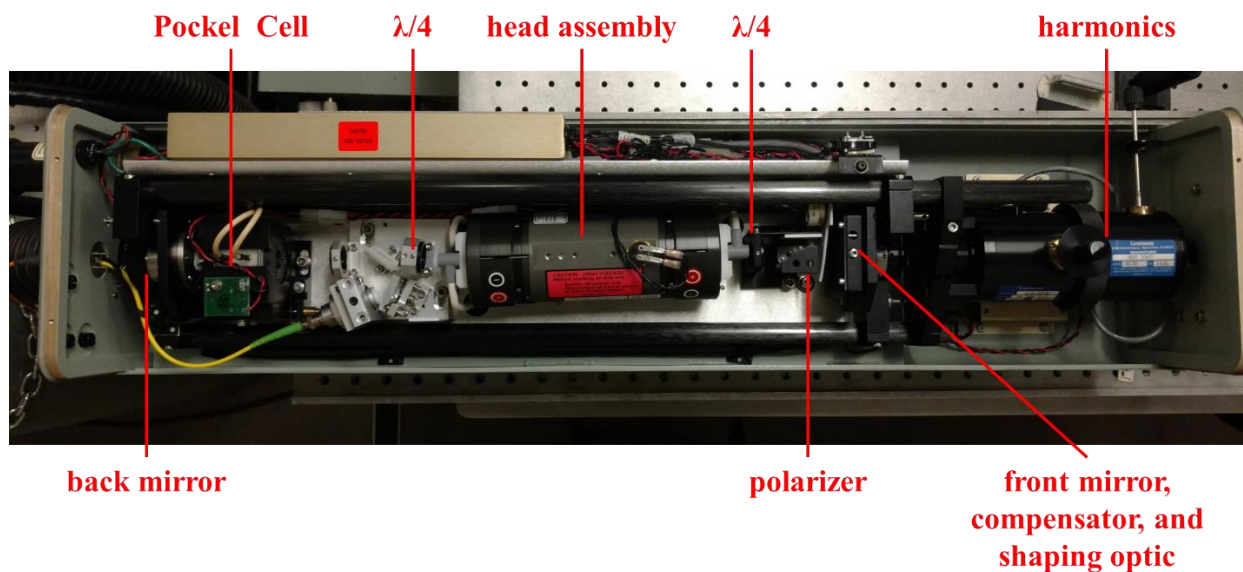


Figure 3.2: Nd:YAG internal components.

3.4 Dye Laser

The dye laser is pumped with the 532nm beam output from the Nd:YAG laser. Fluorescein 548 dye was dissolved in a methanol-sodium hydroxide solution with the following concentrations for the oscillator and amplifier circuits (Table 3.1). These concentrations were determined such that the output 544nm energy was maximized without exceeding the amplified stimulated emission (ASE) threshold caused by an oversaturation of dye. ASE causes an increase in the apparent laser linewidth, thereby invalidating experimental measurements. Wavelength tuning for excitation scans is accomplished with the Jaguar Control software and was scanned at rates of 0.001 nm/s to 0.005 nm/s depending on the type of excitation scan.

Table 3.1: Dye concentrations.

| Unit | CH ₃ OH | NaOH | Dye |
|-------------------|--------------------|-------|-------|
| Oscillator | 400mL | 40mg | 130mg |
| Amplifier | 1000mL | 100mg | 150mg |

The details of alignment are cover thoroughly in [85] and the Jaguar manual. However, it is important to note some key details in aligning the dye laser.

- 1) The location of the pre-amplifier cylindrical lenses (L2 and L3) are as follows. L2 should be placed such that the laser linewidth is minimized and the location of L3 should be placed such that the pre-amplifier beam is maximized. Performing excitation scans for varying L2 locations and use of an energy meter was necessary.
- 2) As an aside to [85], once lasing in the pre-amplifier circuit is achieved optimization of the pre-amplifier circuit may be performed successfully and perhaps more efficiently with the amplifier dye cell removed and an energy meter placed downstream of the output. Adjustments of the furthest upstream beam splitters (BS1 and BS2) all the way through the oscillator dye cell should be made to maximize the pre-amplifier energy. Typical maximum energy values are approximately 2% of 532nm values.
- 3) The inclusion of a Bethune cell for the amplifier circuit eliminates the need for the cylindrical lens upstream of the amplifier dye cell, making alignment much more simplified. First, coarse adjustments of the location and tilt of the Bethune cell are made. Like (2), adjustments of mirror 3 (M3), the upstream Galilean telescope lenses, and the Bethune cell should be adjusted to maximize the energy. Typical values are 15% of the input 532nm energy.
- 4) Lastly, minor manipulation of the optics in (3), namely the pre-amplifier Galilean telescope, were made to achieve a full 544nm beam profile. This was done in conjunction with an energy

meter to ensure there was no reduction in the energy. The goal was to create a symmetrical intensity and near-circular beam. Using calculated quarter turns, the optics and dye cell were adjusted such that the energy does not decrease. After each adjustment, the beam profile post-544nm Galilean telescope downstream of the dye laser was viewed using Zap-It burn paper. Single optic adjustments were performed until degradation of the profile is observed. Degradation of the energy or profile prompted the user to return to the prior location and continue to the next optic. This was a highly iterative process between the Galilean telescope within the dye laser, M3, and the Bethune cell.

3.5 RFLSE Injection Seeder

The injection seeder uses a fiber optic (yellow) to input an IR beam of known wavelength (± 0.001 nm resolution) into the Nd:YAG cavity to effectively harmonize the output laser pulses. It takes the laser lineshape from multimodal (mode hopping) to single mode, dictated by the wavelength commanded in the SI-2000 SeedLaser software. This value was kept at 1064.196 – 1064.197nm for Kr PLIF excitation scans to minimize the laser linewidth. The seeder controls a piezoelectric mount which translated the Nd:YAG back mirror forward and backward to control the cavity length, and in turn controlled the laser mode/wavelength. This essentially concentrated all laser power at a single mode by constantly adjusting the position of the back mirror to match the injection wavelength. The seeder operates on a feedback loop with feedback obtained from cavity leakage and transmitted through an orange fiber optic cable.

Figure 3.3 shows the input circuit of the injection seeder, which features the launch optics, an alignment mirror, a polarizer, and a $\lambda/4$ plate. A polarizer downstream of the yellow input fiber prevented feedback from going through the input, thereby preventing damage of the yellow fiber. The waveplate ensured the polarization of the injection beam matched the pump beam. For the

purposes of alignment, the only optics adjusted were the launch mount and alignment mirror. To align the seeder circuit properly, it was necessary to use an IR phosphor card to permit tracing of the seeder beam. First, the IR beam was traced to the front of the Pockel Cell (PC). The top mounted screws on the launch mount were adjusted to center the IR beam on the center of the PC/back mirror. The IR beam was then centered with the Nd:YAG rod and the exit port of the laser by adjusting the side mounted screws of the alignment mirror. This step was most easily done with the harmonics removed and the shutter up. Tracing between the wave plates, YAG rod ports, polarizers, compensator, and shaping optic was necessary to ensure the injection seeder beam was successfully aligned. Adjustment of the launch mount and alignment mirror was performed iteratively until centering was achieved with the waveplate/PC/back mirror, YAG rod, compensator, and the laser exit port.

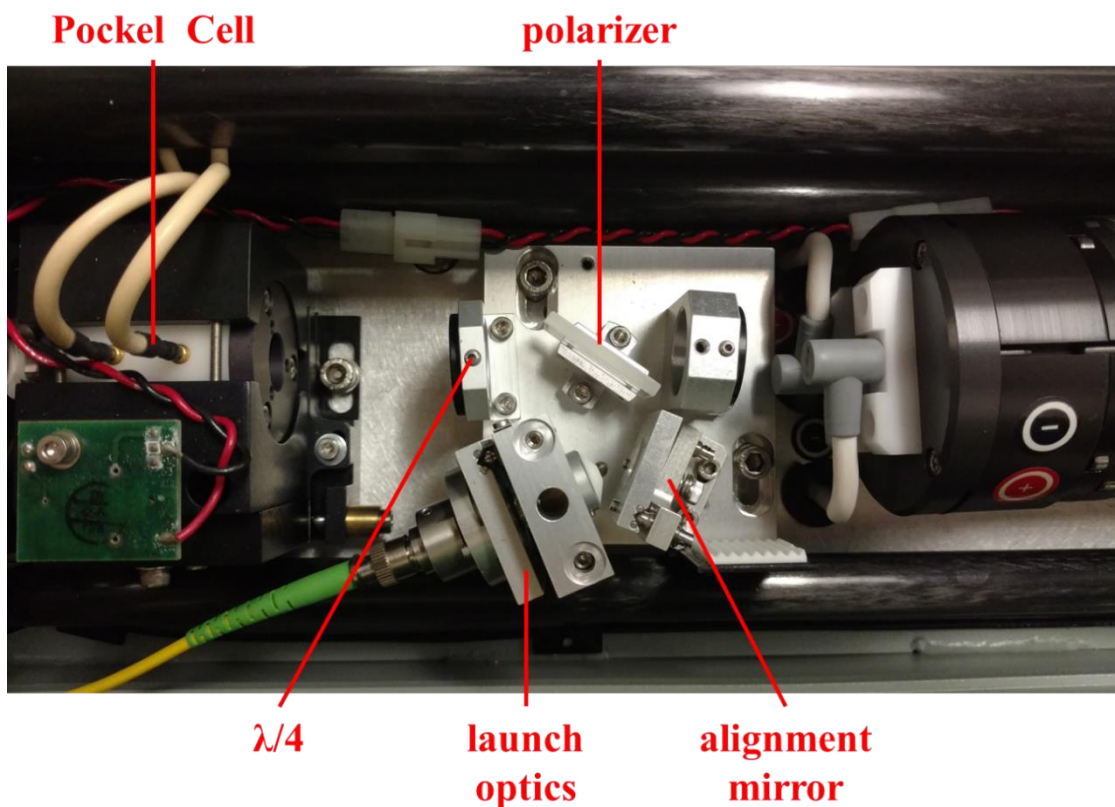


Figure 3.3: Injection seeder circuit.

Further minor adjustments of the launch mount and mirror were necessary to maximize the build-up reduction time (BURT). The build-up time may be thought of as the amount of time necessary for enough photons of correct wavelength to accumulate for proper output. The BURT offers as a suitable measure of the effectiveness of seeding. The BURT was measured by connecting a photodiode to an oscilloscope with the trigger set to the source, i.e. the laser pulse. The photodiode was found to be most effective when viewing scattered 532nm light. Additional adjustments made to the launch mount and alignment mirror yielded changes to the temporal location of the laser pulse in the oscilloscope. The screws on the optical mounts for each component were adjusted such that the BURT was maximized about a central location in the oscilloscope screen. It was important to note the proper temporal orientation of the pulse that yielded an increase in BURT. This proved to be somewhat challenging, as any kind of convective cooling with the Nd:YAG laser lid removed affected the piezoelectric base that controlled the seeding, thus fluctuating the laser pulse on the oscilloscope. It was necessary to ensure proper care was taken to reduce this temporal fluctuation. Once optimized, the BURT was approximately 1.5 times the pulse width, with a temporal jitter of 1 – 3ns at max Q. Jitter may be reduced by using an internal laser trigger due to the inherent noise introduced using external trigger with the SRS pulse generator.

3.6 214nm Generation

The 544nm and 355nm beams were overlapped on a dichroic mirror after exiting the dye laser and traveling through an optical delay loop, respectively. The CVI Lasers dichroic mirror was specifically designed for Nd:YAG lasers and allows transmission of 99% 500 – 550nm while reflecting 99% 355nm. Each beam traveled through their own respective Galilean telescopes to ensure that the highly intense 544nm beam would not damage the BBO crystal housed inside the

AutoTracker III (AT-III) unit, to allow for efficient beam mixing by matching beam size, and to ensure excess 355nm beam that extended beyond the size of the BBO was not wasted.

Alignment of the beams was based upon keeping the 544nm beam as the reference point since its trajectory was a complex function of dye laser alignment. Alignment was first performed without the 355nm Galilean telescope (GT) so that the lenses would not misalign the beam's initial trajectory. First, the 544nm GT lenses and dichroic were adjusted such that they were centered about the beam. The beam would then pass through the AT-III, and far field alignment was performed to keep the beam perpendicular with its initial point and parallel to the optical table. Translation and elevation of the AT-III was necessary multiple times for proper alignment. The AT-III was also kept level for proper functioning. With the 544nm beam and AT-III fixed, the 355nm beam was spatially overlapped on the dichroic mirror using the nearest upstream 355nm mirror. Next, beams were far field overlapped by viewing the AT-III output and adjusting the dichroic via tilt adjustment knobs and a translation stage. The two previous steps were iterated until near field and far field alignment was achieved. Once aligned, the 355nm GT is put in place, centering the lenses, and the procedure repeated itself. Once aligned, the phase compensator housed within the AT-III was manually adjusted to the optimum tilt angle to achieve maximum 214nm conversion. The Coherent Fieldmax II energy meter was used throughout this process. As a final step, both 544nm and 355nm convex lenses in their respective GTs were adjusted in the axial direction to further increase 214nm energy. This changed alignment slightly, requiring further adjustments to the realign circuit. A Pelin Broca crystal downstream of the AT-III separated all output wavelengths as the 214nm was isolated and directed perpendicularly towards a UV mirror (90% 214nm reflectance) to be used for experimentation.

Prior to experimentation, the AT-III phase compensator was manually adjusted using the “red-blue shift” adjustment options on the AT-III’s control screen at a fixed dye laser wavelength. Adjustment was made to maximize 214nm energy. A pair of internal photodiodes monitored a highly attenuated reflected 214nm beam which were necessary for auto-tracking. During wavelength tuning, the AT-III unit was set to “auto”, as tuning the frequency of the dye laser would require necessary changes to the phase compensator orientation. An auto-track speed of three was used. The energy was monitored throughout the day to ensure auto-tracking did not diverge. Typical 214nm unseeded energies are approximately 60% of seeded energies.

3.7 Triggering and Camera Systems

As mentioned previously, experiments were performed using both “internal” and “external” triggering systems. Although internal triggering was used most frequently, descriptions of each process will be provided. This is best accomplished by viewing the following figures, Figure 3.4 and Figure 3.5. With an internal trigger, the laser electronics would command the SRS box i.e. the camera delays, and the injection seeder. The SRS box sent a fixed TTL signal to both the ICCD and CCD to successfully trigger the camera gate with each laser pulse. Both cameras operated on the same SRS channel as their delays were identical. Gate delay alignment was made possible with the use of a photodiode that recorded the temporal signature of the laser pulse and an oscilloscope to monitor all equipment. Q-switch delays were controlled from the laser control panel, which would prompt corrections to camera delays if changed.

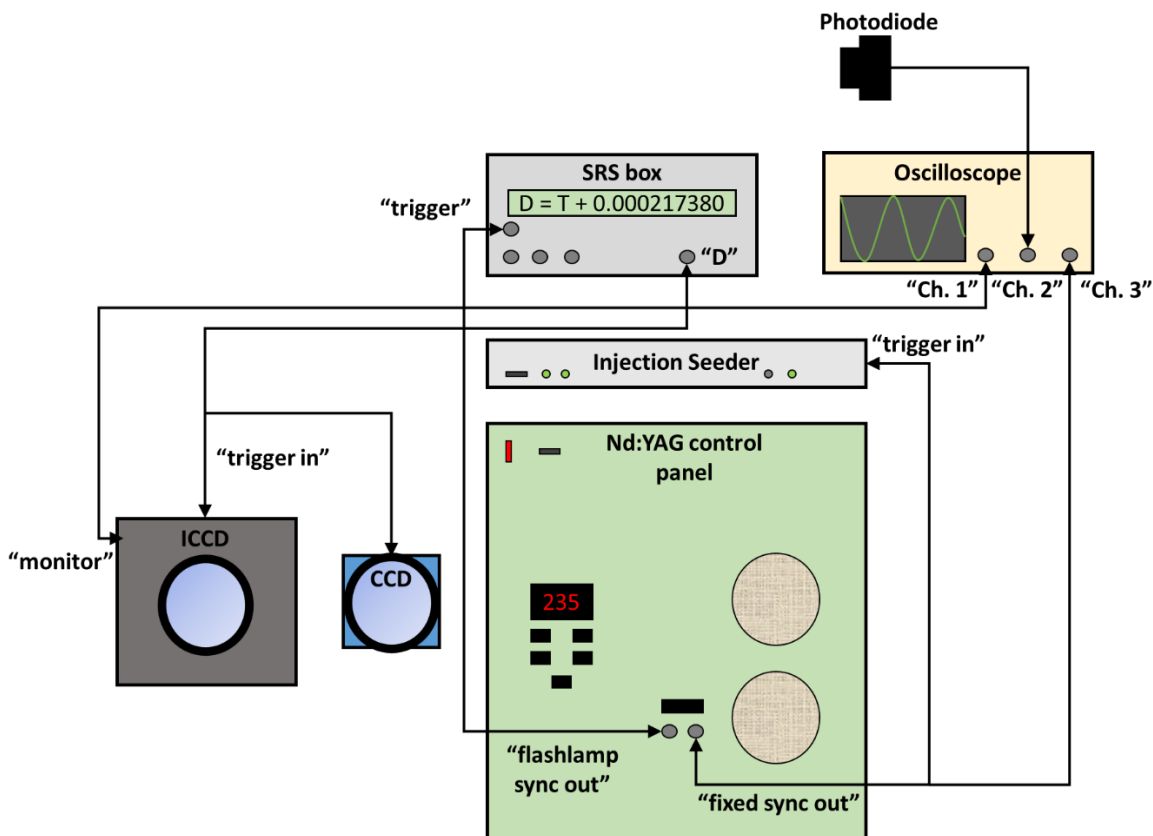


Figure 3.4: Diagram illustrating the internal triggering system.

The setup for external mode was very similar to internal mode, with the differences illustrated in Figure 3.5. In external mode, the SRS box sent fixed TTL signals to the cameras and laser. Though the laser pulse frequency could be reduced below 10Hz, this was not done to prevent damage to the laser. Instead, flash lamp firing and Q-switch delay settings were controlled through the SRS box between channels "A" and "B", respectively. Camera delay and exposure control was accomplished in an identical manner to internal mode.

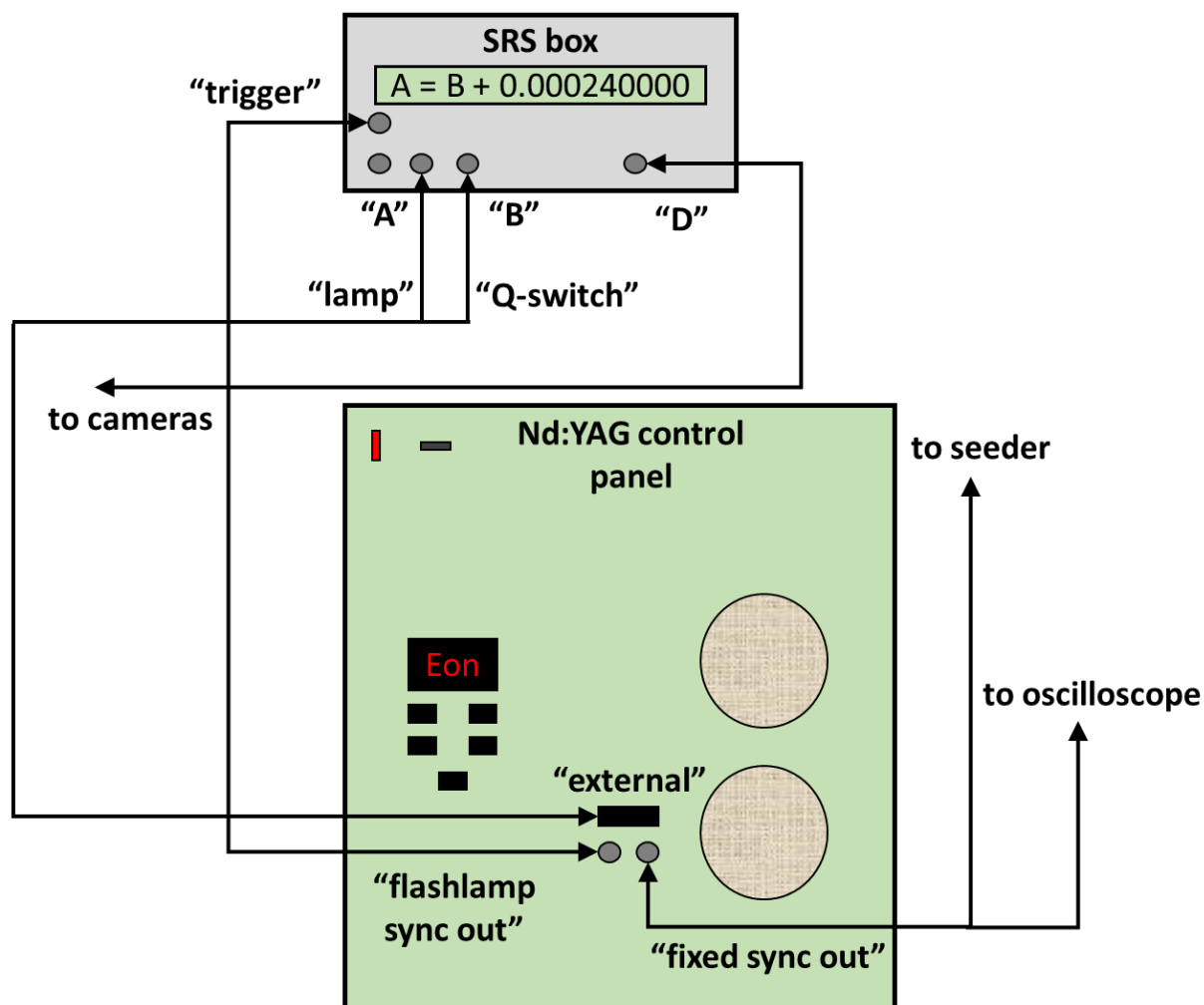


Figure 3.5: Diagram illustrating the external triggering system.

In internal mode, ICCD and CCD exposures were set within their software to $4\mu\text{s}$ and $1\mu\text{s}$, respectively. This was the minimum allowable exposure for the CCD camera, and was done to limit shot noise as much as possible. In external mode, the ICCD exposure may be set as low as 50ns , which proved very useful for unseeded Rayleigh scattering measurements to reduce unwanted reflections from burner surfaces. Fluorescence measurements did not take advantage of this benefit because the SRS box introduced inherent noise into the injection seeding process. Despite the potential improvements to camera SNRs, the detraction to seeding negated the use of external triggering for fluorescence experiments for this study. For steady laminar Rayleigh scattering measurements, On-CCD accumulation was also employed to further increase signals

without increasing noise levels. Lastly, the ICCD camera contained an internal delay option that was held constant at 50ns for both internal and external settings. Typical intensifier gain values for fluorescence measurements were 50 – 80, while Rayleigh scattering used 5 – 10. These settings were changed, and image acquisition was made possible with the Princeton Instruments LightField software.

3.8 Experimental Apparatuses

3.8.1 Static Test Cell

Multiple experimental apparatuses were used throughout this experimental investigation. A basic schematic of the temperature and pressure controlled static test cell used for low pressure scans and compositional scaling scans is shown below in Figure 3.6. The cell comprised of a stainless-steel housing, two quartz/fused silica windows, and six stainless steel flanges. At each flange, copper gaskets and vacuum grease were used to create a proper seal. The 214nm excitation beam entered the cell through a fused silica window and the rear flange of the test cell acted as a beam stop. The Torr Seal and flanges held the windows in place and were also used for attaching gas lines and measurement devices. The access ports consisted of a vacuum pump, a Kr gas line, a pressure gauge, a thermocouple, and a gas supply line for all perturber gases. All gas lines included manual needle valves to facilitate the exact concentration of Kr and test gas. The pressure and temperature were monitored by an Omega digital pressure gauge, which was accurate within 1 torr up to a maximum value of 1400 torr, and a K-type thermocouple that was accurate to within 0.1 K.

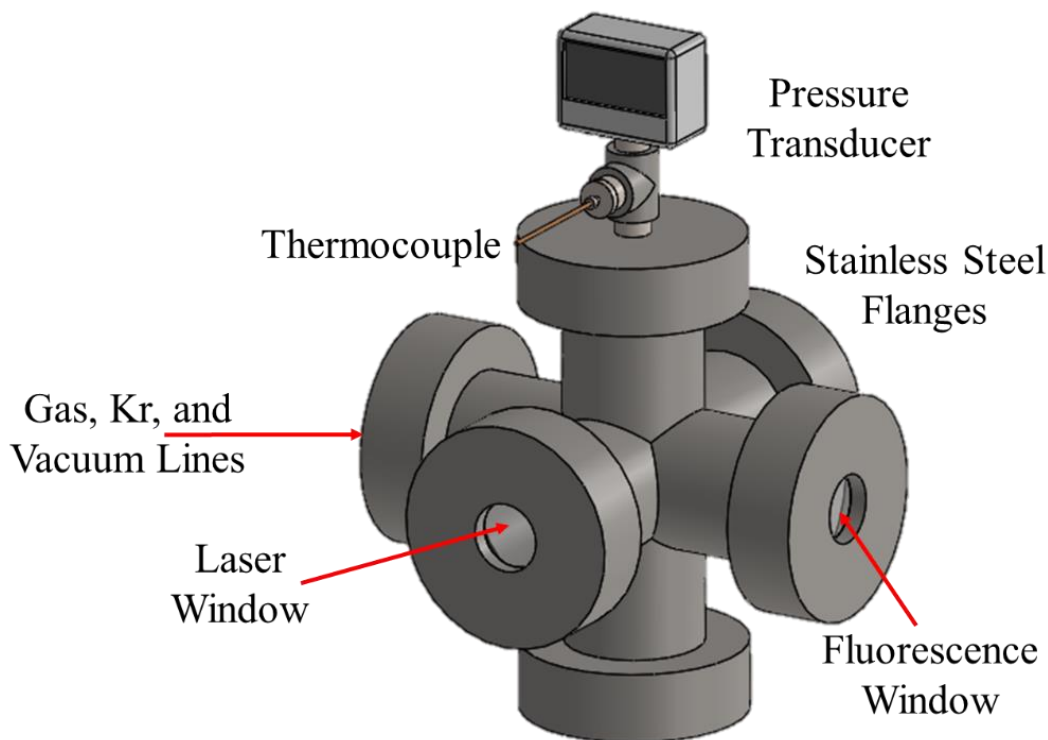


Figure 3.6: Schematic of the static test cell used for low pressure and compositional scaling scans.

Prior to each experimental campaign, the static cell was evacuated to 4 torr of Kr pressure and an excitation scan was performed to provide the accurate value of the laser centerline at vacuum conditions (collisional shift is negligible at 4 torr), enabling the calculation of collisional shift. Additionally, the static reference cell also served as a vacuum furnace that was heated to temperatures in the range of 300 – 500K under low pressure conditions (4 torr) to determine the scaling of Doppler widths on temperature under two-photon excitation. Heat addition was produced by using a standard 120V plug-in heating cable connected to a variable voltage controller. To reduce losses, Zircar alumina insulation was employed (Appendix A).

3.8.2 In-House Designed Jet in Co-Flow and Premixed Burner

Flame experiments were conducted with an in-house designed, reconfigurable jet flame in co-flow or premixed flat flame burner. A 3D model displaying the burner in the jet flame configuration is shown in Figure 3.7. The burner housing was constructed of multiple 6" diameter

steel pipe stages (labeled 1 – 3) that were welded to 1/8” steel plates that act as custom flanges and are attached by using six 3/8”-16 bolts. The base of the burner is a 3/8” thick circular steel plate, which enabled mounting of the burner to the experimental setup’s optical table. The base was threaded (1/4”-20) for connecting ThorLabs posts and post holders. A half inch hole was cut out of the center to press-fit the fuel jet tube. Water jetting of the ceramics and steel plates was performed by NCSU MAE’s machine shop and welding was performed by NCSU’s Weaver Labs. Compressed between each flange and the base plate were multipurpose neoprene gaskets to prevent co-flow gas leaks. Dry air entered stage 1 through two tangential entry 1/2” steel tubes that have been welded to the interior of the 6” steel tube housing. Multiple tangential entries were used to promote mixing and an even distribution of gas momentum. Downstream of stage one lies a stainless-steel wire mesh (mesh size of 20 × 20, opening size of 0.034”, and wire gauge of 0.016”) to evenly distribute co-flow/premixed fuel. Stage 2 and stage 3 each contained a 300-CPSI ceramic honeycomb flow conditioner to deliver highly uniform co-flow exit conditions. Fuel was delivered through 1/4” stainless steel tubing (wall thickness 1/16”) and expansion was made possible by way of an expanding elbow installed underneath the burner baseplate. The jet exit plane was flush with the co-flow exit plane and the end of the jet tube was not sharpened to allow for some recirculation around the jet tube thickness, which provided a stable attached flame during experiments. The fuel was issued from the jet tube that had an ID of approximately 9.15mm. Detailed drawings and an exploded view of this burner are featured in Appendix B.

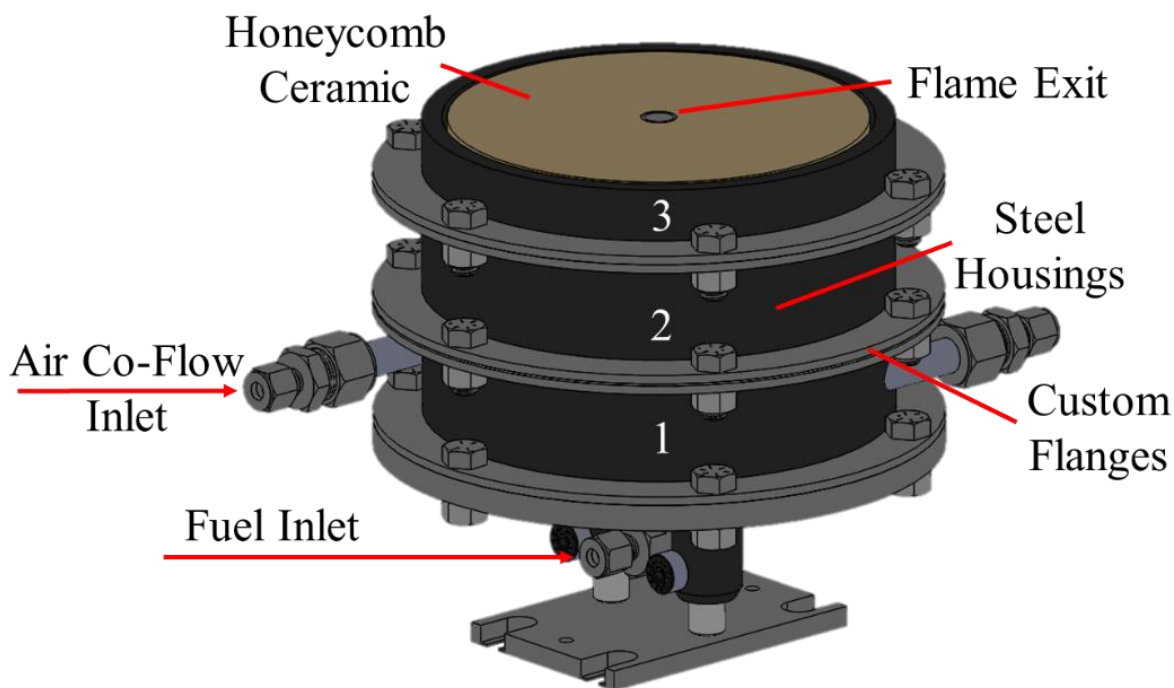


Figure 3.7: In-house designed reconfigurable jet in co-flow or premixed flat flame burner.

The burner depicted in Figure 3.7 was reconfigured when needed to produce stable, premixed flat flames by removing the jet tube and replacing the base plate and flow conditioning ceramics with identical components omitting the center hole. This setup was used to determine the temperature dependence of Doppler width and collisional broadening parameters at elevated temperatures. The fine structure of the ceramic produced uniform lean premixed methane flames, which were highly suitable for temperature calibration measurements.

3.8.3 Electric Heater

Experiments for obtaining the temperature dependence for the collisional parameters were accomplished by using an Osram SureHeat Jet electrical heater, with the manufacturer published technical specifications listed in Appendix C. A 1" NPT stainless-steel elbow was fitted at the heater exit to achieve vertical flow normal to the laser sheet propagation. To reduce heat losses, Zircar alumina insulation (Appendix A) was attached to the elbow using copper wire. A small

honeycomb ceramic was inserted in the elbow to drastically improve flow quality. It also acted as a heat bed to improve temperature stability and uniformity. An Omega K-type thermocouple provided temperature verification at each control panel setting with a very consistent maximum temperature reading of 900K.

3.8.4 High-Pressure Cell

High pressure excitation scans were accomplished with a high-pressure cell [86]. For the purposes of this research, pressures up to 10 atm were used. The vessel comprised of 3-inch cubic 4140-steel alloy housing that has a yield strength 85,000 psi. Three 3/4" NPT mounted Corning fused quartz 7980 optical windows were installed for 214nm entry and exit, and for ICCD fluorescence detection. The windows can withstand an internal pressure of 3040 psi and an external pressure of 145 psi. An NIST certified digital pressure gauge was thread mounted to the top of the cell. This gauge had a maximum reading of 1000 psi and a 1 psi resolution. A pop-safety valve with a set pressure of 1000 psi was also installed for safety purposes. Two needle valves were installed for perturber gas/Kr addition and vacuum pump evacuation. This device operates on a similar premise as the static cell in Figure 3.6.

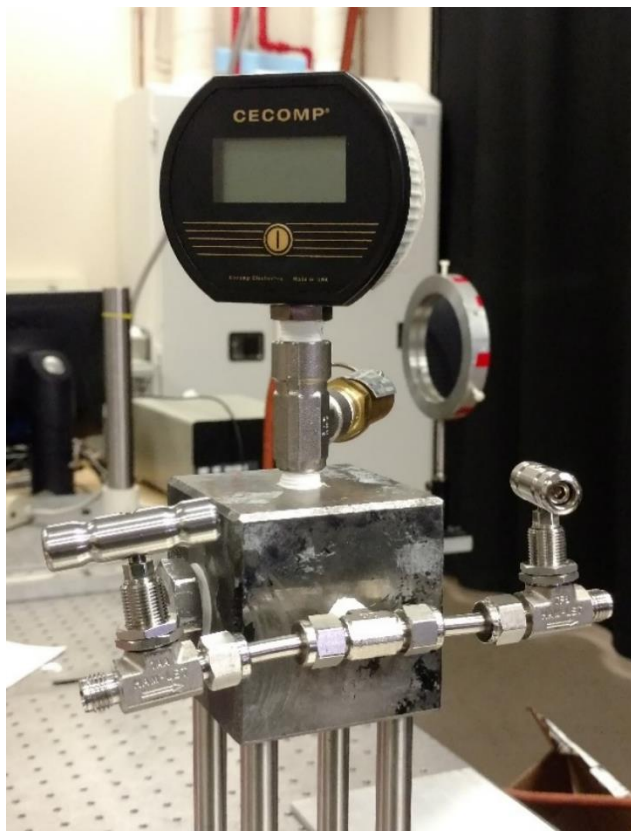


Figure 3.8: High-pressure cell.

3.8.5 Gas Circuit and Fittings

The gas circuit used for combustion experiments and general gas delivery needs is shown in Figure 3.9. Gas was delivered to the circuit from large AirGas brand compressed gas tanks controlled via pressure regulators and needle valves (not pictured). The inert gases used for this study included N_2 , CO_2 , He, and Ar. Fuel species include CH_4 , C_3H_8 , and C_2H_4 . Most of the tubing used was $\frac{1}{4}$ " or $\frac{1}{2}$ ", either stainless steel and high temperature polymer or PVC tubing. Gas flow was controlled by manual needle valves and in-line check valves to prevent reverse flow. Flow rates were monitored with numerous Omega FMA series digital flow meters. Flow meter ranges and precisions were 100 ± 0.1 SLPM for air, 10 ± 0.01 SLPM for inert gas, 1 ± 0.001 SLPM for Kr, and 10 ± 0.1 SLPM for fuel. In the case of electric heater experiments, inert gas or fuel was bypassed

through the 100 SLPM flow meter due to flow rate requirements. Specific fittings used for all components in this dissertation were of Swagelok/Yor-lok variety or NPT.

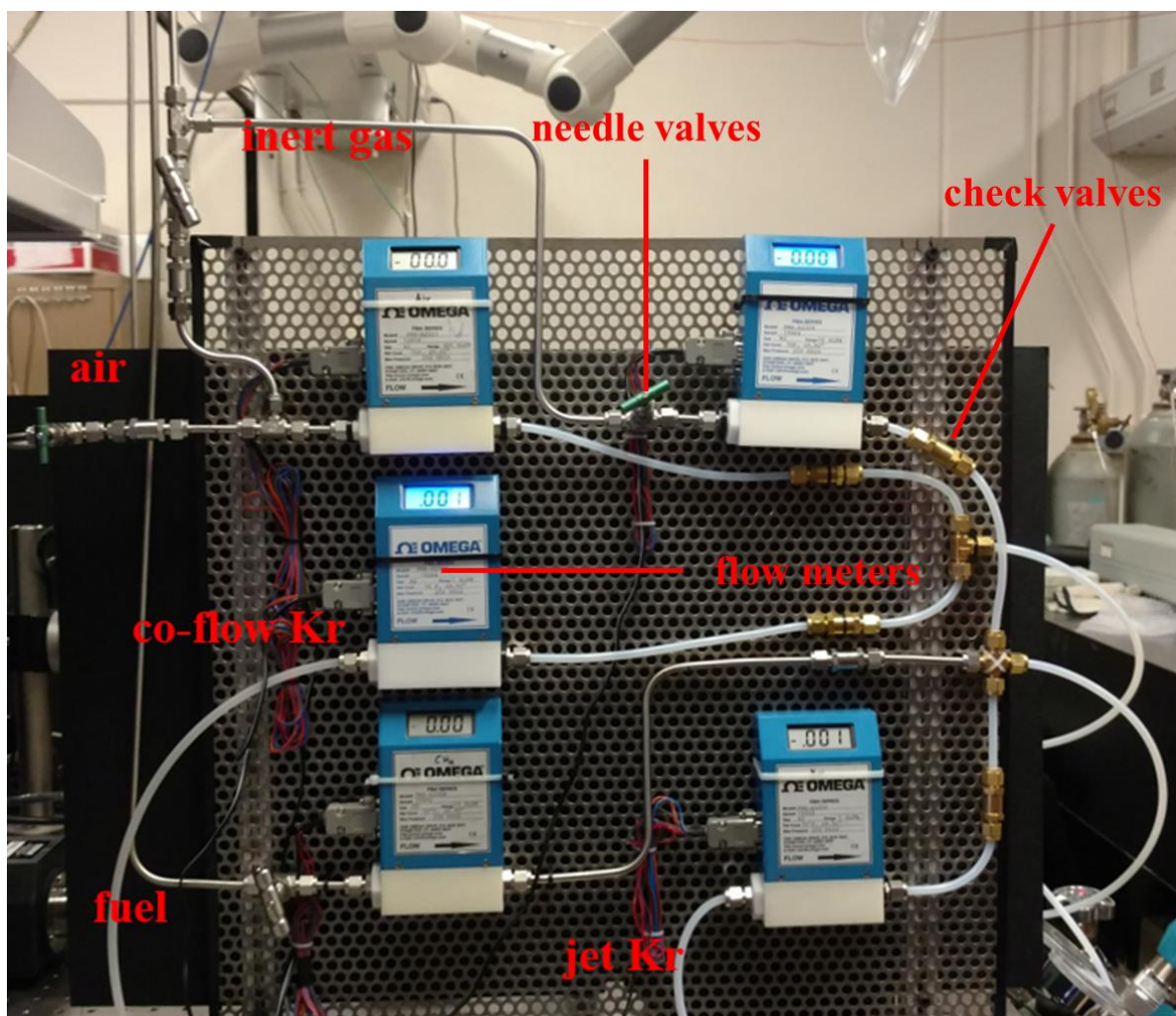


Figure 3.9: Gas circuit.

Chapter 4 : Data Processing

The purpose of this chapter is to provide an overview of the data processing routines as the same processes apply to multiple chapters throughout this dissertation. Minor changes or details specific to an experimental investigation will be covered in its associated chapter, if need be.

4.1 Kr PLIF Excitation Scans

Central to this investigation involves performing Kr PLIF excitation scans by varying the wavelength output of the dye laser and collecting the fluorescence images with the ICCD camera. Kr PLIF excitation scan images were processed to remove background intensities and corrected for shot-to-shot energy fluctuations obtained from the laser sheet intensity images from the CCD camera using developed MatLab codes. A quadratic energy dependence of fluorescence signals is assumed during the correction, since the saturation effects are negligible. Multiple regions spanning the fluorescence sheet were extracted from the images and were used for further data analysis. Data analysis of Kr PLIF images involved obtaining the magnitudes of w_c , δ_c , and w_G (Doppler width and instrument broadening) for each data selection region that provided the best fit for the Voigt spectra. Gaussian and Lorentzian spectra were obtained by least-squares fitting the Voigt excitation scans. First, the total Voigt FWHM (w) and center wavenumber were determined from the experimental data. Next, data processing codes iteratively convolved numerous Gaussian and Lorentzian spectra of varying widths to determine the best synthetic fit for the Voigt excitation scan. The resulting fit that minimized the RMS deviation from the experimental data was chosen to correspond to the Voigt excitation scan's Gaussian and Lorentzian contributions. This curve fitting procedure deconvolved the Voigt spectra without introducing noise into the system.

4.2 Rayleigh Scattering

Rayleigh scattering was performed to determine temperatures of premixed flame exhaust, to use as an input to composition-independent thermometry techniques, and as an imaging technique to elucidate different regions of reacting environments. For all applications listed, Rayleigh scattering signals were acquired at 1 atm and 300K for i number of calibration gases (He, Air, N₂, CO₂ and CH₄) of varying scattering cross-sections [87, 88, 89]. Calibration of the images was necessary to subtract the reflective signal produced by diffuse light striking the burner surfaces and to determine the experimental system constant k to map the scattering intensity to camera signal counts.

$$\begin{aligned} S_{camera}(x, y) &= S_{RS}(x, y) + S_{reflective}(x, y) \\ S_{camera}(x, y) &= k\sigma_{RS,i}I_0 \frac{p}{k_B T}(x, y) + S_{reflective}(x, y) \end{aligned} \quad (27)$$

The corrected Rayleigh scattering (S_{RS}) can now be expressed as the following.

$$S_{RS} = k\sigma_{RS}I_0 \frac{p}{k_B T} \quad (28)$$

Since the polluting signal was disbursed unequally throughout the images, the calibration procedure was performed on a pixel-by-pixel basis to ensure all reflective signal is removed from the background subtracted images. Additionally, all Rayleigh scattering images were normalized with laser intensity readings recorded with the Coherent Fieldmax II energy meter.

Chapter 5 : Compositional Scaling of Kr LIF Collisional Parameters

Collisional broadening of the krypton $4p^6 S_0^1 \rightarrow 5p \left[\begin{smallmatrix} 3 \\ 2 \end{smallmatrix} \right]_2$ transition centered at 107.3 nm caused by common combustion species is investigated in this chapter. Specifically, the compositional dependencies of the collisional parameters between collision partners with similar electronic energy level gaps is studied. In this situation, the classical expression of dispersive energy during collisions cannot be simplified to obtain closed form equations for the collisional parameters. The broadening parameters, namely w_c and δ_c were obtained through a two-photon excitation scan of krypton present in a mixture containing krypton and the collision partner at 300K and 101 kPa. The compositional scaling of w_c and δ_c are compared with scaling at situations corresponding to both large and small perturber electronic energy level gaps as compared to the absorber's electronic energy level gap. Further, contributions from dispersive and non-dispersive forces were computed and compared to assess the validity of the experimental findings.

5.1 Experimental Procedure

Experimentation involved performing excitation scans of the krypton fluorescence under near vacuum conditions (500Pa of Kr gas only) and with different perturber gases at 1 atm and 300K. The dye laser was scanned at a rate of $0.034 \text{ cm}^{-1}/\text{s}$ and 10 images were acquired per second resulting in a wavenumber resolution of $0.0034 \text{ cm}^{-1}/\text{s}$. This resolution is at least 20 folds better than typical collisional shifts and FWHMs observed with different perturbers. Prior to performing excitation scans, the laser energy was calibrated using the integrated fluorescence signals of the glass flat collected by the CCD camera. Typical energy fluctuation during the excitation was approximately 5%.

After calibration, the test cell (Figure 3.6) was prepared for low pressure scans to acquire the vacuum centerline of the transition. The test cell was evacuated using a vacuum pump, with

krypton contributing to more than 80% of cell pressure. At this cell pressure (500Pa), the collisional shift is approximately 0.002cm^{-1} , which was comparable to the wavenumber resolution. Subsequently, excitation scans were performed at a 1 atm and 300K with several perturber gases; the partial pressure of krypton is set at 500Pa for all cases. Laser energy from the CCD camera and fluorescence images using the ICCD camera were acquired simultaneously during all excitation scans.

5.2 Data Analysis

Figure 5.1 shows a sample experimental excitation scan with air as the perturber and the synthetic Voigt profile fitted using in-house developed codes. In the figure, $\omega - \omega_0 = 0$ corresponds to vacuum center, obtained experimentally. Since the excitation energy stayed within $\pm 5\%$, no energy correction to the scan was performed, which resulted in a very small amount of scatter in the data. Uncertainty in the measured spectral broadening arises because of residual contamination from the unseeded Nd:YAG laser spectrum, jitter in Nd:YAG and dye laser linewidth, contamination from cavity harmonics of the dye laser, as well as from the stepper motor lag during an excitation scan. The effect of camera noise on determining the spectral broadening and shift was mitigated by using the Voigt fit to determine the collisional broadening FWHM and shift. The RMS variation in the spectral scan FWHM and shift with air as the perturber, computed using 15 data-sets obtained on different days, were 0.03cm^{-1} and 0.02cm^{-1} respectively. These form the mean uncertainty of w_c and δ_c for this study.

The instrument broadening is due to the linewidth of the dye laser, whose FWHM is specified by the manufacturer as $w_L = 0.06\text{cm}^{-1}$. Following Friehtner & Gord [90] the effective laser linewidth in a two-photon process is $\sqrt{2}w_L = 0.085\text{cm}^{-1}$, which was validated using experimental tests at very low pressures ($\sim 500\text{Pa}$) where the collisional broadening is negligible.

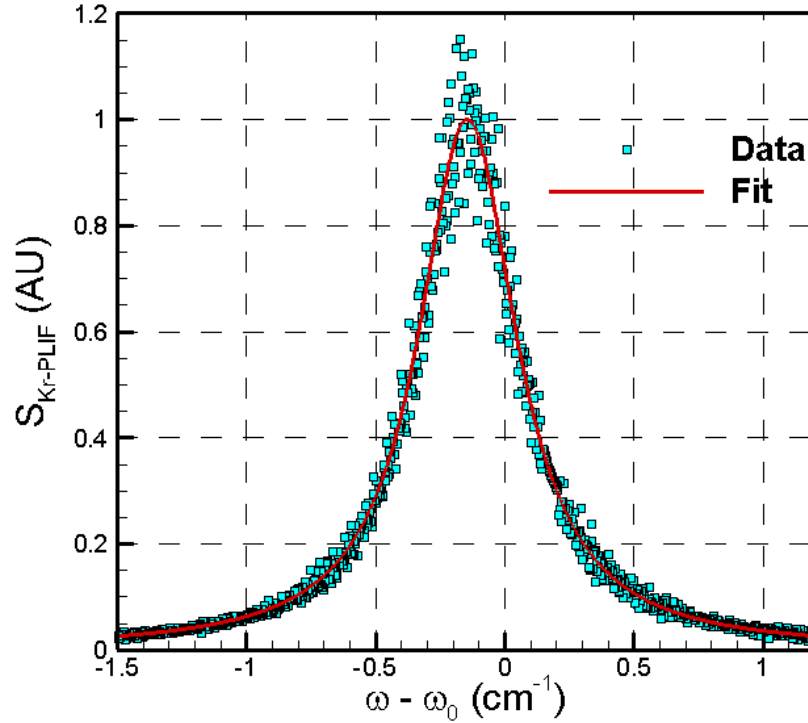


Figure 5.1: Sample excitation scan with air as the perturber and the corresponding Voigt fit.

5.3 Results and Discussion

For this investigation, it was important to evaluate a broad range of diverse test gases with different molecular weights, molecular chemistry, and refractive indexes. Table 5.1 shows the different gases employed and their relevant properties.

Table 5.1: Absorber and perturber properties.

| Gas | M (kg/kmol) | $(n-1) \times 10^6$ | \bar{p} (D) |
|-----------------------------------|---------------|---------------------|--------------------|
| Kr | 84 | 470 | 0 |
| Air | 28.97 | 293 | 0 |
| CO₂ | 44.01 | 451 | 0 |
| N₂ | 28.01 | 297 | 0 |
| Ar | 39.95 | 281 | 0 |
| CH₄ | 16.04 | 444 | 5×10^{-6} |
| C₃H₈ | 44.1 | 1100 | 0.083 |
| R-134a | 102.03 | 1100 | 2.08 |

Seven different perturber species were chosen to cover a large range of molecular weights and polarizability values. The gases used have a six-fold variation in molecular weight, over four-fold variation in polarizability, and seven-fold variation in molecule size (effective diameter). The perturber gases included diatomic and polyatomic species, inert gases, polar and non-polar gases, as well as asymmetric and symmetric molecules. An important combustion species that was missing from this list due to experimental difficulties was water vapor. Previous works by DiRosa & Hanson on NO collisional broadening showed significant deviations in FWHM results with water vapor as the perturber, which they attributed to its large permanent dipole moment [74]. In the list of perturber gases, it should be noted that Freon (R-134A) has a larger permanent dipole moment than water (1.74D). Hence, if there existed deviations in water vapor as the perturber, it was hypothesized that such deviations should also be present with Freon for this study.

Table 5.2 shows the experimental and theoretical collisional broadening FWHM and shift for different perturber species. The theoretical values of collisional FWHM, shift, and impact radius are obtained by using the semi-classical Lindohm-Forley theory (assuming large perturber energy spacing compared to absorber energy spacing) outlined in Thorne et al. [68]. Details of these calculations are provided in Appendix D.

Table 5.2: Experimental and theoretical values of collisional width and shift.

| Perturber | w_c ($\text{cm}^{-1}/\text{atm}$) | δ_c ($\text{cm}^{-1}/\text{atm}$) | w_c (theoretical) | δ_c (theoretical) |
|-----------------------------------|--|---|------------------------|-----------------------------|
| Air | 0.399 | -0.145 | 0.244 | -0.0870 |
| CO₂ | 0.440 | -0.131 | 0.255 | -0.0912 |
| N₂ | 0.408 | -0.149 | 0.248 | -0.0884 |
| Ar | 0.374 | -0.138 | 0.218 | -0.0777 |
| CH₄ | 0.559 | -0.170 | 0.344 | -0.1227 |
| C₃H₈ | 0.606 | -0.168 | 0.365 | -0.1302 |
| R-134a | 0.539 | -0.111 | 0.284 | -0.1012 |

It can be observed that the theoretical estimates of both FWHM and shift are within the same order of magnitude as the experimental values. This corroborates that the collisional interactions indeed occur in the impact broadening regime. Because of the empirical assumptions on some of the theoretical parameters, the theoretical values are not expected to be in exact agreement with the experimental results. Interestingly, the predicted theoretical trend of collisional FWHM is in excellent qualitative agreement with experimental results. In contrast to w_c scaling, theoretical predictions of δ_c show a completely opposite trend to the experimental observations. For example, while the theoretical estimate for CO₂ shows a larger shift compared to air, the experimental values show the opposite. Thus, the previously developed classical theory assuming large perturber energy gap exhibit stark deviations from experimental values of collisional shift, while having a qualitative agreement in FWHM trends.

Using the experimentally determined collisional parameters listed in Table 5.2, the composition scaling of w_c and δ_c in the present situation is delineated. First, the closed-form scaling for the two extreme situations discussed previously are examined to assess their applicability. The rationale behind this approach stems from the physical origins (rather than empirical fitting) that had resulted in scaling of these extreme situations. Figure 5.2 shows collisional FWHM data plotted with scaling corresponding to large absorber energy separation ($w_c \propto \mu^{-0.3}$) and large perturber energy separation ($w_c \propto (n_p - 1)^{0.4} \times \mu^{-0.3}$), respectively. The scaling parameters are normalized with the corresponding values for air. The error bars in Figure 5.2 represent (two-sided) 95% confidence interval obtained using at least 5 experimental runs per gas performed at different days. Whereas Figure 5.2a shows large scatter within the data, Figure 5.2b shows the data collapsing to a straight line. The dashed line in Figure 5.2b shows the expected collisional FWHM with the scaling $w_c \propto (n_p - 1)^{0.4} \times \mu^{-0.3}$. The maximum deviation of 5% from this scaling was

by CH₄ among all gases test. This tight collapse with the scaling shows that $w_c \propto (n_p - 1)^{0.4} \times \mu^{-0.3}$ adequately describes the collisional broadening FWHM in Kr LIF with major combustion species as perturbers.

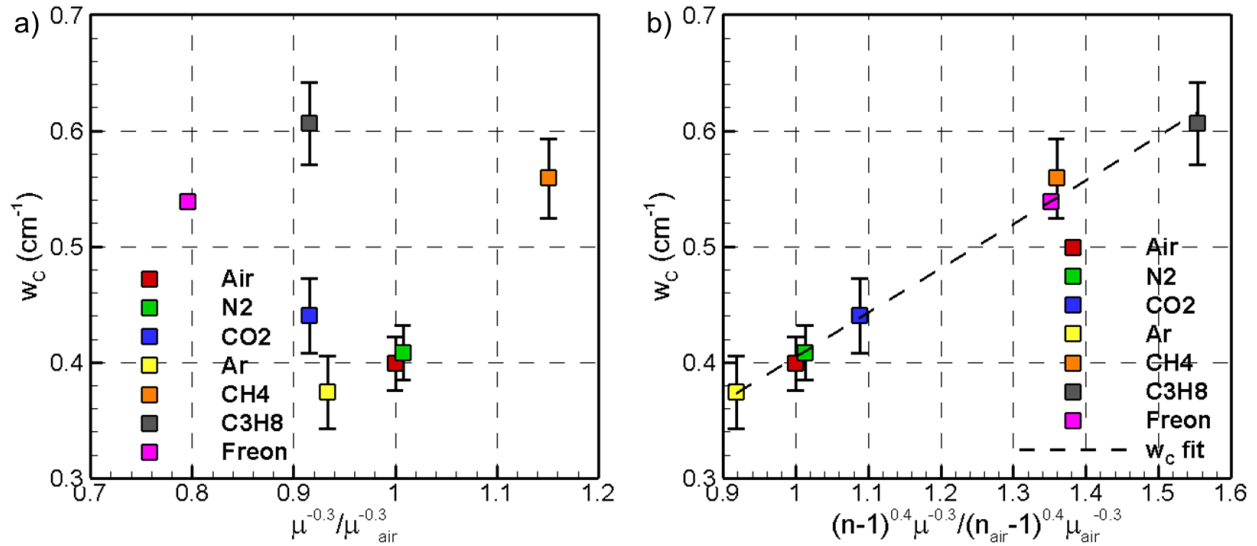


Figure 5.2: Comparison of compositional scaling of w_c based on (a) $\mu^{-0.3}$ and (b) $(n_p - 1)^{0.4} \mu^{-0.3}$. The scaling parameters are normalized by those of air.

A similar exercise was performed to learn if the collisional shift scaling fits into either of the extreme conditions. Figure 5.3 shows collisional shift data plotted with scaling corresponding to large absorber energy separation ($\delta_c \propto \mu^{-0.3}$) and large perturber energy separation ($\delta_c \propto (n - 1)^{0.4} \times \mu^{-0.3}$) respectively. The error bars in Figure 5.3(a) represent a (two-sided) 95% confidence interval obtained using at least 5 experimental runs per gas performed at different days. Once again, the scaling parameters are normalized by the corresponding values for air. In contrast to w_c , the δ_c values show a good collapse when scaled using $\mu^{-0.3}$ and a large scatter when scaled using $(n - 1)^{0.4} \times \mu^{-0.3}$. The dashed line shows the expected value of collisional shift using the scaling $\mu^{-0.3}$. All gases other than propane show a very good agreement within 0.02 cm⁻¹. Considering that the uncertainty in collisional shift is approximately 0.017 cm⁻¹ because of the dye laser scanning speed, this agreement is excellent. It is believed that the observed large deviation in

collisional shift with propane is due to its large FWHM, which causes difficulty in precisely locating the centerline of the fitted spectra. Barring the exception of propane, it is clear from Figure 5.3 that the collisional shift indeed scales as $\delta \propto \mu^{-0.3}$.

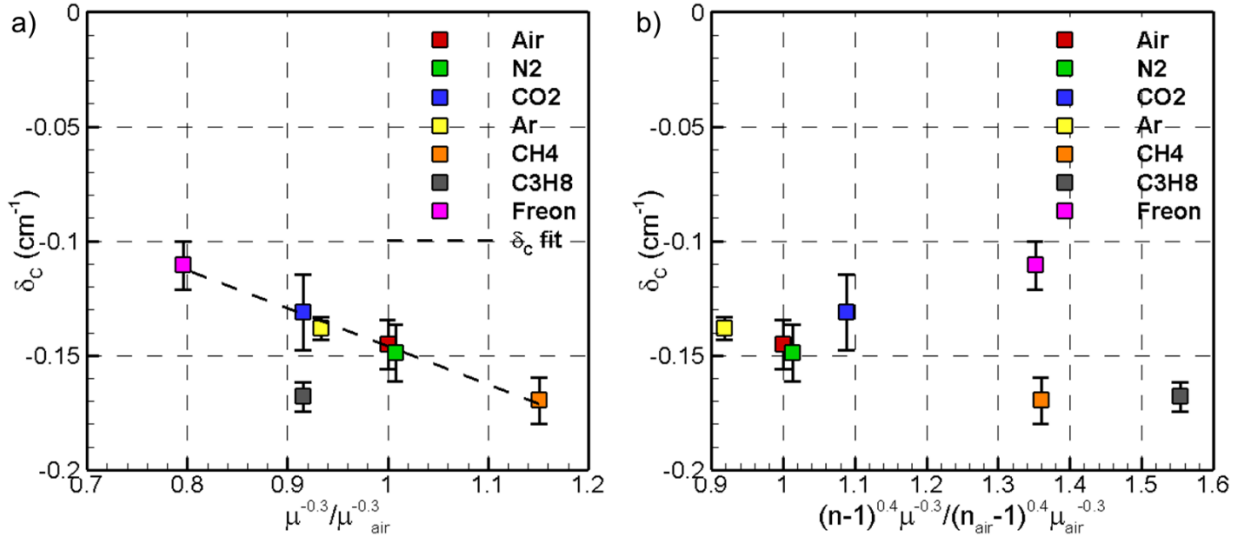


Figure 5.3: Comparison of compositional scaling of δ_c based on (a) $\mu^{-0.3}$ and (b) $(n_p - 1)^{0.4} \mu^{-0.3}$. The scaling parameters are normalized by those of air.

To summarize, the following are the scaling relations for collisional FWHM and shift for the krypton/perturber combinations tested in this study.

$$w_c \propto (n_p - 1)^{0.4} \times \mu^{-0.3} \quad (29)$$

$$\delta_c \propto \mu^{-0.3} \quad (30)$$

The observation of effective scaling of the collisional FWHM and shift suggests that the collisional parameters are indeed dominated by dispersion forces. Verification of this hypothesis was performed theoretically by evaluating the contributions from different interaction potentials on total interaction energy. Since krypton has a zero-permanent dipole, the electrostatic forces are non-existent. The interaction energies due to induced-dipole and dispersive interactions are computed using the following reduced relations from [91].

$$U_{\text{ind}} = \frac{p_p^2 \times \alpha_a}{R^6} \quad (31)$$

$$U_{disp} = \frac{\Delta C_6}{R^6} \quad (32)$$

Using these relations, contributions from U_{ind} and U_{disp} were computed for CH₄ (red) and Freon (black). Gas properties may be found in Table 5.1. Figure 5.4 shows the corresponding absolute contributions from U_{ind} (dashed line) and U_{disp} (solid line) over a range of approximately half of the impact parameter through five-times larger than impact parameter. The energies are normalized by Boltzmann's constant to report units of Kelvin. In each plot, the corresponding value of the impact parameter (ρ_w) is also marked by a '+' sign for each perturber. It can be observed from Figure 5.4 that over the range of separation distances relevant for collisions, the magnitude of U_{disp} is several orders of magnitude larger than U_{ind} for both perturbers considered. Thus, the theoretical calculations strongly support the hypothesis that the dispersive forces dominate the collisional interactions, which results in a very tight scaling of w_c and δ_c . The reader should be reminded that Freon (R-134A) has a large dipole moment, which exceeds the dipole moment of many of the polar species that occur in combustion mixtures (e.g., water). Hence, it is hypothesized that dispersive interactions will dominate other electrostatic and induced-dipole interactions with other major combustion species as perturbers.

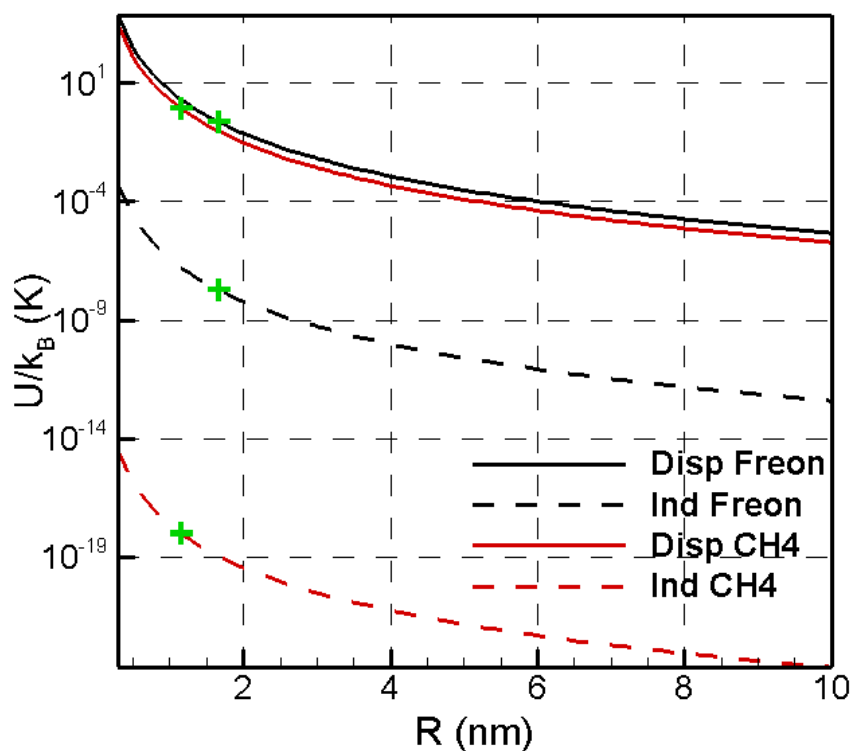


Figure 5.4: Dispersive and inductive atomic energies for freon and CH_4 as a function of distance R . The impact parameter is marked by a '+' symbol.

5.4 Generality of Scaling

This section addresses the generality of the compositional scaling of w_c and δ_c given in Equations (29) and (30) for any absorber/perturber combinations with similar electronic energy gaps between ground and excited states. Considering the transition probability is highest for the first excited state, the energy level difference between ground and the first excited state for different absorber/perturber species combinations is considered. A literature survey was undertaken to locate studies on such absorber/perturber combinations with similar electronic energy gaps. This resulted in identifying previous works on NO [92, 91, 73, 93, 94] and CO [95] as absorbers and different combustion species as perturbers. Owing to the large number of perturbers used for NO studies, the accuracy of w_c and δ_c scaling obtained for Kr LIF (Equations (29) and (30)) was studied for NO/perturber combinations and is presented here.

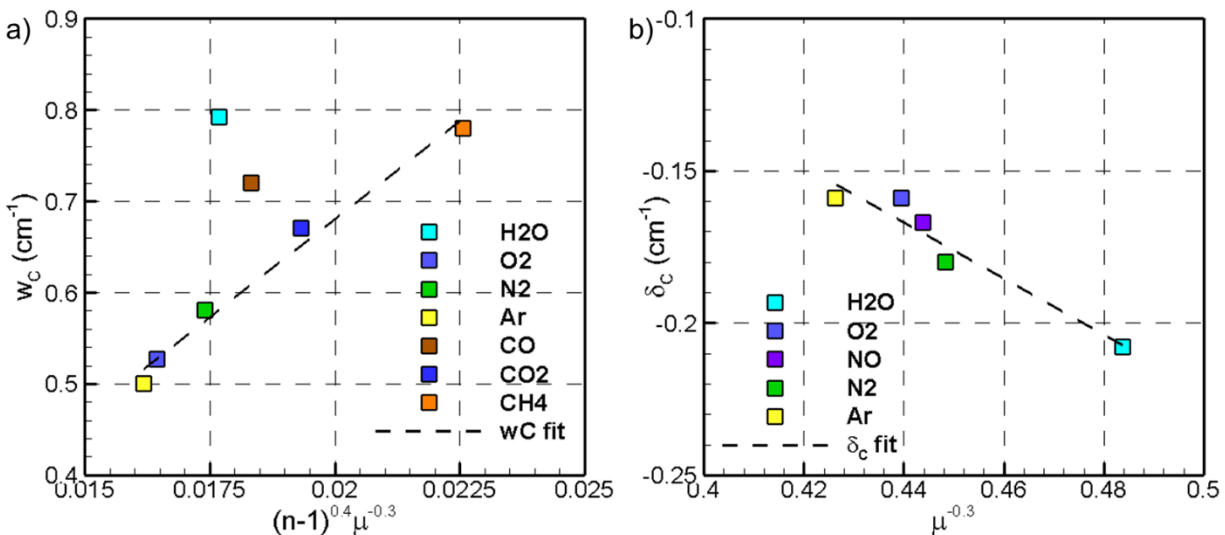


Figure 5.5: Compositional scaling of w_c and δ_c of NO (γ band) on reduced mass and refractive index with data from [92, 91, 73, 93, 94]: (a) w_c scaled using Equation (29); and (b) δ_c scaled using Equation (30). Dashed line represents the expected value based on the scaling from the present work.

Figure 5.5 shows that the exceptions to the scaling of collisional FWHM of NO absorption occur with H₂O and CO as perturbers. DiRosa [91] hypothesized that the deviations in scaling with H₂O occur because of the significant contributions of dipole-dipole and dipole-quadrupole interactions towards energy transfer during collisions in addition to dispersive forces. These additional interactions occur because of the large permanent dipole moment of H₂O and the static dipole moment of NO molecules. Further, DiRosa & Hanson [92] hypothesized deviations exist with CO due to the occurrence of inelastic collisions. These inelastic collisions cause rovibronic transitions in CO, which produces the observed deviations in the case of CO as the perturber. Considering that perturber species with permanent dipole moments (Freon R134-A) do not cause deviations in scaling with Kr as absorber, it appears that one of the important parameters that define deviation from scaling is the presence of a permanent dipole in the absorber, which results in appreciable contributions from electrostatic and dipole-induced forces towards the interaction potential. In the situation with Kr as the absorber, the absorber permanent dipole is zero and, hence, the deviations due to perturber dipole moments do not occur, as shown previously. However, it is

not clear if deviations due to inelastic collisions causing rovibronic transitions can still occur if molecules without permanent dipoles (N_2 , O_2 , air, Ar, CO_2) are used as absorbers.

While it is known that metal/inert gas combinations correspond to the extreme situation of a large perturber energy gap, the objective of this study was to determine an approximate boundary of absorber and perturber energy gaps when deviations from Equations (29) and (30) begin to occur. Once again, a literature survey was undertaken and was found that w_c and δ_c compositional scaling with I_2 as the absorber and air or N_2 as the perturber [72] had better agreement with the situation corresponding to a large perturber electronic energy gap (Equations (21) and (22)) compared to the similar energy gap situation (Equations (29) and (30)). While an exact boundary in terms of the ratio of absorber to perturber energy gap could not be delineated to describe when Equations (29) and (30) will fail, the magnitude of I_2/N_2 energy gaps ($\approx 2\text{eV}/\approx 6 - 12\text{eV}$) can make an approximate guide.

Chapter 6 : Two-Photon Excitation Doppler Broadening Temperature Scaling

The following chapter presents the determination of the temperature scaling to the Doppler width corresponding to a two-photon process. The principle of thermometry of a composition-independent technique to be developed in this work relies upon extracting the Doppler broadening from the excitation scan and inferring temperature from it. The previous chapter [96] provided the collisional widths and shifts of Kr for various perturber species at constant temperature and pressure but could not provide any further details on the Doppler broadening aside from the total Gaussian width at room temperature. This finite amount of Gaussian width may be attributed to the Doppler broadening at 300K and the inherent Gaussian laser linewidth.

Classically, the single photon excitation Doppler width is represented by the following equation.

$$w_D = \omega_0 \sqrt{\frac{8 \ln(2) (k_B) (T)}{M_{Kr} c^2}} \quad (33)$$

Substituting the values for Kr, for single-photon excitation at 214nm $w_D = 0.063 \sqrt{\frac{T}{300}} \text{ cm}^{-1}$. Though the theory on single-photon excitation Doppler widths is well documented and may be regarded as general, an investigation into the temperature calibration of the two-photon excitation Doppler width may deem appropriate to prove if a two-photon process may or may not be represented by some scaling parameter, i.e. $w_D = K_D \sqrt{\frac{T}{300}}$. At the very least, this experimental campaign would shed light on the contributions between the Doppler broadening and laser linewidth towards the total Gaussian width, w_G .

6.1 Experimental Procedure

Doppler broadening temperature scaling calibration experiments involved obtaining excitation scans of krypton fluorescence in low pressure, elevated temperature environments and premixed methane flame exhaust. The dye laser was gradually tuned over the absorption band at a uniform rate of $0.034 \text{ cm}^{-1}/\text{s}$. Ten images were acquired per second, resulting in a frequency resolution of $0.0034 \text{ cm}^{-1}/\text{frame}$. First, multiple excitation scans were performed at low pressures and 300K conditions to ensure consistency in the laser linewidth and centerline for accurate collisional shift calculations for the hot exhaust gases. Following the acquisition of the vacuum FWHM and centerline, elevated temperature scans were performed to determine the Doppler broadening scaling for a two-photon process.

Homogenous high-temperature environments for the Doppler broadening investigation were produced by heating the static test cell containing 4 torr of Kr and no perturber gas using a 120V plug-in heating cable and a variable voltage controller. Temperatures of 300K, 370K, 470K, and 500K were obtained using this approach. An Omega K-type thermocouple provided these temperature measurements. Alumina insulation was employed to reduce heat losses and kept the temperature consistent during excitation scans. The rationale behind performing excitation scans in a so-called “vacuum furnace” setting (i.e. no perturber gas) stems from the fact that the deconvolution procedure described in Chapter 4 experiences increased difficulty to deconvolve smaller Doppler widths from large Lorentzian, collisionally dominated spectra. These low-pressure high-temperature environments proved to be highly Gaussian in post processing.

This study also employed premixed CH_4 flat flames to achieve exhaust temperatures in the range of 1600K to 2000K. Equivalence ratios of 0.65, 0.7, and 0.8 with mixture velocities of $0.063 - 0.065 \text{ m/s}$ were used. At these temperatures, the collisional broadening and shift were suspected

to be quite low to enable accurate extraction of the Gaussian width via deconvolution. Laminar flame calculations (equilibrium chemistry and unity Lewis number assumption) were performed to determine the theoretical temperatures and exhaust compositions. These temperatures were also experimentally verified using Rayleigh scattering imaging measurements. Addition of krypton (0.5% by volume) did not cause any measurable or noticeable changes to the flame.



Figure 6.1: Photograph of a premixed flat flame used for Doppler broadening temperature calibration.

6.2 Data Analysis and Results

Excitation scans were performed in the heated static cell and premixed flames, then deconvolved to obtain Gaussian widths at each temperature. As previously alluded, it is not clear if the general equation for w_D (Equation (33)) should remain the same for two-photon excitation at 214nm. Let the w_D for the two-photon process be represented by $w_D = K_D \sqrt{\frac{T}{300}}$. To determine the value of K_D , it is useful to note that the Gaussian broadening FWHM obtained from the excitation scan may be represented by the following form:

$$w_G^2 = w_D^2 + w_L^2 \quad (34)$$

$$w_G^2 = K_D^2 \frac{T}{300} + w_L^2 \quad (35)$$

While static cell temperatures could be verified with thermocouple readings, premixed methane flat flame exhaust required the use of Rayleigh scattering thermometry. Adiabatic flame calculations were performed for each equivalence ratio to obtain the Rayleigh scattering cross-section of the hot exhaust/air mixture due to entrainment. The temperatures at a height of 10mm above the burner surface evaluated using this technique are shown in Figure 6.2. Average values for each equivalence ratio were found to be $1679\text{K} \pm 4.5\text{K}$, $1772\text{K} \pm 5.5\text{K}$, and $1980\text{K} \pm 7.5\text{K}$ for 0.65, 0.7, and 0.8 respectively. Furthermore, the premixed configuration of the burner depicted in Figure 3.7 proved to be a very effective temperature calibration device, as the flat flame provided extremely uniform temperatures across the radius of the ceramic and temperatures very near to the adiabatic flame temperature up to 10mm downstream.

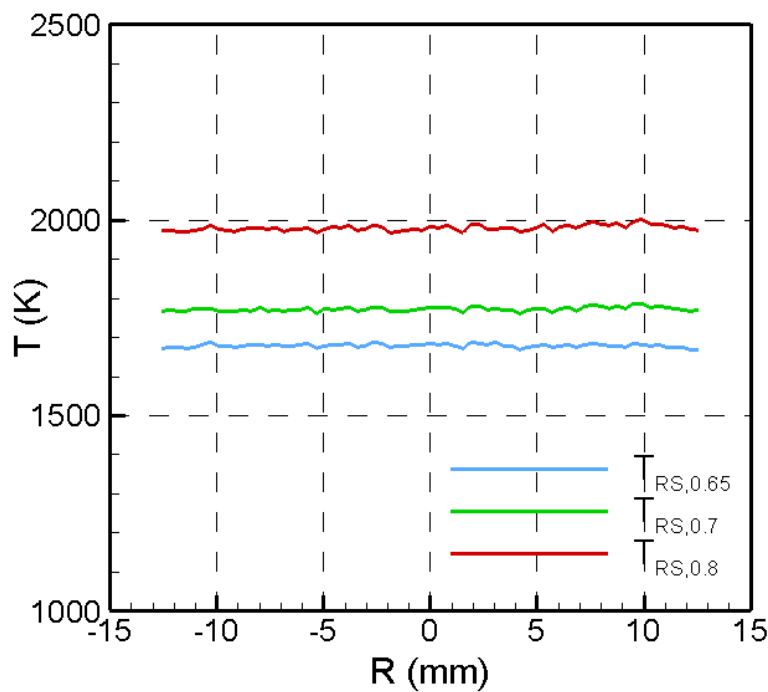


Figure 6.2: Rayleigh scattering temperature measurements for the premixed CH_4 flat flames used in this study.

The results of w_G from the high temperature Kr PLIF excitation scans is shown in Figure 6.3. More than 10 samples were acquired for each temperature and RMS deviations for the data points did not exceed 0.01cm^{-1} . As a first sanity check, the experimentally obtained w_L from the fit intercept was compared to the manufacturer specified value. Accounting for the fact that the apparent laser linewidth during a two-photon process is $\sqrt{2}w_L$ [97], the experimental value (0.057cm^{-1}) compares very favorably with manufacturer specified value (0.06cm^{-1}). The slope of the fit was then determined to obtain the value of K_D . From Figure 6.3, the scaling for w_D with temperature for two-photon excitation at 214nm is given by

$$w_D = 0.093 \sqrt{\frac{T}{300}} \text{ cm}^{-1} \quad (36)$$

which is about a factor of $\sqrt{2}$ larger than the corresponding w_D for single photon absorption. A few caveats should, however, be exercised while interpreting the increased broadening in two-photon excitation, as the authors are not aware of any theories that support or oppose the enhanced Doppler broadening in two-photon excitation. The first caveat is that the actual laser line profile was not measured for these set of experiments. Further, while the excitation scans in the low-pressure furnace were largely Gaussian at these pressures, there still existed very minor residual errors in the synthetic fits. Without measuring the laser spectrum directly due to a lack of resources, it is hypothesized that these residual errors appear due to departure of the laser spectrum from being strictly Gaussian. Furthermore, it should be noted that in the high temperature exhaust experiments, the Voigt spectra did have a non-trivial contribution from collisional broadening. The uncertainty in w_D values from the latter is estimated at 0.02cm^{-1} for this data. Accounting for this uncertainty, the value of K_D is conservatively estimated to deviate by less than 10%, thus remaining close to the scaling proposed in Equation (36). Finally, it should be noted that regardless of whether

the enhanced broadening is purely a laser artifact or not, the Doppler broadening scaling in Equation (36) is still valid for the thermometry techniques demonstrated in this dissertation since the w_D scaling was calibrated for the same laser system that was used for the thermometry experiments.

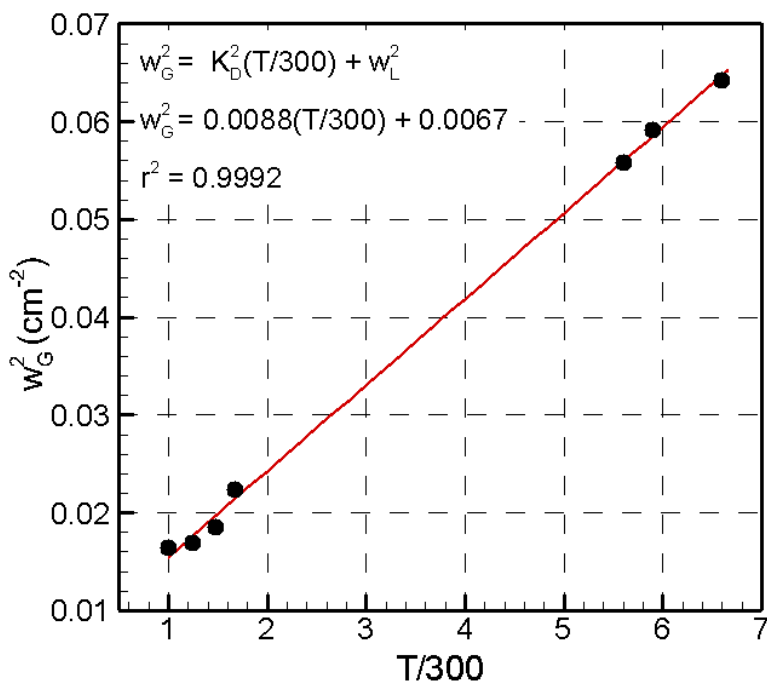


Figure 6.3: Variation of the Gaussian FWHM with temperature obtained from excitation scans at different temperatures. Data shown compiles the experiments performed in vacuum furnace as well as premixed flat flame exhaust at 1 atm.

Chapter 7 : Collisional Parameter Temperature Scaling

While the collisional width and shift contain known compositional dependencies as described by Equations (29) and (30) [96], their temperature dependencies are still unknown. Development of composition-independent thermometry techniques depend heavily on the precise determination of closed formed solutions for all spectral broadening parameters. Classically, these dependencies take the following power law dependence form:

$$w_c \sim \left(\frac{T}{300}\right)^{-j}, \delta_c \sim \left(\frac{T}{300}\right)^{-i}$$

According to dispersive interaction theory, the values of j and i are predicted to be 0.7 for both collisional parameters [68], but have reported values in the range of 0.5 – 1 in numerous studies featuring NO [73, 74, 91] and CO [95]. Therefore, a similar temperature scaling procedure must be performed for the collisional broadening to precisely obtain the values of these exponents.

7.1 Procedure

High-temperature environments for obtaining temperature exponents for the collisional parameters were achieved by using an Osram SureHeat Jet electrical heater. Unlike the Doppler broadening scaling investigation, atmospheric conditions were employed to produce an adequately collisionally broadened and shifted spectra. Additionally, multiple gases were used to investigate whether the temperature exponents are general and independent upon gas composition. The gases included air, N₂, CO₂, and CH₄. Temperatures in the range of 300 – 900K were produced which is safely below the autoignition temperature of methane.

An identical experimental procedure was followed as in the previous chapter. Following the acquisition of the vacuum FWHM and centerline, heated gas scans were performed to determine temperature power law dependencies for the collisional parameters of multiple gases.

Each gas was flowed through the heater at a rate of 65 SLPM to ensure the heater was operating in a safe range. Kr flowed through the heater at approximately 1 – 1.5% by volume depending on the gas. Signal levels were kept within an acceptable range to ensure the scans were not saturated. After room temperature scans, the temperature controller was set to its max setting for the system to reach its equilibrium point. From that point forward, the temperature was reduced to the next temperature condition. This method proved to produce very stable temperatures (within 5K) with rapid stabilization periods (approximately 1 minute).

7.2 Results

A similar temperature scaling procedure that was performed for the Doppler broadening was employed to determine the temperature dependencies for w_C and δ_C . The electrical heater was used to heat air, N₂, CO₂, and CH₄ at atmospheric conditions from 300K to 900K. Figure 7.1 displays the collisional width and shift of N₂, CO₂, and CH₄ in a log-log plot with temperature to obtain the exponents j and i in the context $w_C \sim \left(\frac{T}{300}\right)^{-j}$ and $\delta_C \sim \left(\frac{T}{300}\right)^{-i}$. Air is omitted from this plot due to extremely similar values with N₂. Table 7.1 displays the results for each of the gas' temperature exponents. These values are within very close agreement with one another (RMS deviations of 0.008 and 0.02), suggesting that the collisional width and shift temperature exponents in the Kr LIF spectrum are independent of gas composition. Furthermore, average values of approximately 0.8 for w_C and 0.6 for δ_C agree very well with the value of 0.7 as predicted by dispersive interaction theory [68], and are consistent with the range of values observed in NO [73, 74, 91] and CO [95]. The slight deviation of the CH₄ collisional shift temperature exponent is hypothesized to arise from the fact that CH₄ broadens significantly more than the other gases used in this study, and thus is more challenging to pinpoint the centerline when fitting with a Voigt

profile. Nonetheless, these results provide promise that the temperature scaling of the collisional parameters in the Kr LIF system is general for any given gas composition.

Table 7.1: Temperature exponents for the collisional width and shift of air, N₂, CO₂, and CH₄.

| Gas | j | i |
|-----------------|-------|-------|
| Air | 0.794 | 0.59 |
| N ₂ | 0.798 | 0.588 |
| CO ₂ | 0.789 | 0.613 |
| CH ₄ | 0.807 | 0.63 |

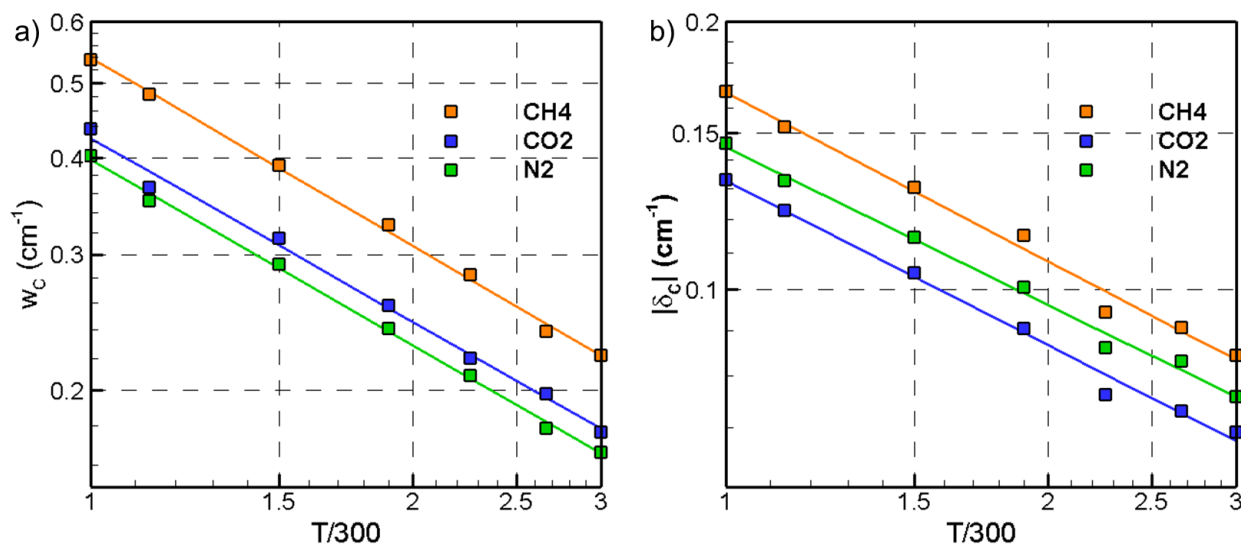


Figure 7.1: Temperature scaling of the a) collisional FWHM and b) collisional shift for N₂, CO₂, and CH₄.

Though these conclusions are quite favorable for Kr PLIF thermometry efforts, the results do not provide elevated temperatures that one would expect in flames and practical combustion applications. There may exist a multiple power law exponent dependence for temperatures exceeding 1000K, for example. Fortunately, considering that the temperature exponents are independent on composition as illustrated in in Figure 7.1, the collisional parameters determined experimentally for air in the temperature range of 300 – 900K may be combined with the collisional parameters for premixed methane flame exhaust that were obtained in the exercise in the previous chapter. These results are provided in Figure 7.2. It should be noted that the air and

premixed exhaust measurements have been normalized such that their compositional differences have been eliminated. The collisional FWHM and shift have been fitted with curves corresponding to temperature exponents of 0.8 and 0.6 respectively, corroborating the findings of Table 7.1 and Figure 7.1. In summary, the closed form solutions for w_C and δ_C may be represented as the following in Equations (37) and (38).

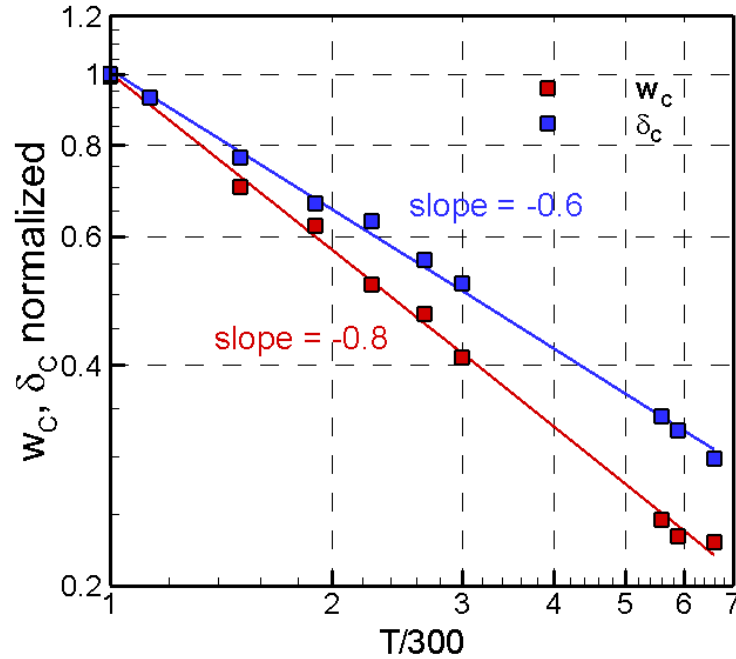


Figure 7.2: Temperature scaling of the collisional parameters of air and premixed methane exhaust corrected for compositional differences.

$$w_C [cm^{-1}] = 0.40p \left(\frac{T}{300} \right)^{-0.8} \left(\frac{n-1}{n_{air}-1} \right)^{0.4} \left(\frac{\mu}{\mu_{air}} \right)^{-0.3} \quad (37)$$

$$\delta_C [cm^{-1}] = -0.145p \left(\frac{T}{300} \right)^{-0.6} \left(\frac{\mu}{\mu_{air}} \right)^{-0.3} \quad (38)$$

Chapter 8 : Development and Demonstration of Composition-Independent Kr PLIF

Thermometry Techniques Using the Spectral Line

Two composition-independent thermometry methods are demonstrated in this chapter, both of which make use of spectral lineshape information obtained from excitation scans of the Kr $4p^6 S_0^1 \rightarrow 5p \left[\frac{3}{2} \right]_2$ transition. In the first method, the local Doppler broadening is extracted from an excitation scan to yield the corresponding temperature, while the second method utilizes compositional scaling information of the collisional broadening and collisional shift to determine the temperature. Both methods are demonstrated by measuring the radial temperature profile of a steady laminar CH₄/N₂ diffusion flame with an air co-flow. The accuracy of the temperature measurements obtained using both methods are evaluated using corresponding temperature profiles determined from computational simulations.

8.1 Relations for Thermometry Methods 1 and 2

To determine the local temperature using Method 1, the Doppler broadening width was determined from the Voigt profile using deconvolution methods implemented using in-house codes. The local temperature was determined from the Doppler broadening FWHM using Equations (35) and (36). This approach is similar to that demonstrated in [98] where two-photon excitation of atomic nitrogen and oxygen were used to measure velocity and temperature of high-enthalpy arc-heated flows by extracting the Doppler shift and Doppler width, respectively.

In contrast to Method 1, no deconvolution procedures were adopted in Method 2. Instead, an algebraic expression provided by [99], which relates the total Voigt FWHM (w) to w_G and w_C , was used. This expression provides error less than 0.02% for the range of w_G and w_C employed in this work [99].

$$w = 0.5346w_c + \sqrt{0.2166w_c^2 + w_G^2} \quad (39)$$

It may be observed that the collisional parameter equations provide two relations between three unknown variables (T , $n-1$, and μ). To close the equations, the third relation was obtained using Rayleigh scattering signal ratios, R_{RS} . By normalizing local Rayleigh signals by that of air at a known temperature (T_{air}) and pressure (p_{air}), the following equation was obtained.

$$R_{RS} = \frac{S_{Ray}(x,y)}{S_{Ray,air}} = \left(\frac{n-1}{n_{air}-1} \right)^2 \frac{p}{p_{air}} \frac{T_{air}}{T} \quad (40)$$

It should be specified that knowledge of the pressure in Equation (40) is necessary to determine the temperature using Method 2. Equations (39) and (40) with supporting relations for w_G and w_C (Equations (35), (36), (37), (38)) provided the full set of equations that were solved to determine the temperature at every super-pixel in the ICCD image.

8.2 Experimental Procedure

The flame used in this study was a CH_4/N_2 steady laminar non-sooting jet diffusion flame (42% and 58% by volume) produced by the in-house jet in co-flow burner (Figure 8.1). The fuel mixture was flowed at a rate of 2.35 m/s ($\text{Re} = 1400$) with a circular co-flow of dry air at a velocity of 0.15m/s surrounding it. Krypton was added in amounts of approximately 0.5% by volume. The measurement domain was centered at approximately 15mm downstream of the burner exit and extended to a region of 6mm \times 50mm. The flames used for experiments were very stable in the measurement domain for several diameters downstream, beyond which the flame appeared unsteady due to buoyancy effects. The choice of this fuel configuration and measurement location stems from the following challenges it poses. Being considerably heavier than the fuel mixture, krypton diffuses significantly slower into the oxidizer stream compared to the fuel mixture; the effect of differential diffusion is strongest close to the jet exit in turbulent flames [100]. For the case of laminar flames, differential diffusion is typically more active over most of the flame

domain than turbulent flames. Krypton, which has a molecular weight of 84 kg/kmol, is over a factor of four larger than fuel and exhaust mixture and is computed to have a binary diffusivity of $0.16 \text{ cm}^2/\text{s}$ into N_2 , compared to $0.23 \text{ cm}^2/\text{s}$ of methane into N_2 [101]. This poses a significant challenge in obtaining adequate krypton concentration across the entire combustion mixture, especially close to reaction zone and in leaner regions. The air co-flow was not seeded with Kr in this study to evaluate how well diffusion occurs across the reaction zone, but also to ensure that signal levels would remain unsaturated. The second feature of this measurement location is that it spans the entire range of combustion temperatures with relatively sharp gradients, which demands the largest dynamic range required for these thermometry techniques. Demonstrating that the thermometry techniques developed in this work can circumvent these challenges should provide promise for its application in more complex combustion situations.

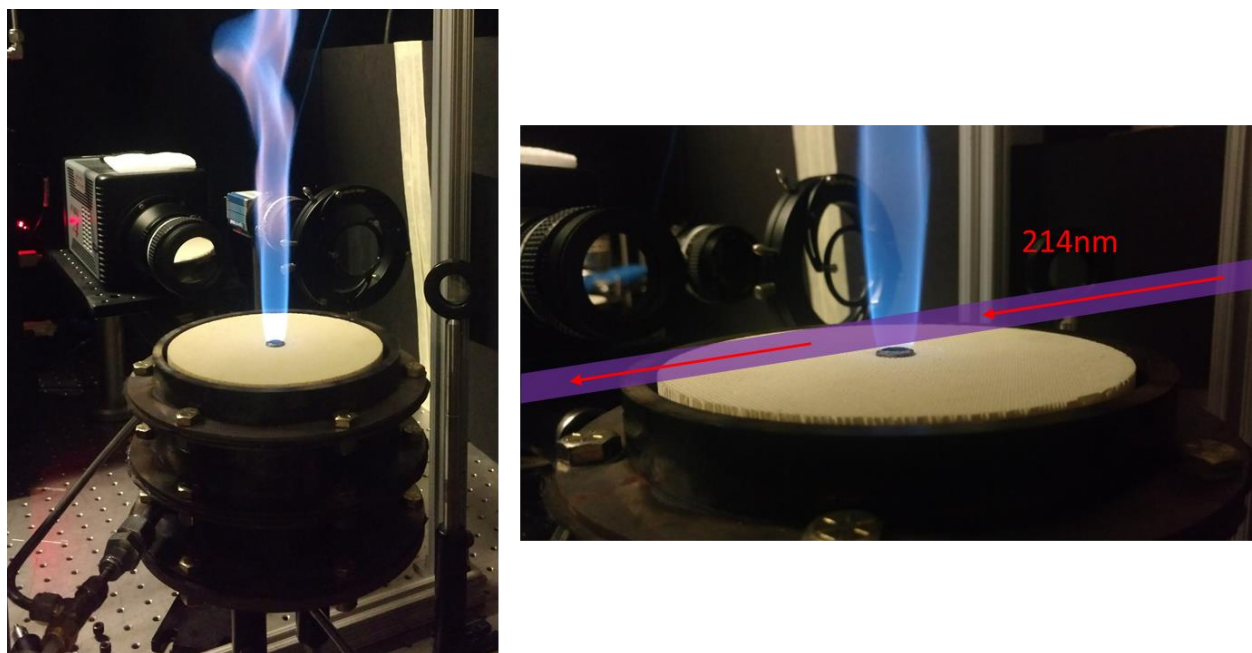


Figure 8.1: Photographs of the CH_4/N_2 diffusion flame used for this work and an illustration of the measurement domain.

Both thermometry methods involved obtaining excitation scans of krypton fluorescence. The dye laser frequency was increased at a uniform rate of $0.0034 \text{ cm}^{-1}/\text{frame}$. This resolution has

proved be satisfactory in prior experimental investigations. Similarly, the 214nm laser sheet profile was also obtained simultaneously from the glass flat fluorescence using the CCD camera for sheet and laser intensity corrections to the fluorescence images.

At the beginning of each experimental session, the static cell was prepared for low pressure excitation scans at 4 torr of Kr at 300K to ensure consistency in the laser linewidth and centerline for accurate collisional shift calculations. Acquisition of the laser centerline was followed by excitation scans in the static cell filled with air at 1 atm and 300K containing 0.5% Kr by volume. These experiments were performed to verify that the broadening parameters matched the extensive database from previous experiments at identical conditions. These values typically stayed constant over the span of 4 – 5 hours, over which the excitation scan of the test configuration was employed. The Kr PLIF excitation scans targeting the CH₄/N₂ diffusion flame followed these consistency tests.

8.3 Data Analysis

Kr PLIF images were processed to remove background intensities and corrected by the laser energy and laser sheet profile. A quadratic energy dependence of fluorescence signals was assumed per Equation (1) during the correction, since the saturation effects were assumed negligible. Subsequently, 10×20 pixels were binned into super-pixels with a spatial resolution of $0.5\text{mm} \times 1\text{mm}$ for further processing.

Figure 8.2a shows a sample experimental excitation scan at the centerline location of the laminar CH₄/N₂ jet used in this study and the best-fit synthetic Voigt profile. In this figure, $\omega - \omega_0 = 0$ corresponds to vacuum center, obtained experimentally. It can be observed from Figure 8.2 that all the data points follow the fit quite faithfully. Upon closer examination of Figure 8.2, some asymmetry in the excitation scans may be observed in the blue spectral wings. This asymmetry

causes some disagreement below approximately 30% of peak signal and was present in all scans that were performed. It was not suspected that the spectrum was influenced by speed-dependent effects, correlations between velocity-changing and state-changing collisions, or the finite duration of collisions, due to the low pressure employed in this work and the large molecular weight of Kr. The handling of background subtraction did not contribute to the asymmetry, as the background intensity counts were proved to be independent of wavelength and dependent only on the spatial location. Nonetheless, an investigation was performed using a simple model to fit an asymmetric Voigt profile. The model used was adapted from the approach used in [102], where the Lorentzian and Gaussian widths could vary sigmoidally based on wavenumber.

$$w_i = \frac{2w_{i,0}}{1 + \exp[a(\omega - \omega_0)]} \quad (41)$$

In the above, w_i represents either the Lorentzian or Gaussian wavenumber dependent FWHM. This expression is advantageous because it allows the width to vary asymptotically between the bounds $0 - 2w_0$. Positive values of the asymmetry parameter skew the spectrum toward lower wavenumbers, while negative values skew towards higher wavenumbers. If the asymmetry parameter is zero, the spectrum is symmetric, and the width takes on a value of w_0 . The corresponding asymmetric Voigt profile is shown in Figure 8.2b, which clearly provides a tighter fit to the blue wing and produces smaller absolute residual values, albeit with an identical FWHM. However, the inclusion of the asymmetry parameter did not bring about any positive impact to the temperature because: 1) only the values of FWHM of the excitation scan (w) was used in Method 2, which did not depend on the spectral tail; and 2) the deconvolution procedure of Method 1 provided excellent accuracy with using the red wing and down to 30% of peak signal of the blue wing, and did not improve noticeably when all of blue wing tail was included. In light of the above

and considering that the asymmetry factor was a correction to obtain a better fit and does not have a physical basis, for all the results presented in this work, the entire red spectral wing and data above 30% of peak signal in the blue spectral wing were considered for further processing, the results of which matched the collisional widths obtained in Chapter 5. Certainly, further work into the cause of asymmetry on Kr PLIF spectra, other than possible dye laser artifacts, is required to help with better processing. This asymmetric lineshape model will be revisited in a later chapter with a deeper analysis into the asymmetry of the Kr LIF lineshape.

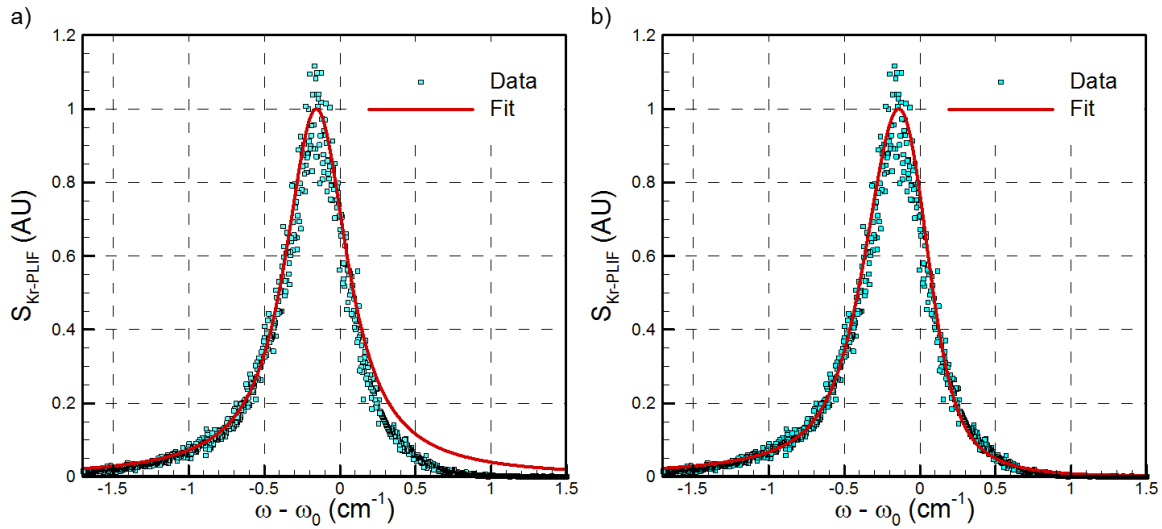


Figure 8.2: Sample experimental excitation scan for the fuel mixture at the jet centerline fitted with (a) Voigt profile and (b) asymmetric Voigt profile. Data points are illustrated with blue squares with the corresponding Voigt fit as a solid red line.

The RMS variation in the spectral scan total FWHM measured in the static cell filled with air at 1 atm and 300 K was 0.0025cm^{-1} . The RMS variation for the collisional shift was obtained by calculating the standard deviation in the spectrum centerline within the potential core (constant temperature and composition) for all excitation scans used for this study. This value was found to be 0.002 cm^{-1} . These values form the mean uncertainty of w and δ_C , respectively.

In a separate experimental campaign, Rayleigh scattering images were acquired to provide an input for thermometry Method 2. Rayleigh scattering images corrected for background and

reflective signals were normalized by the Rayleigh scattering signals of air at 1 atm and 300K to obtain the Rayleigh scattering signal ratio field, R_{RS} .

8.4 Results and Discussion

Results are presented for temperature measurements using both Methods 1 and 2 for a CH_4/N_2 diffusion flame. Before the temperature data is analyzed, the Rayleigh scattering signal profile obtained at $X = 15\text{mm}$ is shown in Figure 8.3 to elucidate the different regions of the combusting mixture and their corresponding extents. The Rayleigh scattering signals are normalized by Rayleigh signals of air at 300K and 1 atm as the scattering the medium. The location $R = 0$ corresponds to the jet centerline. Figure 8.3 shows a plateau region extending from $R = -3$ to 3mm, which corresponds to the unreacted CH_4/N_2 potential core. The constancy of the Rayleigh scattering signal and its relative magnitude with respect to air confirms that the temperature in the core remains constant at 300K. With increasing radial distance, the signal decreases continuously in the shear layer ($|R| = 3$ to 6mm), where the gas temperature increases. This monotonic drop in signal in the shear layer is terminated by a local minimum at $|R| = 7\text{mm}$, identifying the flame location. Beyond $|R| = 7\text{mm}$, the Rayleigh signals increase to recover to the value of ambient air. Temperature measurements using Kr PLIF extend from the potential core until $|R| = 6\text{mm}$. Outside of this range in fuel-lean regions, the Kr PLIF signal levels are quite low making them unfit for temperature determination.

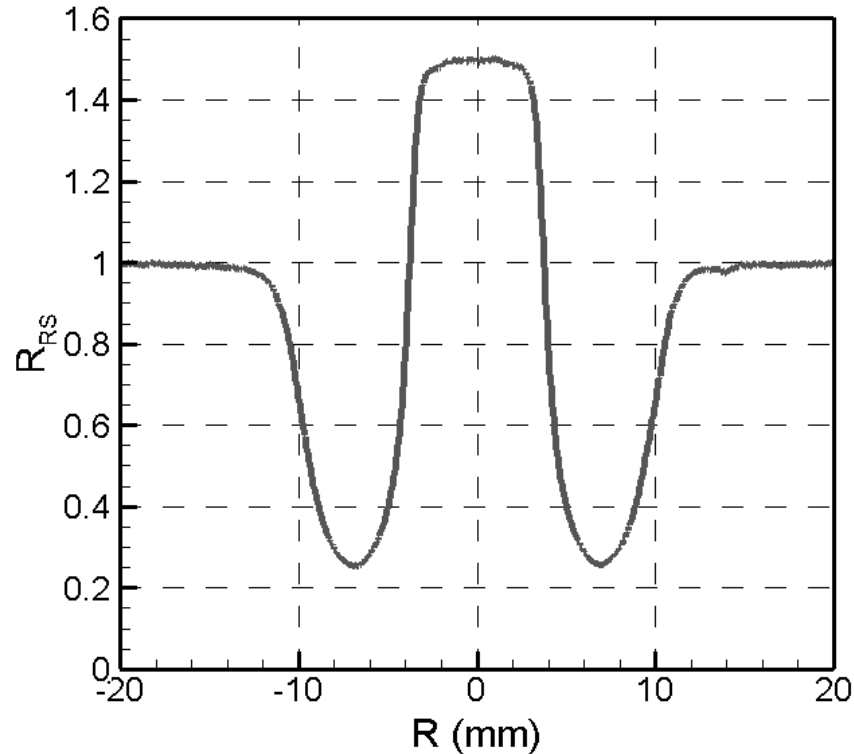


Figure 8.3: Radial profile of the normalized Rayleigh scattering signals across the laminar diffusion flame at an axial location 15mm above the jet exit. The signals were normalized by those of air at 300K and 1 atm.

The Kr PLIF signal levels are first evaluated at the different regions of the combustion environment. Figure 8.4a shows instantaneous images of the background-subtracted non-corrected and sheet-corrected Kr PLIF fields obtained during an excitation scan corresponding to the spectral peak of the fuel mixture ($\omega - \omega_0 = -0.155 \text{ cm}^{-1}$). It can be observed from Figure 8.4a that good signals are obtained along the potential core of the jet which contains highest krypton concentration and lowest temperature. Further, the raw Kr PLIF fields also contain bands of high and low signals caused by laser sheet inhomogeneity. In addition to the studies presented, separated experiments were performed to map the onset of fluorescence saturation by increasing the excitation intensity and investigating at what PLIF signal counts the quadratic energy dependence is lost. Through these tests it was verified that the onset fluorescence saturation of a super pixel occurs at approximately 3000 signal counts for this optical and camera setting. Hence,

proper care was taken to ensure the proper selection of 214nm energy, Kr concentration, and laser sheet height to stay well below the fluorescence onset. Therefore, the maximum signal count of a super-pixel in the potential core along a typical bright band is about 1700 out of the maximum 65000 to keep the fluorescence from saturating. It can further be observed from Figure 8.4a that the signal count decreases to approximately 250 as measurements approach the flame in the reaction zone. This effect is caused by a reduction in Kr mole fraction and gas density as one approaches the reaction zone. The background subtracted Kr PLIF images before sheet correction were also used to determine the signal to noise ratios (SNRs) at different regions of the measurement domain before binning. The local SNR was determined as the ratio of mean signal counts to the standard deviation over at least 100 samples of 10×10 -pixel² bins over three experimental runs. It was observed that the average SNR in the brightest region was approximately 10 in the jet core and decreased to 5 in the reaction zone at the respective peaks of excitation scan. In areas of lowest signal, the SNRs were reduced to 5 in the jet core and 3 in reaction zone. These lower results are primary due to sheet inhomogeneity which are improved considerably after sheet correction and signal averaging is performed. Figure 8.4b shows the corresponding sheet corrected Kr PLIF field assuming a quadratic dependence of Kr PLIF intensity on incident energy, which corresponds to unsaturated fluorescence. It can be observed that signal normalization by a quadratic laser intensity dependence has mitigated the banded structure of the raw Kr PLIF to a large extent, which shows that the fluorescence signals are indeed unsaturated.

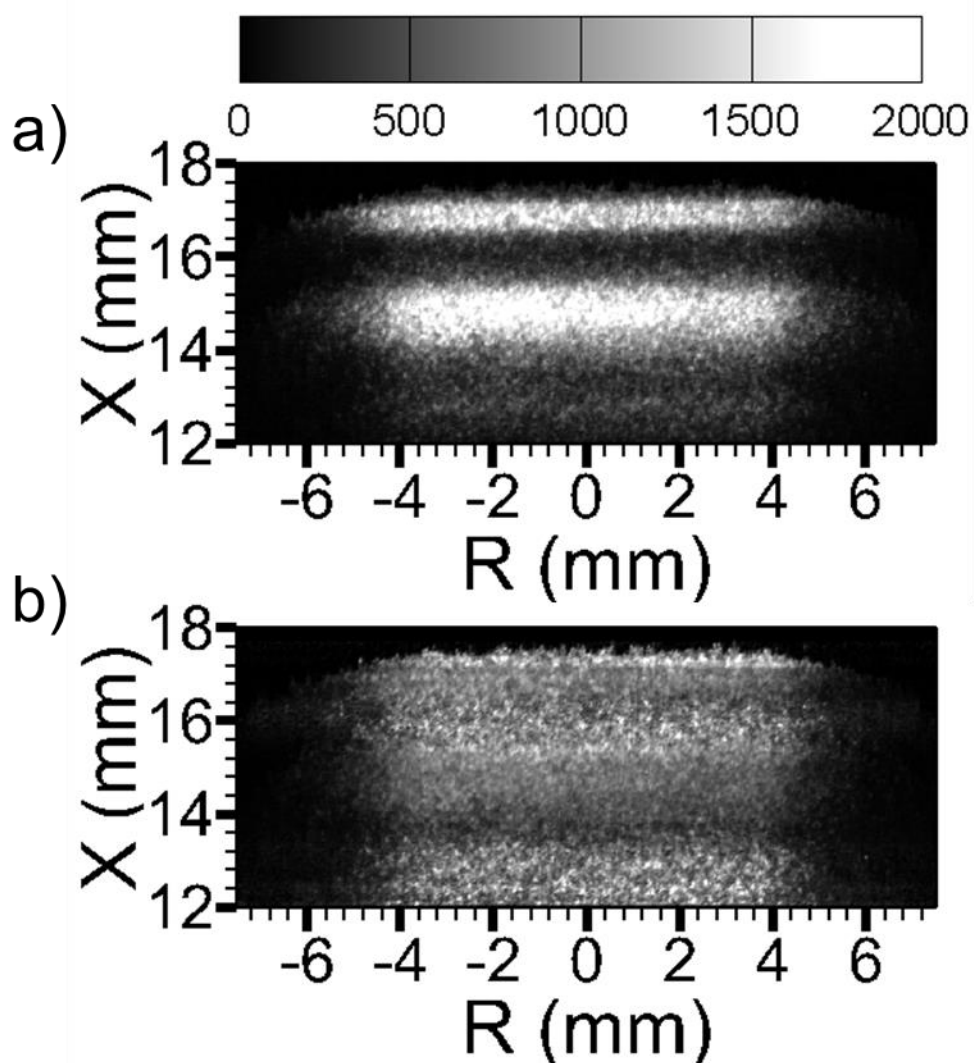


Figure 8.4: Background-subtracted Kr PLIF images of the CH_4/N_2 diffusion flame excitation scan corresponding to peak excitation wavelength of fuel mixture: a) raw Kr PLIF image; and b) sheet corrected Kr PLIF field.

Figure 8.5 shows excitation scans (symbols) and the synthetic spectral fits (solid lines) obtained at three representative locations at $X = 15\text{mm}$: the jet core (Figure 8.5a), the intermediate heating region (Figure 8.5b), and the reaction zone (Figure 8.5c). The data in these figures are the result of an ensemble average of four runs. In Figure 8.5, both experimental data and fit were normalized by the peak of the synthetic fit. It is observed that the scan width (w) and the shift (δ_c) of spectra decrease as measurements approach the reaction zone from the jet core. This is an artifact of increasing temperature and changing composition that together impact the broadening

parameters. The synthetic fits appear to fit the spectra quite well in the red spectral wing and down to 30% of peak signal in the blue wing in the core and down to 10% of the blue wing in the high temperature regions, below which the asymmetry causes some discrepancy. To evaluate the quality of the spectral scans, the average absolute error along the entire red wing between the normalized experimental data and corresponding fit data (shown in Figure 8.5) at a given wavenumber of the scan was computed. The average normalized fit error was 0.025 in the core and about 0.02 in the reaction zone. These close comparisons of the synthetic fit illustrate the high quality of the excitation scans that were used for thermometry.

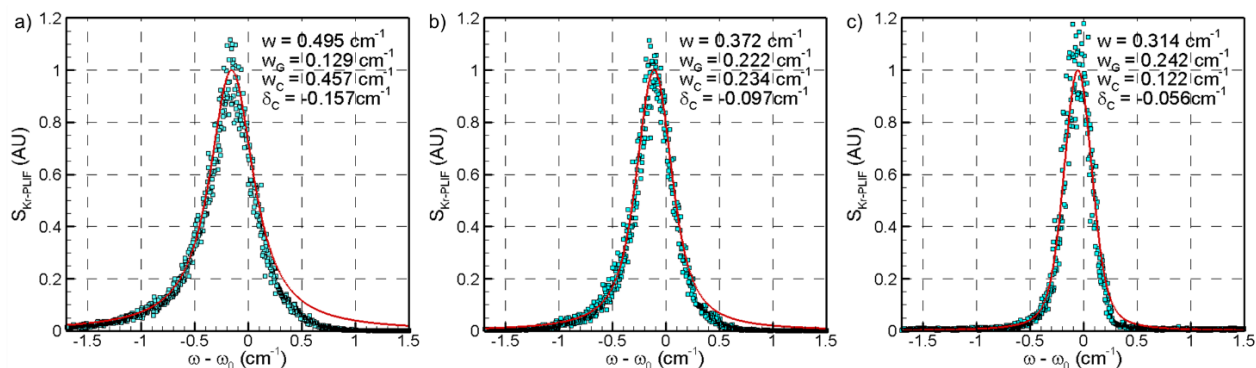


Figure 8.5: Excitation scans corresponding to a) the potential core ($T_{M1} = 340\text{K}$, $T_{M2} = 307\text{K}$), b) the intermediate heating region ($T_{M1} = 1270\text{K}$, $T_{M2} = 1157\text{K}$), and c) the reaction zone ($T_{M1} = 1848\text{K}$, $T_{M2} = 1821\text{K}$).

The lineshape parameters are compared to the Rayleigh scattering signal ratios at $X = 15\text{mm}$ in Figure 8.6. Data for the Kr PLIF lineshape parameters was acquired by the ensemble average of four experimental runs. Lineshape parameters w , w_C , w_G , and δ_C that result from the Voigt profile fitting procedure are represented by the secondary y-axis on the right-hand side of Figure 8.6. The normalized Rayleigh scattering profile is also included in Figure 8.6 to serve as a guide to the different regions. All the lineshape parameters show a flat profile in the potential core region, which is a direct result of constant composition and temperature. Average values for the Rayleigh scattering signal ratios and potential core collisional parameters are in excellent

agreement with theoretical values as determined by the relations developed in [96], exhibiting less than 2.5% variation. Extending to regions of the shear layer, δ_C increases towards zero as measurements approach the reaction zone due to the inverse temperature relation of δ_C . Correspondingly, w_G increases with radial distance because of the increase in Doppler broadening with temperature. In contrast, w and w_C decrease along the radial outward direction, with the decrease in w_C being very steep; this is mainly owing to its $T^{-0.8}$ dependence. The decrease in w is comparatively more gradual due to the net result of the opposite dependence of w_D and w_C on temperature, with $w_D \sim T^{0.5}$ and $w_C \sim T^{-0.8}$.

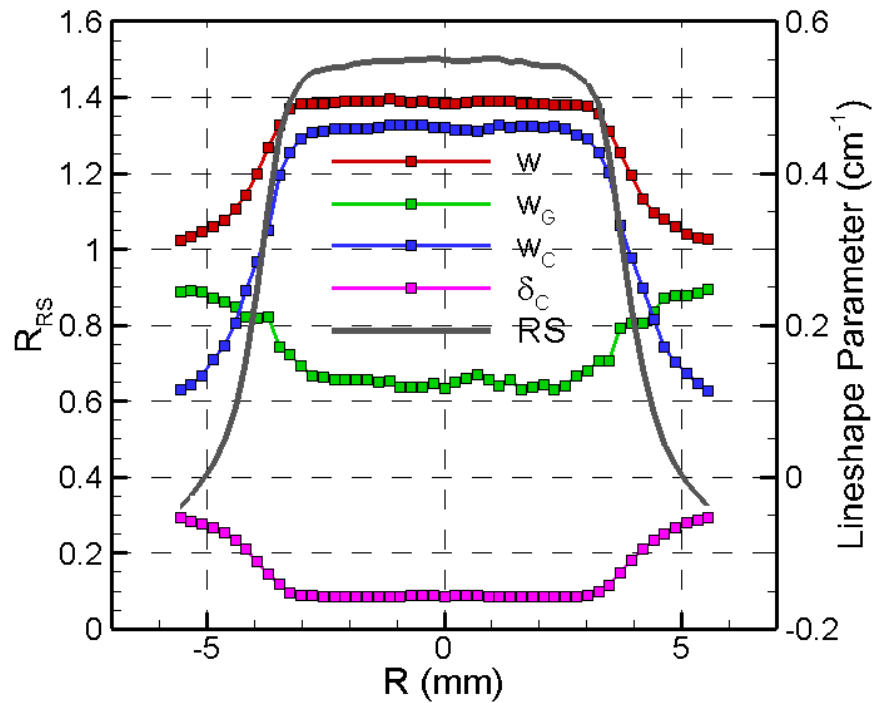


Figure 8.6: Radial profiles of different lineshape parameters obtained from Kr PLIF excitation scans and their comparison with normalized Rayleigh scattering signal radial profile. The radial profiles correspond to an axial location 15mm downstream of the jet exit.

8.4.1 Temperature measurements

Next, temperature profiles obtained using Methods 1 and 2 from the lineshape parameters in Figure 8.6 are individually presented in Figure 8.7a and b, respectively, along with the computational temperature profile obtained using computational codes employing GRI 3.0

mechanism for methane combustion. This CFD simulation was performed using a version of North Carolina State University's REACTMB flow solver [103] that used an eighteen species, 42 reaction methane oxidation model [104]. The Chemkin database provided species thermodynamic and transport data, while constant Schmidt (0.72) and Prandtl (0.27) numbers were assumed. The solver employed axisymmetry and a structured mesh containing 14400 cells. It can be observed that both Methods 1 and 2 exhibits mean potential core temperatures of approximately 304K and 296K, which is within an error of 3 – 4K (~1%) of the predicted value. The temperature increase along the shear layer is also captured very well between the two methods. Whereas both Methods 1 and 2 exhibit very good agreement with the computed profile until the reaction zone, Method 2 exhibits a better comparison with the computed profile across the entire measurement domain with less scatter. It should be noted that Methods 1 and 2 both produce slightly larger temperatures between the potential core and reaction zone. This may be attributed to the conservatively low values of mass diffusion used in the computation. Despite these differences, the similar temperature profiles and precise matching of maximum temperatures are very encouraging.

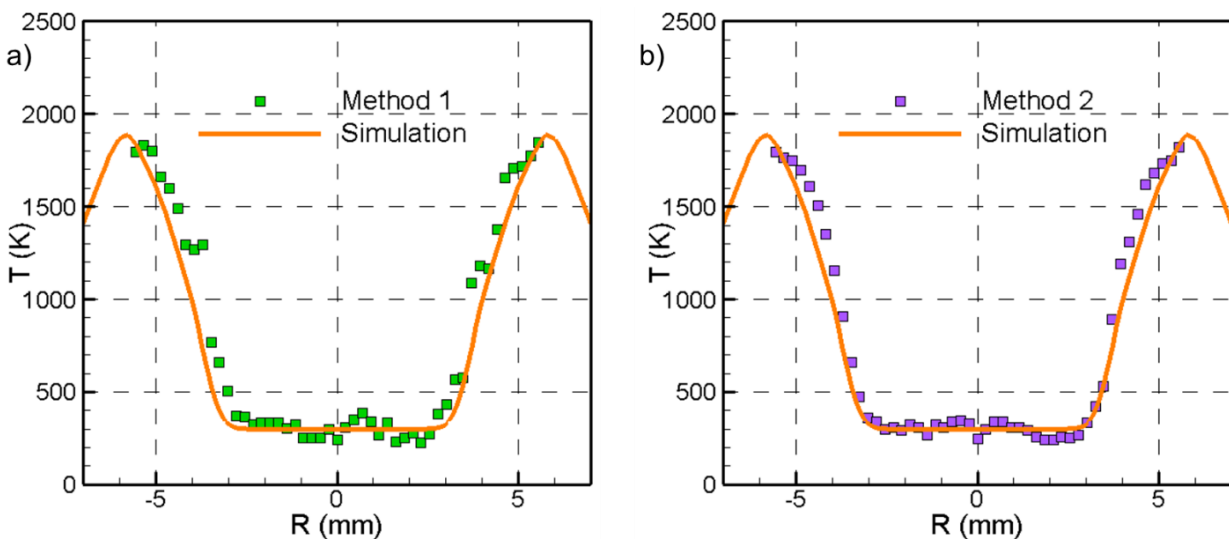


Figure 8.7: Comparison of experimental temperature profiles obtained for the laminar CH_4/N_2 diffusion flame with the computed profile: a) comparison between Method 1 and computed profile; and b) comparison between Method 2 and computed profile. Profiles correspond to an axial location 15mm downstream of the jet exit.

The presence of scatter in the core for Method 1 is mainly attributed to difficulties during Voigt deconvolution at the potential core. The spectral profile in the core is dominated by collisional broadening (Lorentzian profile) due to a modest Doppler broadening component caused by lower temperatures. Deconvolving the less prominent Gaussian contribution out of the Voigt profile becomes more challenging at these temperatures; the error in w_D is further amplified by the quadratic dependence of temperature on w_D . This results in a precision error of 43K in the core from Method 1; the corresponding precision error from Method 2 is 28K. The systematic errors in the mean temperature at other locations were calculated as the absolute difference between the measured and the computed temperature profiles. The error in the temperature is 85K and 60K close to the flame from Method 1 and Method 2, respectively. Upon analysis of the results of Method 2, it was necessary to assess the validity of the power law dependence on temperature demonstrated in Equations (37) and (38). The fact that good agreement in temperature is obtained across a combustion zone with a varying composition and such a large range of temperatures is very encouraging.

After achieving agreement between Method 1 and Method 2 at $X = 15\text{mm}$, Method 2 was applied to additional axial distances of $X = 14\text{mm}$, 16mm , and 18mm . The temperature results provided in Figure 8.8 demonstrate that the potential core persists to regions downstream with a nearly identical radial domain. Core temperatures remain at a precise value of 300K for each axial distance. Furthermore, for $X = 14\text{mm}$ and $X = 16\text{mm}$, the entire temperature profile, including the intermediate region and reaction zone, demonstrate temperature values within values of measurement uncertainty when compared to $X = 15\text{mm}$. It is not until $X = 18\text{mm}$ that differences in the temperature profile are observed. Maximum temperatures for the $X = 18\text{mm}$ case are approximately 1700K as opposed to 1850K, with the temperature distribution in the shear layer

exhibiting a much more gradual slope. This behavior is indicative of the slight radial expansion of the diffusion flame that extends the reaction zone to further radial locations.

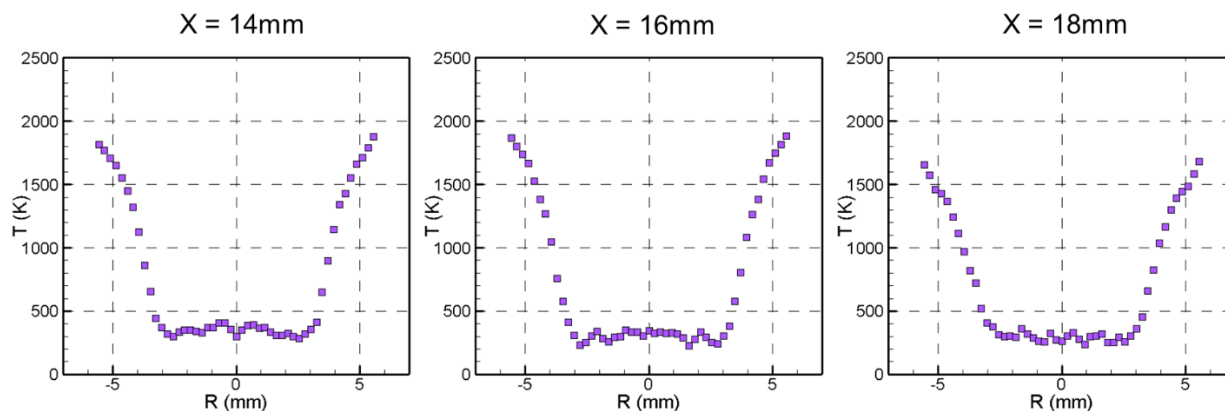


Figure 8.8: Radial temperature profiles using Method 2 at different downstream distances for the CH_4/N_2 flame.

To provide a perspective on the accuracy of the two methods, comparisons are drawn with more established thermometry techniques. Meier et al. [105] reported a mean temperature uncertainty of 3% using Rayleigh scattering imaging in turbulent flames with fuel mixtures that maintain near constant Rayleigh cross-sections over the combustion domain. The Stokes/anti-Stokes ratio method developed by Rabbenstien and Leipertz [43] was evaluated in a 1D premixed laminar flame exhaust, wherein the authors reported an uncertainty of 5 – 6% (80 – 120K) very close to the flame. Hancock et al. [45] evaluated temperature using N_2 and H_2 CARS in an H_2 /air flat flame and reported uncertainties of $\pm 20\text{K}$ and $\pm 70\text{K}$ in flame temperatures with N_2 and H_2 CARS, respectively. More recently, Roy et al. [106] used fs-CARS for thermometry in an H_2 flat flame to result in $\pm 40\text{K}$ uncertainty in flame temperature. Bengtsson [107] performed rotational CARS measurements in a CO /air diffusion flame and reported a temperature uncertainty of 50 – 75K in the flame and “even higher” values outside of the flame in the jet core. All values suggest that thermometry Method 2 is well within the range of uncertainty of previously established techniques, whereas the uncertainty from Method 1 is slightly larger in magnitude.

8.4.2 Uncertainty Analysis

The temperature data presented here is a mean quantity obtained by fitting an excitation scan that extended over 1000 images. Therefore, the causes for systematic error are considered and random error is neglected. In the following, the causes for the systematic error in Methods 1 and 2 are individually presented.

Uncertainty sources of Method 1. The error in the temperature determined using Method 1 can be divided into two distinct sources: 1) error in the determination of w_G and w_D ; and 2) error in the calibration between w_D and temperature.

The first source of error in the determination of w_G is the uncertainty in w . For the determination of the uncertainty in w , values were gathered for 20 different runs for air at 300K and 8 different runs for the CH₄/N₂ mixture. The experiments of which have been performed on different days. The overall uncertainty corresponding to these results in w is 0.0025cm⁻¹. Assuming w_G is a fraction of w and takes a maximum value of approximately 0.8 w at the highest measured temperature, the maximum uncertainty in w_G is estimated to be 0.9% at maximum temperature for this study, corresponding to a temperature uncertainty of 1.8%. The second source of error in determining w_G is the uncertainty produced during the deconvolution procedure, which includes the following: 1) spectral jitter introduced by the dye laser and injection seeder; 2) error from energy correction; and 3) error from overall noise (including fluctuations due to laser jitter, shot noise, dark noise, and readout noise). Because of the lack of manufacturer specified information or in-house tools that can accurately measure the spectral jitter, the spectral jitter in wavelength and linewidth of the dye laser during an excitation was conservatively estimated at 5% of the laser linewidth (Δw_L). While estimating the resulting uncertainty due to laser jitter requires a very involved procedure, the uncertainty in w_D was estimated by assuming that the “effective” w_L is w_L

$\pm \Delta w_L$. This results in 10% (28K) uncertainty in w_D at 300K and 26 K (5%) uncertainty in w_D at 1850K. Compared to the uncertainty introduced by the dye laser jitter, the Nd:YAG injection seeder jitter uncertainty is approximately an order of magnitude smaller. The error caused by energy normalization occurs due to fluorescence saturation, which causes deviations from the quadratic energy dependence, and energy calibration residual error. As demonstrated previously in Figure 8.4 the low excitation energy ensured unsaturated signals. Hence, this source of uncertainty has been neglected for the current measurements. To estimate the uncertainty caused by noise, a theoretical Voigt profile was simulated corresponding to temperatures and composition in both the core and flame region. Random noise with magnitude corresponding to the fit error in excitation scans was then applied to the theoretical Voigt profile. The “noisy” Voigt profile was then compared with the actual values of the broadening parameters to estimate the error due to detector noise. Using this procedure, the estimated error in w_G was determined to be 8% in the core and 1% in the flame. This translates to a mean temperature uncertainty of 78K in the core and 53K in the flame. The impact of the calibration error between w_D and temperature on temperature uncertainty was estimated by determining the difference in calculated temperature between experimental and fit w_D values. This procedure is performed for temperature in the low temperature (< 550K) and high temperature (> 1600K) regions (in reference to Figure 6.3). These fit errors translate to 36 K below 500 K and 16 K uncertainty above 1600 K, respectively. In summary, the overall uncertainties in the core and flame for Method 1 are 119K and 88K, respectively.

From this discussion, it could be concluded that that the dominant source of uncertainty is from the overall noise in the spectral scans, which has contributions from laser spectral jitter and noise left over after binning. It should be noted that the signal levels were deliberately kept low to avoid any instance of saturation causing relatively high noise in relation to signals. Further, the

experiments showed that the signal may be enhanced by another factor of five before any noticeable saturation effects could be observed. These show that there is justification to bring down the uncertainty considerably without entering the saturation regime. There is certainly a non-trivial contribution from the laser jitter, which can potentially be contained further by using external etalon systems.

Uncertainty sources of Method 2. The systematic error in temperature with Method 2 arises from the following: 1) error in w and δ_C from excitation scans; 2) error in the algebraic approximation that relates w as a function of w_C and w_G ; 3) calibration error between w_D and temperature, including uncertainty in w_L ; and 4) uncertainty in the magnitude of Rayleigh scattering signals and the error in spatially matching Rayleigh scattering signals with fluorescence signals.

As mentioned previously, the maximum deviation of w and δ_C from the mean values at a given temperature were determined to be 0.0025cm^{-1} and 0.002cm^{-1} , respectively. The corresponding maximum error in temperature caused by w and δ_C individually was determined by assuming exact values of other parameters except for w or δ_C . The maximum uncertainty caused due to w error is estimated at 43K in potential core and 43K in the flame; the corresponding maximum uncertainty estimates due to δ_C error are 92K in the potential core and 48K in the reaction zone. The identical values of temperature uncertainty in the flame and core due to w is strictly coincidence. The use of the algebraic expression has shown to incur 0.02% error in spectral parameters which translates to less than 5K error across the combustion domain. The impact of the calibration error between w_D and temperature on the temperature uncertainty was estimated by determining the difference in calculated temperature using experimental and fit w_D values. The estimated temperature uncertainty due to the calibration is 39K below 500 K and 18K above 1600

K. The final source of error is from Rayleigh scattering signal, where previous data on scattering cross-sections exhibited up to 4% differences over multiple studies [108] [109]. Using this as a Rayleigh scattering uncertainty estimate, the corresponding uncertainty in temperature is estimated at 1.5%. In summary, the overall uncertainties in the core and flame for Method 2 are 109K and 73K, respectively.

These discussions show that the uncertainty is dominated by the error in the determination of spectral parameters, which in turn is mainly caused by the laser spectral jitter and SNR of the image. As noted previously, both sources of uncertainties can be contained to yield a significantly improved accuracy of the measured temperatures. Finally, the fact that the observed systematic error is considerably less than the RMS of individual error sources for both methods shows that the error estimates are indeed upper bounds of uncertainty caused by different sources.

Chapter 9 : Two-Line Kr PLIF 2D Temperature Imaging Technique

Experiments were performed to demonstrate a dual-wavelength excitation Kr PLIF based 2D temperature imaging technique in multiple laminar non-sooting diffusion flames. The technique exploits the thermochemical dependence of the overlap integral arising from krypton absorption and excitation laser spectra to yield the temperature without the need to know the local mixture composition. The choice of the two excitation wavelengths are made using the knowledge of the fuel mixture and pressure. The two excitation wavelengths lie within the same $4p^6 S_0^1 \rightarrow 5p \left[\frac{3}{2} \right]_2$ transition, and their selection is informed such that the resulting Kr PLIF signal ratio depends primarily on the temperature and negligibly on the local composition. Mean temperature fields show excellent agreement when compared to FLUENT simulations across different regions of the combustion domain, while single-shot temperature measurements exhibit slightly degraded accuracy. Overall, the technique provides very similar figures of merit compared to conventional composition-dependent thermometry approaches and showcases promising scope for application in complex reacting flows.

9.1 Principle of Technique

Development and verification of the thermochemical dependencies of the Kr LIF lineshape parameters has facilitated the development of a two-line Kr PLIF temperature imaging technique that may be used on an instantaneous basis. As in Chapter 8, this technique exploits the thermochemical dependence of the overlap integral to extract temperature from Kr fluorescence in a reacting environment. To understand the basis of this technique, the reader is encouraged to recall Equations (1), (2), (3), (36), (37), and (38), respectively:

$$S_f = C\chi_f N I_o^2 \frac{A}{A+Q} G$$

$$G = \int_{-\infty}^{\infty} g_L(\omega, \omega_L) g_A(\omega, \omega_A) d\omega$$

$$g_A(\omega, \omega_A) = g_D(\omega_0, \omega_D) \otimes g_C(\omega_0 + \delta_C, \omega_C)$$

$$\omega_D [cm^{-1}] = 0.093 \sqrt{\frac{T}{300}}$$

$$\omega_C [cm^{-1}] = 0.4p \left(\frac{T}{300}\right)^{-0.8} \left(\frac{n_{mix} - 1}{n_{air} - 1}\right)^{0.4} \left(\frac{\mu_{mix}}{\mu_{air}}\right)^{-0.3}$$

$$\delta_C [cm^{-1}] = -0.145p \left(\frac{T}{300}\right)^{-0.6} \left(\frac{\mu}{\mu_{air}}\right)^{-0.3}$$

Based on the above, in typical combustion mixtures the cold, unreacted fuel regions will exhibit larger collisional shifts from ω_0 and considerably broader overall absorption spectrum widths when compared to hot gases near the reaction zone [66]. The differences in the absorption spectra across the entire combustion mixture provide the associated changes to G for a given laser spectrum. The present technique leverages these differences by choosing two distinct excitation wavelengths with the same electronic transition such that the resulting Kr PLIF signal ratio is a function of temperature for a given pressure and depends negligibly upon the local composition across the entire combustion domain. The Kr PLIF signal ratio (R_{Kr}) at any location is given by

$$R_{Kr} = \frac{S_{Kr}(\omega_{L1})}{S_{Kr}(\omega_{L2})} = \frac{G(n, \mu, T, \omega_{L1})}{G(n, \mu, T, \omega_{L2})} \approx f(T, \omega_{L1}, \omega_{L2}) \quad (42)$$

Like other two-line approaches, the purpose of utilizing signal ratios is to effectively cancel the local composition dependence of the overlap integral, fluorescence quenching rates, and other parameters that contribute to local fluorescence signals. The choice of ω_{L1} and ω_{L2} are made such that R_{Kr} has adequate sensitivity throughout the entire temperature range, while $S_{Kr}(\omega_{L1})$ and $S_{Kr}(\omega_{L2})$ individually possess high signal-to-noise ratios across the combustion domain.

To demonstrate the principle of the technique, calculations of theoretical R_{Kr} values were performed to simulate the combustion of a CH₄/N₂ diffusion flame (42% and 58% by volume, denoted Flame 1) used in this work. The wavelength combination employed for calculations is also the one used in the experiments. Figure 9.1 shows the computed R_{Kr} of the fuel and stoichiometric product mixtures over a wide range of temperatures. Species concentration values were obtained by Ansys Fluent calculations using 30 species CH₄ Chemkin database files for species transport, thermodynamics, and chemical kinetics. The hypothesis while plotting Figure 9.1 is that the fuel and product mixtures form the bounds of the R_{Kr} curves and the intermediate mixture compositions will have R_{Kr} values that are between these R_{Kr} bounds. This hypothesis will be subsequently evaluated using the experimental temperature fields. The temperature dependence of the refractive index was ignored as it did not change the R_{Kr} values noticeably. It can be concluded from Figure 9.1 that the extreme bounds of R_{Kr} are within respectable levels of agreement. This means that for a given R_{Kr} , the temperature will incur minimal error by assuming either fuel or product mixture. For example, a maximum deviation of 5% occurs at $T = 1500\text{K}$ for the wavelength combination chosen for this study if one assumes the R_{Kr} of fuel across the entire measurement domain. To offset a fraction of this error, one can use an “average” (between fuel and product mixture) R_{Kr} mapping to temperature to obtain the local temperature. In this study, the R_{Kr} mapping of the fuel mixture will be used to make a stricter evaluation of the worst-case scenario.

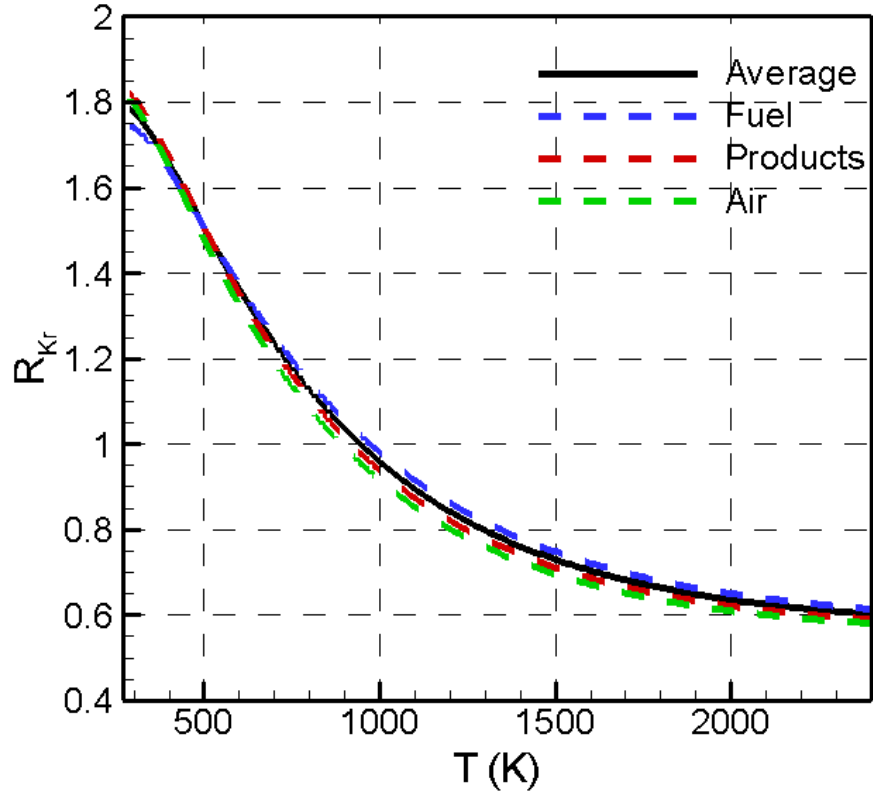


Figure 9.1: Kr PLIF signal ratio (R_{Kr}) as a function of temperature for Flame 1 for the wavenumber combination $\omega_{L1} = \omega_L - 0.255\text{cm}^{-1}$, $\omega_{L2} = \omega_L + 0.1\text{cm}^{-1}$.

At a given signal ratio, the maximum deviation in temperature between pure fuel and pure exhaust occurs at the maximum of the temperature range ($T_{\text{ab CH}_4} = 2200\text{K}$) due to decreasing sensitivity. The value of this discrepancy is 270K, or 12.3%. Despite minor variations in the signal ratio for vastly different compositions, discrepancies in temperature may occur for wavelength combinations lacking temperature sensitivity. This reinforces the idea that wavelength selection is crucial to simultaneously balance temperature resolution and signal-to-noise ratios. Systematic selection routines of wavelength combinations are similar to those outlined in [10]. Though the ascribed reference pertains to two-line molecular PLIF, the choice of wavelengths in Kr PLIF is analogous, and perhaps less complex, to the choice of transitions in OH PLIF. Depending on the fuel, this selection process is certainly not trivial and demands a more in-depth analysis to ensure that $S_{Kr,2}$ produces high enough signals and that R_{Kr} does not depend upon the gas composition.

9.2 Procedure

In addition to Flame 1, this technique was demonstrated on a similar C₂H₄/N₂ diffusion flame using wavelength combinations $\omega_{L1} = \omega_L - 0.25\text{cm}^{-1}$, $\omega_{L2} = \omega_L + 0.095\text{cm}^{-1}$, employing its own separate R_{Kr} vs T mapping for its fuel mixture. This flame, denoted Flame 2, flowed 23% and 77% of ethylene and nitrogen by volume, respectively. Both Flames 1 and 2 were produced using the in-house designed jet in co-flow burner, with fuels issuing from the jet at a velocity of 2.35m/s and an air co-flow velocity of 0.15m/s. Krypton gas was seeded in both the jet and the co-flow at 1.5% by volume. Approximately 5mJ of 214nm was used for all experiments. The measurement domain was centered at approximately 6.5mm downstream of the burner exit and extended to a region of 6mm × 50mm, with a corresponding spatial resolution of 50 μm/pixel.

Experimentation began and ended with Kr PLIF excitation scans performed on the combustion environment of interest for 1) obtaining the centerline wavelength of pure air and pure fuel, 2) verification of the laser line broadening parameters, and 3) ensuring the collisional shift has remained constant from start to finish of the experimental campaign. Collisional shifts were inferred from the centerline value of pure air and pure fuel, whose values are well-known from the vast database of prior experimental studies. Scans were performed at the standard tuning speed of 0.001nm/s (0.0034cm⁻¹/s), which has proved satisfactory in past atmospheric experiments [96, 66]. Next, static wavelength experiments begun. Approximately 200 images were collected at the set wavelength of interest. Because of the resource constraints, a single excitation beam was employed and the S_{Kr} signals for ω_{L1} to ω_{L2} were sequentially obtained spanning two experimental runs. This constraint necessitated the use of laminar flames that provided steady thermochemical conditions between experimental runs. Fortunately, this is not an absolute restriction of this technique. Facilities that employ two laser systems with at least one being injection seeded can extend the use

of this technique to time resolved measurements in turbulent flames, so long as images acquired on a single-shot basis provide adequate SNRs for accurate temperature calculation.

9.3 Results and Discussion

CH* chemiluminescence images were acquired for each flame to ensure that the measurement domain was adequate to resolve different regions of the reacting environment. CH* chemiluminescence is a very useful tool to identify pre-flame regions, thereby serving as a qualitative flame location verification technique. The ICCD was fitted with a 430nm notch filter, and since Flames 1 and 2 are both steady laminar, the exposure was increased to 7.5 μ s with On-CCD accumulations set to 15 frames with a gain of 50. This would ensure enough signal was acquired for average images, as the signal for CH* chemiluminescence is quite low and very susceptible to noise. An external trigger was used as well. These results are shown in Figure 9.2

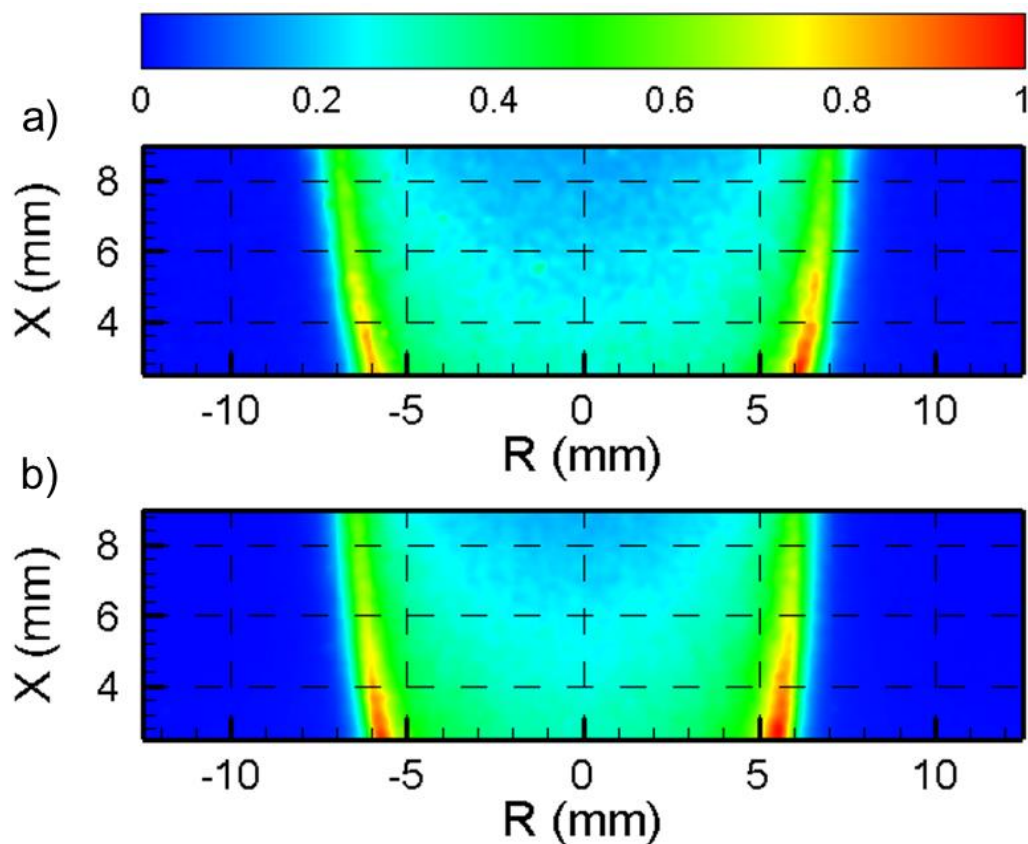


Figure 9.2: CH* chemiluminescence images of a) Flame 1 and b) Flame 2.

The 214nm laser sheet intensity CCD images and the 760nm fluorescence ICCD images were acquired simultaneously for instantaneous correction. It was previously verified that the CCD counts scale linearly with laser energy. Both images were spatially calibrated with one another to account for differing camera resolutions and beam divergence from the concave cylindrical lens. Representative one-dimensional profiles of the fluorescence sheet at a single-pixel column radial location and the 214nm beam versus downstream distance from the jet tube exit (X) are provided in Figure 9.3, demonstrating that the square of CCD pixel intensity is approximately proportional to the ICCD fluorescence signal.

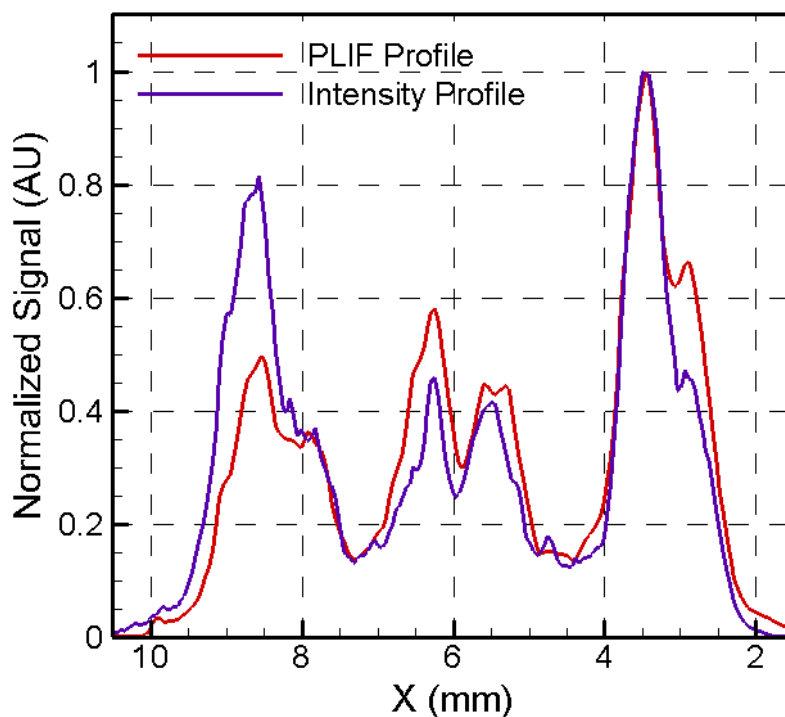


Figure 9.3: 1D profiles of the Kr PLIF signal and square of CCD intensity at a single radial location for Flame 1.

The CCD intensity profile was then used to spatially correct its associated instantaneous fluorescence image, taking into account beam divergence with increasing R . Two hundred images at each wavelength were processed to remove background intensities and corrected for the laser sheet inhomogeneity assuming a quadratic dependence of PLIF signal on local intensity

(unsaturated regime). Figure 9.4a and b show sample background-subtracted fluorescence images for Flame 1, $S_{Kr,1}(\omega_{LI})$ before and after sheet correction, respectively. Also included is the CCD laser sheet image, showing select band locations. It can be observed from Figure 9.4b that nearly all sheet inhomogeneities in the PLIF field were removed after correction, which confirms the fluorescence is in the unsaturated regime at all locations. The sheet-corrected fields were subsequently low-pass filtered using a Gaussian kernel ($0.25\text{mm} \times 0.25\text{mm}$) that effectively sets the spatial resolution. Signal to noise ratios (SNRs) were calculated by sampling $5\text{-pixel} \times 5\text{-pixel}$ areas ($0.25\text{mm} \times 0.25\text{mm}$) across an entire energy-corrected PLIF image. The SNRs were found to be approximately 20 (25) and 10 (15) in the potential core and flame regions before (after) low pass filtering, respectively, for Flame 1. Similar values were obtained for Flame 2. The large differences in SNRs for the cold and hot regions are strongly due to decreasing Kr number density and drastic changes in the absorption spectrum in high temperature regions. By comparison, signal levels for $S_{Kr,2}$ (shown in Figure 9.5) exhibited a much gradual signal distribution, i.e. less contrast between core and flame, since ω_2 lies significantly closer to vacuum center than ω_1 , where high temperature absorption spectra will approximately peak. This adjustment in the overlap integral compensates for decreasing Kr number density in high temperature regions.

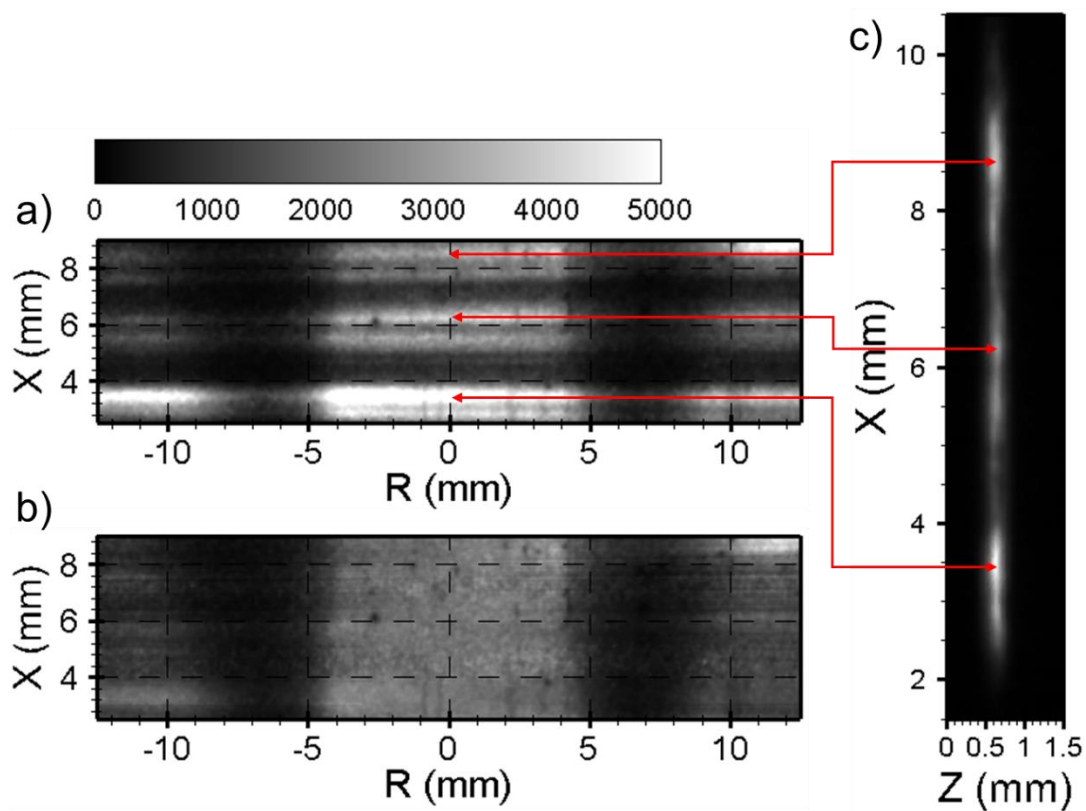


Figure 9.4: (a) Raw and (b) corrected Kr PLIF sheet images at ω_{L1} with (c) the associated CCD intensity image for Flame 1.

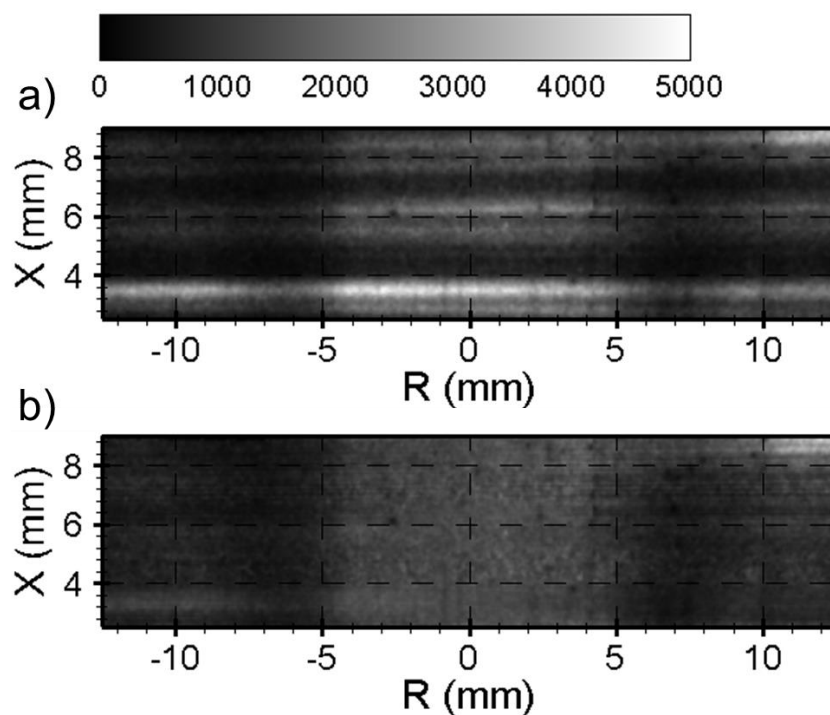


Figure 9.5: (a) Raw and (b) corrected Kr PLIF sheet images at ω_{L2} for Flame 1.

The spatial signal variation throughout the core region that remains after correction resulted in variable SNRs, and thus in random error. To analyze this, SNRs were also calculated on a shot-basis to evaluate the effect of camera noise and laser energy fluctuations. Temporal SNRs for this study were approximately 7 and 4 in the unreacted fuel core and flame regions, respectively.

Figure 9.6 and Figure 9.7 and show the mean R_{Kr} fields for Flames 1 and 2 obtained by taking a ratio of 200-shot averaged Kr PLIF fields at ω_{L1} and ω_{L2} . Rayleigh scattering images obtained at $\lambda = 532\text{nm}$ at the same measurement region is also shown in Figure 9.6b and Figure 9.7b to provide an independent qualitative verification of the different flow regions imaged in the R_{Kr} field. In addition to background-subtraction, Rayleigh scattering images have been calibrated to remove reflective signal, energy corrected, and normalized by air to remove camera dependencies. Below 4mm, the reflective signal produced by the burner polluted the Rayleigh scattering signal in excessive amounts and have thus been omitted. The extent of the unreacted fuel core between both images shows respectable similarity, spanning $-3\text{mm} \leq R \leq 3\text{mm}$. Also, similarity between the R_{Kr} core value corresponds to the fuel mixture at 300K exhibited in Figure 9.1 for Flame 1. Interestingly, Figure 9.6a and Figure 9.7a provide greater contrast in demarcating different regions of the flow due to the weak compositional dependence of R_{Kr} compared to Figure 9.6 and Figure 9.7b, where the strong compositional dependence of Rayleigh scattering cross-sections dictate signal levels. The radial locations of the flame front corresponding to a minimum value of R_{Kr} is in excellent agreement with RS field. The radial symmetry of the mixing and reacting regions (yellow through blue contours) of R_{Kr} suggests only modest absorption and steering of the beams across the flame. Finally, the R_{Kr} values of the air co-flow return to the same nominal value of $R_{Kr} = 1.75$ and $R_{Kr} = 1.6$ on either side for Flames 1 and 2, which correspond to a temperature of 300K.

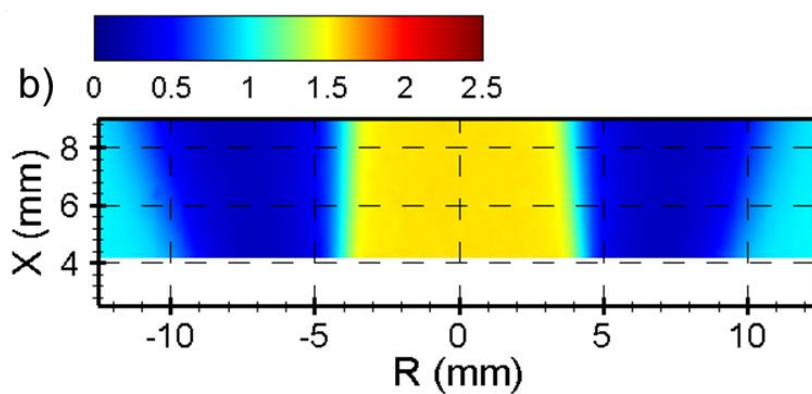
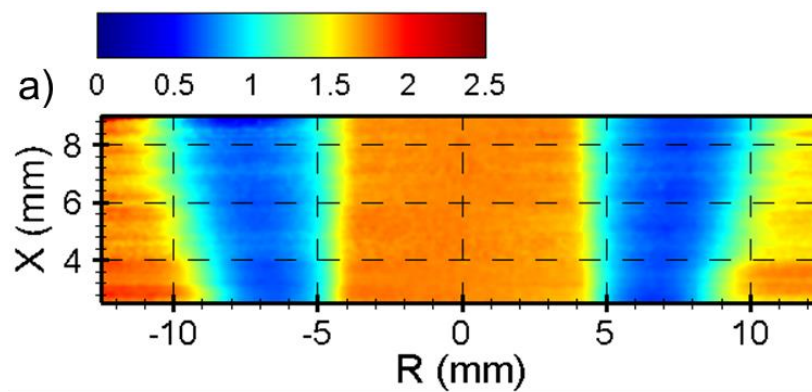


Figure 9.6: (a) R_{Kr} and (b) Rayleigh scattering (RS) fields of Flame 1.

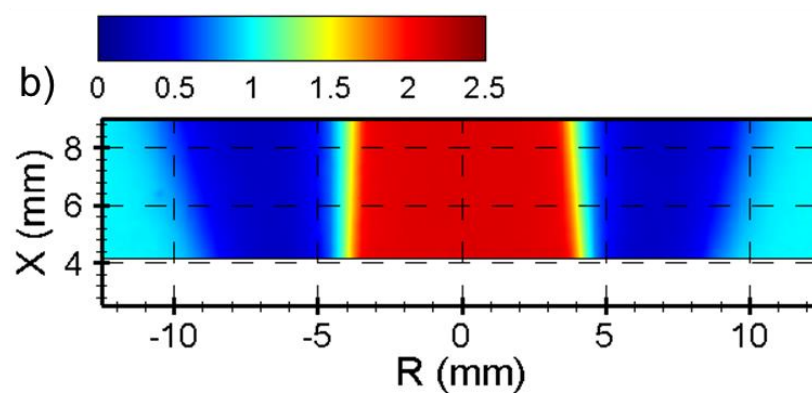
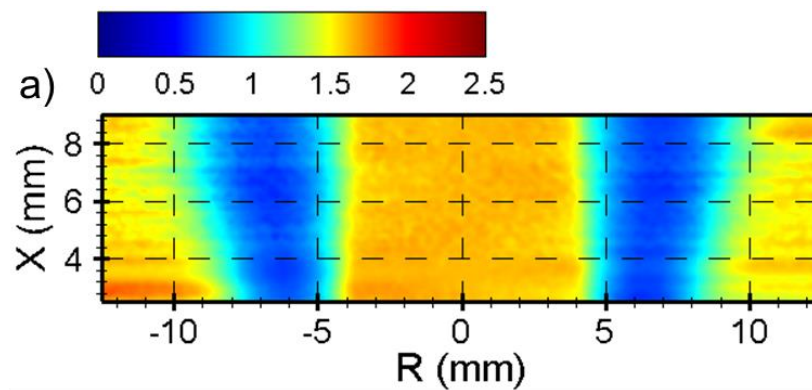


Figure 9.7: (a) R_{Kr} and (b) Rayleigh scattering (RS) fields of Flame 2.

Temperature fields calculated from R_{Kr} fields for Flames 1 and 2 based on 200-shot average Kr PLIF fields (a) and single-shot Kr PLIF fields (b) are provided in Figure 9.8 and Figure 9.9, respectively. Consistent with R_{Kr} fields, Figure 9.8 and Figure 9.9 show that the Kr PLIF technique performs well in distinguishing the unreacted fuel core, the intermediate mixing layers, and the flame region when compared to FLUENT simulations (Figure 9.8c). Unfortunately, simulations could not be provided for Flame 2 due to the unavailability of accurate Chemkin database files for C_2H_4 . Both average and single-shot images faithfully predict temperatures of around 300K in the potential core and begin to increase monotonically to the adiabatic flame temperature with increasing radial distance. Past the flame, temperatures decrease monotonically to approach 300K, representative of the air co-flow. Overall, both average and single-shot fields perform admirably in demarcating different combustion features, such as the tapering of the potential core cross-section with increasing axial distance and convex structure of the flame region, among others. Considering that the mixing layer in the fuel rich and lean branches exhibit continuous change in local composition, the fact that good agreement was obtained in the temperature values validates the adherence of intermediate compositions to the same R_{Kr} mapping for each of the respective fuel mixtures, as postulated previously.

The difficulties in correcting for the slight excitation sheet divergence (most likely due to a non-Gaussian beam profile) become apparent in the temperature fields of Figure 9.8 (e.g., $X = 4.5\text{mm}$ and $X = 7\text{mm}$), where the flame temperatures are consistently higher on the right side by 200K. Additionally, the lack of perfect sheet correction become apparent in the high temperature region where both average and single-shot temperature fields are unable to resolve the axial temperature gradients near the flame when compared to FLUENT computations. It should be noted that most of these errors can be offset by employing wavelength combinations that have a greater

sensitivity to temperatures, having a near-Gaussian and a more uniform excitation beam profile, and employing improved sheet correction procedures such as using a Kr gas cell for obtaining laser sheet profiles [62].

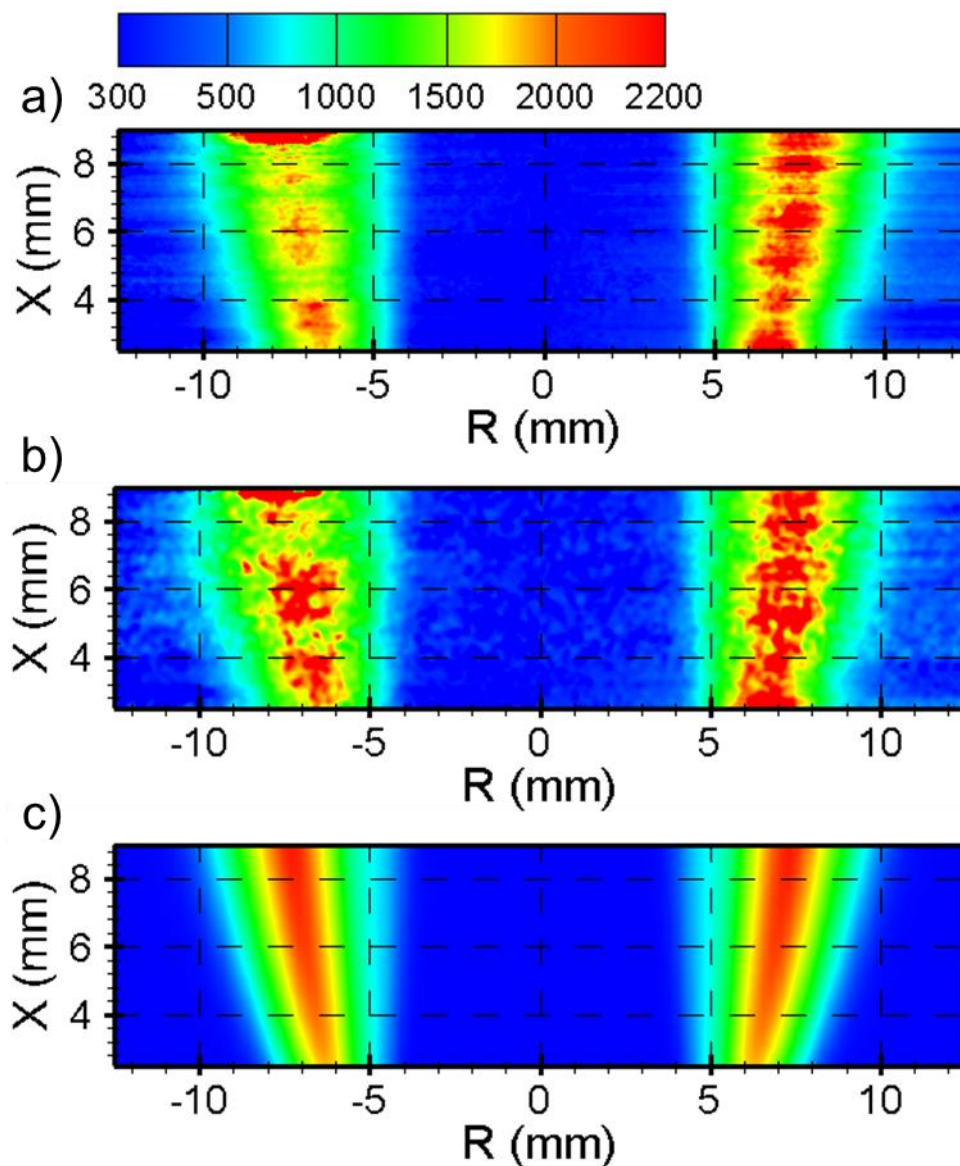


Figure 9.8: Temperature fields of the Kr PLIF two-line thermometry technique for (a) average and (b) single-shot images, with (c) a FLUENT simulation for comparison for Flame 1.

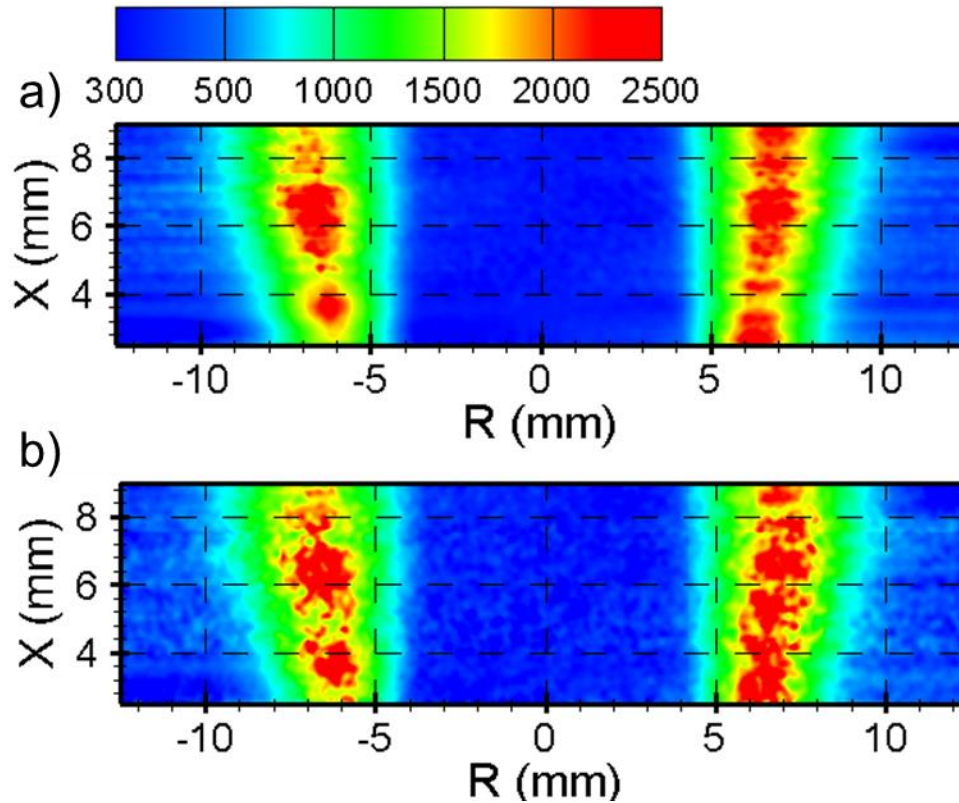


Figure 9.9: Temperature fields of the Kr PLIF two-line thermometry technique for (a) average and (b) single-shot images for Flame 2.

Comparisons of the single-shot and mean radial temperature profiles from experiments versus the Fluent simulation are presented in Figure 9.10 corresponding to $X = 6\text{mm}$ for a direct comparison of temperature profiles. It can be observed that both mean and single-shot temperature profiles match quite well with the simulated profiles in Figure 9.10a, including the mixing regions where the compositional differences in R_{Kr} are considerable, illustrating the composition-independent nature of this technique. Between simulated and experimented profiles, there exists noticeable deviation in temperature for $R > 7\text{mm}$ for both flames, which is most likely attributed to differences in mass diffusivities and co-flow velocities. The systematic bias in the core and near the flame in the mean temperature field (compared to simulations) were 20K and 150K, respectively for Flame 1. The temperature fields, namely the single-shot temperature fields, are met with considerable precision error due to residual noise (i.e. shot noise, dark noise, and readout

noise) and laser spectral fluctuations. This is exhibited by the inability of the core and co-flow to reach a uniform temperature of 300K, and the residual errors within the shear layers and flame regions. The precision error in temperature was calculated by sampling $5\text{-pixel} \times 5\text{-pixel}$ areas ($0.25\text{mm} \times 0.25\text{mm}$) across the entire mean and single-shot temperature fields. These values were approximately 20K in the core and 100K in the flame for average fields, and 30K in the core and 180K in the flame for single-shot fields. The shot-to-shot variations in the single-shot temperature fields were obtained from a 99% confidence interval of the data over 50 single-shot temperature fields. These values stood at 40K for core, 155K for the flame, and 60K for the co-flow. While these values are slightly elevated compared to conventional composition-dependent approaches, the authors posit a substantial improvement can be made by optimizing the laser linewidth to balance temperature sensitivity and compositional influence reduction, and improved sheet correction procedures. Hence, the two-line Kr PLIF technique offers promise for composition-independent thermometry, with a natural extension to turbulent flames.

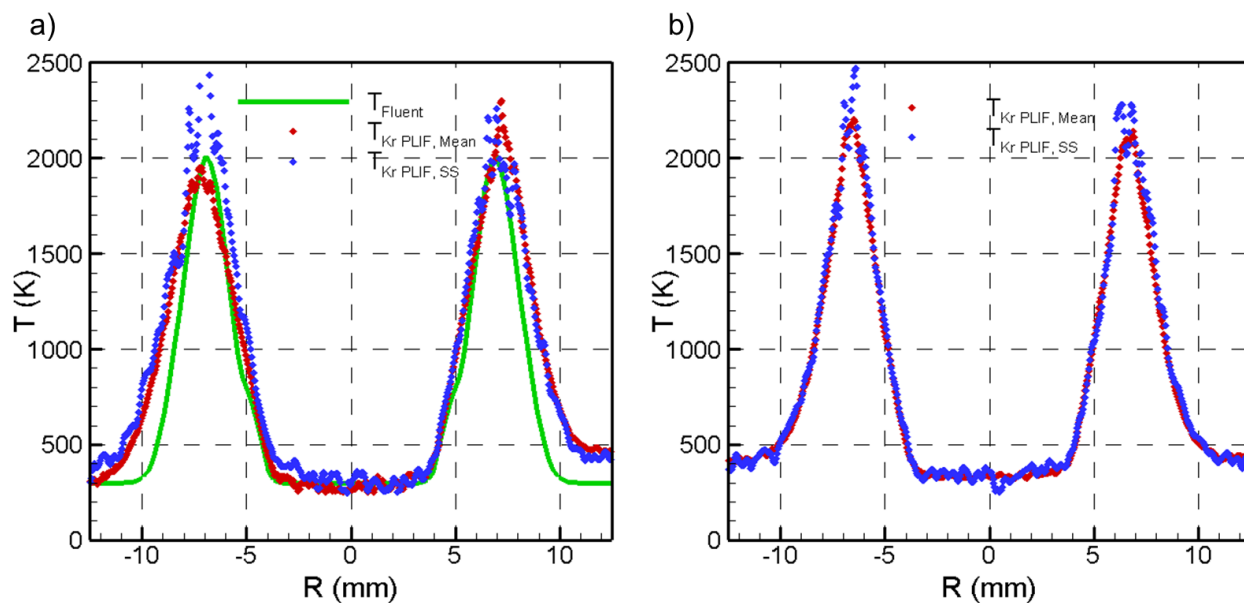


Figure 9.10: a) Radial temperature profiles of the Kr PLIF fields and FLUENT simulation at $X = 6\text{mm}$ for Flames 1 and 2.

Lastly, a demonstration of this technique is provided at different wavelength combinations $\omega_{L1} = \omega_L - 0.255\text{cm}^{-1}$, $\omega_{L2} = \omega_L + 0.11\text{cm}^{-1}$ for Flame 1 and $\omega_{L1} = \omega_L - 0.25\text{cm}^{-1}$, $\omega_{L2} = \omega_L + 0.06\text{cm}^{-1}$, both employing their respective R_{Kr} vs T mappings to obtain temperature. Average temperature fields and shown below in Figure 9.11

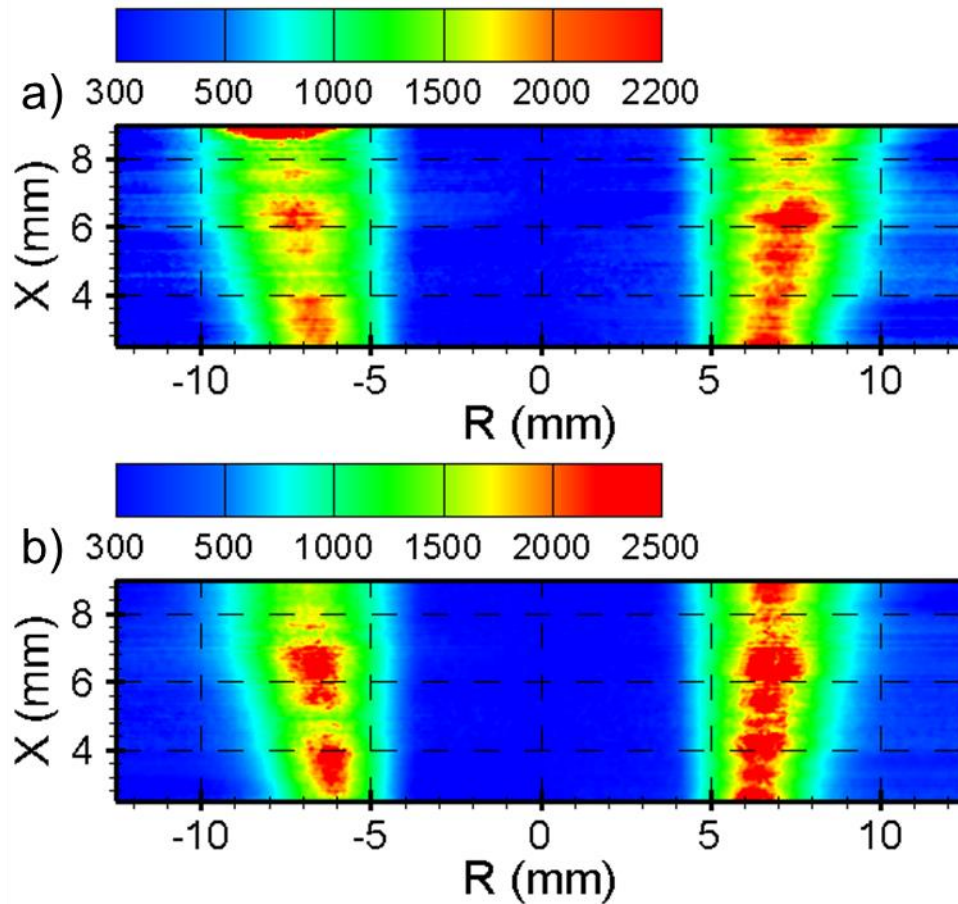


Figure 9.11: Average temperature flames for a) Flame 1 using $\omega_{L1} = \omega_L - 0.255\text{cm}^{-1}$, $\omega_{L2} = \omega_L + 0.11\text{cm}^{-1}$ and b) Flame 2 using $\omega_{L1} = \omega_L - 0.25\text{cm}^{-1}$, $\omega_{L2} = \omega_L + 0.062\text{cm}^{-1}$.

9.3.1 Uncertainty Analysis

The sources of temperature uncertainty for this measurement technique are quantified in this section. The primary sources of random error originate from 1) the uncertainty in the laser linewidth, 2) the uncertainty in the excitation wavelength due to laser jitter when set to an excitation wavelength, and 3) laser energy fluctuation.

1. The uncertainty in the laser linewidth is estimated at approximately $\pm 5\%$ due to lack of specified manufacturer information or laboratory resources. This value was obtained by deconvolving vacuum scans to isolate the laser linewidth and Doppler broadening and evaluating the RMS deviation in w_L . Temperature was calculated using the actual laser linewidth and compared to temperature measurements obtained with this deviation. For Flame 1, the temperature uncertainty due to laser linewidth fluctuations was found to be 12.5K in the fuel, 40K in the flame, and 7.5K in the co-flow. For Flame 2, the temperature uncertainty due to laser linewidth fluctuations was found to be 5K in the fuel, 60K in the flame, and 10K in the co-flow.
2. The uncertainty in the excitation wavelength due to laser jitter was estimated by assuming a $\pm 0.002\text{cm}^{-1}$ deviation in both ω_{L1} and ω_{L2} and taking the difference between the actual temperature and the deviated temperature. Since this source is considered a random source of error with two input values, wavenumber values of (+), (-), and (0) shifts of 0.002cm^{-1} were taken for both ω_{L1} and ω_{L2} , resulting in 8 different cases of temperature deviation. These results are provided in the tables below.

Table 9.1: Temperature uncertainty due to wavenumber deviation caused by spectral jitter in Flame 1

| Flame 1 | | Source 2 | | |
|--|--|----------|-----------|-------------|
| $\Delta\omega_{L1}$ (cm^{-1}) | $\Delta\omega_{L2}$ (cm^{-1}) | Fuel (K) | Flame (K) | Co-Flow (K) |
| +0.002 | 0 | 15 | 95 | 10 |
| +0.002 | +0.002 | 35 | 175 | 25 |
| +0.002 | -0.002 | 10 | 25 | 5 |
| -0.002 | 0 | 15 | 90 | 10 |
| -0.002 | +0.002 | 10 | 15 | 5 |
| -0.002 | -0.002 | 30 | 160 | 35 |
| 0 | +0.002 | 20 | 85 | 15 |
| 0 | -0.002 | 20 | 70 | 10 |
| Average | | 19.375 | 89.375 | 14.375 |

Table 9.2: Temperature uncertainty due to wavenumber deviation caused by spectral jitter in Flame 2

| Flame 2 | | Source 2 | | |
|---|---|-----------------|-----------|-------------|
| $\Delta\omega_{L1}$ (cm ⁻¹) | $\Delta\omega_{L2}$ (cm ⁻¹) | Fuel (K) | Flame (K) | Co-Flow (K) |
| +0.002 | 0 | 10 | 160 | 10 |
| +0.002 | +0.002 | 25 | 275 | 25 |
| +0.002 | -0.002 | 5 | 40 | 5 |
| -0.002 | 0 | 10 | 120 | 10 |
| -0.002 | +0.002 | 5 | 30 | 5 |
| -0.002 | -0.002 | 25 | 200 | 20 |
| 0 | +0.002 | 15 | 110 | 15 |
| 0 | -0.002 | 15 | 100 | 15 |
| Average | | 13.75 | 129.375 | 13.125 |

3. The uncertainty due to laser energy fluctuations has been accounted for since the ICCD fluorescence counts have been corrected by the CCD intensity counts on a shot-to-shot basis. Therefore, the resulting temperature uncertainty due to this source may be neglected.

The primary sources of systematic error originate from 1) the uncertainty in the excitation wavelength as a result of the resolution error of the dye laser scanning software, 2) errors in energy corrections due to saturation, 3) differences in R_{Kr} vs T mappings between pure fuel and pure product mixtures, and 4) absorption of 214nm at different excitation wavelengths.

1. The systematic uncertainty in ω_{L1} and ω_{L2} arises from the resolution error of the dye laser scanning software. This software has a resolution of 0.00005nm, or approximately 0.0017cm⁻¹. Using a similar analysis to the above, this translates to a temperature uncertainty of 16.25K (fuel), 81.25K (flame), and 11.25K (co-flow) in Flame 1 and 13.125K, 112.5K, and 11.25K in Flame 2.
2. As previously mentioned, the error due to energy correction inadequacies produced temperature differences of approximately 200K in the flame when comparing opposite sides of the combustion domain. However, in the case of saturation, possible temperature

errors may arise due to the intensity deviations between the square of CCD intensity and ICCD fluorescence. To analyze this, axial profiles of the unreacted fuel core (constant composition and temperature) were obtained for each flame. The RMS deviation in the core axial temperature distribution which spanned multiple fluorescence fringes was found to be no more than 30K in Flame 1 and Flame 2. Therefore, the effects of saturated signals are expected to be miniscule for these data sets.

3. The systematic bias introduced by 214nm absorption at different excitation wavelengths coupled with low Kr number density in high-temperature regions may lead to systematic errors in temperature. To evaluate these effects, average radial profiles of $S_{Kr,1}$ and $S_{Kr,2}$ were extracted at select fringe locations to compute and average radial R_{Kr} . If absorption effects are present, the signal ratio distribution will be asymmetric or skewed to one side. This analysis resulted in signal ratio differences of 1.7 to 1.6 in the air co-flow and 0.67 to 0.64 in the flame, from one side to the other. No noticeable changes occurred in the fuel core. This equates to temperature differences of +90K at 300K and +220K in the flame according to the R_{Kr} vs T mapping for Flame 1. The slight decrease in signal ratio with increasing beam propagation distance indicates a reduction of 214nm energy at ω_{LI} due to absorption.
4. The uncertainty in R_{Kr} vs T is determined by taking the differences on the three curves in Figure 9.1. Since pure fuel mapping was used for both flames, this curve serves as a reference point. At a maximum flame temperature of approximately 2200K for Flame 1, the temperature difference between pure fuel and pure products translates to 270K. At 300K for an air co-flow, the temperature difference between pure fuel and pure air translates to 40K. Similar results are reported for Flame 2.

From the above discussion, the temperature uncertainty is dominated by the uncertainty of the excitation wavelengths created by laser jitter, systematic errors created from the energy correction procedure and differential absorption, and the systematic bias created due to using a pure fuel R_{Kr} vs T mapping. Uncertainty in the laser linewidth or excitation wavelengths caused by spectral jitter may be reduced by employing external etalon systems such as a wave-meter for accurate spectral determination. Certainly, the energy correction procedure may be enhanced by using a more sophisticated approach to correct for differences in fringe intensities, such as employing a static Kr gas cell and a more sophisticated optical setup to reduce beam divergence and non-Gaussian characteristics. As noted previously, the difference incurred due to the temperature mapping function may be mitigated by a great extent if using an “average” function between fuel and stoichiometric products. Lastly, the fact that the observed precision error is considerably less than the RMS of individual error sources for this method shows that the error estimates are indeed upper bounds of uncertainty caused by different sources.

9.3.2 Pressure and Velocity Sensitivity

In general situations where flow velocities may not be considered sufficiently 1D and pressure fluctuations are present, temperature errors produced by this technique may arise due to Doppler shift and variations in the collisional broadening and shift due to non-constant pressure. This was evaluated by calculating theoretical R_{Kr} vs. p and v mappings for air at 300K, 1000K, and 2000K using $\omega_{L1} = \omega_L - 0.25\text{cm}^{-1}$, $\omega_{L2} = \omega_L + 0.1\text{cm}^{-1}$. The Doppler shift was calculated using the following equation [98].

$$\delta_D = -\frac{\omega_0}{c} \mathbf{V} \cdot \mathbf{i}_L \quad (43)$$

To incur a temperature error of 5%, pressure fluctuations of 2 – 3% are needed. Similarly, velocity components of $\pm(5 - 15)$ m/s are needed for 5% temperature error.

Chapter 10 : An introduction to the Kr PLIF Spectral Line at High Pressures

The following chapter investigates the Kr LIF spectral line when subjected to high pressures, serving as an introduction to determining the mechanism(s) responsible for line shape abnormalities. Increased perturber pressures may introduce additional mechanisms leading to asymmetric profiles and other lineshape deviations. Such deviations exist due to the correlation between Doppler broadening and collisional broadening. As previously stated, the motion of the absorber alters the spectrum due to the Doppler effect, but also determines the relative perturber-absorber velocity distribution, and through that the collisional broadening [70]. Therefore, Doppler and collisional effects may not be treated as independent, yet they are treated as such in many instances to simplify analysis of the spectral line. Such a simplification allows deconvolution of the Doppler broadening from the Voigt profile to obtain the collisional broadening, as performed previously in this study. However, the combined effect of Doppler and collisional mechanisms has been shown to reduce the Doppler broadening profile and produce asymmetric lineshapes by multiple mechanisms, with Dicke narrowing, correlations between velocity-changing and state-changing collisions, and speed-dependent effects being the major contributors [69]. The use of an inappropriate lineshape function can give rise to systematic errors when obtaining lineshape parameters, and as such it may be important to take these phenomena into account. Additionally, at extreme perturber densities departure from the impact broadening theory becomes more likely due to collision-time asymmetry, as the system in question may become more accurately explained by the quasistatic approximation.

First, a description of Dicke narrowing, correlations between velocity-changing collisions and state-changing collisions, speed-dependent effects, collision-time asymmetry, and line mixing will be provided. For the sake of brevity, an exhaustive summary on studies that induce these

effects in the spectral line will not be covered, but the reader is encouraged to review the attached references in Appendix E from which the conclusions in this chapter are drawn. Following this discussion will be the experimental evaluation of Kr LIF excitation scans with N₂ as the perturbing gas at pressures up to 10atm. Finally, a discussion of the high-pressure excitation scan results is provided, hypothesizing the effect that these mechanisms may or may not have, and to what degree they are present.

10.1 Review of the Spectral Line at Increased Perturber Pressures

10.1.1 Dicke Narrowing

The Dicke effect, otherwise known as collisional narrowing, refers to the narrowing of the Doppler broadening profile due to collisions the emitting species experiences with the perturbing species, violating the assumption of free motion. The increased perturber density causes the mean free path to decrease. When the mean free path of a species becomes on the order of the wavelength of radiative transition, the atom changes velocity and directions numerous times during the emission or absorption of a photon due to increasing collision rates. In this situation, the absorber experiences a drag force in a constant radiation field. This interaction causes an averaging over numerous Doppler states and results in a narrower Doppler linewidth. As an alternative description, Allard and Kielkopf describe Dicke narrowing as a decrease in the Doppler linewidth due to the Doppler shift of one phase in the radiator cycle being cancelled by the shift in another phase. This in turn produces a Lorentzian dominated profile. Dicke narrowing, however, becomes negligible in collisionally dominated regimes (high pressure) and therefore only occurs in the onset of increasing pressure when the collisional FWHM is much less than the Doppler FWHM. It is only in the case of negligible collisional broadening where the linewidth is inversely proportional to pressure in the limit of high pressure [110]. Therefore, in many studies that investigate Dicke

narrowing, Dicke narrowing is observed in pressure ranges coincident with the impact approximation. Collisional broadening of such lineshapes under this influence may still be described by impact theory.

Dicke narrowing may be explained using the uncertainty principal, noting that both the position and momentum cannot be measured simultaneously. Thus, paraphrasing from [111] and [69]:

“A photon carrying h/λ is only capable of determining the displacement of a species (atom/molecule) larger than $\lambda/2\pi$. The velocity of the species contributing to the Doppler shift will therefore be the mean velocity through the displacement of $\lambda/2\pi$. In low collision rates, the mean free path of a species is greater than $\lambda/2\pi$, so no narrowing occurs, and absorber’s velocity may be represented by a Maxwell-Boltzmann distribution. When the collision rate increases to the extent that the mean free path is less than $\lambda/2\pi$, the velocity experienced is the mean velocity of the molecules due to collisions averaged over displacement $\lambda/2\pi$. This collisional averaging effect results in a narrower Doppler profile.”

In other words, the Doppler portion decreases with pressure since the mean velocity of the absorber will decrease with pressure when it moves over a distance on the order of the wavelength of radiation. Collisional narrowing was first discussed theoretically by Robert H. Dicke [112], and has since garnered a significant amount of discussion amongst the spectroscopy community. For Dicke narrowing to occur, collisions that cause broadening and narrowing must be independent, i.e. no correlation between velocity-changing (perturbations of translational state) and state-changing collisions (perturbations of molecular internal state). In general, lineshape parameters

depend on the relative velocity between the absorber and perturber, and this approximation is valid only if the perturber is much lighter (hence moving faster) than the absorber (neglecting speed-dependent effects) [111]. One of the earliest works to study the simultaneous effects of both collisional broadening and narrowing was [113]. Rautian & Sobel'man found that the dominant effect of the collisions is to damp out the free translational motions of the molecules at low densities, but at high densities the dominant effect of collisions is to perturb the internal states of atoms/molecules (broadening). If correlations between velocity-changing collisions and dephasing collisions exist, the lineshape may reflect asymmetric behavior, and should be considered in many cases [113].

10.1.2 Correlations Between Velocity-Changing and State-Changing Collisions

The correlation between collisions that change the velocity and collisions that change the internal state of the absorber has been explored in multiple studies that have analyzed the effects of Dicke narrowing on the spectral line. As mentioned previously, Dicke narrowing is the reduction of the Doppler broadening due to collisions that change the absorbers' velocity numerous times. Dicke narrowed profiles assume that the collisions that perturb the velocity are independent from the collisions that perturb the internal molecular state of the absorber that result in broadening, i.e. there is no correlation between narrowing and broadening. The statistical independence from these two collision mechanisms results in a narrowed, yet symmetric profile. However, as alluded in the above, the assumption of uncorrelated broadening and narrowing is violated in certain collisional situations. One of the earliest works to study the simultaneous effects of both collisional broadening and narrowing was [113]. Rautian and Sobel'man found that if correlations between velocity-changing collisions and dephasing collisions exist, the lineshape may reflect asymmetric behavior, and should be considered in many cases [113]. This correlation

may lead to a reduction or even an elimination of Dicke narrowing [114]. These effects become more prominent with increasing m_p/m_A (perturber mass to absorber mass) ratios. Essentially, with increasing perturber to absorber mass ratios, the emitters move faster in an environment of stationary perturbers, allowing to emitters to suffer more collisions and therefore show a greater width and shift. The wings of the profile, which are due to the atoms/molecules with at least one large component of velocity, will tend to show greater pressure effects than the core [115].

10.1.3 Speed-Dependent Effects (SDEs)

Speed-dependent effects (SDEs) of the spectral line arise when correlations exist between the thermal motions (Doppler broadening) and the pressure broadening, i.e. the collisional broadening and shift become dependent on the absorber's speed. If the Doppler broadening and collisional broadening are uncorrelated, the convolution results in a Voigt profile. However, [116] and [117] have shown that these correlations cannot be omitted, particularly if the perturber is much heavier than the absorber ($m_p \gg m_A$). This theory was first predicted by [116] and [117], and originates from the fact that different velocity groups of molecules experience their own homogeneous collisional broadenings which is determined by the relative speeds of the absorbers and perturbers. This implies that not all velocity classes have the same Lorentzian profile [69]. Because of this, the total response may not be represented by a simple convolution that results in a Voigt profile. In this situation, the collisional broadening may be represented as the weighted sum of different Lorentzian profiles corresponding to different velocity groups of atoms/molecules, each weighted by the Maxwell speed distribution, given by the following expression and distribution in Figure 10.1. Since the average speed does not occur at the peak of the distribution, the resulting spectrum that is influenced by SDEs takes on an asymmetric form. In addition to asymmetry, narrowing of the collisional broadening may result.

$$f(v) = 4\pi \left(\frac{M}{2\pi\bar{R}T} \right)^{\frac{3}{2}} v^2 \exp\left(-\frac{Mv^2}{2\bar{R}T}\right) \quad (44)$$

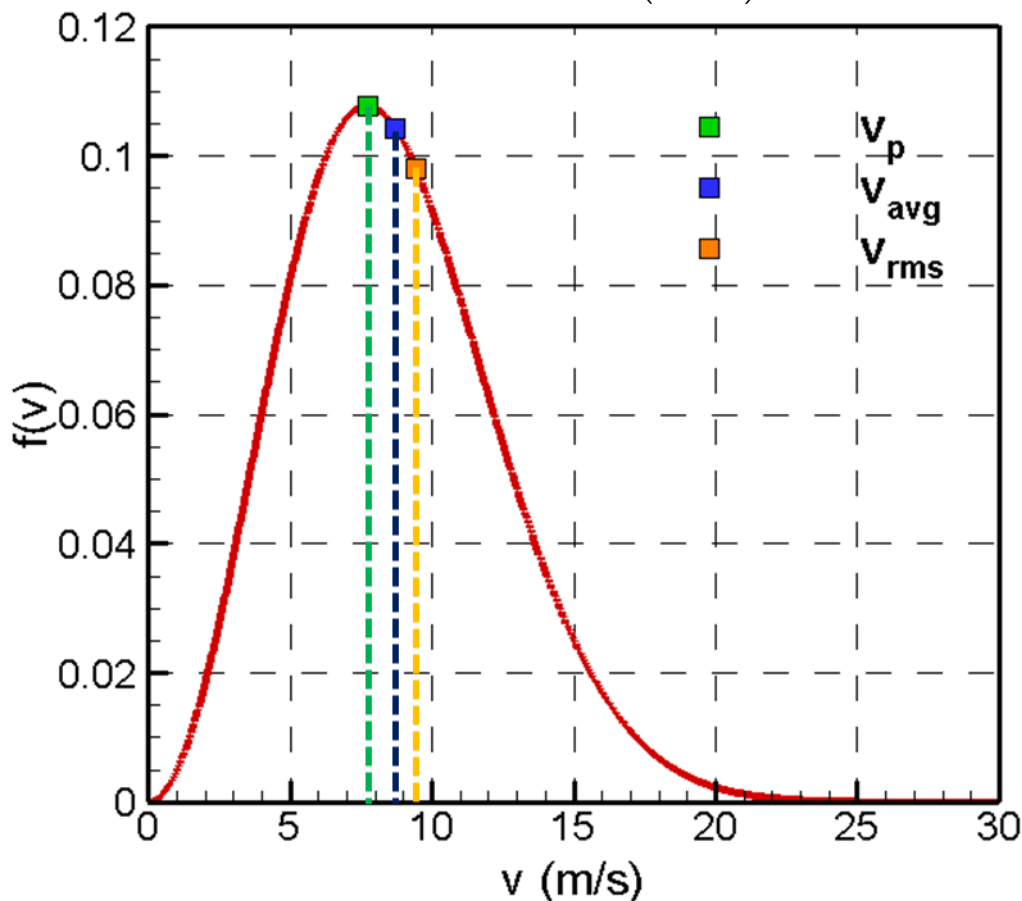


Figure 10.1: Speed probability density function at a temperature of 300K for Kr.

In calculations performed by [116] and [117], the asymmetry indicative of speed-dependent effects results in the peak shifting less than the center of gravity of the lineshape. SDEs most likely occur in the pressure-dominated regime, within room temperature and at pressure above those for Dicke narrowing. As mentioned previously, SDEs occur only when $m_P \gg m_A$ and become stronger as this mass ratio increases. In general, lineshape parameters depend on the relative velocity between the absorber and perturber. If $m_A \gg m_P$, and hence allowing the perturber to move much faster than essentially stationary absorbers, collisional broadening and shift is not dependent on the speed of the absorber, and any resulting asymmetry is most likely the result of

collision duration [77]. The similarities of asymmetries of these two mechanisms requires extreme care for quantitative interpretation [114]. Despite slight asymmetries, lineshapes affected by SDEs have been shown to follow impact broadening theory.

10.1.4 Collision-Time Asymmetry

At sufficiently high pressures, the impact approximation will break down because the time between collisions is not substantially greater than the actual time of collisions. Gaussian, Lorentzian, and/or Voigt behavior as described by the impact limit is valid so long as the radiation emitted during the time of collision is neglected and asymmetries are small, which is violated when the finite duration of collisions is appreciable. The result of this violation is a near-constant perturbation in which collisions may not take place instantaneously, reflecting the behavior of the quasistatic approximation. An investigation of perturbed gas systems subject to the finite time of collision has been shown to produce an effect known as collision-time asymmetry that is manifested by an asymmetric dispersion distribution of the Lorentzian profile [77, 116, 115, 118]. The convolution of the Gaussian distribution with a sum of Lorentzian and dispersion profiles will give rise to the asymmetric Voigt profile. Such asymmetries are far more pronounced than those produced by the above mechanisms.

10.1.5 Line Mixing

The dispersion asymmetry described by collision-time asymmetry may also be the result of line mixing, or spectral overlap. It is often assumed that each spectral line can be treated as isolated from all other, but if lines are sufficiently broadened by increased perturber densities, neighboring lines may “overlap” or “mix”. The intensity of the overlap region is not simply the sum of the intensities of the neighboring lines; instead, the wave functions of the energy levels are mixed by the perturbation, causing the Lorentzian component in the wings to become distorted

[68]. Substantial overlap occurs when the collision rate is on the order of the separation between the lines:

$$\frac{1}{t_0} = |\omega_{\alpha\beta} - \omega_{\alpha'\beta'}| \quad (45)$$

At high pressure, the impact model will break down resulting in non-Lorentzian profiles, and at extreme pressure the collisional couple between lines can be so rapid to lead to the collapse of a single line [75]. Fortunately, lines under investigation in most studies may be considered sufficiently isolated, and do not experience line mixing [118].

10.1.6 Goals

The purpose of this chapter is to provide insight into the Kr LIF spectral line when subjected to high perturber pressures. However, based on the above, there may exist multiple mechanisms that influence the Kr LIF spectral line, so it is unclear as to what extent these mechanisms may or may not be present. Numerous studies (Appendix E) have addressed spectral systems in which multiple mechanisms are present and have developed complex lineshape models to physically interpret each of the above. To this point in Kr LIF, perturber pressures up to 1 atm have been considered, with slight asymmetries noted in Chapter 8. Therefore, the following questions must be asked:

1. Do the collisional width and shift still scale linearly with pressures above 1 atm?
2. Are excitation scans performed at lower pressures met with pronounced collisional narrowing?
3. Is the current asymmetry noted at 1 atm an artifact of the experimental setup (i.e. dye laser stepper motor hysteresis) or is it a result of physical phenomena as described by the above?

4. If the asymmetry at 1 atm is the result of physical phenomena, can a modified Voigt spectrum be fit to the data and does there exist an asymmetry parameter that scales linearly with increasing pressure?

10.2 Experimental Procedure

Kr LIF excitation scans were performed with N₂ as the perturbing gas species at pressures spanning from 2 torr of Kr up to 10 atm of N₂. Nitrogen was selected as the perturbing gas species due to its similar molecular weight with common combustion mixtures, its prominence in combustion mixtures, and its low collisional quenching, requiring less Kr for adequate signal levels. To start, vacuum scans were performed in the high-pressure cell (Figure 3.8) to obtain accurate values of the centerline wavelength, Doppler broadening, and laser spectra, calculated using the least-squares fitting and deconvolution procedure explained in Chapter 4. Next, approximately 0.5 atm of Kr was added to the cell to prepare for high-pressure experiments. The cell was filled with 10 atm of N₂, meaning that Kr comprised of approximately 4 – 5% by volume. Though this concentration is significantly higher than previously performed excitation scans, the high collisional quenching rates of 10 atm of perturber pressure demanded it. Because of this, values of the Kr collisional broadening and shift have been calculated per Equations (29) and (30) to adjust the experimental results. Values of self-broadening and shift of Kr are provided in Table 10.1 at various Kr pressures.

Table 10.1: Self-broadening and shift of Kr at various pressures.

| Kr pressure (atm) | $w_{C, \text{Kr}} (\text{cm}^{-1})$ | $\delta_{C, \text{Kr}} (\text{cm}^{-1})$ |
|--------------------------|---|--|
| 0 | 0 | 0 |
| 0.1 | 0.0381 | -0.0119 |
| 0.2 | 0.0762 | -0.0237 |
| 0.25 | 0.0952 | -0.0297 |
| 0.3 | 0.1143 | -0.0356 |
| 0.4 | 0.1524 | -0.0475 |
| 0.5 | 0.1905 | -0.0593 |

Scans were performed in order of decreasing pressure to simplify the experimental procedure. A vacuum pump was used to reduce the gas mixture pressure at the conclusion of each pressure data point. However, with a starting Kr concentration of 5%, this would undoubtedly cause saturation in the low-pressure regime. Therefore, dilution was employed to half the Kr concentration at each pressure step. Using this procedure, no more than 1200 maximum signal counts were obtained for each scan, ensuring the scans were unsaturated. Testing characteristics for each data point are provided below. From this testing matrix and with the corroboration of Table 10.1, it was determined that self-broadening and shifting of Kr would only be appreciable at pressures of 0.13 atm (5 atm of N₂) and 0.5 atm (10 atm of N₂), and negligible for all other pressures. Maximum 214nm energy was employed (10mJ) and was formed into a sheet to acquire multiple selection regions. Using a Q-switch delay corresponding to maximum energy ensured maximum energy stability throughout scans. After passing through a single fused quartz window of the high-pressure cell, energy was reduced by approximately 25%.

Table 10.2: Testing conditions for the Kr PLIF high-pressure lineshape examination.

| N₂ pressure (atm) | Kr pressure | scan speed (nm/s) |
|-------------------------------------|--------------------|--------------------------|
| 0 | 2 torr | 0.001 |
| 0.25 | 2 torr | 0.001 |
| 0.5 | 2 torr | 0.001 |
| 0.75 | 2 torr | 0.001 |
| 1 | 6 torr | 0.002 |
| 2 | 0.03 atm | 0.005 |
| 5 | 0.13 atm | 0.005 |
| 10 | 0.5 atm | 0.005 |

10.3 Data Analysis

Kr PLIF excitation scan images were background subtracted and sampled at 20 pixel \times 20 pixel regions throughout the measurement domain to obtain multiple spectra at a given pressure run. Energy/sheet correction was not performed as the energy remained within 5% throughout the

duration of any excitation scan. Each scan was exactly 1000 frames, lasting just under two minutes per experimental run.

Given that scans at 1 atm of perturber pressure have exhibited asymmetric lineshapes in previous studies, modifications to the present Voigt fitting technique were required. The model used was adapted from the approach used in [102] and implemented briefly in Chapter 8, where the collisional width varied sigmoidally based on wavenumber.

$$w_c = \frac{2w_{c,0}}{1 + \exp[a(\omega - \omega_0)]} \quad (46)$$

In the above, $w_{c,0}$ represents the “average” collisional width. The collisional width was chosen as the value to vary asymmetrically based upon wavenumber because in previous experiments, spectra with greater values of w_c qualitatively exhibited enhanced asymmetry, suggesting that the asymmetric mechanism originates from the collisional broadening (see Figure 8.5). This expression is advantageous because it allows the width to vary asymptotically between the bounds $0 - 2w_{c,0}$. Positive values of the asymmetry parameter skew the spectrum toward lower wavenumbers, while negative values skew towards higher wavenumbers. If the asymmetry parameter is zero, the spectrum is symmetric, and the width takes on a value of $w_{c,0}$. Though this asymmetry parameter does not have a physical basis as described by the mechanisms in Section 10.1, this simple lineshape model will serve as an adequate starting point to assess asymmetric lineshapes induced by high-pressure. It is important to note that this model does not account for Doppler broadening reduction as described by Dicke narrowing. This is because Dicke narrowing is expected to be absent in such pressure dominated regimes, and previous experimental results have shown that Doppler widths remain quite constant from room temperature vacuum conditions to atmospheric conditions. Additional details on this justification will be provided in a later section.

This modified fitting procedure operated on a similar premise to the symmetric Voigt deconvolution procedure described in Chapter 4, but with an additional variable. Several theoretical excitation spectra were simulated using a range of values of the Lorentzian width, Gaussian width, and asymmetry parameter and compared to the experimental data. The simulated spectrum (and the lineshape parameters contained within) that exhibited the minimum RMS error compared to the experimental data was the resulting fit. Though this strategy was computationally more time consuming, accurate fits were obtained reliably for all excitation scans.

10.4 Results

In the lowest pressure limit of the scans performed (2 torr of Kr), the broadening mechanisms present should be the Doppler broadening and the laser linewidth in the absence of a perturbing gas. In processing, it was observed that the vacuum scans contain Gaussian widths corresponding to Doppler broadening values at room temperature and a highly Lorentzian component that must be attributed to the spectral broadening of the excitation beam. On average, this finite Lorentzian width was calculated to be $w_L = 0.160\text{cm}^{-1}$, which has not been observed in previous studies such as those in Chapter 8. This increase of spectral laser width may be attributed to the inclusion of a Bethune dye cell in the Jaguar. Radiant Dyes, the manufacturer, has reported that users have experienced differences in laser spectra when compared to using conventional dye cells. A Bethune cell was implemented to improve 544nm beam quality, and thus improve laser sheet correction procedures in developing and demonstrating the two-line Kr PLIF thermometry technique in Chapter 8. Despite this difference in laser spectra, the relations developed for the Doppler broadening and the collisional broadening, i.e. the absorption spectra, in this dissertation are still valid. Results presented in tables and scaling graphs in this chapter have been corrected due to this change. In other words:

$$w_{Lor} = w_{C,N_2} + w_{C,Kr} + 0.16cm^{-1} \quad (47)$$

With $w_{C,Kr}$, if appreciable, representing the self-broadening of Kr described in the previous section.

Excitation scans and theoretical asymmetric fits are provided in the figures below. The results shown here are the product of ensemble averaging multiple experimental runs for each pressure to reduce noise in each scan for improved synthetic fits. This is verified by the RMS error of the data to the fit, which is approximately 0.025 for 0 – 1 atm, on average. The line broadening parameters shown in Table 10.3 were those extracted from the synthetic fits. Figure 10.2 displays excitation scans and fits for perturber pressures of 0 – 1 atm, which clearly shows an increase in width and shift with increasing pressure. Though faint, slight asymmetry arises in the line profile at pressures above vacuum conditions, with the most notable asymmetry occurring in 1 atm. Referencing Table 10.3, it is observed that the asymmetry parameter approximately increases with pressure in this pressure range, but the asymmetry is so slight that these effects may be deemed negligible depending on the application. It is only until 1 atm that the asymmetry becomes pronounced using a qualitative comparison, as all cases under 1 atm have an asymmetry parameter of approximately 0.5. In all cases, the asymmetry occurs in the red wing, which is the same orientation as the collisional shift. Furthermore, the Gaussian width for the scans in the pressure regime approximately correspond to the Doppler width at room temperature (0.094 cm^{-1}). Some deviations from this value exist because, as mentioned in Chapter 8, it becomes increasingly difficult to extract smaller Gaussian widths from highly collisionally broadened spectra where Lorentzian behavior dominates.

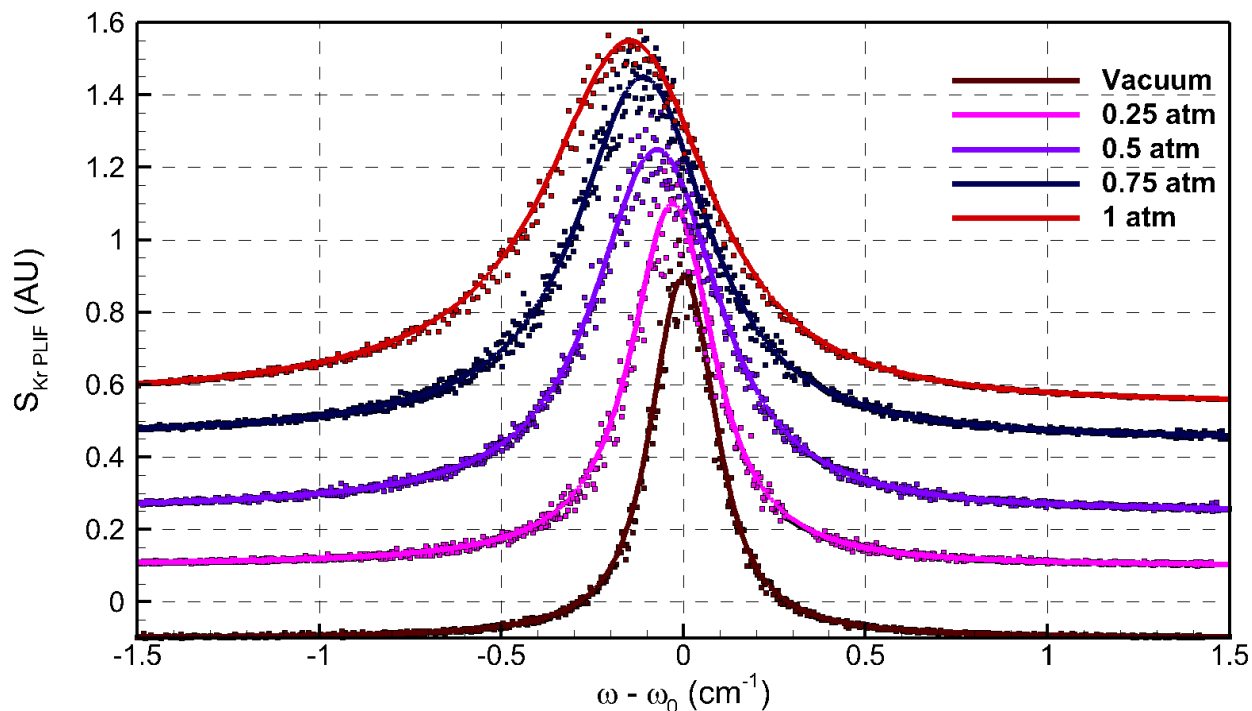


Figure 10.2: Excitation scans of Kr fluorescence 0 - 1 atm. Profiles have been offset vertically for legibility.

To determine the efficacy of using an asymmetric lineshape model in the pressure regime of 0 – 1 atm, the same data was fit to a symmetric lineshape, with the results listed in Table 10.4. Values of the collisional shift are not included as peak locations did not change between various fitting procedures. Interestingly, values of the total FWHM are identical, because the asymmetry in this pressure range extends to, at most, 30% of peak signals in the red wing. Furthermore, results for the collisional FWHM and Gaussian/Doppler width are within respectable agreement with one another, considering that the RMS error in FWHM is approximately 0.03 cm^{-1} in this range for this experimental campaign. Still, some deviations do exist in determining the correct Doppler width for $T = 300\text{K}$, but this is expected because of the disagreement in the red and blue wings of the excitation scans, especially at $p = 1 \text{ atm}$ where the asymmetry is more noticeable. The only area of significant differentiation is the RMS error of the synthetic fits, showing that very minor improvements on an absolute scale can be made by using an asymmetric lineshape. For 0 – 0.75 atm, there is only a 5% improvement in this regard. It is not until 1 atm of pressure where a fit can

improve noticeably (approximately 30% improvement in error), yet the line broadening parameters remain relatively constant for each fitting procedure. From the results in Table 10.4, and comparing with those in Table 10.3, the claim can be made that a symmetric Voigt profile may successfully be used to describe 0 – 1 atm of perturber pressure for the Kr LIF system. This supports the assertion of the impact broadening theory, which accurately predicts Voigt behavior in the line core. Therefore, the impact broadening theory is valid for 0 – 1 atm. Furthermore, these findings corroborate the temperature measurements obtained by Methods 1 and 2 in Chapter 8, and by the two-line approach in Chapter 9. Considering that the absorption spectrum remains unchanged at 300K between models (i.e. w_A , w_C , w_D , and δ_C and the relations developed), temperature measurements are possible in the pressure range of 0 – 1 atm using these techniques. It is hypothesized that results for temperature would further improve at increased temperatures due to the decrease in collisional broadening, and thus, a decrease in the asymmetry. Now, it should be noted that the differences in the laser spectrum produced by the Bethune cell do cause differences in the spectral line, but these changes may still be accounted for to adapt the thermometry techniques developed in this dissertation, i.e. adapting relations for the Gaussian width developed in Chapter 6 and correcting the Lorentzian/collisional width as shown in this chapter. Lastly, using either fitting routine, the collisional widths of 0.75 atm and 1 atm are slightly underpredicted from those predicted by Equation (29). Possible reasons for this include the introduction of deviations when ensemble averaging different experimental runs, an increased dye laser scan speed causing the spectra to appear more Gaussian, and changes in the Lorentzian portion of the laser linewidth due to spectral jitter. The subtraction of 0.16cm^{-1} from the total Lorentzian FWHM is an aggressive adjustment, and thus accurate determination of the laser spectrum is necessary.

Next, the asymmetric Voigt model was applied to scans of 2, 5, and 10 atm of N₂ pressure to determine if the collisional FWHM, shift, and asymmetry scale linearly with the pressure. However, the data for this pressure regime could not be represented by a symmetric Voigt profile, as shown by Figure 10.3. The data in the red wing is heavily skewed by asymmetric behavior, with these effects increasing with increasing pressure (Table 10.3) proving that a physical phenomenon is causing the asymmetry. In contrast to the blue wing, the red wing is highly Lorentzian. Apart from 10 atm, δ_C is predicted quite well when compared to values calculated using Equation (30). This discrepancy in the collisional shift for 10 atm is most likely attributed to the increased broadening and RMS error making the peak difficult to locate. Furthermore, though the values of collisional width compare quite well with theoretical values, there exists a drastically enhanced amount of Gaussian width as predicted by the asymmetric model. All scans were performed at 300K, meaning that the Gaussian width should correspond approximately to $w_D = 0.0945$. This arises from the fact that w for 2, 5, and 10 atm are well above their predicted values, which suggests impact theory fails to describe the line core. Also, inspection of the blue wing for each pressure above 1 atm qualitatively shows an increased Gaussian contribution which is not present in the low-pressure regime. The asymmetric lineshape model is forced to correct for the enhanced broadening and highly Gaussian blue wing with an overcompensation of Gaussian width. The effects of saturation were not likely to be present as signal levels were kept to a minimum. Ensemble averaging did not contribute to this effect, as individual runs exhibited similar results to the average with increased noise. Certainly, development of an accurate lineshape model that accounts for the physical interaction at play is necessary to describe the high-pressure Kr LIF lineshape. One that accurately predicts the Doppler width according to room temperature or physically describes the enhanced Gaussian widths.

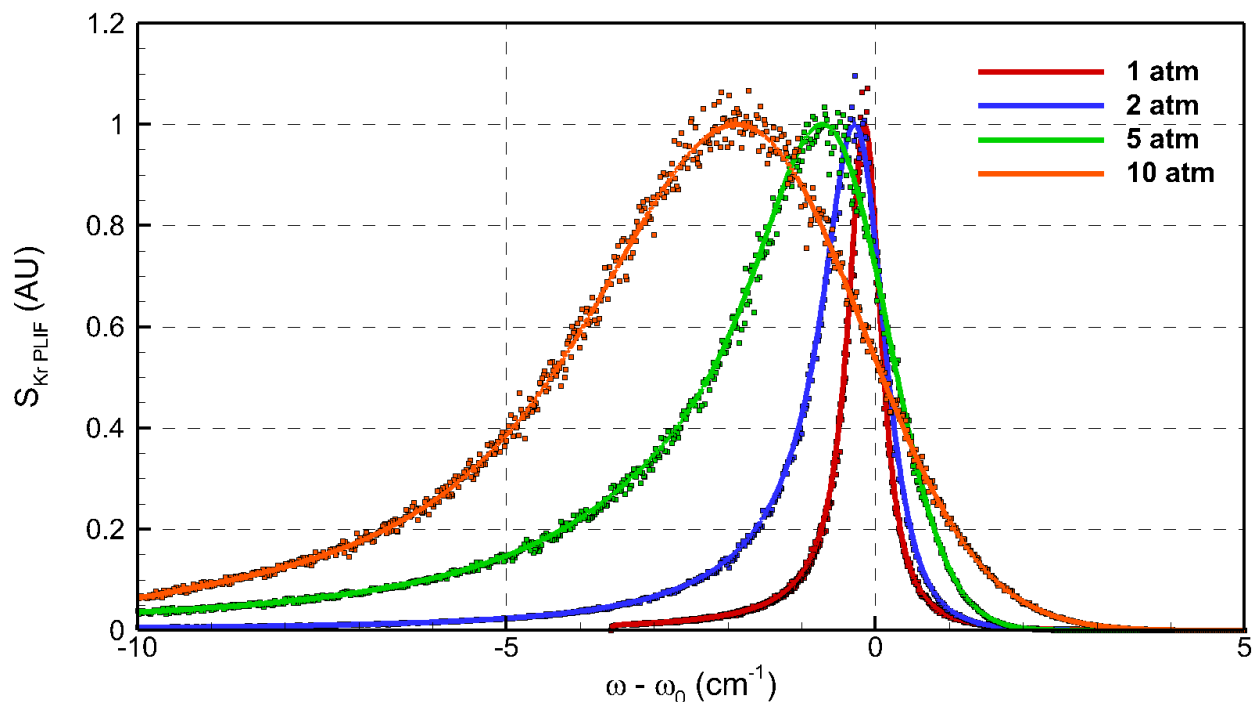


Figure 10.3: Excitation scans of Kr fluorescence 1 – 10 atm.

Table 10.3: Results of lineshape parameters obtain from the synthetic asymmetric fits at each pressure. Widths and shifts are in units cm^{-1} and a is unitless. RMS errors are normalized.

| p (atm) | w | w_G | w_{Lor} | w_C | $w_{C\ theo}$ | δ_C | $\delta_{C\ theo}$ | a | RMS fit |
|-------------|--------|--------|-----------|--------|---------------|------------|--------------------|--------|---------|
| 0 | 0.2027 | 0.0945 | 0.1715 | 0.0115 | 0.0000 | 0.0000 | 0.0000 | 0.0000 | 0.0247 |
| 0.25 | 0.2770 | 0.0814 | 0.2493 | 0.0893 | 0.1013 | -0.0312 | -0.0365 | 0.4245 | 0.0255 |
| 0.5 | 0.4087 | 0.1330 | 0.3638 | 0.2038 | 0.2026 | -0.0727 | -0.0731 | 0.5592 | 0.0253 |
| 0.75 | 0.4391 | 0.1015 | 0.4110 | 0.2510 | 0.3039 | -0.1125 | -0.1096 | 0.4980 | 0.0282 |
| 1 | 0.5708 | 0.1348 | 0.5169 | 0.3569 | 0.4053 | -0.1461 | -0.1461 | 0.7857 | 0.0216 |
| 2 | 1.0808 | 0.3684 | 1.0158 | 0.8558 | 0.8105 | -0.2669 | -0.2922 | 1.4276 | 0.0104 |
| 5 | 2.5498 | 1.6053 | 2.1699 | 1.9719 | 2.0263 | -0.7517 | -0.7305 | 3.0510 | 0.0311 |
| 10 | 5.6217 | 3.4017 | 4.2163 | 3.8658 | 4.0525 | -1.8838 | -1.4611 | 6.0837 | 0.0807 |

Table 10.4: Results of lineshape parameters obtained from the synthetic symmetric Voigt fits at each pressure in the 0 – 1 atm pressure range. Widths and shifts are in units cm^{-1} and a is unitless. RMS errors are normalized.

| p (atm) | w | w_G | w_{Lor} | w_C | RMS fit |
|-----------|--------|--------|-----------|--------|---------|
| 0 | 0.2027 | 0.0945 | 0.1715 | 0.0115 | 0.0247 |
| 0.25 | 0.2770 | 0.0945 | 0.2435 | 0.0835 | 0.0259 |
| 0.5 | 0.4087 | 0.1394 | 0.3574 | 0.1974 | 0.0275 |
| 0.75 | 0.4391 | 0.1015 | 0.4110 | 0.2510 | 0.0298 |
| 1 | 0.5708 | 0.1416 | 0.5112 | 0.3512 | 0.0294 |

The results of Table 10.3 are plotted in the proceeding charts to analyze any trends or proportionalities in the lineshape parameters at high pressure. The collisional FWHM, shift, and the asymmetry parameter scale linearly with pressure quite well, except for the collisional shift at 10 atm. This suggests that the Kr LIF spectral line follows impact behavior quite faithfully up to a point. Furthermore, the slopes of the fits for w_c and δ_c match quite well to the theoretical values predicted by Equation (29) and (30) at 1 atm. The y-intercept in Figure 10.6 is the “expected” asymmetry parameter at 0 atm of perturber pressure. Considering this value is quite low in comparison to other results (0.1642), vacuum scans may be accepted as sufficiently symmetric. Additionally, forcing the y-intercept in this equation to zero would result in negligible change to the overall fit. It is expected that different gases follow the linear scaling of FWHM and shift with pressure, but additional work is necessary to determine if the asymmetry parameter scaling is general for different gas compositions. However, these results and conclusions should be accepted with some caution. Considering the enhanced total FWHM for 2, 5, and 10 atm is caused by a large Gaussian component, it is possible that a sophisticated fitting procedure based upon physical principles is needed. Thus, if such a model exists that can produce a Gaussian width corresponding to Doppler broadening at 300K, then enhanced collisional broadening would result to match w , thus invalidating the below linear scaling. This scenario suggests that pressures above (and perhaps including) 1 atm do not fully operate within the impact broadening regime, but instead are best described by an “intermediate” pressure regime, one that may describe the line center using impact theory, while the wings and perhaps even the width, are described using quasistatic theory [119].

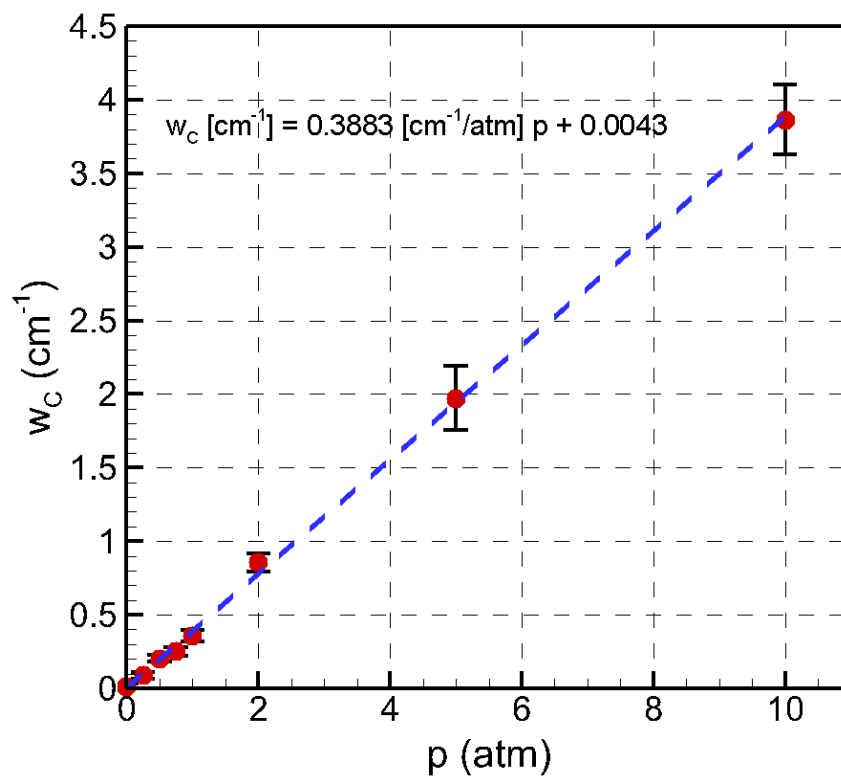


Figure 10.4: Collisional FWHM of N_2 as a function of pressure.

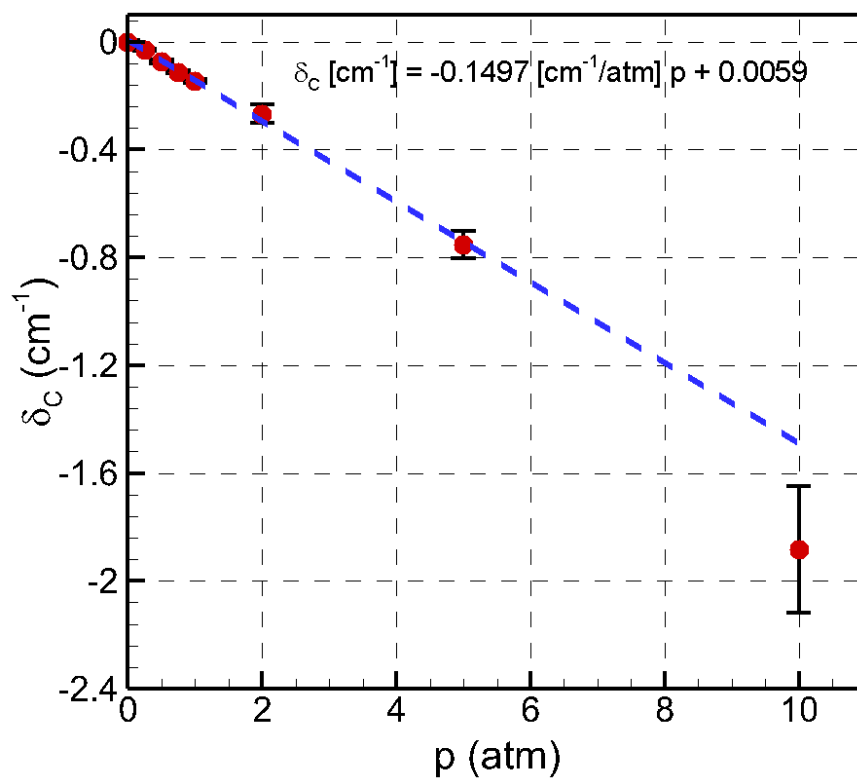


Figure 10.5: Collisional shift of N_2 as a function of pressure.

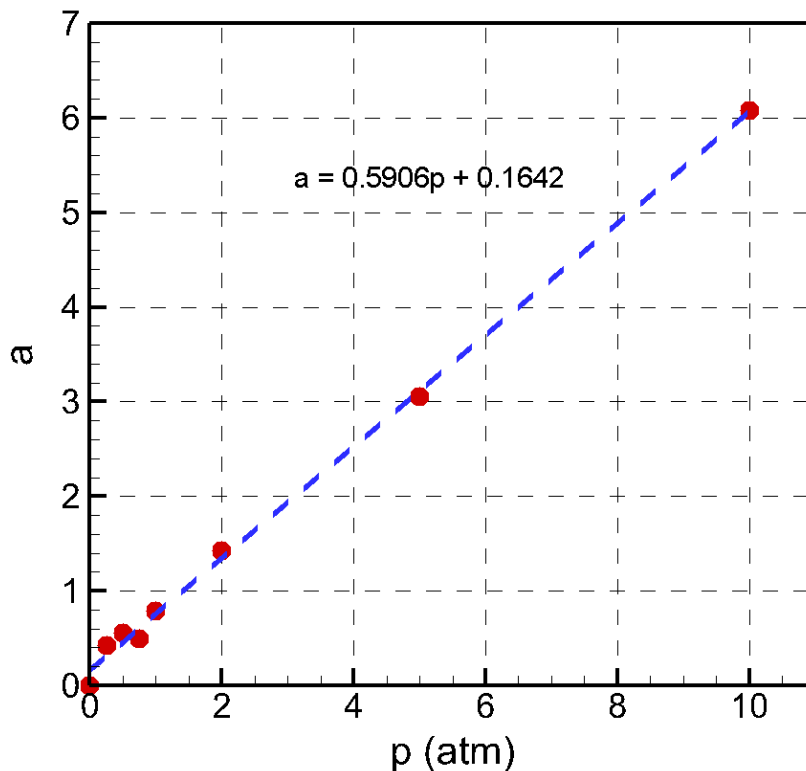


Figure 10.6: Asymmetry parameter of N_2 as a function of pressure.

10.5 Hypothesis on the Pressure-Broadening Mechanisms of the Kr LIF Spectral Line

Now that it has been concluded that a physical mechanism that causes asymmetry in the Kr PLIF spectral line exists, it is necessary to hypothesize the specific mechanism at play. At the start of the chapter, it was summarized that the most common mechanisms are Dicke narrowing, correlations between velocity-changing and state-changing collisions, speed-dependent effects (SDEs), line mixing, and collision-time asymmetry.

10.5.1 Dicke Narrowing

The effect of Dicke narrowing is expected to be absent in the Kr PLIF lineshape for numerous reasons. It has been shown experimentally that Dicke narrowing occurs only in low pressure environments and in the onset of increasing pressure [120, 121]. Also, the mean free path is expected to be significantly more than 214nm where Kr absorbs. Significantly high pressures would be necessary to reduce the mean free path below 214nm. Even so, such an increase in

pressure would cause an increase in collisional broadening, reducing the apparent effects of the Doppler broadened portion because of the dominating Lorentzian profile, violating the low-pressure requirement. According to [110], Dicke narrowing must only be considered when $w_C < w_D$, requiring reduced pressures and high temperatures to observe this effect. Two studies in Appendix E employed elevated temperatures in their Dicke narrowing investigation [122, 123], so further work may be necessary to observe such features. However, these studies employed long excitation wavelengths and high mass ratios. Furthermore, these effects were not observed in heated gas excitation scan experiments or vacuum furnace scans as part of this dissertation. In reference to the above findings, the sub-atmospheric scans did not suffer from a reduction in Doppler width, as values corresponding to room temperature were determined for all scans at $p = 0 - 1$ atm.

Moreover, velocity-changing collisions require the mass of the perturbing gas species to be of similar value or greater than the absorbing species' mass. Pine et al. 1980 showed that velocity-changing collision rates increase with increasing mass of the buffer gas [124]. Considering that Kr has a high molecular weight of 83.8 g/mol and the products of combustion are significantly lighter, velocity-changing collisions would be difficult to achieve unless collision rates are overwhelmingly high. Even so, [125] found that Ar (a heavy perturber) was inefficient in changing the speed of H₂ molecules due to the large mismatch of mass and average speed. Ciurylo et al. 2001 later declared that similar mass gases would be most efficient in changing the velocity [126].

Most studies that have examined Dicke narrowing have done so in such a way to purposefully exacerbate the conditions necessary to observe Dicke narrowing. Some examples are

provided below, all of which use high mass ratios, large excitation wavelengths, and lower pressures.

- [124]: HF in Ne and Ar, mid IR, ~300 - 760 torr
- [110]: HCN in N₂ and Ar, 3 μ m
- [121]: HCl in Ar, 3.5 μ m, 250 torr – 760 torr
- [122]: H₂O in Ar, 7185.6 and 7154.35 cm⁻¹ at 296 – 1100K and 6 – 830 torr
- [123]: H₂O in N₂ and CO₂, 4029.52 and 4041.29 cm⁻¹, 650K – 1325K and 2 – 760 torr
- [127]: C₂H₂ in Xe, 3 μ m excitation vs a mean free path of 0.14 μ m, less than 404 torr

In contrast to the above, studies that employed 326.1nm excitation in a Cd LIF application [114, 128] noted negligible narrowing, even when using Xe, a high-mass perturber. This further supports that Dicke narrowing is not present in Kr LIF. Nonetheless, if Dicke narrowing is indeed present in the Kr LIF lineshape, it should be noted that such effects will most likely occur in negligible amounts at increased pressures. According to Table 10.3, quite the contrary occurs as Doppler widths alarmingly increase past 1 atm. As noted by [111], there is little incentive to replace the Voigt profile with a collisionally narrowed profile such as the Galatry. To do so would be computationally more expensive due to the addition of an extra parameter. Since these differences can be quite miniscule, it would be difficult to detect residuals when compared to experimental noise. Furthermore, if other mechanisms are present such as narrowing of the Lorentzian profile due to SDEs, it would be difficult to distinguish contributions from one another [127].

10.5.2 Correlations between velocity-changing and state-changing collisions

It is also suspected that the asymmetric contribution produced by correlations between velocity-changing and state-changing collisions is not the observed mechanism in the data. Simply put, this is due to the inability of the much lighter combustion products to change the velocity of

the more massive Kr atoms. The approximation of uncorrelated effects is valid so long as the perturber is much lighter than the absorber, as given by [111]. If there are no velocity-changing collisions, Dicke narrowing may not occur, and therefore no such correlations may exist. Significantly high pressures would be necessary to change the Kr atom's velocity, and higher temperatures would also be necessary to reduce the collisional broadening component to observe Dicke narrowing and in turn, the asymmetries produced by these effects. Even so, these effects have not been observed in pressures above 1 atm, as exhibited by the findings in [129]. Lastly, the lineshapes for pure mixtures of HF [124, 129] and H₂O [122, 123] did not exhibit the same narrowing or asymmetries as those perturbed by heavier perturbers, further suggesting Kr is not affected by this influence.

10.5.3 Speed-Dependent Effects

The mass ratio of combustion products to Kr is not conducive to producing SDEs. As shown by the theoretical findings of [116], [117], and [130], the asymmetries and/or narrowing/broadening of the spectral line caused by SDEs requires high perturber to absorber mass ratios. If $m_A \gg m_P$, and hence allowing the perturber to move much faster than essentially stationary absorbers, collisional broadening and shift is not dependent on the speed of the absorber, and any resulting asymmetry is most likely the result of collision duration [77]. Again, most studies that examined SDEs purposefully attempted to induce such affects with large mass ratios, such as HF-Ar, H₂-Ar, Cd-Xe, Ca-Kr, C₂H₂-Xe, etc. Additionally, SDEs were observed only at low to intermediate pressures (around 1 atm) for most of the references in Appendix E, suggesting their influence is negligible or unnoticeable at elevated pressures. Even so, such effects were not present in the excitation scans ranging from 0 to 1 atm, as the asymmetries predicted were of the same

magnitude (therefore, no scaling present in this range) and the symmetric fits described the pressure regime with adequate fidelity.

Though SDEs are not suspected in the Kr PLIF lineshape, it is important to note that non-Lorentzian features reported in [125] increased with increasing temperature at constant pressure due to an increasing Doppler width and decreasing collisional width. This asymmetry provided an opposite result, and the authors concluded these effects may persist at elevated temperatures and pressures. Considering that most experiments referenced in Appendix E were performed below 1000K, an evaluation of these effects may be necessary to assess the validity for use in combustion environments. As is the case with any system with combined mechanisms, similarities of asymmetries of SDEs and the finite duration of collisions requires extreme care for quantitative interpretation [129, 114].

10.5.4 Line Mixing

Line mixing is not suspected in the Kr PLIF lineshape. The closest lines in both emission (819nm) and absorption (216.6nm) are sufficiently separated from 760.2nm and 214.7nm [67]. According to [131], line mixing must only be considered for pressures above 100 atm.

10.5.5 Collision-Time Asymmetry

Unlike the above, it is highly probable that the Kr LIF lineshapes presented in this chapter were affected by collision-time asymmetry, especially at significantly high pressures where the impact approximation ceases to be valid. Instead, the Kr LIF lineshape above 1 atm is most likely described by the quasistatic approximation considering the increased FWHM values, inexplicable Gaussian component, shift deviations at 10 atm, non-Voigt behavior in the core, and extreme asymmetry in the wings. Throughout the references in Appendix E, no comments are made about the influence of mass ratios or a definitive pressure limit where the effects of collision-time

asymmetry may be neglected, apart from the fact that the finite duration of collisions need only be considered at “high” pressures. This arbitrary pressure level denoted by several studies suggests that the pressure at which these effects becomes appreciable is dependent upon the perturber-absorber gas mixture.

Marteau et al. studied finite duration collision asymmetry for the HF rovibrational lines perturbed by Ar atoms [118]. Their main findings confirmed the expected behavior based on theoretical analysis of the finite duration effect on the spectral line in the core region at moderate pressures. The data was well represented by the usual Lorentzian lineshape with the addition of a dispersion component, which is proportional to a characteristic asymmetry parameter. The width, shift, and asymmetry parameter used in the fitting procedure were all linear of gas density, very similar to the Kr LIF results presented here. Marteau et al. 1984 also reported that the asymmetry should take on the same sign as the shift, which corroborates the current Kr LIF lineshape results across the entire pressure regime. The sign and “intensity” of the asymmetry were both found to be directly connected to the intermolecular potential, supporting the basis of the quasistatic approximation.

Harris et al. 1984 studied collision-time asymmetry by analyzing calcium resonance lines perturbed by krypton [115]. This is the closest experimental configuration to Kr LIF found in the extensive literature review, which matches quite well to the experimental configurations employed in this dissertation. The Ca-Kr mixture was held at 870K, 800 torr, and possessed a perturber-absorber mass ratio of 2.1. The lineshape used contained both Lorentzian and dispersion shaped components. Under the effects of the finite-duration of collisions, the line asymmetry was found to show the same sign as the shift, i.e. a red shift corresponded to asymmetry in the red wing, further confirming the Kr LIF results. In contrast to the findings of this dissertation, the Gaussian

component of the Ca LIF line decreased substantially with increasing pressure, which was attributed to the high mass ratio of 2.1. When Ne is substituted for Kr, the variations in the reduced Voigt profile in the line core and wing asymmetry disappeared, suggesting SDEs were present for the Xe case. Interestingly, when using He, the line core was well described by the reduced Voigt profile, but possessed a slight blue asymmetry. Harris et al. concluded that Ca resonance lines perturbed by Kr induced collision-time asymmetry in the impact regime.

As an extension to the work done in [118], the HF-Ar system subjected to $p > 10$ atm was revisited by Boissoles et al. [131] including lineshape models that featured competition amongst multiple mechanisms such as SDEs, Dicke narrowing, and correlation effects in addition to collision-time asymmetry as [132] found these processes occur simultaneously. A simplified fitting model was employed as represented by the following function

$$I(\omega) = \frac{1}{\pi} \left[\frac{\gamma}{\omega - \omega_0 - \delta + \gamma^2} + Y \frac{(\omega - \omega_0 - \delta)}{\omega - \omega_0 - \delta + \gamma^2} \right] \quad (48)$$

Where γ is the width, ω is the wavenumber, ω_0 is the center wavenumber, δ is the shift, and Y is the asymmetry parameter. Beyond 5 atm of Ar pressure, nonimpact effects dominated. From their findings, Boissoles et al. determined that intermediate models describing all mechanisms is necessary at intermediate pressures (1 atm), and that speed-dependent asymmetric profiles may be useful when the SDEs, collisional narrowing, and finite duration of collisions are present around perturber-absorber mass ratios of 1.

To study the simultaneous effects of collision-time asymmetry and SDEs, Bielski et al. performed laser induced fluorescence on the Cd 326.1nm line perturbed by Xe [114]. Xe pressure varied between 5 and 368 torr at room temperature. The authors used numerous lineshape models including or excluding SDE mechanisms and collision-duration mechanisms to logically pinpoint

the phenomenon at play. The profiles that described the system most accurately were the asymmetric Voigt profile (AVP) which included collision-time asymmetry and the speed-dependent asymmetric Voigt profile (SDAVP) which included SDEs and collision-time asymmetry. The AVP provided improvement for the fit only in the wings, suggesting further improvement is necessary. The SDAVP had residual errors spread uniform about zero, which concluded that the Cd-Xe system contained noticeable effects of both collision-time asymmetry and SDEs for the 326.1nm line. Next, Bielski et al. used the AVP and SDAVP to distinguish the mechanisms from one another. For the AVP, the Doppler width decreases with increasing Xe pressure, which was manifested by the Doppler-collision correlation effects, agreeing with the theoretical findings of [116] and [117]. In contrast, there was practically no dependence of Xe pressure on the Doppler width using the SDAVP. For both cases, the shift was toward the red end of the spectrum, and the Lorentzian width and shift were both linearly dependent on perturber pressure. Broadening coefficients were of a negligible difference between the two models (1%), while shift coefficients for the SDAVP were 4% higher than the AVP. The asymmetry parameter was linearly dependent on density for both models, but the asymmetry coefficient for the speed dependent profile was 20% lower than for the AVP. In summary, the SDAVP provided the correct model for the Cd-Xe system, collision-time asymmetry and Dick narrowing were found to play a negligible role, and neglecting SDEs may result in errors of up to 20% for the collisional parameters [114]. Interestingly, it was later asserted by Lisak et al. that the impact approximation for this gas mixture fails at approximately 400 torr [128]. These findings suggest that the pressure limit at which collision-time asymmetry becomes prevalent depends on the perturber-absorber combination.

Thus, there is sufficient evidence that collision duration effects indeed play a role in the Kr LIF results presented in this dissertation, in light of the similarities of the Kr LIF results to other collision partners and other mechanisms lacking the characteristics to do so. In the case that the Kr PLIF lineshape is affected by the finite-duration of collisions, difficulties may arise in distinguishing these asymmetric characteristics from others, as noted by [115] and the multiple lineshape models introduced in [77]. Therefore, the necessity to develop accurate models to describe this physical mechanism that influences the Kr PLIF spectral line is of utter importance. Additionally, future work should be concerned with determining the origin of the increased Gaussian widths predicted by the asymmetric Voigt fit at higher pressures. Prior to performing composition-independent Kr PLIF temperature and/or pressure measurements using the techniques in Chapters 8 and 9 for elevated pressures ($p > 1$ atm), it is first necessary to determine the appropriate lineshape functions and scaling relations to account for unresolved mechanisms. Namely compositional scaling of the collision parameters above 1 atm, asymmetry scaling of different gases at higher pressures, enhanced widths influenced by collision-time asymmetry, and the increased Gaussian components.

Chapter 11 : Summary and Recommendations for Future Study

11.1 Summary

Due to the growing needs to develop diagnostic tools that provide 2D temperature fields in reacting flows while circumventing the obstacle of unknown local gas compositions, the goal of this dissertation was to uncover the thermochemical dependencies of the line broadening parameters from the two-photon Kr LIF $4p^6 S_0^1 \rightarrow 5p \left[\frac{3}{2} \right]_2$ transition centered at 107.3nm, with the focus of developing and demonstrating composition-independent thermometry techniques. The principal of thermometry techniques developed in this work leveraged the thermochemical dependence of the overlap integral, and therefore required an extensive analysis the Kr LIF absorption spectrum.

First, compositional scaling of the collisional broadening parameters was investigated. The studied absorber/perturber combinations differ from previous works in that the electronic energy gap between ground and excited states of the absorber is very similar to that of the perturber. In this situation, the classical expression of dispersive energy during collisions could not be simplified further to obtain closed form equations for compositional scaling of collisional parameters. The compositional scaling issue was addressed by obtaining the absorption lineshape using an excitation scan, from which the collisional broadening parameters were obtained. It was observed that whereas collisional FWHM scales corresponding to the extreme situation of $\Delta E_p \gg \Delta E_a$, the collisional shift scales corresponding to the situation $\Delta E_p \ll \Delta E_a$. In other words:

$$w_c \propto (n_p - 1)^{0.4} \times \mu^{-0.3}$$

$$\delta_c \propto \mu^{-0.3}$$

The reported experimental values of w_c were within the same order of magnitude as theoretical predictions made using the classical impact broadening theory, which confirmed that

the collisional interactions occur at the impact broadening regime. Theoretical estimates of the influence of electrostatic and dipole-induced-dipole forces were also determined, which showed that their magnitudes are several orders of magnitude smaller than the dispersive forces for all the perturber species considered. As a result, the compositional scaling of w_c and δ_c showed very tight scaling even when the perturber had a large permanent dipole moment. Further, the generality of the w_c and δ_c scaling to other absorber/perturber systems with similar electronic energy gaps was studied by examining the scaling of NO as the absorber and different combustion species as perturbers, from previous literature. Overall, the compositional scaling of w_c and δ_c obtained for Kr perturbed by combustion species appeared to hold very well with NO perturbed by combustion species. The largest deviation from the scaling resulted for perturbers with large dipole moments (H_2O), where DiRosa & Hanson [74] argued that the electrostatic forces dominate the dispersive forces. These deviations were not observed in the Kr/perturber system due to the zero permanent dipole moment of Kr.

Upon determining the compositional scaling of the collisional parameters, the temperature scaling of the Doppler broadening according to two-photon excitation was determined. Though the theory on single-photon excitation Doppler widths is well documented and may be regarded as general, a temperature calibration for Kr PLIF Doppler widths was necessary to prove if a two-photon process may or may not be represented by some scaling parameter. Furthermore, this experimental campaign was important to determine the contributions between the Doppler broadening and laser linewidth towards the total Gaussian width. Excitation scans were deconvolved to isolate the Gaussian contribution of various heated environments containing Kr. High-temperature environments were produced by heating the static test cell containing 4 torr of Kr and no perturber gas up to 500K and creating CH_4 flat flames to achieve exhaust temperatures

in the range of 1600K to 2000K. The resulting w_D from a two-photon process was found to be approximately $\sqrt{2}$ times larger than single-photon Doppler widths, and the experimental value $w_L/\sqrt{2}$ (accounting for two-photon excitation) compared quite favorably with the manufactured specified value of 0.06 cm^{-1} . In summary:

$$w_G^2 = w_D^2 + w_L^2; \frac{w_L}{\sqrt{2}} = 0.057 \text{ cm}^{-1}$$

$$w_D = 0.093 \sqrt{\frac{T}{300}} \text{ cm}^{-1}$$

Following the evaluation of two-photon Doppler widths was the determination of the temperature exponents for the collisional width and collisional shift. Development of composition-independent thermometry techniques depended heavily on the precise determination of closed formed solutions for all spectral broadening parameters. High-temperature environments for obtaining collisional parameter temperature exponents were achieved by using an Osram SureHeat Jet electrical heater. Atmospheric air, N_2 , CO_2 , and CH_4 were flowed through the heater with output temperatures in the range of 300 – 900K. The exponents obtained from the slopes of log-log plots for each gas were highly consistent with one another, suggesting that the temperature dependencies for the collisional width and shift do not depend on gas composition. Furthermore, exponents of -0.8 and -0.6 agree well with those predicted with dispersive interaction theory (-0.7) and the range of values presented for similar studies using NO and CO as absorbers. Consistent values of -0.8 and -0.6 were further supported when combining the collisional parameter values of air and premixed methane exhaust, proving the temperature exponents valid for combustion temperatures. Acquisition of these exponents provided the remaining information to develop closed-form solutions for the Kr LIF collisional parameters with combustion species as collision partners:

$$w_c [cm^{-1}] = 0.40p \left(\frac{T}{300} \right)^{-0.8} \left(\frac{n-1}{n_{air}-1} \right)^{0.4} \left(\frac{\mu}{\mu_{air}} \right)^{-0.3}$$

$$\delta_c [cm^{-1}] = -0.145p \left(\frac{T}{300} \right)^{-0.6} \left(\frac{\mu}{\mu_{air}} \right)^{-0.3}$$

With knowledge of the thermochemical dependencies of the Kr PLIF line broadening parameters, two composition-independent thermometry methods were developed and presented in Chapter 8. These methods use spectral lineshape information of krypton excitation scans to obtain the temperature. Demonstration of the technique was performed on a CH₄/N₂ steady laminar non-sooting jet diffusion flame produced by in house designed co-flow burner. In the first method (Method 1), temperature was determined by extracting the Doppler broadening FWHM, obtained directly from the excitation scan using deconvolution procedures. The second thermometry method (Method 2) determined the temperature by using the collisional broadening parameters obtained from the excitation scan and Rayleigh scattering signals. First, the corrected Kr PLIF sheet images suggested that Kr PLIF signal levels possessed a quadratic dependence on the incident laser energy, which confirmed that the measurements were indeed made in the unsaturated regime. Sample excitation scans and the associated lineshape parameters corresponding to different regions in the reaction zone were in excellent agreement with the Rayleigh scattering radial profile. Despite observed asymmetry in the excitation scans, both Methods 1 and 2 exhibit very good agreement with the computational temperature profile, and among the two methods, Method 2 provided a better comparison with the computed temperature profile. The systematic temperature error of approximately 50K with Method 2 is well within the range of uncertainty when compared to other spectroscopic techniques. Uncertainty analysis revealed that the error source was dominated by the modest signal to noise ratio of the images as well as by inherent laser jitter. Since the signal levels were deliberately kept low to ensure unsaturated signals, significant gains in

measurement accuracy can be made by improving on the signal levels. Further improvements may be achieved using etalons to control the laser spectral jitter. Overall, the presented methods show excellent promise as a reliable thermometry tool in reacting flows with arbitrary compositions.

In addition to Methods 1 and 2, a two-line Kr PLIF based 2D temperature imaging technique was developed and demonstrated on steady laminar non-sooting diffusion flames. The choice of the two excitation wavelengths were made using the knowledge of the fuel mixture and pressure. The two excitation wavelengths lie within the same $4p^6 S_0^1 \rightarrow 5p \left[\begin{smallmatrix} 3 \\ 2 \end{smallmatrix} \right]_2$ transition, and their selection is informed such that the resulting Kr PLIF signal ratio depends primarily on the temperature and negligibly on the local composition. This assertion was validated by calculating theoretical R_{Kr} values for air, pure reactants, and pure products for a given wavelength combination.

The technique relied heavily upon laser sheet intensity corrections to homogenize the fringe-like signal distribution of the fluorescence sheet. The square of intensity of the 214nm CCD images agreed respectably to the ICCD fluorescence profile across the entire measurement domain once spatially calibrated to one another, despite slight beam divergence and non-Gaussian behavior. The fluorescence images were adequately corrected to homogenize the fluorescence field and to remove shot-to-shot laser energy fluctuations. These results reinforced the idea that the fluorescence signals were not saturated, thus adhering to the I_o^2 dependence per Equation (1). The SNRs of single fluorescence images were found to be approximately 20 (25) and 10 (15) in the potential core and flame regions before (after) low pass filtering, respectively.

Despite small differences in the R_{Kr} mappings for different gas compositions, the R_{Kr} field images provided an excellent illustration of the combustion environment by distinguishing the unreacted fuel core, the mixing regions, the flame, and the co-flow. Values at 300K for the

reactants and air yielded the same nominal values for R_{Kr} , proving that the signal ratio dependence on gas composition is very weak. The locations of the flames in these images was corroborated with both CH* chemiluminescence images and normalized Rayleigh scattering images. Due to the weak compositional dependence of R_{Kr} and the strong compositional dependence of Rayleigh scattering cross-sections, R_{Kr} fields provided greater contrast in demarcating different regions of the flow.

Consistent with R_{Kr} fields, average and single-shot temperature fields performed well in distinguishing different regions of the flow when compared to FLUENT simulations. Furthermore, extremely similar temperature results were obtained using different wavelength combinations. However, it was observed that difficulties in correcting for the slight excitation sheet divergence (most likely due to a non-Gaussian beam profile) become apparent in the Kr PLIF temperature fields, demonstrating systematic temperature differences in the flame and an inability to resolve the axial temperature gradients. While values of shot-to-shot temperature variation are higher for single-shot fields, improvements may be made by optimizing the laser linewidth to balance temperature sensitivity and compositional influence reduction, and improved sheet correction procedures. Upon evaluating different sources of uncertainty, the temperature uncertainty was dominated by the uncertainty of the excitation wavelengths created by laser jitter, systematic errors created from the energy correction procedure and differential absorption, and the systematic bias created due to using a pure fuel R_{Kr} vs T mapping. However, the fact that the observed precision error was considerably less than the RMS error of individual error sources for this method showed that the error estimates are indeed upper bounds of uncertainty caused by different sources. Hence, the two-line Kr PLIF technique offers promise for composition-independent thermometry, with a natural extension to turbulent flames.

Lastly, an investigation into the Kr LIF spectral line subjected to high perturber pressures was undertaken to determine the possible physical mechanisms at play that caused the asymmetry previously observed in excitation scans. At extreme perturber densities departures from the impact broadening theory becomes more likely, as the system in question may become more accurately explained by the quasistatic approximation. Excitation scans of Kr fluorescence using up to 10 atm of N₂ pressure were performed using a high-pressure cell. The spectra were fit to an asymmetric lineshape model that allowed the Lorentzian width to vary sigmoidally based on wavenumber.

For 0 – 1 atm of N₂, collisional widths and shifts increased linearly with pressure, and there existed a slight asymmetric component for each scan above 0 atm, with the most notable asymmetry occurring at 1 atm. Asymmetry followed the same orientation as the collisional shift, and Doppler widths according to room temperature were achieved. However, the asymmetry was so slight that these effects may be deemed negligible depending on the application. To determine the justification or efficacy of using an asymmetric lineshape model in the pressure regime of 0 – 1 atm, the same data was fit to a symmetric lineshape. Results for the Lorentzian width, Gaussian width, and collisional shift changed negligibly between fitting routines for this pressure range, suggesting that an asymmetric fit was largely unnecessary to extract line broadening parameters for 0 – 1 atm, and that the Kr LIF line core is accurately represented by impact broadening theory. This conclusion supported the strategies in Chapters 8 and 9, validating the temperature measurement methods. It was not until 1 atm of perturber pressure where fit RMS errors improve by a margin of 30%, as compared to approximately a 5% improvement for 0 – 0.75 atm.

The excitation scans of 2, 5, and 10 atm were heavily skewed towards the red wing due to asymmetric deviations, and thus required the use of an asymmetric fit. In contrast to the blue wing, the red wing for each pressure was highly Lorentzian, showing little characteristic Gaussian width.

Though the values of collisional width compared quite well with theoretical values, there existed a drastically enhanced amount of Gaussian width as predicted by the asymmetric model. This arises from the fact that w for 2, 5, and 10 atm were well above their predicted values and the asymmetric lineshape model attempted to overcompensate for this width by inclusion of an additional Gaussian component. Also, inspection of the blue wing for each pressure above 1 atm qualitatively showed an increased Gaussian contribution which was not present in the low-pressure regime. Certainly, development of an accurate lineshape model that accounts for the physical interaction at play is necessary to describe the high-pressure Kr LIF lineshape. One that accurately predicts the Doppler width according to room temperature or physically describes the enhanced Gaussian widths.

For the entire pressure range of 0 – 10 atm, the collisional FWHM, shift, and the asymmetry parameter scale linearly with pressure quite well, except for the collisional shift at 10 atm, suggesting that the Kr LIF line follows impact theory faithfully up to a point. The linear scaling of each parameter was well within acceptable levels of error based on theoretical estimates. However, the results for the collisional width should be taken with some caution due to the enhanced broadening and large Gaussian widths of 2, 5, and 10 atm, suggesting that a sophisticated lineshape model based on physical principals is necessary to describe this effect. This implies that pressures above 1 atm do not fully operate within the impact broadening regime, but instead are best described by an “intermediate” pressure regime; one that may describe the line center using impact theory, while the wings and perhaps even the width, are described using quasistatic theory [119].

It was determined that the effects of Dicke narrowing, correlations between velocity-changing and state-changing collisions, SDEs, and line mixing were not responsible for the lineshape deviations observed in the Kr LIF spectral line. However, there was sufficient evidence

to suggest that such lineshape effects were caused by emission of radiation during collision events i.e. collision-time asymmetry. Rather than impact theory, the Kr LIF lineshape above 1 atm is most likely described by the quasistatic approximation considering the increased FWHM values, inexplicable Gaussian component, shift deviations at 10 atm, non-Voigt behavior in the core, and extreme asymmetry in the wings. In the case that the Kr PLIF lineshape was affected by the finite-duration of collisions, difficulties may arise in distinguishing these asymmetric characteristics from others. Therefore, the necessity to develop accurate models to describe this physical mechanism that influences the Kr PLIF spectral line is of utter importance. Additionally, future work should be concerned with determining the origin of the increased Gaussian widths predicted by the asymmetric Voigt fit at higher pressures.

11.2 Recommendations for Future Work

11.2.1 Short Term

In the intermediate future, there are a number of different tasks that may be performed which would benefit this research. First and foremost, the 214nm laser spectra should be measured. Precise determination of the width and shape of the laser lineshape using devices such as a wave-meter would have been most beneficial for precise determination of the line broadening parameters and the thermometry methods presented in this work, namely those concerned with deconvolution. Instead, experimental calibration procedures and vacuum scan deconvolution was performed.

The thermometry techniques presented in this dissertation may immediately be applied to steady laminar sooting flames. As covered in Chapter 1, several different laser diagnostics approaches have been unable to provide accurate temperature measurements due to soot and particle inference throughout the combustion zone. Interest in thermometry methods applied to sooty flames stems from the strong coupling between soot formation and temperature, as soot must

be reduced due to pollution emissions of fine particles and excessive heat transfer to combustor walls. Developments in the area of NTLAF on indium atoms have since allowed accurate measurements of temperature in sooting flames in the range of 800 – 2600K [32]. Recently, Kr PLIF has been expanded to demonstrate the feasibility of simultaneous measurements of mixture fraction and soot volume fraction in turbulent non-premixed flames [63]. Therefore, there exists considerable interest and scope in developing thermometry techniques applicable to soot laden flows. To reduce the effects of soot interference, camera exposures must be kept to minimum levels ($< 50\text{ns}$) using an externally triggered laser and a narrowband 760nm interference filter. Prior to performing Kr PLIF measurements of sooting flames, an emphasis should be placed on performing laser-induced incandescence (LII) to determine soot volume fractions in various test flames. Additionally, it is imperative that interferences produced by polycyclic aromatic hydrocarbons (PAH) may be mitigated with proper selection of a narrowband interference filter and data processing routines. In experiments involving sooting candle flames, PAH fluorescence has shown appreciable levels of signal which can adversely “drown out” 760nm fluorescence signals. This, when coupled with flame instabilities, causes increased difficulties in removing the polluting signals on a consistent basis. Acceptable soot volume fraction levels determined by the magnitude of ICCD intensity counts must be determined prior to demonstration of the composition-independent thermometry techniques.

In Chapter 10, substantial interest was placed on the necessity to advance efforts on the high-pressure asymmetric Kr LIF spectral lineshape. Such work could uncover the origin of the excess broadening of w observed in 2, 5, and 10 atm scans, namely the inexplicable increased levels of Gaussian widths not present in the low-pressure scans. Certainly, development of an accurate lineshape model that accounts for the physical interactions at play is necessary to describe

the issues encountered in Chapter 10; One that accurately predicts the Doppler width according to room temperature or physically describes the enhanced Gaussian widths at high pressures. A deeper analysis into the interaction potentials of Kr-perturber pairs may be necessary, as the system may be governed by the quasistatic approximation. Furthermore, additional perturber gases should be employed to determine if the broadening parameters at high pressures are independent of gas composition, as numerous studies have suggested that the line broadening parameters at increased perturber densities are dependent of absorber-perturber combinations.

11.2.2 Future of Kr PLIF Thermometry Research

The lineshape analyses and thermometry contributions accomplished in this dissertation has provided motivation to extend Kr PLIF thermometry to turbulent flames and high-pressure flames. Of course, probing turbulent flames necessitates the need to acquire images on an instantaneous basis to resolve fluctuating fluid structures and temporally evolving thermodynamic gradients. Therefore, the mean scanning measurement techniques of Methods 1 and 2 will be unsuitable for this purpose. On the other hand, the two-line technique presented in Chapter 9 was shown to provide temperature measurements on a single-shot basis. In order to adapt the two-line Kr PLIF technique to turbulent flames, signal ratios must be performed on an instantaneous shot-to-shot basis, therefore requiring additional laser, tuning, injection seeding, and detection systems. It is highly encouraged that more sophisticated laser sheet energy correction procedures are implemented such as simultaneous PLIF measurements of a static Kr cell and instantaneously recorded energy meter readings.

Using the information learned from the high-pressure Kr LIF lineshape analysis, substantial interest should be placed on developing high-pressure thermometry strategies using Kr PLIF. This necessitates the need to develop a high-pressure combustion chamber, but also to

advance knowledge of the Kr LIF spectral line at high pressures. The insight acquired from such an experimental campaign is likely to facilitate the extension of Kr PLIF to pressure measurements in reacting environments.

REFERENCES

- [1] R. S. Barlow, "Laser diagnostics and their interplay with computations to understand turbulent combustion," in *Proceedings of the Combustion Institute, Volume 31*, 2007.
- [2] A. C. Eckbreth, *Laser Diagnostics for Combustion Temperature and Species*, East Hartford, Connecticut: Combustion Science & Technology, 1996.
- [3] R. K. Hanson, "Combustion diagnostics: Planar imaging techniques," in *Twenty First Symposium on Combustion*, 1986.
- [4] K. Kohse-Hoinghaus, R. S. Barlow, M. Alden and J. Wolfrum, "Combustion at the focus: laser diagnostics and control," *Proceedings of the Combustion Institute, Volume 30*, pp. 89-123, 2005.
- [5] M. A. Linne, *Spectroscopic Measurement*, First ed., London, UK: Academic Press, 2002.
- [6] R. Hanson, J. Seitzman and P. Paul, "Planar Laser-Fluorescence Imaging of Combustion Gases," *Applied Physics B*, vol. 50, pp. 441 - 454, 1990.
- [7] C. Schulz and V. Sick, "Tracer-LIF diagnostics: quantitative measurement of fuel concentration, temperature and fuel/air ratio in practical combustion systems," *Progress in Energy and Combustion Science*, vol. 31, pp. 75 - 121, 2005.
- [8] J. Heinze, U. Meier, T. Behrendt, C. Willert, K. Geigle, O. Lammel, Lucknerath and R., "PLIF Thermometry Based on Measurements of Absolute Concentrations of the OH Radical," *Zeitschrift für Physikalische Chemie*, vol. 225, pp. 1315 - 1341, 2011.
- [9] J. & H. R. Seitzman, "Two-Line Planar Fluorescence for Temporally Resolved Temperature Imaging in a Reacting Supersonic Flow over a Body," *Applied Physics B*, vol. 57, pp. 385-391, 1993.
- [10] J. Seitzman, R. Hanson, P. DeBarber and C. Hess, "Application of quantitative two-line OH planar laser-induced fluorescence for temporally resolved planar thermometry in reacting flows," *Applied Optics*, vol. 33, no. 18, pp. 4000 - 4012, 1994.
- [11] J. & H. R. Palmer, "Temperature imaging in a supersonic free jet of combustion gases with two-line OH fluorescence," *Applied Optics*, vol. 35, no. 3, pp. 485 - 499, 1996.
- [12] R. Giezendanner-Thoben, U. Meier, W. Meier and M. Aigner, "Phase-Locked Temperature Measurements by Two-Line OH PLIF Thermometry of a Self-Excited Combustion Instability in a Gas Turbine Model Combustor," *Flow, Turbulence, and Combustion*, vol. 75, pp. 317 - 333, 2005.
- [13] J. Seitzman, G. Kychakoff and R. Hanson, "Instantaneous temperature field measurements using planar laser-induced fluorescence," *Optics Letters*, vol. 10, no. 9, pp. 439 - 441, 1985.
- [14] M. Lee, B. McMillin and R. Hanson, "Temperature measurements in gases by use of planar laser-induced fluorescence imaging of NO," *Applied Optics*, vol. 32, no. 27, pp. 5379 - 5396, 1993.
- [15] B. McMillin, J. Palmer and R. Hanson, "Temporally resolved, two line fluorescence imaging of NO temperature in a transverse jet in a supersonic cross flow," *Applied Optics*, vol. 32, no. 36, pp. 7532 - 7545, 1993.

- [16] W. Bessler, F. Hildenbrand and C. Schulz, "Two-line laser-induced fluorescence imaging of vibrational temperatures in a NO-seeded flame," *Applied Optics*, vol. 40, no. 6, pp. 748 - 756, 2001.
- [17] C. Schultz, V. Sick, J. Heinze and W. Stricker, "Laser-induced-fluorescence detection of nitric oxide in high-pressure flames with the A-X(0,2) excitation," *Optical Society of America*, vol. 36, no. 15, pp. 3227 - 3232, 1997.
- [18] W. Bessler, C. Schultz, T. Lee, J. Jeffries and R. Hanson, "Strategies for laser-induced fluorescence detection of nitric oxide in high-pressure flames. I. A-X(0,0) excitation," *Optical Society of America*, vol. 41, no. 8, pp. 3547 - 3557, 2002.
- [19] V. Bermann, W. Meier, D. Wolff and W. Stricker, "Application of spontaneous Raman and Rayleigh scattering and 2D LIF for the characterization of a turbulent CH₄/H₂/N₂ jet diffusion flame," *Applied Physics B*, vol. 66, pp. 489 - 502, 1997.
- [20] W. Meier, R. Barlow, Y. -L. Chen and J. -Y. Chen, "Raman/Rayleigh/LIF Measurements in a Turbulent CH₄/H₂/N₂ Jet Diffusion Flame: Experimental Techniques and Turbulence-Chemistry Interaction," *Combustion and Flame*, vol. 123, pp. 326 - 343, 2000.
- [21] P. Medwell, P. Kalt and B. Dally, "Simultaneous imaging of OH, formaldehyde, and temperature of turbulent nonpremixed jet flames in a heated and diluted coflow," *Combustion and Flame*, vol. 148, pp. 48 - 61, 2007.
- [22] S. A. Kaiser and M. B. Long, "Quantitative planar laser-induced fluorescence of naphthalenes as fuel tracers," *Proceedings of the Combustion Institute*, vol. 30, pp. 1555 - 1563, 2005.
- [23] J. Yoo, D. Mitchell and D. Davidson, "Planar laser-induced fluorescence imaging in shock tube flows," *Experiments in Fluids*, vol. 49, pp. 751 - 759, 2010.
- [24] M. Cundy, P. Trunk, A. Dreizler and V. Sick, "Gas-phase toluene LIF temperature imaging near surfaces at 10 kHz," *Experiments in Fluids*, vol. 51, pp. 1169 - 1176, 2011.
- [25] J. & K. J. Dec, "High Speed Thermometry Using Two-Line Atomic Fluorescence," *Twenty-first Symposium (International) on Combustion/The Combustion Institute*, pp. 1737 - 1745, 1986.
- [26] J. Engstrom, J. Nygren, M. Alden and C. Kaminski, "Two-line atomic fluorescence as a temperature probe for highly sooting flames," *Optics Letters*, vol. 25, no. 19, pp. 1469 - 1471, 2000.
- [27] J. Hult, I. Burns and C. Kaminski, "Two-line atomic fluorescence flame thermometry using diode lasers," *Proceedings of the Combustion Institute*, vol. 30, pp. 1535 - 1543, 2005.
- [28] Q. Chan, P. Medwell, P. Kalt, Z. Alwahabi, B. Dally and G. Nathan, "Temperature Measurements Using Non-linear Two-Line Atomic Fluorescence," in *7th Asia-Pacific Conference on Combustion*, Taipei, Taiwan, 2009.
- [29] Q. Chan, P. Medwell, Z. Alwahabi and B. Dally, "Assessment of interferences to nonlinear two-line atomic fluorescence (NTLAF) in sooty flames," *Applied Physics B*, vol. 104, pp. 189 - 198, 2011.
- [30] D. Gu, Z. Sun, B. Dally, P. Medwell, Z. Alwahabi and G. Nathan, "Simultaneous measurements of gas temperature, soot volume fraction, and primary particle diameter in

- a sooting turbulent ethylene/air non-premixed flame," *Combustion and Flame*, vol. 179, pp. 33 - 50, 2017.
- [31] P. Medwell, Q. Chan, P. Kalt, Z. Alwahabi, B. Dally and G. Nathan, "Development of temperature imaging using two-line atomic fluorescence," *Applied Optics*, vol. 48, no. 6, pp. 1237 - 1248, 2009.
- [32] S. Mahmoud, G. Nathan, P. Medwell, B. Dally and Z. Alwahabi, "Simultaneous planar measurements of temperature and soot volume fraction in a turbulent non-premixed jet flame," *Proceedings of the Combustion Institute*, vol. 35, pp. 1931 - 1938, 2015.
- [33] P. Medwell, R. Masri, P. Pham, B. Dally and G. Nathan, "Temperature imaging of turbulent dilute spray flames using two-line atomic fluorescence," *Experiments in Fluids*, vol. 55, no. 1840, 2014.
- [34] R. Miles, W. Lempert and J. Forkey, "Laser Raleigh scattering," *Measurement Science and Technology*, vol. 12, pp. 33 - 51, 2001.
- [35] S. Kaiser, J. Frank and M. Long, "Use of Rayleigh imaging and ray tracing to correct for beam-steering effects in turbulent flames," *Applied Optics*, vol. 44, no. 31, pp. 6557 - 6564, 2005.
- [36] R. A. Patton, K. N. Gabet, N. Jiang, W. R. Lempert and J. A. Sutton, "Multi-kHz temperature imaging in turbulent non-premixed flames using planar Rayleigh scattering," *Applied Physics B*, vol. 108, pp. 377 - 392, 2012.
- [37] C. Epsey, J. E. Dec, T. A. Litzinger and D. A. Santavicca, "Planar laser Rayleigh scattering for quantitative vapor-fuel imaging in a diesel jet," *Combustion and Flame*, vol. 109, pp. 65 - 86, 1997.
- [38] R. B. Miles, A. P. Yalin, Z. Tang, S. H. Zaidi and J. N. Forkey, "Flow field imaging through sharp-edged atomic and molecular 'notch' filters," *Measurement Science and Technology*, vol. 12, pp. 442 - 451, 2001.
- [39] J. N. Forkey, "Development and demonstration of filtered Rayleigh scattering - a laser based flow diagnostic for planar measurements of velocity, temperature, and pressure," 1996.
- [40] G. S. Elliot, N. Glumac and C. D. Carter, "Molecular filtered Rayleigh scattering applied to combustion," *Meas. Sci. Technol.*, vol. 12, pp. 452 - 466, 2001.
- [41] T. McManus and J. Sutton, "Quantitative 2D Temperature Imaging in Turbulent Nonpremixed Jet Flames using Filtered Rayleigh Scattering," *AIAA 2017-1408*, 2017.
- [42] B. J. Kip and R. J. Meier, "Determination of the Local Temperature at a Sample during Raman Experiments Using Stokes and Anti-Stokes Raman Bands," *Applied Spectroscopy*, vol. 44, pp. 707 - 711, 1990.
- [43] F. Rabenstein and A. Leipertz, "Two-dimensional temperature determination in the exhaust region of a laminar flat-flame burner with linear Raman scattering," *Applied Optics*, vol. 36, pp. 6989 - 6996, 1997.
- [44] S. Roy, J. Gord and A. Patnaik, "Recent advances in coherent anti-Stokes Raman scattering spectroscopy: Fundamental developments and applications in reacting flows," *Progress in Energy and Combustion Science*, vol. 36, pp. 280-306, 2010.

- [45] R. D. Hancock, K. E. Bertagnolli and R. P. Lucht, "Nitrogen and Hydrogen CARS Temperature Measurements in a Hydrogen/Air Flame Using a Near-Adiabatic Flat-Flame Burner," *Combustion and Flame*, vol. 109, pp. 323 - 331, 1997.
- [46] F. Vestin and P. Bengtsson, "Rotational CARS for simultaneous measurements of temperature and concentrations of N₂, O₂, CO, and CO₂ demonstrated in a CO/air diffusion flame," *Proceedings of the Combustion Institute*, vol. 32, pp. 847 - 854, 2009.
- [47] M. Woodmansee, V. Iyer, J. Dutton and R. Lucht, "Nonintrusive Pressure and Temperature Measurements in an Underexpanded Sonic Jet Flowfield," *AIAA*, vol. 42, no. 6, pp. 1170 - 1180, 2004.
- [48] P. Danehy, S. O'Byrne and S. Tedder, "Coherent Anti-Stokes Raman Spectroscopy (CARS) Measurements in Supersonic Combustors at NASA Langley Research Center," Hampton, VA, 2005.
- [49] Y. Zezek, I. Choi, M. Uddi, I. V. Adamovich and W. R. Lempert, "Pure rotational CARS thermometry studies of low-temperature oxidation kinetics in air and ethene-air nanosecond pulse discharge plasmas," *J. Phys. D: Appl. Phys.*, vol. 43, p. 12401 (12pp), 2010.
- [50] M. Allen, "Diode laser absorption sensors for gas-dynamic and combustion flows," *Measurement Science and Technology*, vol. 9, pp. 545 - 562, 1998.
- [51] R. Hanson and P. Falcone, "Temperature measurement technique for high-temperature gases using a tunable diode laser," *Applied Optics*, vol. 17, no. 6, pp. 2477 - 2480, 1978.
- [52] J. Liu, G. Rieker, J. Jeffries, M. Gruber, C. Carter, T. Mathur and R. Hanson, "Near-infrared diode laser absorption diagnostic for temperature and water vapor in a scramjet combustor," *Applied Optics*, vol. 44, no. 31, pp. 6701 - 6711, 2005.
- [53] G. Rieker, H. Li, X. Liu, J. Jeffries, R. Hanson, M. Allen, S. Wehe, P. Mulhall and H. Kindle, "A diode laser sensor for rapid, sensitive measurements of gas temperature and water vapour concentration at high temperatures and pressures," *Measurement Science and Technology*, vol. 18, pp. 1195 - 1204, 2007.
- [54] L. Phillippe and R. Hanson, "Laser diode wavelength-modulation spectroscopy for simultaneous measurement of temperature, pressure, and velocity in shock-heated oxygen flows," *Applied Optics*, vol. 32, no. 30, pp. 6090 - 6103, 1993.
- [55] J. Forkey, *Development and demonstration of filtered Rayleigh scattering - a laser based flow diagnostic for planar measurement of velocity, temperature, and pressure*, 1996.
- [56] J. George and T. Jenkins, "Diagnosis of High Speed Flows using Filtered Rayleigh Scattering," in *AIAA Aerodynamic Measurement Technology and Ground Testing Conference*, Atlanta, GA, 2014.
- [57] G. Elliott and M. Samimy, "Rayleigh scattering technique for simultaneous measurements of velocity and thermodynamic properties," *AIAA*, vol. 34, no. 11, pp. 2346 - 2352, 1996.
- [58] M. Boguszko and G. S. Elliott, "On the use of filtered Rayleigh scattering for measurements in compressible flows and thermal fields," *Experiments in Fluids*, vol. 38, pp. 33 - 49, 2005.
- [59] J. Palmer and R. Hanson, "Shock tunnel flow visualization using planar laser-induced fluorescence imaging of NO and OH," *Shock Waves*, vol. 4, pp. 313 - 323, 1995.

- [60] V. Narayanaswamy, R. Burns and N. T. Clemens, "Kr-PLIF for scalar imaging in supersonic flows," *Optics Letters*, vol. 36, no. 21, pp. 4185-4187, 2011.
- [61] W. Hargus Jr., "A Preliminary Study of Krypton Laser-Induced Fluorescence," AFRL, Edwards Air Force Base, CA, 2010.
- [62] A. Hsu, V. Narayanaswamy, N. T. Clemens and J. H. Frank, "Mixture Fraction Imaging in Turbulent Non-premixed Flames with Two-photon LIF of Krypton," *Proceedings of the Combustion Institute*, vol. 33, pp. 759-766, 2010.
- [63] O. Buxton, R. Burns and N. Clemens, "Simultaneous krypton PLIF, LII and PIV measurements in a sooting jet flame," in *Proceedings of 51st AIAA Aerospace Sciences Meeting*, Grapevine, Texas, 2013.
- [64] K.-Y. Lam, J. Pickles, V. Narayanaswamy, C. Carter and R. Kimmel, "High-Speed Schlieren and 10-Hz Kr PLIF for the new AFRL Mach-6 Ludwig Tube Hypersonic Wind Tunnel," in *55th AIAA Aerospace Science Meeting*, Grapevine, TX, 2016.
- [65] N. Parziale, M. Smith and E. Marineau, "Krypton tagging velocimetry of an underexpanded jet," *Applied Optics*, vol. 15, no. 16, pp. 5094 - 5101, 2015.
- [66] D. Zelenak and V. Narayanaswamy, "Composition-independent mean temperature measurements in laminar diffusion flames using spectral lineshape information," *Experiments in Fluids*, vol. 58, no. 147, 2017.
- [67] J. Miller, "Two-photon resonant multiphoton ionization and stimulated emission in krypton and xenon," *Physical Review A*, pp. 6969 - 6976, 1989.
- [68] A. Thorne, U. Litzen and S. Johansson, *Spectrophysics: Principles and Applications*, Springer Science & Business Media, 1999.
- [69] J. Wang, "Dicke narrowing and speed-dependent effects in dispersion signals," 2013.
- [70] N. Allard and J. Kielkopf, "The effect of neutral nonresonant collisions on atomic spectral lines," *Review of Modern Physics*, vol. 54, no. 4, pp. 1103 - 1182, 1982.
- [71] W. Hindmarsh, A. Petford and G. Smith, "Interpretation of Collision Broadening and Shift in Atomic Spectra," *Proceedings of the Royal Society of London. Series A*, vol. 297, pp. 296 - 304, 1967.
- [72] D. Fletcher and J. McDaniel, "Collisional Shift and Broadening of Spectral Lines in Air near 543nm," *J. Quant. Spectrosc. Radiat. Transfer Vol 54, No. 5*, pp. pp. 837 - 850, 1995.
- [73] A. Chang, M. DiRosa and R. Hanson, "Temperature Dependence of Collision Broadening and Shift in the NO A-X(0, 0) Band in the Presence of Argon and Nitrogen," *Journal of Quantitative Spectroscopy and Radiative Transfer*, pp. pp375 - 390, 1992.
- [74] M. D. DiRosa and R. K. Hanson, "Collision Broadening And Shift Of NO Y(O,O) Absorption Lines By O2 And H2O At High Temperatures," *Journal of Quantitative Spectroscopy and Radiative Transfer*, vol. 52, no. 5, pp. 515 - 529, 1994.
- [75] H. Rabitz, "Rotational and rotational-vibrational pressure broadened spectral lineshapes," *Annual Review of Physical Chemistry*, pp. 155 - 177, 1974.
- [76] R. Hedges, D. Drummond and A. Gallagher, "Extreme-Wing Line Broadening and Cs-Inert-Gas Potentials*," *Physical Review A*, pp. 1519 - 1544, 1972.
- [77] R. Ciurylo, "Shapes of pressure- and Doppler-broadened spectral lines in the core and near the wings," *Physical Review A*, pp. 1029 - 1039, 1998.

- [78] C. Bielschowsky, C. Lucas, G. de Souza and J. Nogueira, "Generalized oscillator strength for the 3s-3p and 2p-3s transitions in the sodium atom," *Physical Review A* 43, Number 11 1 June 1991, vol. 43, no. 11, pp. 5975 - 5979, 1991.
- [79] A. Schadee, "The Relation Between The Electronic Oscillator Strength And The Wavelength For Diatomic Molecules," *J. Quant. Spec. Rad. Transfer*, vol. 7, pp. 169 - 183, 1967.
- [80] P. Griffin and J. Hutcherson, "Oscillator Strengths of the Resonance Lines of Krypton and Xenon," *Journal of the Optical Society of America*, vol. 59, no. 12, pp. 1607 - 1613, 1969.
- [81] K. Kirbey-Docken, C. Cerjan and A. Dalgarno, "Oscillator Strengths And Photodissociation Cross Sections For Li_2^+ And N_2^+ ," *Chemical Physics Letters*, vol. 40, no. 2, pp. 205 - 209, 1976.
- [82] L. Piper and L. Cowles, "Einstein coefficients and transition moment variation for the $\text{NO}(\text{A } 2\Sigma^+ - \text{X } 2\Pi)$ transition," *The Journal of Chemical Physics*, vol. 85, pp. 2419 - 2422, 1986.
- [83] W. Koechner and M. Bass, *Solid State Lasers: A Graduate Text*, New York: Springer, 2003.
- [84] C. Langrok, D. Hum, E. Diamanti and M. Charbonneau-Lefort, "Flash Lamp Pumped Quanta Ray Nd:YAG Laser Experiment," *IEEE*, pp. 101 - 104, 2002.
- [85] F. G. Kidd, "Development of a Novel Temperature Measurement Scheme Through the Two-Photon Excitation of Krypton," North Carolina State University, Raleigh, North Carolina, 2014.
- [86] S. K. Bavgi, "Flow Diagnostics using Filtered Rayleigh Scattering," North Carolina State University, Raleigh, North Carolina, 2017.
- [87] Shardanand and A. Prasad Rao, "Absolute Rayleigh Scattering Cross Sections of Gases and Freons of Stratospheric Interest in the Visible and Ultraviolet Regions," NASA, Wallops Flight Center, VA, 1977.
- [88] M. Snee and W. Ubachs, "Direct measurement of the Rayleigh scattering cross section in various gases," *Journal of Quantitative Spectroscopy & Radiative Transfer*, vol. 92, pp. 293 - 310, 2005.
- [89] J. Sutton and J. Driscoll, "Rayleigh scattering cross sections of combustion species at 266, 355, and 532 nm for thermometry applications," *Optics Letters*, vol. 29, no. 22, pp. 2620 - 2622, 2004.
- [90] G. J. Fiechtner and J. R. Gord, "Absorption and the dimensionless overlap integral for two-photon excitation," *Journal of Quantitative Spectroscopy & Radiative Transfer*, vol. 68, pp. 543 - 557, 2001.
- [91] M. D. DiRosa, "High-resolution line shape spectroscopy of transitions in the gamma bands of nitric oxide," ProQuest, 1996.
- [92] M. D. DiRosa and R. K. Hanson, "Collision-Broadening and -Shift of $\text{NO } Y(0, 0)$ Absorption Lines by H_2O , O_2 , and NO at 295K," *Journal of Molecular Spectroscopy*, pp. pp 97 - 117, 1994.
- [93] L. Dodge, J. Dusek and M. Zabielski, "Line Broadening And Oscillator Strength Measurements For The Nitric Oxide Band," *Journal of Quantitative Spectroscopy and Radiative Transfer*, vol. 24, pp. 237 - 249, 1980.

- [94] A. Vryodov, J. Heinze and U. Meier, "Collisional Broadening Of Spectral Lines In The A-X(0-0) System Of NO By N₂, Ar, And He At Elevated Pressure Measured By Laser Induced Fluorescence," *Journal of Quantitative Spectroscopy and Radiative Transfer*, vol. 53, pp. 227 - 287, 1995.
- [95] M. D. DiRosa and R. L. Farrow, "Temperature-dependent collisional broadening and shift of Q-branch transitions in the BQX(0,0) band of CO perturbed by N₂, CO₂ and CO," *Journal of Quantitative Spectroscopy & Radiative Transfer*, vol. 68, pp. 363 - 375, 2001.
- [96] D. Zelenak, W. Sealy and V. Narayanaswamy, "Collisional Broadening of Kr (4p6 S01 5p[3/2]2) transition with combustion species as collision partners," *Journal of Quantitative Spectroscopy and Radiative Transfer*, vol. 174, pp. 28-38, 2016.
- [97] G. Fiechtner and J. Gord, "Absorption and the dimensionless overlap integral for two-photon excitation," *Journal of Quantitative Spectroscopy and Radiative Transfer*, vol. 68, pp. 543 - 557, 2001.
- [98] J. Grinstead, B. Porter and J. Carballo, "Flow Property Measurement Using Laser-induced Fluorescence in the NASA Ames Interaction Heating Facility," in *AIAA*, Moffett Field, CA, 2005.
- [99] J. Olivero and R. L. Longbothum, "Empirical Fits to the Voigt Line Width: A Brief Review," *Journal of Quantitative Spectroscopy and Radiative Transfer*, vol. 17, pp. 233-236, 1977.
- [100] R. Barlow and G. Wang, "The correlation of differential diffusion and scalar dissipation in turbulent CH₄/H₂/N₂ flame," *Third European Combustion Meeting*, 2007.
- [101] D. Green and R. Perry, *Perry's Chemical Engineer Handbook*, McGraw-Hill, 1999.
- [102] A. Stancik and E. Brauns, "A simple asymmetric lineshape for fitting infrared absorption spectra," *Vibrational Spectroscopy*, vol. 47, pp. 66 - 69, 2008.
- [103] J. Edwards and C. Roy, "Preconditioned Multigrid Methods for Two-Dimensional Combustion Calculations at All Speeds," *AIAA*, vol. 36, no. 2, pp. 185 - 192, 1998.
- [104] A. Larsson, N. Zettervall, T. Hurtig, E. Nilson, A. Ehn, P. Petersson, M. Alden, J. Larfeldt and C. Fureby, "Skeletal Methane-Air Reaction Mechanism for Large-Eddy Simulation of Turbulent Microwave-Assisted Combustion," *Energy Fuels*, vol. 31, no. 2, pp. 1904 - 1926, 2017.
- [105] W. Meier, R. S. Barlow, Y.-L. Chen and J.-Y. Chen, "Raman/Rayleigh/LIF Measurements in a Turbulent CH₄/H₂/N₂ Jet Diffusion Flame: Experimental Techniques and Turbulence-Chemistry Interaction," *Combustion and Flame*, vol. 123, pp. 326 - 343, 2000.
- [106] S. Roy, P. Kinnius, R. Lucht and J. Gord, "Temperature measurements in reacting flows by time-resolved femtosecond coherent anti-Stokes Raman scattering (fs-CARS) spectroscopy," *Optics Communications*, vol. 281, pp. 319 - 325, 2008.
- [107] F. Vestin and P.-E. Bengtsson, "Rotational CARS for simultaneous measurements of temperature and concentrations of N₂, O₂, CO, and CO₂ demonstrated in a CO/air diffusion flame," *Proceedings of the Combustion Institute*, vol. 32, pp. 847 - 854, 2009.
- [108] J. Sutton and J. Driscoll, "Rayleigh scattering cross sections of combustion species at 266, 355, and 532 nm for thermometry applications," *Optics Letters*, vol. 29, no. 22, pp. 2620 - 2622, 2004.

- [109] M. Sneeep and W. Ubachs, "Direct measurement of the Rayleigh scattering cross section in various gases," *Journal of Quantitative Spectroscopy & Radiative Transfer*, vol. 92, pp. 293 - 310, 2005.
- [110] P. Varghese and R. Hanson, "Tunable diode laser measurements of spectral parameters of HCN at room temperature," *Journal of Quantitative Spectroscopy and Radiative Transfer*, pp. 545 - 559, 1983.
- [111] P. Varghese and R. Hanson, "Collisional narrowing effects on spectral line shapes measured at high resolution," *Applied Optics*, pp. 2376 - 2385, 1984.
- [112] R. H. Dicke, "The Effect of Collisions upon the Doppler Width of Spectral Lines," *Physical Review*, pp. 472 - 473, 1953.
- [113] S. Rautian and I. Sobel'man, "The effect of collisions on the Doppler broadening of spectral lines," *SOVIET PHYSICS USPEKHI*, pp. 701 - 716, 1966.
- [114] A. Bielski, R. Ciurylo, J. Domyslawska, D. Lisak, R. Trawinski and J. Szudy, "Laser-induced fluorescence study of collision-time asymmetry and speed-dependent effects on the 114Cd 326.1nm line perturbed by Xe," *Physical Review A*, pp. 1 - 10, 2000.
- [115] M. Harris, E. Lewis, D. McHugh and I. Shannon, "The full Voigt profile and collision time asymmetry for profiles of calcium 442.7 nm perturbed by krypton," *Journal of Physics B.*, pp. L661 - L667, 1984.
- [116] P. Berman, "Speed-dependent collisional width and shift parameters in spectral profiles," *Journal of Quantitative Spectroscopy and Radiative Transfer*, pp. 1331 - 1342, 1972.
- [117] J. Ward, J. Cooper and E. Smith, "Correlation effects in the theory of combined Doppler and pressure broadening - I. Classical theory," *Journal of Quantitative Spectroscopy and Radiative Transfer*, pp. 555 - 590, 1974.
- [118] P. Marteau, C. Boulet and D. Robert, "Finite duration of collisions and vibrational dephasing effects on the Ar broadened HF infrared line shapes: Asymmetric profiles," *Journal of Chemical Physics*, pp. 3632 - 3639, 1984.
- [119] A. O. Vyrodov, J. Heinze and U. E. Meier, "Collisional broadening of the spectral lines in the A-X (0-0) system of NO by N₂, Ar, and He at elevated pressures measured by laser induced fluorescence," *Journal of Quantitative Spectroscopy and Radiative Transfer*, vol. 53, no. 3, pp. 277 - 287, 1994.
- [120] V. Cooper, A. May, E. Hara and H. Knapp, "Dicke narrowing and collisional broadening of the S₀(0) and S₀(1) Raman line of H₂," *Canadian Journal of Physics*, pp. 2019 - 2023, 1968.
- [121] D. Ramachandra Rao and T. Oka, "Dicke Narrowing and Pressure Broadening in the Infrared Fundamental Band of HCl Perturbed by Ar," *Journal of Molecular Spectroscopy*, pp. 16 - 27, 1987.
- [122] L. Hejie, A. Farooq, J. Jeffries and R. Hanson, "Diode laser measurements of temperature-dependent collisional-narrowing and broadening parameters of Ar-perturbed H₂O transitions at 1391.7 and 1397.8nm," *Journal of Quantitative Spectroscopy and Radiative Transfer*, pp. 132 - 143, 2008.
- [123] C. Goldenstein, J. Jeffries and R. Hanson, "Diode laser measurements of linestrength and temperature-dependent lineshape parameters of H₂O-, CO₂-, and N₂-perturbed H₂O

- transitions near 2474 and 2482nm," *Journal of Quantitative Spectroscopy and Radiative Transfer*, pp. 100 - 111, 2013.
- [124] A. Pine, "Collisional Narrowing of HF Fundamental Band Spectral Lines by Neon and Argon," *Journal of Molecular Spectroscopy*, pp. 435 - 448, 1980.
- [125] R. Farrow, L. Rahn, G. Sitz and G. Rosasco, "Observation of a Speed-Dependent Collisional Inhomogeneity in H₂ Vibrational Line Profiles," *Physical Review Letters*, pp. 746 - 749, 1989.
- [126] R. Ciurylo, A. Pine and J. Szudy, "A generalized speed-dependent line profile combining soft and hard partially correlated Dicke-narrowing collisions," *Journal of Quantitative Spectroscopy and Radiative Transfer*, pp. 257 - 271, 2001.
- [127] D. Lisak, G. Rusciano and A. Sasso, "Speed-dependent and correlation effects on the line shape of acetylene," *Physical Review A*, pp. 012503-1 - 012503-8, 2005.
- [128] D. Lisak, A. Bielski, R. Ciurylo, J. Domyslawska, R. Trawinski and J. Szudy, "On the role of Dicke narrowing in the formation of atomic lineshapes in the optical domain," *Journal of Physics B: Atomic, Molecular, and Optical Physics*, pp. 3985 - 3998, 2003.
- [129] A. Pine, "Line shape asymmetries in Ar-broadened HF(V= 1 - 0) in the Dicke-narrowing regime," *Molecular Physics Division*, pp. 3444 - 3452, 1994.
- [130] R. Ciurylo and J. Szudy, "Speed-dependent pressure broadening and shift in the soft collision approximation," *Journal of Quantitative Spectroscopy and Radiative Transfer*, pp. 411 - 423, 1997.
- [131] J. Boissoles, F. Thibault, C. Boulet, J. Bouanich and J. Hartmann, "Spectral Lineshape Parameters Revisited for HF in a Bath of Argon," *Journal of Molecular Spectroscopy*, pp. 257 - 262, 1999.
- [132] A. Pine, "Asymmetries and correlations in speed-dependent Dicke-narrowed line shapes of argon-broadened HF," *Journal of Quantitative Spectroscopy and Radiative Transfer*, pp. 397 - 423, 1999.

APPENDICIES

Appendix A: Zircar Ceramic Insulation



General Information

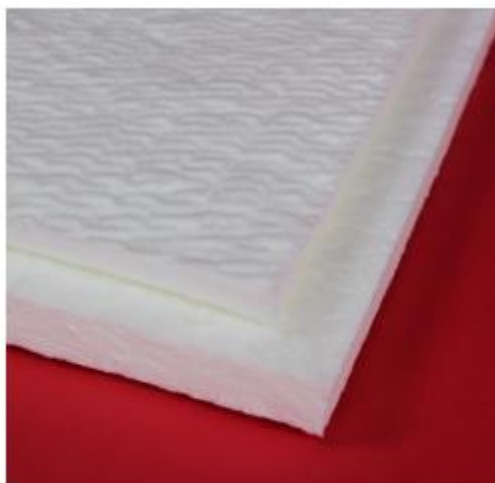
ZIRCAR Ceramics' Alumina Blankets Type NAB & Type NMB are mechanically-needled blankets made from shot-free, high-purity polycrystalline alumina fiber (PCW). These blankets contain no organic sizings and can be applied to numerous applications with continuous temperatures as high as 1800°C (2912°F).

These high-performance blankets exhibit light weight, low thermal conductivity, low thermal mass and immunity to thermal shock. NAB's high-alpha alumina and NMB's mullite fiber composition give both blankets good strength and high-temperature dimensional stability in applications with elevated temperatures and aggressive chemical environments.

NAB is most suitable in applications where SiO₂ cannot be tolerated and where the most chemically-stable blanket is needed.

NMB has good strength and can be cut into die-cut parts, incorporated into stack-bonded fiber modules or used in full roll lengths.

Alumina Blanket Type NAB & Type NMB



Characteristics & Properties

| Type | NMB | NAB |
|---|-------------------------------|----------|
| Nominal Composition, wt.% of fiber | | |
| Al ₂ O ₃ | 80 | 95 |
| SiO ₂ | 20 | 5 |
| α Al ₂ O ₃ | 5 maximum | 30 to 50 |
| Mullite | 50 to 70 | 5 to 16 |
| Al ₂ O ₃ + SiO ₂ | 99.7 minimum | |
| Fe ₂ O ₃ | 0.2 maximum | |
| Color | White | |
| Density (blanket), g/cc (pcf) | 0.1 (6.24) | |
| Average Fiber Diameter, μm | 3 to 5 | |
| Maximum Use Temperature*, °C (°F) | 1800 (2912) | |
| Loss on Ignition, wt.% | 0.3 maximum | |
| Shot Content, (% ≥ 100μm) | 2 maximum | |
| Linear Shrinkage, % after 24 hrs at 1500°C (2732°F) | Width and Length [†] | ≤1 |
| | Thickness** | ≤3 |

ZIRCAR Ceramics, Inc.

PO Box 519
100 N. Main St., Florida, NY 10921-0519
Telephone: (845) 851-8600
E-mail: sales@zircarceramics.com

Technical Data Bulletin
Alumina Blanket Type NAB & NMB
www.zircarceramics.com
Page 1 of 2

Alumina Blanket Type NAB & NMB

Characteristics & Properties Continued

| Thermal Conductivity, ASTM C177-76, W/m ² K (BTU/hr ft ² °F/in) | |
|---|-------------|
| 315°C (599°F) | 0.07 (0.50) |
| 540°C (1000°F) | 0.09 (0.70) |
| 780°C (1400°F) | 0.13 (0.90) |
| 980°C (1796°F) | 0.17 (1.25) |
| 1200°C (2192°F) | 0.23 (1.60) |
| 1425°C (2597°F) | 0.30 (2.15) |
| Tensile Strength, kg/cm ² | 0.2 minimum |
| Compressibility, % | 5 minimum |
| Resiliency, % | 5 minimum |

The data presented herein is intended to help the user to determine the appropriateness of this material for their application.

This data is a nominal representation of this product's properties and characteristics and therefore should not be used in preparing specifications.

* Maximum use temperature is dependent on variables such as stresses, both thermal and mechanical, and the chemical environment that the material experiences. ** Properties expressed parallel to thickness. † Properties expressed perpendicular to thickness.

Suggested Applications

Primary and backup thermal insulation in both periodic and continuous furnaces, and thermal process systems operating to 1600°C (2912°F).

Furnace insulation packing around sight tubes, burner blocks, ports, expansion joints, and masonry cracks.

Fabricating into shot-free folded and stack-bonded modules used in steel industry reheat furnaces.

Availability of Standard Blanket

| ITEM # | DESCRIPTION |
|----------|------------------------------------|
| D121D-01 | NMB, 620mm x 450mm x 12.5mm, SHEET |
| D121D-02 | NMB, 620mm x 1800mm x 12.5mm, ROLL |
| D121D-03 | NMB, 620mm x 7200mm x 12.5mm, ROLL |
| D121D-04 | NMB, 620mm x 450mm x 25mm, SHEET |
| D121D-05 | NMB, 620mm x 1800mm x 25mm, ROLL |
| D121D-06 | NMB, 620mm x 7200mm x 25mm, ROLL |
| D121A-01 | NAB, 620mm x 450mm x 25mm, SHEET |
| D121A-02 | NAB, 620mm x 1800mm x 25mm, ROLL |
| D121A-03 | NAB, 620mm x 7200mm x 25mm, ROLL |

To Order

Standard blanket: order online or specify quantity, item # and description.

Standard items are available for immediate shipment from stock.

Custom thicknesses (NMB), roll and sheet sizes, and die-cut parts can be manufactured.



ZIRCAR Ceramics, Inc.

PO Box 519

100 N. Main St., Florida, NY 10921-0519

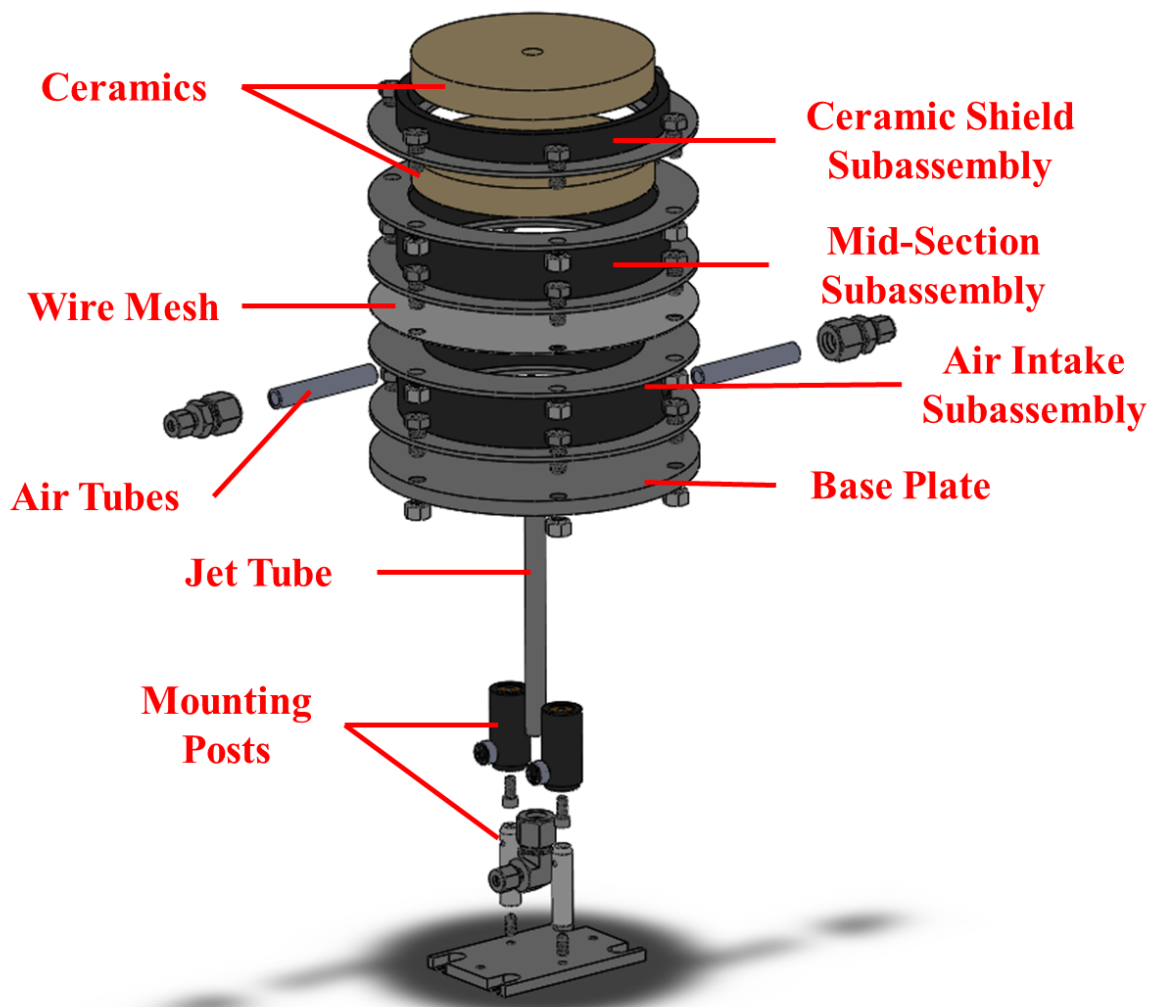
Telephone: (845) 651-6600

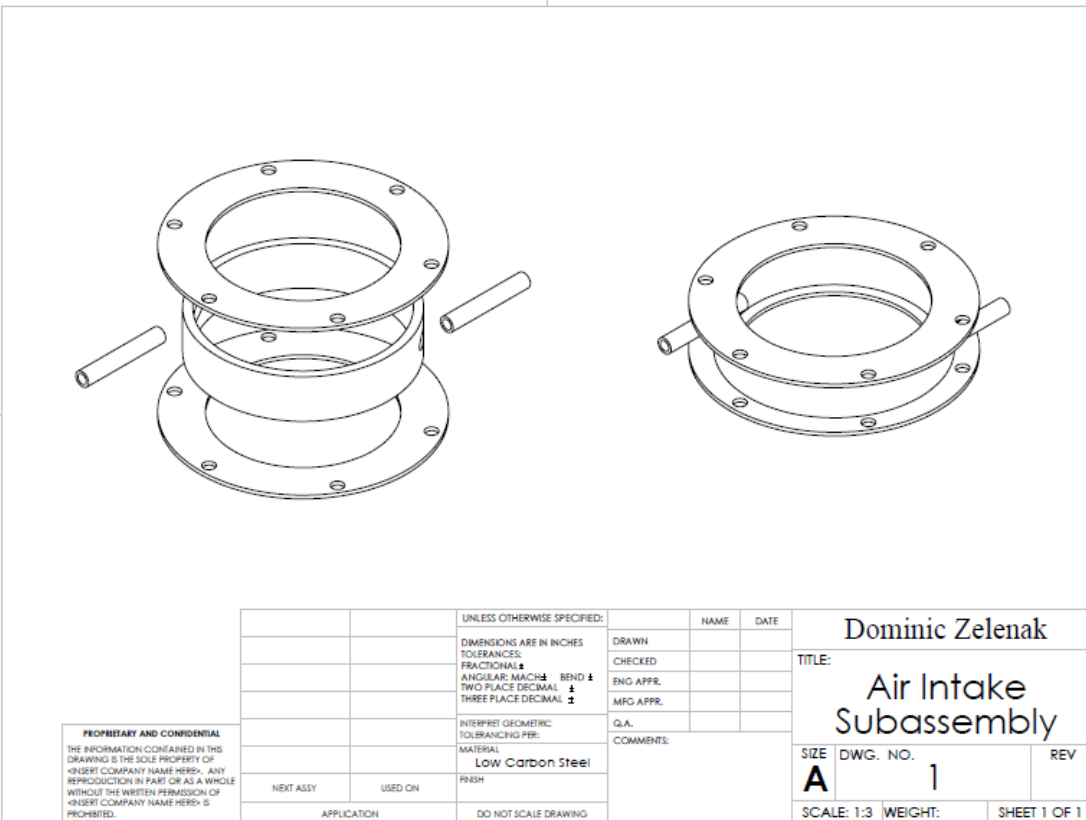
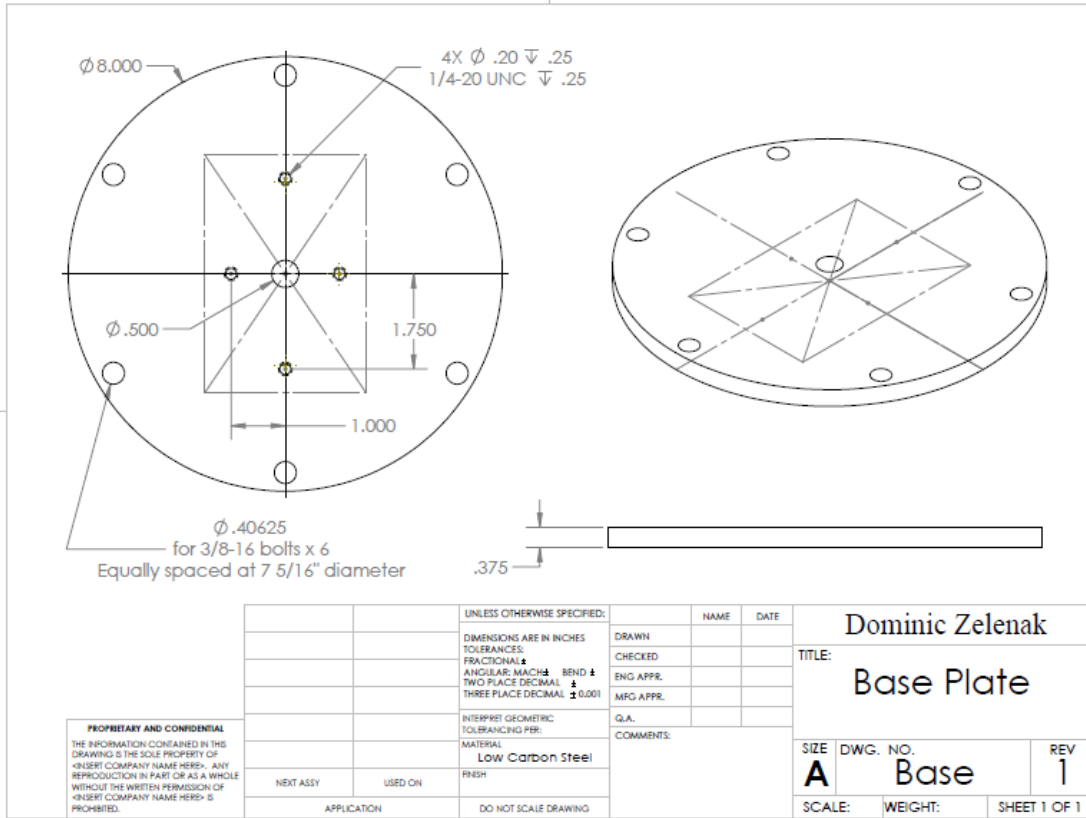
E-mail: sales@zircarceramics.com

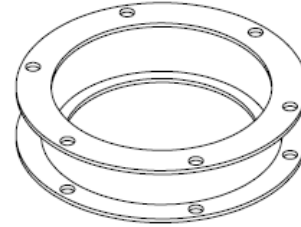
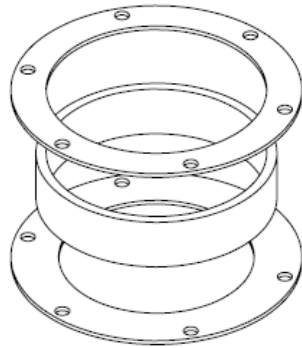
www.zircarceramics.com

Revision Date Dec. 8, 2016

Appendix B: Burner



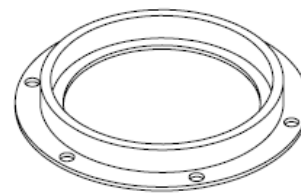
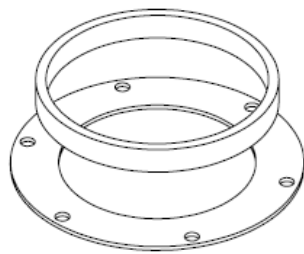




PROPRIETARY AND CONFIDENTIAL
 THE INFORMATION CONTAINED IN THIS DRAWING IS THE SOLE PROPERTY OF <INSERT COMPANY NAME HERE>. ANY REPRODUCTION IN PART OR AS A WHOLE WITHOUT THE WRITTEN PERMISSION OF <INSERT COMPANY NAME HERE> IS PROHIBITED.

| | | | | |
|-------------|---------|--------------------------------------|-----------|------|
| | | UNLESS OTHERWISE SPECIFIED: | NAME | DATE |
| | | DIMENSIONS ARE IN INCHES | DRAWN | |
| | | TOLERANCES | CHECKED | |
| | | FRACTIONAL ± | ENG APPR. | |
| | | ANGULAR: MATCH ± BEND ± | MFG APPR. | |
| | | TWO PLACE DECIMAL ± | Q.A. | |
| | | THREE PLACE DECIMAL ± | COMMENTS: | |
| | | INTERPRET GEOMETRIC TOLERANCING PER: | | |
| | | MATERIAL | | |
| | | Low Carbon Steel | | |
| NEXT ASSY | USED ON | FINISH | | |
| | | | | |
| APPLICATION | | DO NOT SCALE DRAWING | | |

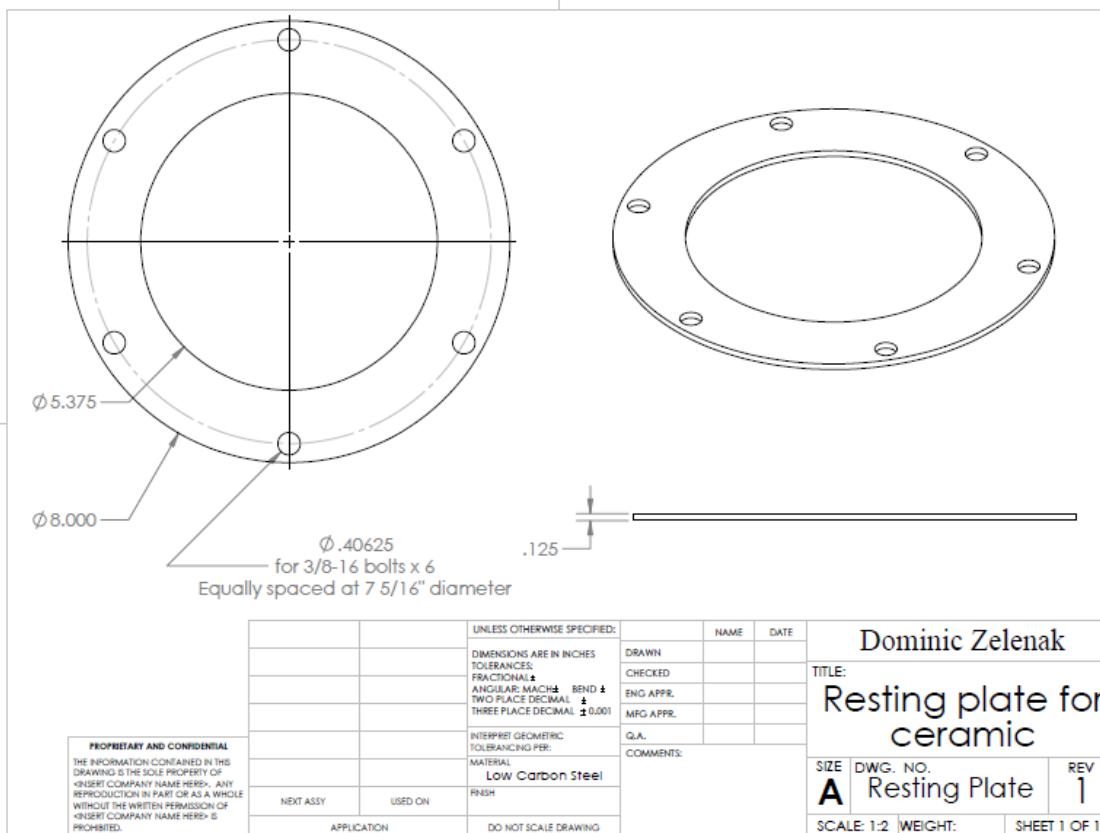
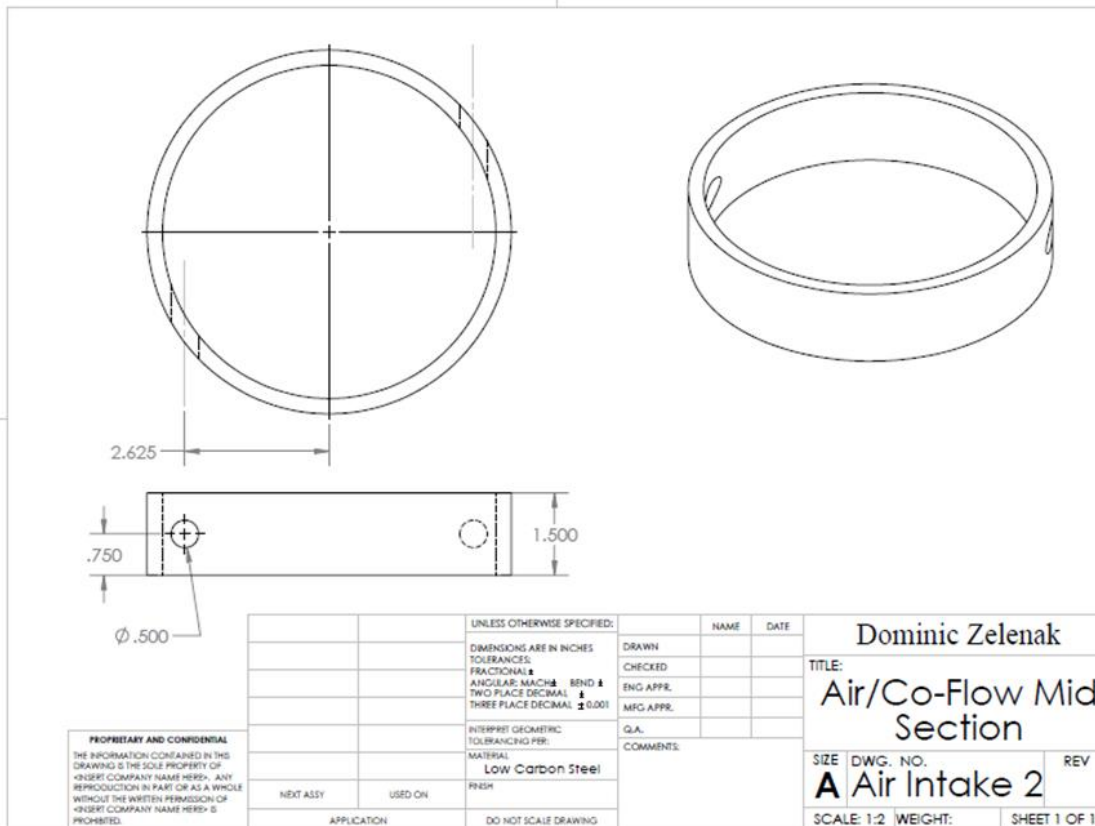
| | | |
|-------------------------|----------|--------------|
| Dominic Zelenak | | |
| TITLE: | | |
| Mid Section Subassembly | | |
| SIZE | DWG. NO. | REV |
| A | 2 | |
| SCALE: 1:3 | WEIGHT: | SHEET 1 OF 1 |

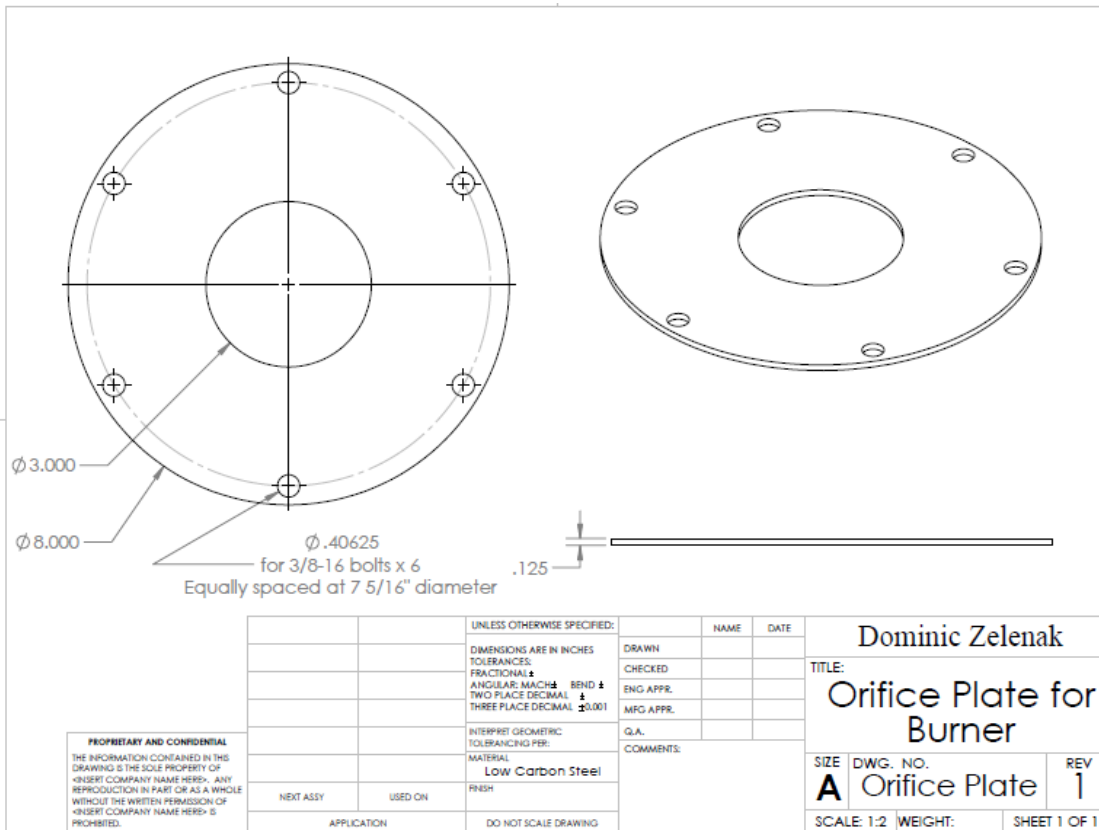
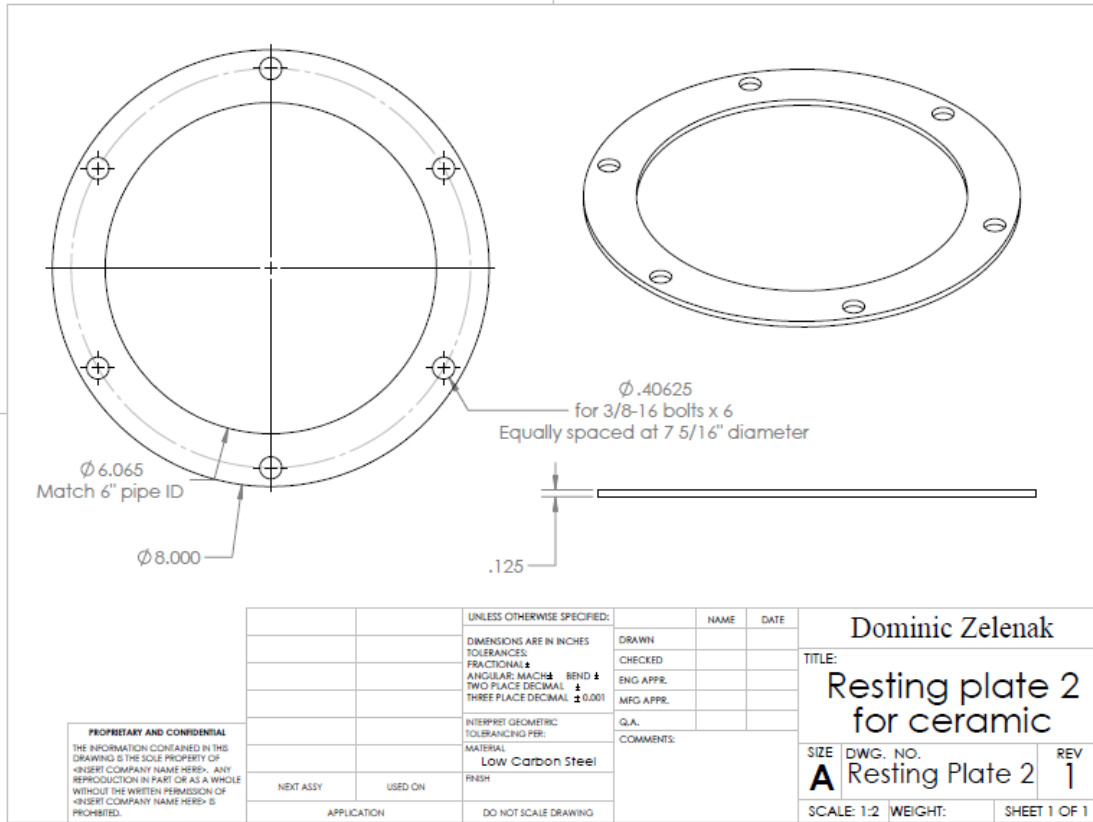


PROPRIETARY AND CONFIDENTIAL
 THE INFORMATION CONTAINED IN THIS DRAWING IS THE SOLE PROPERTY OF <INSERT COMPANY NAME HERE>. ANY REPRODUCTION IN PART OR AS A WHOLE WITHOUT THE WRITTEN PERMISSION OF <INSERT COMPANY NAME HERE> IS PROHIBITED.

| | | | | |
|-------------|---------|--------------------------------------|-----------|------|
| | | UNLESS OTHERWISE SPECIFIED: | NAME | DATE |
| | | DIMENSIONS ARE IN INCHES | DRAWN | |
| | | TOLERANCES | CHECKED | |
| | | FRACTIONAL ± | ENG APPR. | |
| | | ANGULAR: MATCH ± BEND ± | MFG APPR. | |
| | | TWO PLACE DECIMAL ± | Q.A. | |
| | | THREE PLACE DECIMAL ± | COMMENTS: | |
| | | INTERPRET GEOMETRIC TOLERANCING PER: | | |
| | | MATERIAL | | |
| | | Low Carbon Steel | | |
| NEXT ASSY | USED ON | FINISH | | |
| | | | | |
| APPLICATION | | DO NOT SCALE DRAWING | | |

| | | |
|----------------------------|----------|--------------|
| Dominic Zelenak | | |
| TITLE: | | |
| Ceramic Shield Subassembly | | |
| SIZE | DWG. NO. | REV |
| A | 3 | |
| SCALE: 1:3 | WEIGHT: | SHEET 1 OF 1 |





Appendix C: Osram SureHeat Jet

OPERATING INSTRUCTIONS
Doc #ZDF 2835463 Rev. 01 - Uncontrolled
09/07/2012



SureHeat[®] JET Air Heater & Control Panel

FOR SAFETY & LONG HEATER LIFE, CAREFULLY READ THIS MANUAL BEFORE USE.



Safety



SHOCK HAZARD!

Only qualified individuals should install this heater and related controls. Follow all applicable electrical codes and use proper wiring.



BURN/FIRE/EXPLOSION HAZARD!

Do not use in hazardous environments, and/or near explosive or reactive gases, or combustible materials. Avoid contact with the heater or exit accessories during or soon after operation. **DO NOT USE NEAR VOLATILE OR COMBUSTIBLE MATERIALS.**

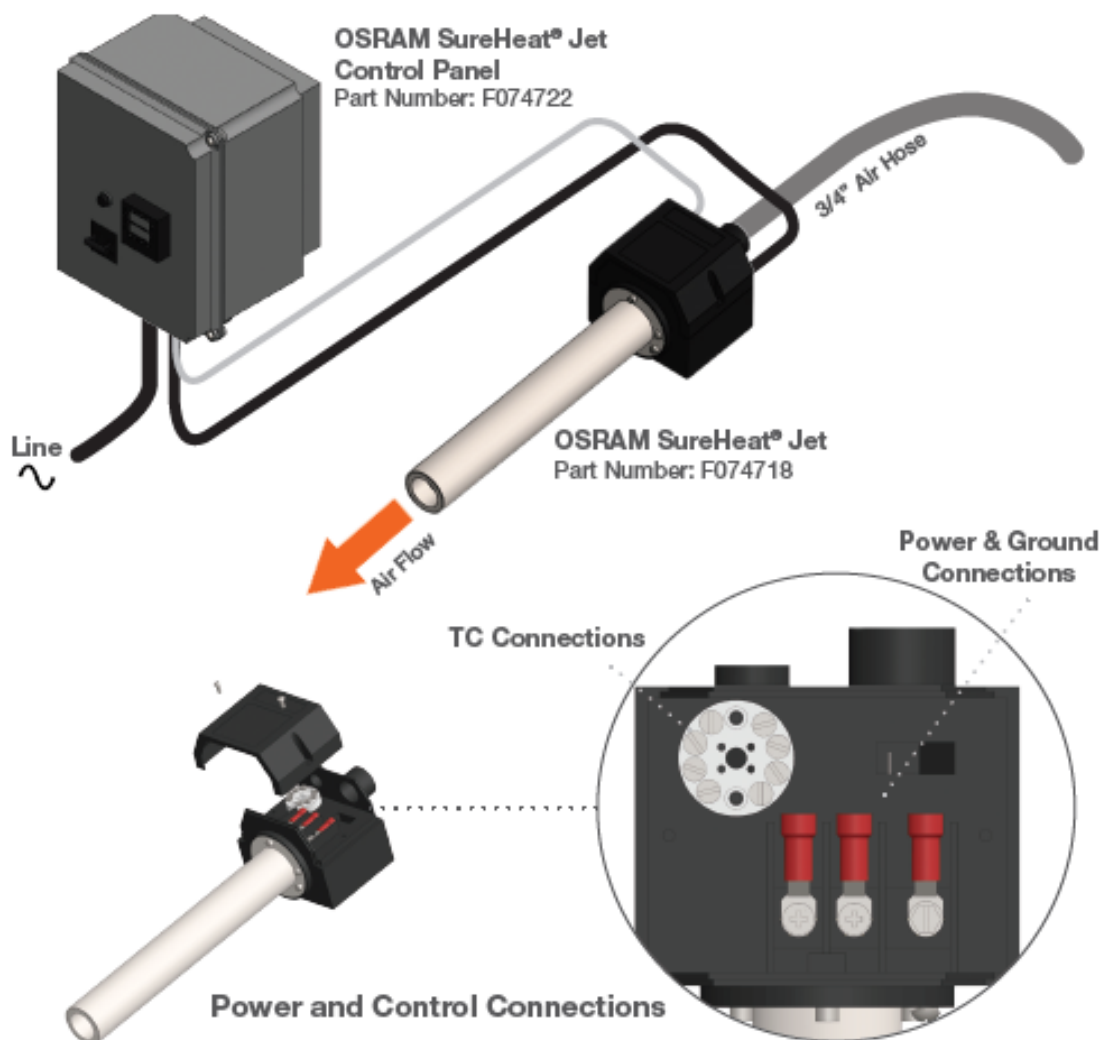
OSRAM SYLVANIA • 129 Portsmouth Avenue • Exeter, NH 03833 USA
☎ 800-258-8290 / 603-772-4331 📠 603-772-1072
Website: www.sylvaniaheaters.com E-mail: airheatersalesupport@sylvania.com

SureHeat® Jet Air Heater

General Description

The SureHeat® JET provides a compact and efficient heater solution for air temperatures up to 1400°F (760°C). Available in a 3.0kW or 8.0kW, 240V 1ø unit, the SureHeat® Jet offers two type "K" thermocouples with a convenient terminal block for easy wiring. To ensure safety, power and perfect control, connect with the optional SureHeat® Jet Control Panel. Each heater has a convenient method for mounting the housing and offers a ground stud located at the inlet of the heater.

Closed-Loop Connection Diagram



Heater Models and Parts List

| Part Number | Maximum Wattage | Maximum Volts | Maximum Amperage | Maximum Temperature |
|-------------|-----------------|---------------|------------------|---------------------|
| F074718 | 3000 | 240 – 1Ø | 12.5 | 1400°F / 760°C |
| F074719 | 8000 | 240 – 1Ø | 33.3 | 1400°F / 760°C |

Specifications

| | |
|-------------------------------|---|
| Maximum Inlet Air Pressure | 60 PSI (4 BAR) |
| Maximum Inlet Air Temperature | 200°F (93°C) |
| Maximum Exit Air Temperature | 1400°F (760°C) (see page 10 for Performance Curves) |
| Minimum Airflow | 120 SCFH (57 SLPM) |

| | |
|-----------------------|---|
| Exit Air Connection: | 1" FNPT |
| Inlet Air Connection: | 3/4" FNPT |
| Safety Approvals: | Heater: CE, UL Recognized, CSA Control Panel: CE, UL Listed, CSA |

| | |
|------------------------|---|
| Control/limit sensors: | Type "K" isolated, ungrounded, exposed junction TCs: S1 measures Inlet temperature S2 measures Exit temperature |
|------------------------|---|

General Information

| | |
|----------------------------------|-----------------------------|
| Environmental Conditions: | |
| Ambient Temperature | 32°F to 104°F (0°C to 40°C) |
| Humidity | 0% to 95% R.H. |

Ventilation:

Use in a well-ventilated area away from excess dust, dirt, and moisture.

Cleaning:

With unit OFF and unplugged, exterior surfaces may be wiped clean using a dry, lint-free cloth.

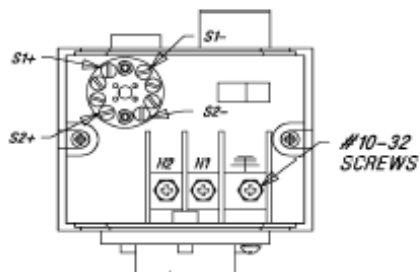
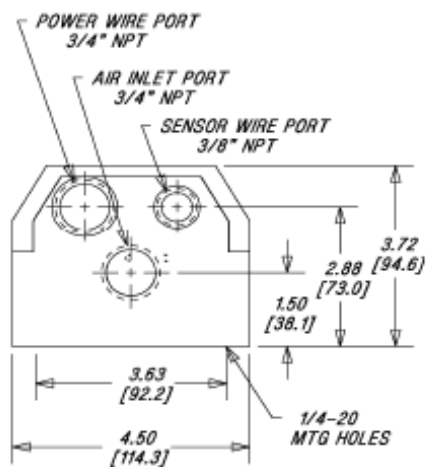
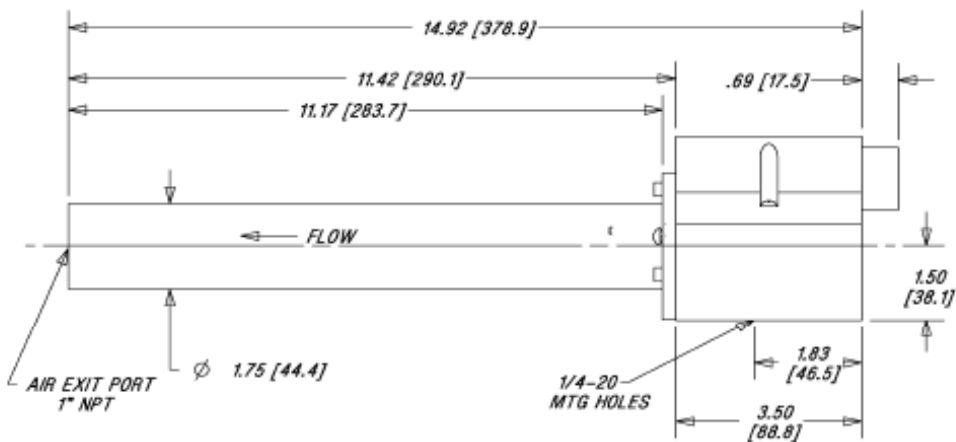
Protective Earthing:

Each heater comes with a convenient grounding stud and hardware located at the inlet of the heater for protective means of earthing.

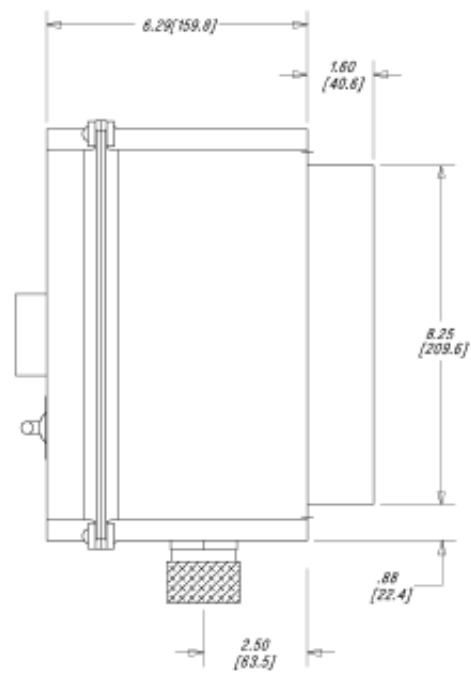
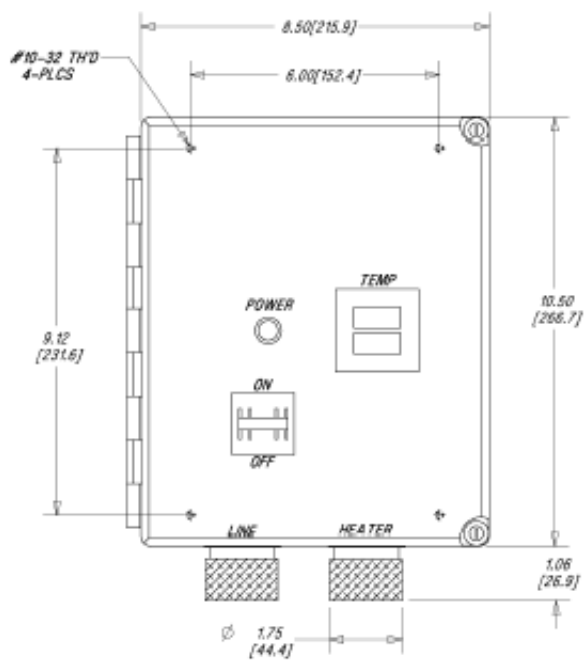
Dimensions/Mounting

NOTE: The inlet side of the heater is located where the leads/power feedthrus come out of the housing. Failure to install the heater in its proper orientation can result in heater damage and is not covered under the manufacturer's warranty.

Heater Dimensions:

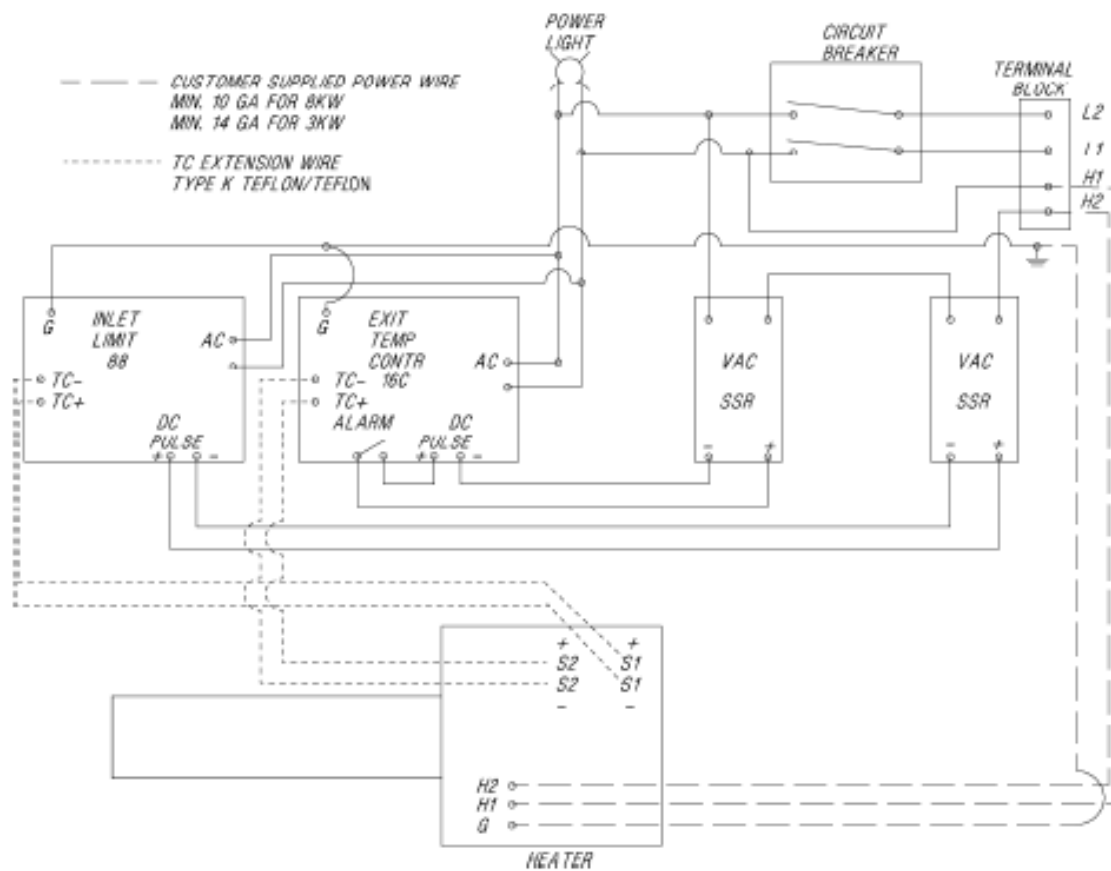


WARNING: Avoid Damage to Housing
 3/8" NPT (Sensor): 4 ft-lb
 3/4" NPT (Power): 25 ft-lb
 3/4" NPT (Air): 25 ft-lb
 (Excessive force will crack housing and void warranty)

SureHeat® JET Control Panel Dimensions:

Typical Wiring:

SureHeat® JET Control Panel for Closed Loop Control



Operation (with Heater)

START-UP

1. Reference the Performance Curves section (see page 10) for operational parameters before attempting to operate heater(s).
2. Connect air source to heater.
3. Turn on air and set pressure or flow to desired operating level.
4. Energize MAIN POWER line, and turn on SureHeat® JET CONTROL circuit breaker.
5. During operation, with constant airflow, the exit temperature will vary only a few degrees from set point. Although the heater will not burn out with zero airflow, if the heater is operated in a vertical downward position and an airflow of 2 SCFM or less is run through the heater, the inlet temperature of the heater will exceed 300°F (150°C) and the low limit controller will begin to limit power to the heater.
6. If using a closed loop system (SureHeat® JET Control Panel), turn on power to the temperature and power controller, then set the desired temperature on the temperature controller. If using an open loop system, increase power to the heater through the power controller until the desired temperature is attained.

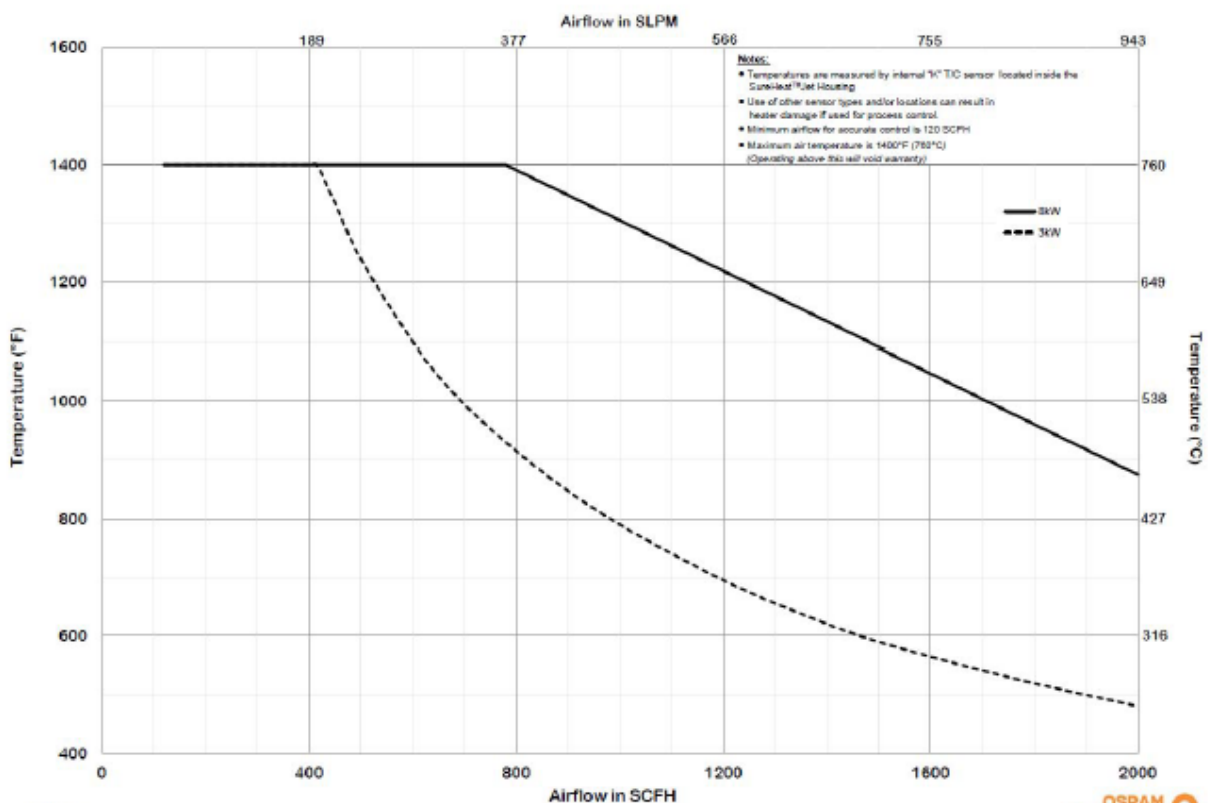
SHUT-DOWN

1. Turn off SureHeat® JET CONTROL circuit breaker, or disconnect MAIN POWER line.
2. Allow air to continue to flow for a minimum of 1 minute or until exit air temperature is 300°F (150°C) or less for safety. Continue airflow longer as necessary to prevent burn hazard to personnel.
3. Turn off air to the system.

Performance Curves

The attached performance curves show exit air temperatures at different airflows and voltages. Pressure readings (longer dashed lines) are measured at the inlet to the heater with no entrance or exit restrictions. Solid lines indicate safe, normal-life operating conditions. The shorter dash lines indicate marginal, shorter-life operating conditions leading to premature burnout. With a known flow (or pressure) at the heater entrance, follow the flow (or pressure) line across until it meets the desired temperature curve. Drop a line straight down to intersect the x-axis. This point, along the "Heater volts – true RMS" axis, represents the voltage required to generate the desired exit air temperature at the chosen flow rate (inlet pressure).

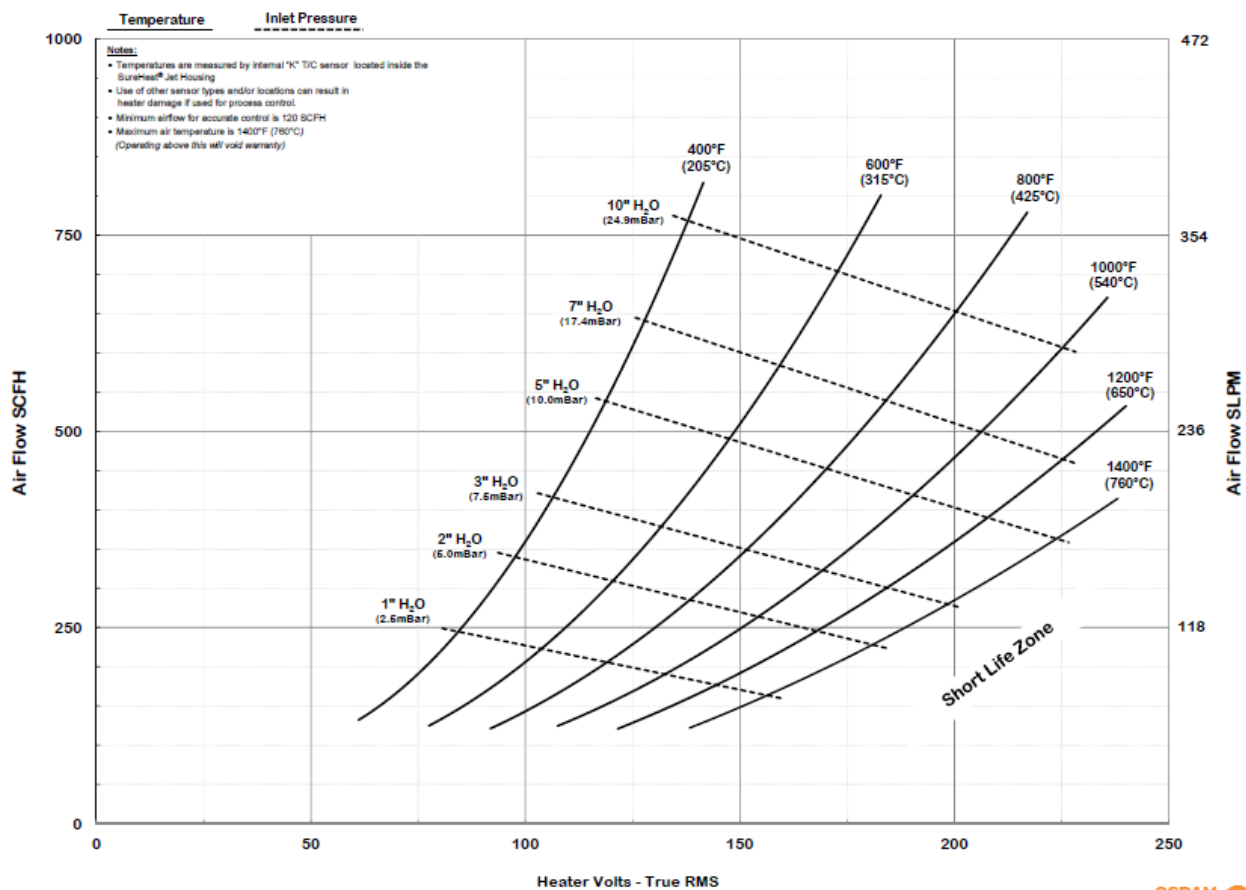
SureHeat® Jet Maximum Performance



Rev: 05/12



SureHeat® Jet Performance Curve - 3kW



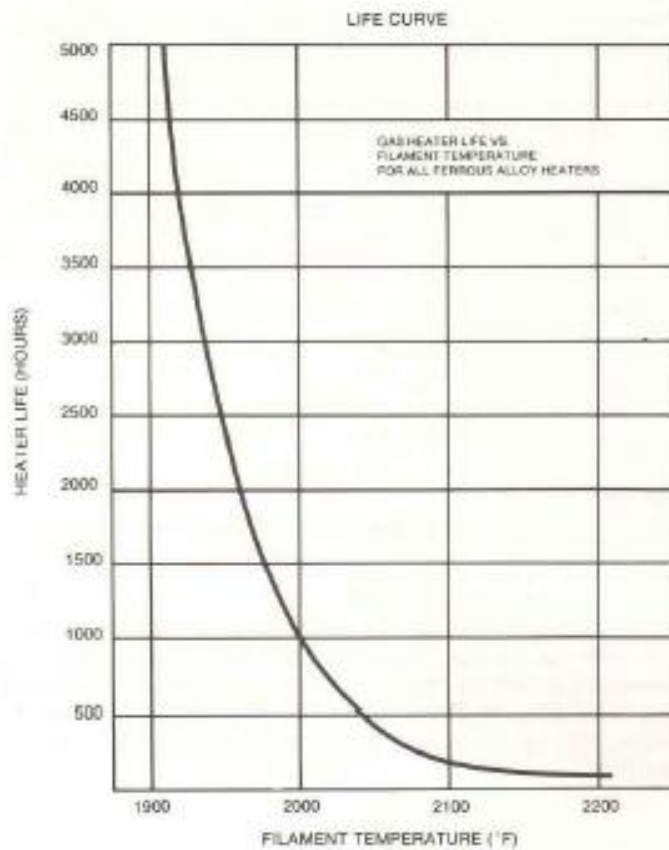
Rev: 10/15



Element Life Curve

(This is published by the element wire manufacturer. It is considered typically and not a guaranteed life)

The life of an OSRAM SYLVANIA heater is directly based on the temperature of the filament wire. The curve below shows that 5000 hours of life can be obtained by maintaining a filament temperature below 1900°F (1038°C). Also note that the element does not fail until it reaches more than 2200°F (1204°C)!



Appendix D: Theoretical Calculations of w_c and δ_c

From [68], the collisional broadening FWHM and shift for a perturber gas may be approximated using the following expressions:

$$w_c \text{ (cm}^{-1}\text{)} = \frac{1}{2} \rho_w^2 N_p \frac{\bar{v}}{c} \quad (49)$$

$$\delta_c \text{ (cm}^{-1}\text{)} = \frac{w_c}{2.8} \quad (50)$$

The value of N_p and \bar{v} are given by

$$N_p = \frac{p}{k_B T} \quad (51)$$

$$\bar{v} = \sqrt{\frac{8RT}{\pi\mu}} \quad (52)$$

Further, ρ_w for a London dispersive interaction dominated system may be obtained using

$$\rho_w = \left(\frac{2\pi\Delta C_6}{\bar{v}} \right)^{\frac{1}{5}} \quad (53)$$

The value of ΔC_6 may be calculated as

$$\Delta C_6 = \frac{5C_6}{h} \quad (54)$$

$$C_6 = \frac{\alpha_p \overline{p_a^2}}{(4\pi\epsilon_0)^2} \quad (55)$$

It should be noted that the factor of 5 in Equation (53) was obtained from the empirical difference of C_6 values between the ground and excited energy levels of NO [91] which had a similar electronic energy gaps as krypton. In the above, $\alpha_p = \frac{2\epsilon_0(n_p-1)}{n_0}$ and $\overline{p_a^2}$ is the mean square dipole moment of absorber. As an order of magnitude for $\overline{p_a^2}$, [68] suggests using the following relation $\overline{p_a^2} = e^2 9a_0^2$.

Appendix E: High-Pressure Lineshape Supplemental References

- Allard, N., & Kielkopf, J. (1982). The effect of neutral nonresonant collisions on atomic spectral lines. *Review of Modern Physics*, 54(4), 1103 - 1182.
- Berman, P. (1972). Speed-dependent collisional width and shift parameters in spectral profiles. *Journal of Quantitative Spectroscopy and Radiative Transfer*, 1331 - 1342.
- Bielski, A., Ciurylo, R., Domyslawska, J., Lisak, D., Trawinski, R., & Szudy, J. (2000). Laser-induced fluorescence study of collision-time asymmetry and speed-dependent effects on the ^{114}Cd 326.1nm line perturbed by Xe. *Physical Review A*, 1 - 10.
- Boissoles, J., Thibault, F., Boulet, C., Bouanich, J., & Hartmann, J. (1999). Spectral Lineshape Parameters Revisited for HF in a Bath of Argon. *Journal of Molecular Spectroscopy*, 257 - 262.
- Ciurylo, R. (1998). Shapes of pressure- and Doppler-broadened spectral lines in the core and near the wings. *Physical Review A*, 1029 - 1039.
- Ciurylo, R., & Szudy, J. (1997). Speed-dependent pressure broadening and shift in the soft collision approximation. *Journal of Quantitative Spectroscopy and Radiative Transfer*, 411 - 423.
- Ciurylo, R., Pine, A., & Szudy, J. (2001). A generalized speed-dependent line profile combining soft and hard partially correlated Dicke-narrowing collisions. *Journal of Quantitative Spectroscopy and Radiative Transfer*, 257 - 271.
- Cooper, V., May, A., Hara, E., & Knapp, H. (1968). Dicke narrowing and collisional broadening of the S₀(0) and S₀(1) Raman line of H₂. *Canadian Journal of Physics*, 2019 - 2023.
- Dicke, R. H. (1953). The Effect of Collisions upon the Doppler Width of Spectral Lines. *Physical Review*, 472 - 473.
- Farrow, R., Rahn, L., Sitz, G., & Rosasco, G. (1989). Observation of a Speed-Dependent Collisional Inhomogeneity in H₂ Vibrational Line Profiles. *Physical Review Letters*, 746 - 749.
- Galatry, L. (1961). Simultaneous Effect of Doppler and Foreign Gas Broadening on Spectral Lines. *Physical Review*, 1218 - 1223.
- Goldenstein, C., Jeffries, J., & Hanson, R. (2013). Diode laser measurements of linestrength and temperature-dependent lineshape parameters of H₂O-, CO₂-, and N₂-perturbed H₂O transitions near 2474 and 2482nm. *Journal of Quantitative Spectroscopy and Radiative Transfer*, 100 - 111.
- Harris, M., Lewis, E., McHugh, D., & Shannon, I. (1984). The full Voigt profile and collision time asymmetry for profiles of calcium 442.7 nm perturbed by krypton. *Journal of Physics B*, L661 - L667.
- Hedges, R., Drummond, D., & Gallagher, A. (1972). Extreme-Wing Line Broadening and Cs-Inert-Gas Potentials*. *Physical Review A*, 1519 - 1544.
- Hejje, L., Farooq, A., Jeffries, J., & Hanson, R. (2008). Diode laser measurements of temperature-dependent collisional-narrowing and broadening parameters of Ar-perturbed

- H₂O transitions at 1391.7 and 1397.8nm. *Journal of Quantitative Spectroscopy and Radiative Transfer*, 132 - 143.
- Lisak, D., Bielski, A., Ciurylo, R., Domyslawska, J., Trawinski, R., & Szudy, J. (2003). On the role of Dicke narrowing in the formation of atomic lineshapes in the optical domain. *Journal of Physics B: Atomic, Molecular, and Optical Physics*, 3985 - 3998.
- Lisak, D., Rusciano, G., & Sasso, A. (2005). Speed-dependent and correlation effects on the line shape of acetylene. *Physical Review A*, 012503-1 - 012503-8.
- Marteau, P., Boulet, C., & Robert, D. (1984). Finite duration of collisions and vibrational dephasing effects on the Ar broadened HF infrared line shapes: Asymmetric profiles. *Journal of Chemical Physics*, 3632 - 3639.
- Nelkin, M., & Ghatak, A. (1964). Simple Binary Collision Model for Van Hove's $G_s(r,t)$. *Physical Review*, A4 - A9.
- Pine, A. (1980). Collisional Narrowing of HF Fundamental Band Spectral Lines by Neon and Argon. *Journal of Molecular Spectroscopy*, 435 - 448.
- Pine, A. (1994). Line shape asymmetries in Ar-broadened HF($V=1-0$) in the Dicke-narrowing regime. *Molecular Physics Division*, 3444 - 3452.
- Pine, A. (1999). Asymmetries and correlations in speed-dependent Dicke-narrowed line shapes of argon-broadened HF. *Journal of Quantitative Spectroscopy and Radiative Transfer*, 397 - 423.
- Pine, A., & Looney, J. (1987). N₂ and Air Broadening in the Fundamental Bands of HF and HCl. *Journal of Molecular Spectroscopy*, 41 - 55.
- Rabitz, H. (1974). Rotational and rotational-vibrational pressure broadened spectral lineshapes. *Annual Review of Physical Chemistry*, 155 - 177.
- Ramachandra Rao, D., & Oka, T. (1987). Dicke Narrowing and Pressure Broadening in the Infrared Fundamental Band of HCl Perturbed by Ar. *Journal of Molecular Spectroscopy*, 16 - 27.
- Rautian, S., & Sobel'man, I. (1966). The effect of collisions on the Doppler broadening of spectral lines. *SOVIET PHYSICS USPEKHI*, 701 - 716.
- Thorne, A., Litzen, U., & Johansson, S. (1999). *Spectrophysics: Principles and Applications*. Springer Science & Business Media.
- Varghese, P., & Hanson, R. (1983). Tunable diode laser measurements of spectral parameters of HCN at room temperature. *Journal of Quantitative Spectroscopy and Radiative Transfer*, 545 - 559.
- Varghese, P., & Hanson, R. (1984). Collisional narrowing effects on spectral line shapes measured at high resolution. *Applied Optics*, 2376 - 2385.
- Wang, J. (2013). *Dicke narrowing and speed-dependent effects in dispersion signals*.
- Ward, J., Cooper, J., & Smith, E. (1974). Correlation effects in the theory of combined Doppler and pressure broadening - I. Classical theory. *Journal of Quantitative Spectroscopy and Radiative Transfer*, 555 - 590.